University of Bath

PHD

Synthesis, self-assembly and liquid structure in deep eutectic solvents

Atri, Ria

Award date:
2023

Awarding institution:
University of Bath

Link to publication

Alternative formats
If you require this document in an alternative format, please contact:
openaccess@bath.ac.uk

Copyright of this thesis rests with the author. Access is subject to the above licence, if given. If no licence is specified above, original content in this thesis is licensed under the terms of the Creative Commons Attribution-NonCommercial 4.0 International (CC BY-NC-ND 4.0) Licence (https://creativecommons.org/licenses/by-nc-nd/4.0/). Any third-party copyright material present remains the property of its respective owner(s) and is licensed under its existing terms.

Take down policy
If you consider content within Bath's Research Portal to be in breach of UK law, please contact: openaccess@bath.ac.uk with the details. Your claim will be investigated and, where appropriate, the item will be removed from public view as soon as possible.

Download date: 19. Oct. 2023

Synthesis, self-assembly and liquid structure in deep eutectic solvents

submitted by

Ria Atri

for the degree of Doctor of Philosophy

of the

University of Bath

Department of Chemistry

March 2022

COPYRIGHT

Attention is drawn to the fact that copyright of this thesis/portfolio rests with the author and copyright of any previously published materials included may rest with third parties. A copy of this thesis/portfolio has been supplied on condition that anyone who consults it understands that they must not copy it or use material from it except as licenced, permitted by law or with the consent of the author or other copyright owners, as applicable.

Access to this thesis in print or electronically can be obtained from the University of Bath Library.

Signed on behalf of the Doctoral College ....

Abstract

Deep eutectic solvents (DES) are a relatively recently reported class of solvent, typically synthesised through the formation of a eutectic mixture between Lewis acidic and Lewis basic components at a particular molar ratio, such as an organic halide salt and a neutral molecule. The most well known example of a DES is the eutectic formed between choline chloride and urea in a 1:2 molar ratio. Over the last two decades, DES have been increasingly investigated as non-aqueous alternative solvents in a wide range of processes, from chemical synthesis to separations and extractions. One property which makes them especially suitable for applications such as the synthesis of functional materials is the ability to tune the solvent properties, and hence the nature of the product, simply through a variation of the DES composition. Additionally, they can provide structural directing effects and novel reaction pathways which make them ideally suited to the development of functional materials. To be able to exploit this fully, it is also crucial to gain a fundamental understanding of the liquid structure of the DES and its interactions with other molecules, such as surfactants or water. In this thesis the synthesis of materials, the self-assembly of surfactant molecules and the liquid structure of DES is explored. The work is presented as three self-contained projects, each related to furthering the understanding of the properties and applications of DES.

The possibility of synthesising transition metal oxides and sulfides via a solvothermal synthesis method was first explored, together with some characterisation of the morphology and electrochemical performance of the products. For the synthesis of oxides in choline chloride:urea, it was shown that reactions typically proceed only when water is added to the DES. The reactions attempted during this project were summarised and the limitations of the solvothermal method were discussed. A polymeric DES based on polyethylene glycol-200 was investigated for the synthesis of mixed Co-Fe sulfides. The catalytic activity of the samples towards the hydrogen evolution reaction (HER) was assessed using a three-electrode electrolytic cell.

DES have also been investigated in recent years for their ability to support the self-assembly of molecules, which introduces the possibility of synthesising porous materials via the use of surfactants as soft templates. Designing systems which support both the micellisation of surfactants and the synthesis of materials is therefore advantageous. In the second part of this project, the self assembly of cationic alkyltrimethylammonium bromide surfactants, which are insoluble in choline chloride:urea, was successfully demonstrated in a three component system comprising choline chloride, urea and glycerol. The physiochemical properties of the three component DES were characterised, and the factors which influence the solubility and micellisation of C_{16}TAB was investigated using small-angle neutron scattering (SANS). It was determined that the degree of elongation in the micelles could be controlled by varying the urea:glycerol ratio in the DES, and this was attributed to the degree of solubility of the surfactant counterion in each solvent composition. The effect of water and metal ion addition on the DES was also discussed. Finally, experiments were also carried out to explore the use of these surfactant/DES mixtures for the synthesis of metal oxide materials.

In the last section of this this thesis, the liquid structure of the ChCl:urea:glycerol DES was investigated using total neutron scattering, in order to characterise the intermolecular interactions present within the system and determine the effect on the structure of varying the component ratio. The effect of water and metal ion addition on the structure was also investigated. Empirical Structure Potential Refinement (EPSR) was used as an analysis method to extract key parameters from the experimental data.

Acknowledgements

Firstly, I would like to thank my supervisors; Professor Karen Edler, Dr Hannah Leese and Dr Salvador Eslava for their continued guidance and support throughout this project. Thank you especially to Karen and Hannah for all the help and moral support when navigating this PhD project in the tough final stages and during a pandemic.

To my friends and colleagues in the Edler and Eslava groups, in particular Oli, Iva, Niamh, Elly, Miriam, Emma, and Shawn, thanks for all your help and support with experiments, and for making my PhD experience so enjoyable.

I would also like to thank the numerous people without whom this PhD project could not have been realised. Firstly, I would like to thank the instrument specialists from MC^2 at the University of Bath. Thanks to Dr Rèmi Castaing for training and help with SAXS measurements and for carrying out BET measurements. Dr Gabriele Kociok-Kohn provided training and support with XRD and collected measurements during the COVID-19 pandemic. Thank you to Ursula Potter, Dr Philip Fletcher and Diana Lednitzky for assisting with SEM measurements. Dr Martin Levere assisted with collecting DSC data.

My sincere thanks must also go to the instrument scientists on NIMROD, SANDALS and ZOOM at ISIS Neutron and Muon Source - Dr Tom Headen, Dr Tristan Youngs, Dr James Doutch, Dr Sabrina Gaertner, Dr Oliver Alderman and Dr Daniel Bowron. Thank you for your support with experiments and data analysis, and for running samples during the COVID-19 pandemic. Your interest and enthusiasm for neutrons and this work made every beamtime a fun experience. To Daniel, an extra thank you for helping me get my head around EPSR and for being so patient with my multiple requests for help.

This PhD project received funding from the EPSRC Centre for Doctoral Training in Sustainable Chemical Technologies, EPSRC Grant EP/L016354/1 and ISIS Neutron and Muon Source (STFC) under experiment numbers RB1910484, RB2010640 and

RB2010653.

Being part of the CSCT also allowed me to meet some wonderful people. Thank you also to Cohort '16 for your friendship and good humour, and especially to Vicky, Liana, Alba, Izzy, Megan, Natalie, Helen, Jess, Stef and Ioli. My time in Bath was made so much better because of the numerous office chats, coffee trips, board game evenings, film nights and spontaneous evening gelato expeditions.

To the friends whom I have been fortunate to know for so many years - Kristina, Dan, Ange, Pallavi, Holly and Paul - even though we have been scattered across the country for several years, you have always been there for me.

My final thanks go to my wonderful parents, my sister Sara and to James. Thank you for all your love, patience and support which got me to the end of this long journey.

Declaration of authorship

The material presented here for examination for the award of a higher degree by research has not been incorporated into a submission for another degree.

I am the author of this thesis, and the work described therein was carried out by myself personally, with the following exceptions:

Chapter 4

Small-angle neutron scattering experiment RB1910484 was jointly carried out by me and Dr Iva Manasi. XRD measurements for ZnO powder were collected by Dr Gabriele Kociok-Kohn, and nitrogen adsorption measurements were carried out by Dr Rèmi Castaing due to laboratory access restrictions during the COVID-19 pandemic.

Chapter 5

The neutron diffraction experiment RB2010653 was run remotely due to facility access restrictions during the COVID-19 pandemic. Samples were prepared by me at Bath and sent to ISIS, where they were run on the NIMROD instrument by Dr Tom Headen and Dr Tristan Youngs.

[redacted]

Ria Atri
March 2022

Contents

List of Abbreviations

Abbreviation	**Meaning**
API	Active pharmaceutical ingredient
ATLAS	Analysis of Time-of-flight diffraction data from Liquid and Amorphous Samples
C_{12}TAB	Dodecyltrimethylammonium bromide
C_{16}TAB	Hexadecyltrimethylammonium bromide
$C_{16}TANO_3$	Hexadecyltrimethylammonium nitrate
ChCl	Choline chloride
CMC	Critical micelle concentration
DES	Deep eutectic solvent(s)
DFT	Density functional theory
DSC	Differential scanning calorimetry
EPSR	Empirical Potential Structure Refinement
HBA	Hydrogen bond acceptor
HBD	Hydrogen bond donor
IL	Ionic liquid
MC	Monte Carlo (simulation)
MD	Moledular dynamics (simulation)
NADES	Natural deep eutectic solvents
NIMROD	The Near and Intermediate Range Order Diffractometer
PCF	Pair correlation function
PEG	Polyethylene glycol
RDF	Radial distribution function
RMC	Reverse Monte Carlo

SANDALS	Small Angle Neutron Diffractometer for Amorphous and Liquid Samples
SANS	Small-angle neutron scattering
SAXS	Small-angle X-ray scattering
SDF	Spatial density function
SDG(s)	Sustainable Development Goal(s)
SDS	Sodium dodecyl sulfate
SEM	Scanning electron microscopy
SLD	Scattering length density
TEM	Transmission electron microscopy
THEDES	Therapeutic deep eutectic solvents
VFT	Vogel–Fulcher–Tammann (equation)
XRD	X-ray diffraction

List of Figures

List of Tables

Chapter 1

Introduction

This thesis concerns an exploration of synthesis, self-assembly and the liquid structure of deep eutectic solvents (DES). In this chapter, solvents in general are first introduced and the development of deep eutectic solvents (DES) is described, together with a discussion of their properties and applications. Finally, an overview of the structure of the thesis is given.

1.1 Solvents

The use of solvents is critical to the global supply chain. They are used in a vast range of industrial processes; to extract and process raw materials, to manufacture goods and facilitate their distribution. The global solvent market is valued at tens of billions of US dollars and some examples of the main industries where solvents are used include paints and coatings, inks, pharmaceuticals, cleaning, personal care products and adhesives. The idea of 'conventional' solvents applies mainly to molecular liquids, with common examples including water, alcohols, ketones, hydro- and fluorocarbons, amines and carboxylic acids.

Amongst the United Nations' 17 Sustainable Development Goals (SDGs) [26], there are several which can be related to the improvement of current industrial processes to make them more sustainable, either through improving efficiency, better sourcing and use of materials or reducing waste. Organic solvents are prevalent in many chemical industries, as mentioned above, and several synthesis or processing steps produce large amounts of solvent waste [27]. Additionally, most of these solvents are derived from non-renewable fossil fuel sources, in addition to some having significant drawbacks such as high flammability, toxicity, non-biodegradability and the resulting atmospheric accumulation [28]. With a view to encouraging the use of more environmentally friendly solvents, many 'solvent selection' guides have been produced both by pharmaceutical companies and other agencies [29–31].

The strategies for solvent selection, in which certain solvents are often recommended to be avoided and others suggested as suitable replacements within a certain category, typically focus on finding alternative molecular solvents for use in a certain process. Another popular strategy for better embracing the principles of green chemistry is to focus research on replacing these solvents with alternative neoteric solvents which may not only be more environmentally benign, but may even enhance the efficiency of the existing process due to their unique properties. Amongst those solvents investigated are water, supercritical fluids, liquid polymers, solvents derived from biomass/renewable sources, ionic liquids, and deep eutectic solvents [32].

1.2 Ionic liquids

The chemist Paul Walden reported the first ionic liquid (IL) over a century ago, when he observed that the salt ethylammonium nitrate (melting temperature = 12 °C) remained in the liquid state at room temperature [33,34]. The electrical conductivity of this liquid was that which one would expect to observe for a mixture consisting almost purely of anions and cations. Since then, mostly within the last thirty years, many more ionic liquids have been reported and investigated for a variety of applications, some of which will be outlined below. Research in this field has been further accelerated by the focus on green solvents as alternatives to conventional organic solvents, for the reasons outlined in the previous section.

Ionic liquids exist in the liquid state at ambient temperatures due to the destabilisation of the solid-phase crystal, achieved through careful selection of the cationic and anionic components, some examples of which are given in Figure 1.1. ILs are typically classified by their structural types, including protic, chiral, polarisable, amphiphilic, and metal salt-based ILs [35]. They possess several favourable properties which make them suitable both as alternative solvents and for other applications. They typically have very low vapour pressures and so low volatilities [36], can facilitate the dissolution of a range of polar and non-polar substances [37] and have high chemical and thermal stabilities [38].

The tunable nature of ILs means that careful choice of components can be used to synthesise a solvent with the required properties for a specific application. In chemical processes, ILs have had multiple functions: as reagents, solvents, catalysts or a mixture of these [39]. Some examples of the applications for which ILs have been used include organic transformations, extraction processing, analytical chemistry including chromatography techniques, biomedical applications, and in electrochemistry (both in devices and for electrofinishing applications) [40].

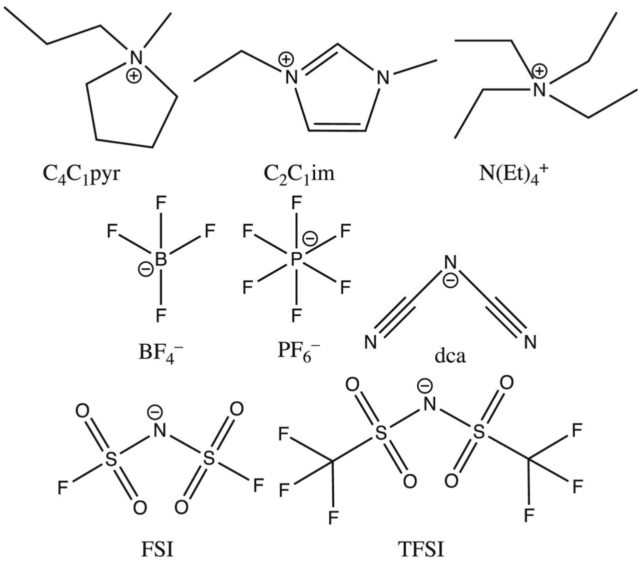

Figure 1.1: Some examples of ions commonly used in the synthesis of ILs, together with their abbreviations. Reproduced from Reference [1] under a Creative Commons Attribution Licence.

Although ILs are commonly accepted as alternative solvents, they do pose significant drawbacks, especially where the aim of modifying a process may be to make it more environmentally benign by taking into account green chemistry principles. There are many concerns as to the complex and expensive manufacturing process, often requiring materials sourced from fossil fuels and generating harmful intermediates [41, 42]. This can, in part, be improved by investigating alternative synthesis methods, such as selecting bio-based or renewable cations/anions [43, 44] and using heating methods such a microwave-assisted synthesis [45].

1.3 Deep eutectic solvents

1.3.1 Introduction to deep eutectic solvents

It is commonly reported in the field that the formation of a deep eutectic solvent (DES) was first reported in 2001 by Abbott et al., discovered during the group's search for low transition temperature liquid electrolytes [46], although prior to this there were studies in the literature concerning eutectic liquids containing a mixture of phamaceutical components [47]. It was observed that the quaternary ammonium salt choline chloride (ChCl), acting as a hydrogen bond acceptor in combination (with urea as a neutral hydrogen bond donor) combined in a specific molar ratio (1 ChCl : 2 urea) gave rise to a stable mixture with a melting point far lower than the melting point of their individual components (Figure 1.2). The term *deep eutectic solvent* was not used to refer to these mixtures until two years later [48].

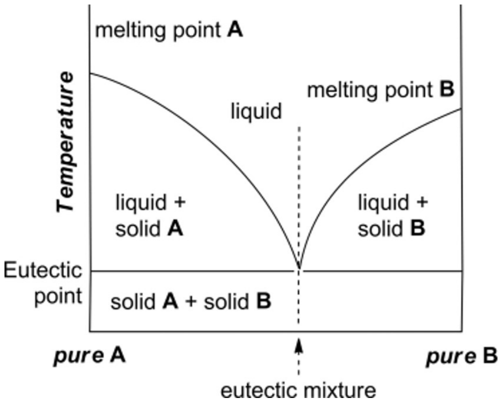

Figure 1.2: A phase diagram showing the formation of the eutectic mixture from the solid components A and B. Reproduced with from Reference [2] with permission from Wiley-VCH. © 2016 Wiley-VCH Verlag GmbH & Co. KGaA, Weinheim.

DES are widely defined as a sub-class of ionic liquids, and indeed are very often compared to them in the literature, but the presence of a significant molecular component in a typical DES structure gives them a hybrid molecular/ionic nature in contrast to the entirely ionic nature of ILs. The most commonly identifiable type is the combination of a quaternary ammonium salt (as the hydrogen bond acceptor) with a hydrogen bond donor molecule. Some examples are given in Table 1.3.1. Several studies have revealed that the structure of a DES is governed by an extended hydrogen-bonded network.

DES are typically binary mixtures, though systems with more components have also been reported [49, 50]. DES are typically classified into four categories [51] according to the nature of their components:

- Type I DES, formed through the complexation of a quaternary ammonium salt with a metal chloride, where the metals might include zinc, iron, aluminium or indium. Many early ionic liquids, such as halometallate ionic liquids, may also be included in this category.

- Type II DES, which are similar to type I DES, except that the metal halide is hydrated.

- Type III DES, formed from a quaternary ammonium salt and a hydrogen bond donor molecule are the most recognised DES types. Many hydrogen bond donor molecules have been reported to date, including urea, alcohol molecules such as ethylene glycol, and various carboxylic acids. The most well-known of these is the above mentioned choline chloride:urea DES.

- Type IV DES, metal salts such as those based on zinc or cerium in combination with a hydrogen bond donor molecule such as urea, acetamide or ethylene glycol.

Two more categories of DES have since been reported; 'natural deep eutectic solvents' (NADES) [52], comprising mainly plant-based primary metabolites including sugars, alcohols, amino acids, amines and organic acids, which have favourable properties such as hydrophobicity and high polarity [53]. DES containing an active pharmaceutical component (API) have also been reported and termed 'therapeutic deep eutectic solvents' (THEDES) [54], though these in themselves could be described as a sub-category of NADES. To date, over 130 NADES have been reported with applications in synthesis and separation/extractions.

Figure 1.3 shows a number of the molecules which have been reported as DES components in the literature, though it is hypothesised that there could be tens of millions of possible combinations of components [59]. This vast range of possibilities has led to DES often being described as the 'ultimate' designer solvent, providing the opportunity to tailor the properties of a chosen DES directly to suit a certain application. Often, the components are cheap, non-toxic and biodegradable (especially in the case of NADES) [60, 61], an advantage which is not often the case with ionic liquids.

Research into deep eutectic solvents is a rapidly expanding field, with DES continually being investigated in more and more applications (Section 1.3.3). Figure 1.4 lists the approximate number of publications per year concerning deep eutectic solvents, found by carrying out a keyword search on the SciFinder database [4].

A topic which has become increasingly relevant as the number of novel DES being reported in the literature has grown rapidly is the definition of a DES, which continues

Table 1.1: Examples of some commonly investigated DES based on choline chloride, including the molar ratio of the components and the melting points of the HBA, HBD and the eutectic mixture. Melting points of individual DES components were obtained from the work of Garcia et al. [22].

HBA	HBD	Molar ratio	T_{melt} (HBA)	T_{melt} (HBD)	T_{melt} (eutectic)	Reference
ChCl	Urea	1:2	303 °C	134 °C	12 °C/24.5 °C[a]	[55, 56]
ChCl	Glycerol	1:2	303 °C	17.8 °C	-40 °C	[51]
ChCl	EG[b]	1:2	303 °C	-12.9 °C	-36 °C	[57]
ChCl	Citric acid	1:1	303 °C	149 °C	69 °C	[55]
Proline	Glycerol	1:3	205-228 °C	303 °C	-60 °C	[58]

[a] The melting point of the ChCl:urea DES was originally reported as 12 °C by Abbott and co-workers [55], but several subsequent studies have suggested that the melting point is actually higher [56], and so both examples have been reported here.

[b] EG = ethylene glycol

to be debated by some in the field. Typically, as discussed previously, DES are defined as solvents formed when two or more components associate with each other through the formation of hydrogen bonds to form a stable liquid mixture, characterised by a significant depression in the freezing point relative to that of the individual components. Coutinho and Pinho have made the argument that all solid mixtures which have the capacity to associate through the formation of hydrogen bonds may have a eutectic point, and that a more rigorous definition of a DES is required away from their relation to ionic liquids [62]. The same group [63] have further made the case that a system can only be defined as a 'deep eutectic' where the depression in the freezing point is lower than the ideal eutectic temperature. They thus proposed that the reported temperature depression should be the defined as the difference in the ideal and real eutectic points. Alternative terms such as 'deep eutectic *systems*' instead of solvents [64] have also been proposed in the literature, which can be considered a more inclusive term as it also applies to those mixtures which are liquids but not necessarily at the eutectic ratio.

Another factor is that DES are often referred to as stable liquids, even though the most well studied DES, choline chloride:urea has been shown to begin to freeze at 25 °C [65] (as compared to the originally reported eutectic temperature of 12 °C) when prepared in its pure state from fully dried components. The definition has further been called into question when considering the water content of several NADES, or when considering mixtures of components with properties similar to DES but which do not have a true eutectic point [66]. It can be argued however that this topic, whilst being an important

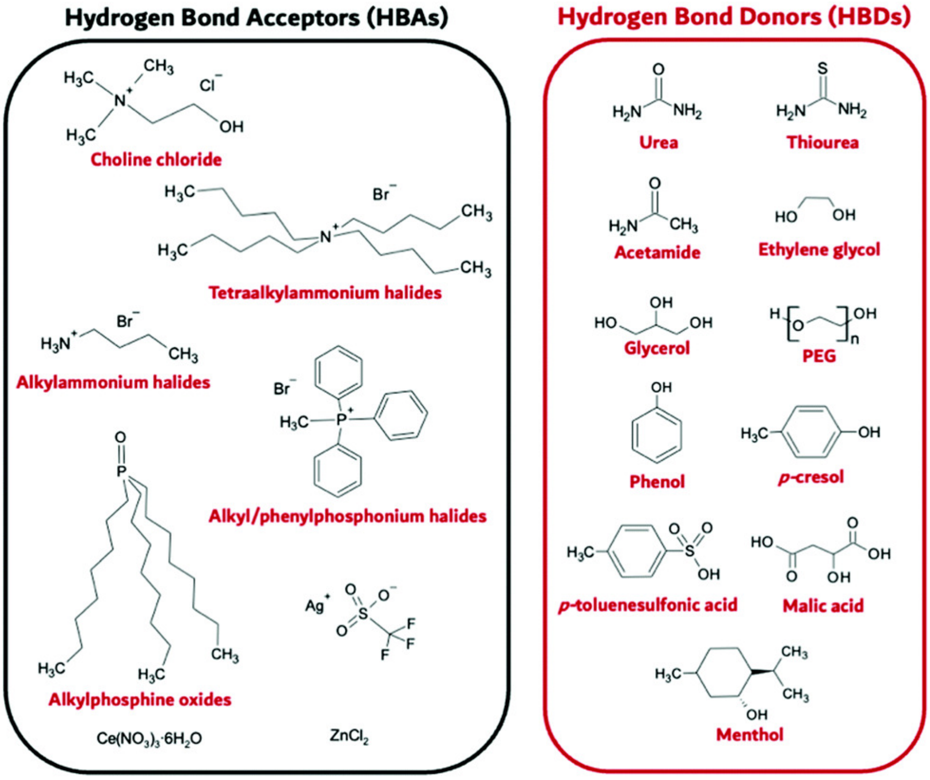

Figure 1.3: A selection of hydrogen bond donor and acceptor molecules which are commonly used as DES components. Reproduced from Reference [3] under a Creative Commons Attribution Licence.

scholarly debate, should not obstruct the development of any systems which can lead to an improvement in the efficiency or environmental impact of industrial processes.

1.3.2 Properties of deep eutectic solvents

Due to their tunable nature, the physical and chemical properties of DES are largely dictated by the choice and molar ratios of components. This has allowed for the synthesis of DES with a wide range of physiochemical properties including varying conductivity, viscosity, biodegradability, density, and electrochemical behaviour. One extreme example is the development of several hydrophobic DES [67] in contrast to the hydrophilic choline chloride-based solvents.

Inevitably, the properties of DES are often compared with those of ionic liquids. They are widely touted as ‘green alternatives’ to ILs as several DES can be synthesised from components which are cheap, widely available and with low toxicity. DES share some of the properties which make ionic liquids so favourable, including low vapour pressure

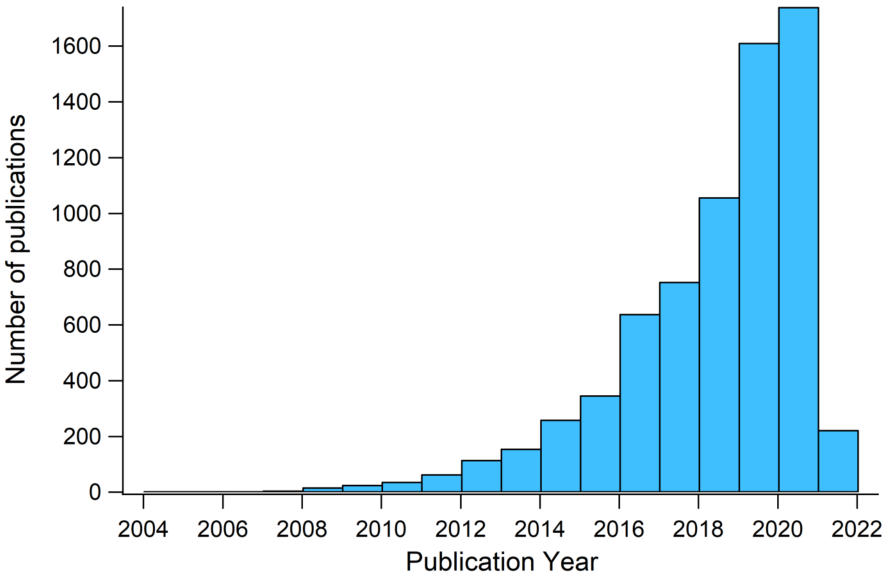

Figure 1.4: A graphical representation of the number of publications on the topic of DES since 2005. Data obtained from a keyword search of 'deep eutectic solvents' on the SciFinder database [4], accurate as of February 2022.

(though often still higher than that for ILs), low volatility and flammability, thermal stability, good conductivity, operation over a wide potential window and recyclability.

Additionally, compared to ILs, which can be complicated to prepare and require special techniques such as air-sensitive chemistry, the synthesis procedures for most DES are very straightforward and do not result in a large amount of waste. Typically, they simply require the combination of the components in the desired molar ratio and stirring or agitation, occasionally with heating, until a homogeneous mixture is formed. Some preparation methods are more complex, involving combining solid components in a pestle and mortar [68] or through the lyophilisation of aqueous solutions of the DES components [69]. This second method has been used for the preparation of NADES, in order to incorporate self-assembled structures into the DES or where the DES will not readily form solely by combining the components [70]. Other methods have involved using a microwave-assisted preparation [32] or by melting the component with the lowest melting point before adding others [71].

The phase behaviour of DES has already been represented in Figure 1.2. The depression in the freezing point of the eutectic mixture compared to the melting points of the individual components may be related to the strength of the interaction between components and is generally not thought to be correlated to the melting points of the components – that is, a greater degree of association between the components leads to a greater depression in the freezing point. A body of work, largely carried out by Abbott et al. has determined other factors which affect the eutectic point [51]. The choice of hydrogen bond donor, organic salt and HBA/HBD molar ratio, and even the preparation method can have an effect. The densities of many DES are typically higher than that of water, ranging between 1.0 and approximately 1.6 g cm^{-3}, though certain hydrophobic DES can have densities lower than these values [72]. Similar to the eutectic point, the choice of HBD and the molar ratio can effect the density of a DES, and additionally a linear correlation with temperature (whereby the density is lowered with increasing temperature) is often observed.

In general, DES have quite high viscosities compared to organic solvents and ILs. This can prove a disadvantage when considering their industrial use, though low viscosities have been reported in the case of certain hydrophobic DES such as those based on DL-menthol [73]. As with many systems, the viscosity is temperature-dependent and can be significantly lower when one of the DES components is a liquid at room temperature (e.g. glycerol or ethylene glycol). Higher values of viscosity can have a detrimental effect on ionic conductivity by affecting ion motion and give rise to higher values of surface tension. Often, water is added to DES in order to lower its viscosity and increase its practicality for certain applications. These physical properties of DES have previously been rationalised using hole theory, whereby 'void' spaces exist in the melt due to local density fluctuations, the distribution of which is influenced by the choice of components. Ionic motion is proposed to be limited by the availability of this free volume, into which the ions would move [74]. Due to discrepancies between experimental and predicted values for the properties of certain DES, however, it is suggested that hole theory may describe trends across different DES but may not be an accurate predictor of physical properties [75].

1.3.2.1 DES toxicity

Though DES are typically referred to as being composed of non-toxic components, the toxicity of many DES is something which is important to investigate and it must not be simply assumed that the combination of non-toxic components will result in a non-toxic DES. For example, although the choline chloride-based DES investigated by Hayyan et al., were classed as non-toxic materials, the cytotoxicity was greater than that measured for the individual component molecules [76, 77]. Similar results were obtained by Radošević et al., who found that similar DES had low phytotoxicity and were readily biodegradeable [78]. An investigation into the effect of certain NADES on certain bacteria classed only the organic acid-containing solvents showing toxicity towards the bacteria samples [79].

These toxicology studies do not, however, take into account those DES which contain metal salts (Types I, II and IV) when pronouncing DES to be largely 'non-toxic', as these DES will contain toxic components which do not biodegrade readily. More recently, a computational modelling approach has been used to evaluate the toxicity of several DES and DES components [80] with a view to provide a 'virtual screening' tool when considering the design of new solvents. Bystrzanowska and Tobizewski, however, make the point that compared to ionic liquids there have been relatively few robust investigations into the 'real-life' toxicity and biocompatibility of DES, and more rigorous investigation would be required prior to employing them in industrial processes [81].

1.3.3 Applications of deep eutectic solvents

This section will provide an overview of some research areas where DES have found application, but as Figure 1.4 suggests, the range of applications for which DES are being explored is ever expanding. They include synthesis, polymer chemistry, electrofinishing, self-assembly, biological applications, batteries and solar energy devices. Most of these were not investigated in this project, so an exhaustive literature review of these is not relevant to this thesis. Where required, a directly relevant review of the literature is given within the three experimental chapters in order to better provide the background and reasoning for the motivation, experimental design and discussion of results.

1.3.3.1 Chemical transformations

Chemical transformations (specifically, organic synthesis and polymerisations) are one field where common organic solvents are being replaced with DES. Transformations thus far achieved in this way include esterifications [82–84], the synthesis of heterocycles [85] , Diels-Alder reactions [86–88] halogenation, [89], epoxide ring opening [90] and the synthesis of phenols [91].

Several studies have demonstrated that reactions which are traditionally carried out using air and moisture sensitive techniques, such as those that use organometallic reagents, can be carried out on at room temperature and without the need for an inert atmosphere using DES such as ChCl:glycerol with high yields ($\geqslant 95$ % in most cases) still maintained [92, 93]. Cross-coupling reactions catalysed by transition metal-based catalysts such as the Heck, Sonogashira and Suzuki-Miyara reactions have also been successfully carried out in DES using milder synthesis conditions, with a comparable efficiency to the original method [94, 95]. For biocatalytic reactions, an argument has been made that the physical properties of DES can resemble the cellular environment [96, 97] and improve reaction rates in the case of reagents with poor water solubility or where there may be competing hydrolysis pathways [98].

As solvents in polymer synthesis, DES can offer access to polymers with unique properties, as well as a more benign and often efficient reaction as compared to conventional organic solvents [99]. DES have also been used as soft templates or a ligand source for the plasticisation of a range of starch-based materials [100–102], and as monomers for the production of polymeric DES which have been investigated for separation and extraction applications [103, 104].

Across many of these examples, the replacement of organic solvents with DES has served to enhance the synthetic process, giving access to higher yields, better atom economy and milder synthesis conditions. Several papers go so far as to report the triple function of a eutectic system as a solvent, reactant and catalyst within the system [90, 105, 106].

1.3.3.2 Synthesis of inorganic materials

It has been shown that for materials targeted towards specific applications, control over the morphology, structure and composition can have a great effect on their performance [107]. The highly tunable nature of DES suggests that they may be the ideal media for the synthesis of these functional materials. ILs have found extensive use in inorganic synthesis applications but the environmental advantages of DES may make them more suitable for industrial scale-up. A short summary is presented below, as this application is expanded upon in the literature review presented in Chapter 3.

Early studies published soon after DES were first reported revealed the structure-directing effect DES could have on the synthesis of open framework materials [108,109]. Oxide, phosphide, sulfide and even layered double hydroxide (LDH) materials have been synthesised using solvothermal methods, occasionally precipitating and isolating solid powder products using anti-solvent techniques [110–112]. This technique has used the variation of the ratio of the anti-solvent to obtain control over particle morphologies has been demonstrated, an example being the synthesis of crystalline zinc oxide nanostructures from a solution of ZnO in ChCl:urea [113]. It has also been possible to achieve this morphological control by varying the DES composition itself.

Synthesis methods have varied, but have included heating in a sealed pressure vessel, microwave-assisted synthesis, standard bench-top heating and condensation reactions. More recently, surfactant templating has been used to create porous zeolitic imidazolate frameworks (ZIFs) [114]. Although the physical properties of DES have been extensively explored, reaction mechanisms were typically not investigated in detail and were instead proposed based on prior knowledge of DES components or degradation products. It is only in recent years that advanced experimental techniques have been used in order to elucidate the mechanism of particle formation [115, 116] in DES.

1.3.3.3 Separations and extractions

The efficient extraction of bio-active compounds from waste streams and by-products is an essential aspect of waste valorisation. These by-products, often generated from agricultural and food manufacturing industries, contain a wealth of compounds such as proteins, sugars, lipids, phenolics and alkaloids [117] which may be recovered and treated to produce useful metabolites.

Traditional methods of extraction include the use of solid-phase extraction (SPE), organic solvents and water in conjunction with chromatographic techniques. Ionic liquids have been investigated extensively as extraction media, but DES have gained popularity as an alternative to overcome the shortcomings of ILs. A range of techniques including ultrasound-assisted, microwave-assisted, enzyme-assisted and heat-assisted extraction have been paired with various DESs, from the popular choline chloride-based solvents [118–121] to less investigated organic-acid based solvents and beyond. Additionally, DES have also been investigated for use in carbon capture technologies [122–124] and desulfurisation processes [125, 126].

The tunable nature of DES which has been discussed numerous times already allows for the design of solvents which are hydrophilic or hydrophobic in nature and with varying polarities, such that the range of compounds and materials for which a certain DES is the ideal solvent is vast. This in turn means that research focusing on separations and extraction processing is widespread and producing a comprehensive list of studies would prove a difficult task.

1.3.3.4 Electrochemical applications

The earliest and arguably one of most popular fields where DES have substituted other solvents is for various electrochemical purposes, for which ionic liquids have also been investigated extensively.

DES have been employed as highly effective electrolyte solutions, offering low toxicity, good conductivities, excellent solubilising properties for metal oxides insoluble in aqueous electrolytes, and tunability through composition variation. Similar to other applications, choline chloride based DES such as ChCl:urea and ChCl:ethylene glycol are amongst the most commonly investigated electrolytes for electrodeposition. The reduction of several metals in the DES (such as Al, Cu, Zn, Co, Ni and Zn) to produce various metal and alloy coatings have been studied [51]. Additionally, the electrochemical synthesis of nanoparticles has been achieved [127], with the products having superior performance for their intended applications in comparison to those synthesised using other methods. A control over morphology has also been demonstrated through varying the composition of the electrolyte. These processes have been further improved through the use of additives into the electrolyte, such as amines or various acids to optimise the morphology of the deposits or to improve surface properties such as smoothness/cohesion [128,129]. Therefore, DES may prove a useful alternative to aqueous electrolytes for the deposition of materials where control over morphology, smaller particle sizes and minimal aggregation is an advantage. Some examples of functional nanomaterials which have been synthesised through deposition include TiO_2 semiconductor films [130], Zn-Ni-P alloys [131], and Co oxides [132].

This application, and in particular the deposition of functional materials using DES-based electrolytes will not be elaborated upon here, as it is further discussed in Chapter 3.

1.4 Outlook and structure of thesis

This chapter has given a general introduction to solvents in industrial processes, discussed the drive towards finding alternatives to molecular liquid solvents and presented a brief overview of the properties and applications of deep eutectic solvents. The unique properties of DES have led them to be investigated in a diverse range of fields, and the aim of this PhD project was to further explore how these properties could be exploited for applications such as the design and synthesis of novel functional materials. However, this requires an understanding of the liquid structure of DES and their interaction with other molecules such as surfactants.

The experiments carried out during this PhD are presented in this thesis as three separate self-contained, each exploring a different aspect of the overall aim of deepening the understanding of the structure, properties and interactions of DES. A chapter containing the theory behind the experimental characterisation carried out during this project is first presented, combined with some of the general experimental methods used throughout this thesis.

In the first section of this project, we sought to build on published work within the group concerning the synthesis of iron oxide nanoparticles in ChCl:urea using a facile solvothermal method by expanding it to include other metal-based oxide materials which were suitable as electrocatalysts for water splitting applications.

Next, we looked at the possibility of synthesising porous materials using DES, and facilitated this by designing a three component system involving choline chloride, urea and glycerol. A a range of techniques have been used to determine the physiochemical properties of this DES. Small-angle scattering techniques have been used to explore how the DES can support and direct the self-assembly of amphiphilic molecules and preliminary experiments to synthesise materials using these mixtures have been carried out.

In the final section, we explored the liquid structure of the ternary DES and its interaction with metal ions using wide Q-range neutron diffraction techniques to gain an understanding of the intermolecular interactions within this system and how they may be influenced by varying the DES composition.

Chapter 2

Theory and methods

2.1 Neutron and X-ray scattering theory

This section covers neutron and X-ray scattering theory as it applies to the experimental techniques used in this thesis, namely small-angle X-ray (SAXS) and neutron (SANS) scattering, and total neutron scattering. Although a discussion of X-ray scattering cannot be avoided in order to provide a background to the laboratory-based characterisation carried out in Chapter 4, the content of this section will be heavily weighted towards the theory behind neutron scattering as that is the predominant experimental technique used throughout this thesis. The theory behind the two is almost identical, differing mainly in the way that neutrons and X-rays interact with matter. This is reflected in the equations used to describe them (discussed below). The two techniques may be used together as they provide complementary information about a system. More detail concerning the specific experimental techniques will be provided in the relevant chapters.

The theory presented here is largely adapted from *Introduction to the Theory of Small-Angle Neutron Scattering and Neutron Reflectometry* by A.J. Jackson, 2008 [133].

2.1.1 Introduction to scattering

X-rays are typically referred to as waves with wavelength λ in the range 10^{-8} m - 10^{-12} m. Neutrons are uncharged particles contained in the nuclei of atoms, with a mass of 1.675 x 10^{-27} kg, which exhibit wave-particle duality. The wavelength of such particles may be related to their momentum using the de Broglie equation:

$$\lambda = \frac{h}{p} \tag{2.1}$$

where h = Planck's constant, 6.626 x 10^{-34} m^2 kg s^{-1} and p is the momentum, related to the particle's velocity by $p = mv$ [134].

As neutrons are uncharged, they can be used to probe the bulk of materials, interacting with nuclei of atoms within a sample through short range nuclear forces. Their magnetic moment (-1.913 nuclear magnetons) also allows neutron-based techniques to be used in experimental physics for the study of magnetic structures. Both X-ray and neutron scattering, being non-destructive techniques capable of providing real-time structural information over a wide range of length scales (0.1 Å - 1 µm) are therefore ideal choices for analysing a range of samples, including colloidal mixtures, crystalline structures and various biological systems [135].

The interaction between a beam of particles and a target (sample) can result in a range of elastic, inelastic and absorption processes. Whilst the latter two can provide useful information about systems, for simplicity this section will focus mostly on elastic interactions. In these, the kinetic energy and momentum of the system are conserved, and they are exploited in the experimental techniques used in this thesis.

First, the outcome when an incident beam interacts with the nucleus of a single atom must be considered (Figure 2.1). A monochromatic beam of X-rays or neutrons can be defined as a planar wave with amplitude ψ_i, which may be further expressed as:

$$\psi_i = e^{ikr} \tag{2.2}$$

where **k** is the wavevector which follows the trajectory of the neutron beam. In equation 2.2, r is the distance from the point scatterer in the direction of propagation. In the case of neutron scattering, the spherically symmetrical wavefunction of the scattered wave arising from the interaction of the incident wave with the atom will be:

$$\psi_s = -\frac{b}{r}e^{ikr} \tag{2.3}$$

where b is the neutron scattering length. This scattering length is a value which is used to represent the interaction of the scatterer with the radiation beam and describes the phase shift between the incident and scattered wave in a scattering event. For comparison, the equivalent parameter for X-ray scattering is the atomic form factor.

Assuming the atom as a spherically symmetric particle, the form factor is derived from the Fourier transform of the electron density of the atom.

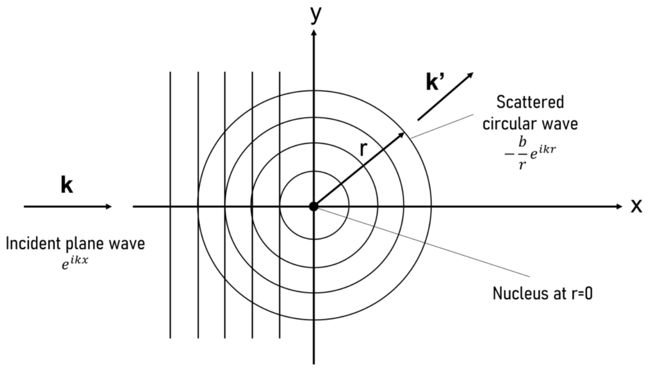

Figure 2.1: A diagram depicting a scattering event which occurs when an incident wave scatters through interaction with a point scatterer. Figure adapted from Reference [5].

Although simplifying the scattering event as the scattering from a point charge aids understanding of the phenomenon, real systems contain ensembles of atoms. For scattering from a three-dimensional ensemble of particles (as above, in the case of neutrons), the wavefunction ψ_s is now defined as:

$$\psi_s = -\sum_i \frac{b_i}{r} e^{ikr} e^{i\mathbf{q}\cdot\mathbf{r}} \tag{2.4}$$

The new variables introduced into the equation are $\mathbf{q}$, which is the scattering vector. Its value is equal to the momentum lost by the sample (and so gained by the scattered particle), defined as the difference between the wavevectors of the incident and scattered radiation, such that

$$\mathbf{q} = \mathbf{k} - \mathbf{k}' \tag{2.5}$$

For an elastic scattering process, the magnitude of the wavevectors for the incident ($\mathbf{k}$) and scattered ($\mathbf{k}'$) radiation are the same, as no energy is lost and the momentum changes direction, but not magnitude. The wavevector can therefore be related to the wavelength of the incident beam:

$$\mathbf{k} = \mathbf{k}' = \frac{2\pi}{\lambda} \tag{2.6}$$

The scattering vector, **q** therefore correlates with the directional change of the scattered beam as it is scattered at an angle of 2θ (Figure 2.2).

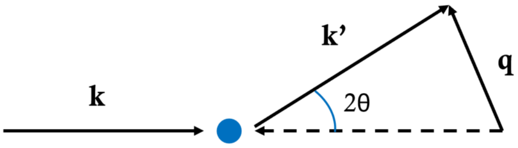

Figure 2.2: A diagram depicting a scattering event, showing the wavevectors of the incoming and scattered radiation and defining the scattering vector. Adapted from the work of Pynn [5].

By examining Figure 2.2, we can see that for an elastic scattering event the magnitude of q can be related to the scattering angle, 2θ by:

$$|\mathbf{q}| = 2ksin\theta = \frac{4\pi}{\lambda}sin\theta \tag{2.7}$$

Using Bragg's law (Equation 2.13), the scattering vector is related to the parameter d by:

$$q = \frac{2\pi}{d} \tag{2.8}$$

The above equation presents an inverse relationship between the scattering vector and the lattice parameter, and hence large-scale structures may be examined by small values of q, whilst scattering at higher q values will represent smaller length scales. Designing experiments and representing data in terms of a q-range therefore helps to standardise the length scale of interest of experiments, irrespective of technique or incident radiation.

In a scattering experiment, the quantity which is actually measured is the scattering cross-section, (σ), which is an indication of how strongly a neutron interacts with the nucleus of a certain atom. As such, it is typically described as the probability of a neutron being scattered by an atom through a given scattering angle. The differential cross-section, $\frac{d\sigma}{d\Omega}$ of neutrons scattered into the solid angle $d\Omega$ in the direction θ, ϕ, is the number of neutrons scattered per second (intensity, I) divided by the product of the incident neutron flux (Φ_0) and the solid angle ($d\Omega$):

$$\frac{d\sigma}{d\Omega} = \frac{I}{\Phi_0 d\Omega} \tag{2.9}$$

Experimentally, the scattering per unit volume is calculated by dividing the cross-section by the scattering volume to obtain the scattering section per atom or molecule. Dividing Equation 2.9 by the number of molecules and using the equation for ψ_s (Equation 2.4), the differential cross-section along the scattering vector $\mathbf{q}$ becomes:

$$\frac{d\sigma}{d\Omega}(\mathbf{q}) = \frac{1}{N}\left|\sum_{i=1}^{N} b_i e^{i\mathbf{q}\cdot\mathbf{r}}\right|^2 \tag{2.10}$$

The total scattering cross-section, σ_{tot} is made up of the coherent, incoherent and absorption components. The coherent component represents constructive interference from scattered waves at a certain scattering angle and therefore gives structural information about the sample most relevant to this thesis. For samples containing a lot of hydrogen, as many DES samples do, the incoherent scattering from hydrogen (which has an incoherent scattering cross-section several times greater than other elements of interest in the system) gives rise to a strong background in the scattering pattern (Table 2.1). The absorption cross-section is related to an imaginary component of the the scattering length.

Table 2.1: The coherent (σ_{coh}) and incoherent (σ_{inc}) scattering cross-sections of some of the elements of interest in this thesis, given each time to 1 decimal place. Values obtained from Reference [23].

Isotope	σ_{coh}	σ_{inc}
^{1}H	1.8	80.3
^{2}H	5.6	2.1
C	5.6	0.0
N	11.0	0.5
O	4.2	0.0
Fe	11.5	0.4

When measuring large-scale structures, composed of several molecules, it is not necessary to treat all of the atoms in the system individually and therefore it becomes simpler to define a scattering length density (SLD), which averages the scattering length contributions from all of the atoms in a system relative to a certain volume. For neutrons, this is given by the equation:

$$SLD = \frac{\sum_i^n b_i}{V} \tag{2.11}$$

where b is the bound coherent scattering length and V corresponds to the volume which is occupied by n atoms[3]. X-rays interact with the electron cloud of atoms and are therefore sensitive to the atomic number of the atom. This is reflected in the equation for the scattering length density specific to X-ray radiation:

$$SLD = \frac{\sum_i^n Z_i r_e}{V} \tag{2.12}$$

This is similar to Equation 2.11, but includes the atomic number, Z_i of the atom to which the scattering is proportional, and the classical electron radius, r_e (2.818x10^{-15} m), which reflects the interactions of X-rays with the electron cloud of the atom.

This approach works best with small-angle techniques, where the q-range of interest is at relatively low values and large-scale structures are to be studied. Inhomogeneities in the SLD are best seen here, whereas at a certain radius the probability of finding an atom within an amorphous material becomes essentially constant. Therefore, for wide-angle or total scattering experiments which examine smaller-scale correlations between individual atoms, describing the scattering using SLD values is not appropriate.

Now that an introduction to the theory of scattering has been presented, subsequent sections will focus on the more practical aspects of running an experiment, describing the generation of X-rays and neutrons for research and how the techniques of isotopic labelling and contrast variation may be used to extract structural information about a complex system.

2.1.2 Generation of X-rays and neutrons

2.1.2.1 Generation of X-rays

It is possible to generate X-rays in a laboratory setting, which makes X-ray scattering (through techniques such as XRD or SAXS) a popular analysis choice for characterising a vast range of samples without the use of specialist external facilities. In these instruments, X-rays are typically generated through the bombardment of a metal target with electrons, and different wavelengths for the incident beam can be achieved through variation of the metal target. For example, typical sources for an X-ray diffractometer include Cu, Mo and Co, yielding incident radiations of wavelengths 1.54 Å, 0.7107 Å and 1.7902 Å, respectively. The X-rays can then be passed through collimators and focused on the sample. This method, however, does not produce X-rays with significant flux for many experiments and the production of high-energy X-ray (and neutron) beams requires large-scale, specialist facilities.

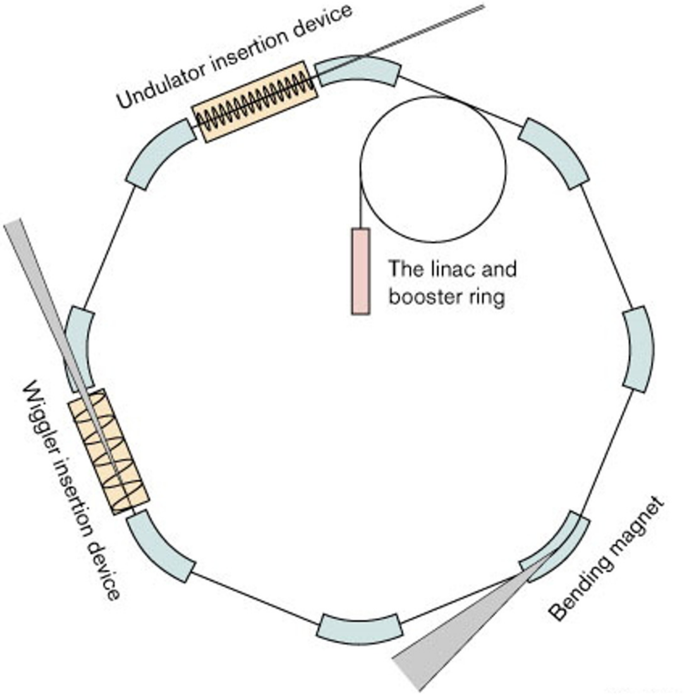

Figure 2.3: A schematic showing the key components of a synchrotron. Reproduced from Reference [6] © 1999, with permission from Elsevier.

The second commonly used method for producing X-rays which do have the required flux is via synchtrotron radiation. The first dedicated synchrotron facility for X-ray production was the Synchrotron Radiation Source (SRS) at Daresbury, England in 1980 [136]. For simplicity, the operation of a synchrotron described here is that of the Diamond Light Source, UK. Electrons are released from an electron gun are accelerated through a linear accelerator and a booster synchrotron to relativistic speeds via a series of magnetic fields. The accelerated beam is then introduced into the storage ring, where it is bent by a series of magnetic fields around the ring, which results in the emission of electromagnetic waves in the direction of circulation of the electrons. These waves are then channelled out to various beamlines, as required by each particular instrument [137]. A simplified schematic highlighting the key components of a synchrotron, including the source, linear accelerator, booster/storage rings, and various magnets is presented in Figure 2.3. As synchrotron X-ray radiation has not been used for characterisation in this project, an in-depth discussion of the operation of a synchrotron is outside the scope of this thesis.

2.1.2.2 Generation of neutrons

A free neutron has an average lifetime of approximately 900 s, so in order to carry out experiments it is necessary to produce neutrons on-site. Neutrons are typically generated in two distinct ways, either in reactor-based sources (by nuclear fission) or at spallation sources which use particle accelerators. Before the development of fission reactors in the 1940s, neutrons such as those produced by the irradiation of beryllium metal with α particles did not have sufficient flux for a successful scattering experiment. Nuclear fission reactors produced neutrons via the fission of uranium-235, which occurs when the uranium nuclei absorb thermal neutrons, causing the emission of fission fragments and high energy thermal neutrons (MeV scale).

High energy neutrons produced in this fission process must be moderated to lower energies (meV) in order to create a sustainable chain reaction, whereby some emitted neutrons will be absorbed by and and catalyse the fission of more ^{235}U atoms. This moderation is also required in order to obtain the desired energy distribution for a particular application, and the choice of moderator (for example heavy hydrogen, $^2H_2$, heavy water, ^2H_2O, or graphite) can determine the energy and so the wavelength of the neutrons. The wavelength distribution can be further narrowed by the use of monochromators, velocity selectors or choppers to produce the neutron energies required for the instrument. This method for generating neutrons for research remains the most popular, and one prominent example of a neutron reactor source is the Institut Laue-Langevin (ILL) in Grenoble, France, though many others exist across the world [138].

The neutron scattering experiments in this thesis were conducted at the ISIS Neutron and Muon Source at Rutherford Appleton Laboratories in the UK, which produces pulsed neutrons via the second method, spallation. This method has become increasingly more popular since the 1980s and involves the bombardment of a heavy metal target such as tungsten, tantalum or vanadium by high energy particles, in many cases (and as is the case at ISIS) by protons accelerated to 800 MeV in a synchrotron. In a similar way to those generated by fission, these high energy neutrons must be moderated until the desired wavelengths for scattering experiments are obtained [139].

At ISIS, there are two target stations - Target Station 1 (TS1), and Target Station 2 (TS2). The total proton beam current generated by the synchrotron is approximately 225 µA, with TS1 receiving 180 µA and TS2 receiving the remaining 45 µA. The

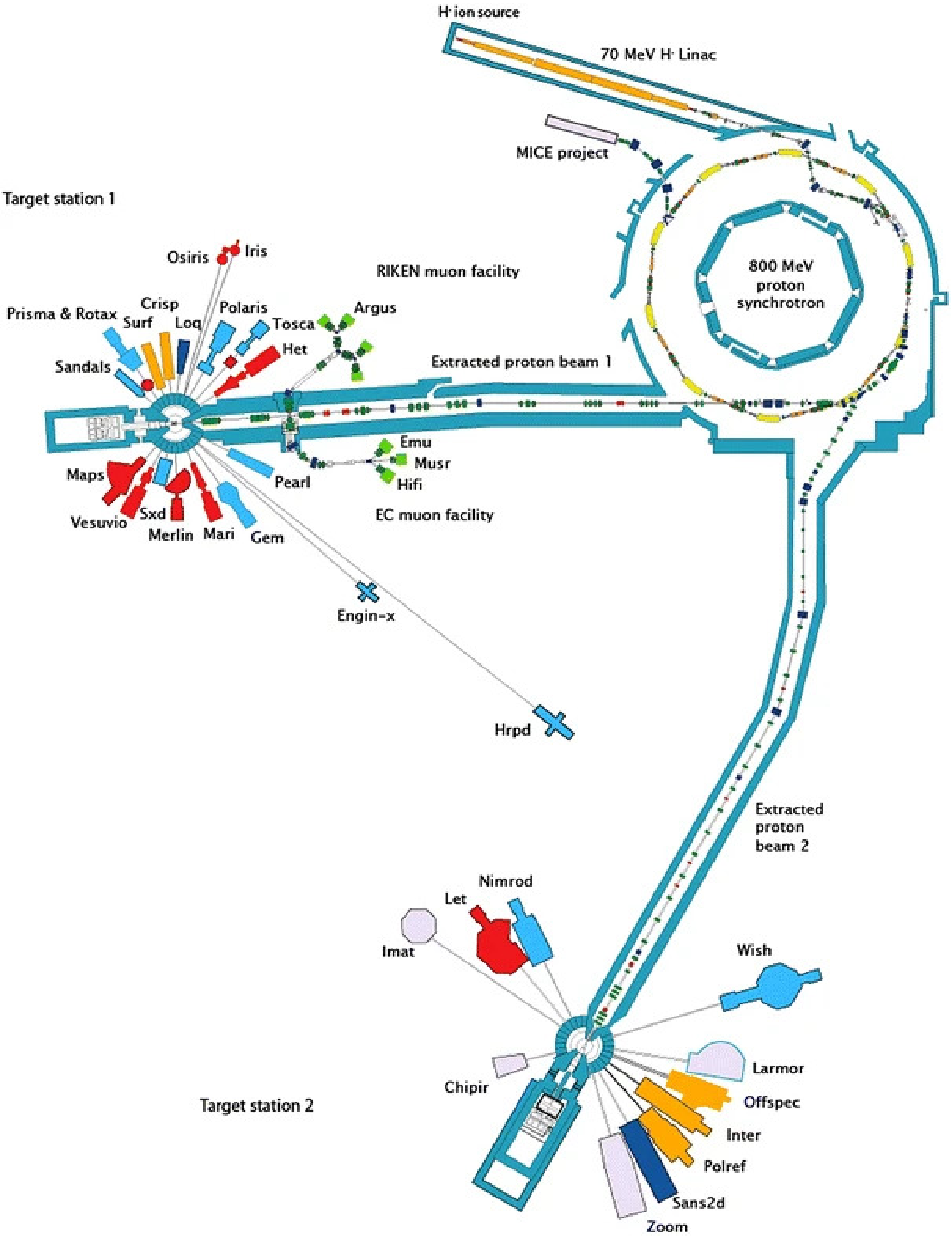

Figure 2.4: A schematic showing the layout of the ISIS Neutron and Muon facility, consisting of the linear accelerator and proton synchrotron and two target stations . Reproduced from Reference [7] under a Creative Commons Attribution Licence.

neutron beam produced by the bombardment of the tantalum-covered tungsten targets can be channelled out to the various instruments contained in the target stations, and further modifications to the beam flux or wavelength can be made through the use of choppers. As the neutrons are generated in pulses, time-of-flight (TOF) techniques may be used, where the time taken for the neutron to travel from the moderator to the detector, passing through the sample on its route can be measured. This allows for the calculation of the scattering vectors and so the energy and momentum exchange [140]. A schematic showing the layout of the ISIS facility, including the synchrotron and two target stations containing the tantalum-covered tungsten targets, with particular instruments used in the experimental work for this thesis is highlighted in Figure 2.4.

2.1.3 Choice of probe - comparison between neutrons and X-rays

As discussed above, the techniques needed to generate neutrons for use in scattering experiments are limited, costly and not available in a conventional laboratory setting. While many X-ray experiments are carried out using synchrotron radiation, they are also readily available in many settings and the underlying principle of X-ray and neutron diffraction is similar. It might seem, therefore, that these two techniques are interchangeable and X-rays are the most suitable choice for most experiments due to their comparative availability.

In this thesis, X-rays have been used both for sample characterisation (XRD) and for carrying out preliminary experiments to gather initial information about a system to support the choice and design of experiments at a neutron facility (SAXS). However, a distinct case can be made for the use of neutrons as the probe of choice for the majority of experiments carried out during this project, as explained below.

Table 2.2: Neutron and X-ray scattering lengths of some elements of interest in this thesis. Values obtained from Reference [23].

Isotope	Atomic number (Z)	Neutron scattering length (10^{-13} cm)	X-ray scattering length (10^{-13}) cm
^{1}H	1	-3.74	2.80
^{2}H	1	6.67	2.80
^{12}C	6	6.65	16.90
^{14}N	7	9.37	19.70
^{16}O	8	5.80	45.00

For experiments looking at the structure of DES (and amorphous liquids in general), hydrogen bonding within the system is an essential interaction to study. As such, a probe which is sensitive to the position of hydrogen atoms within the structure is needed. Additionally, the molecular structures within the samples contain several light elements. It has previously been mentioned in this section that neutrons interact with the nuclei of atoms, whilst X-rays interact with the electron cloud surrounding the nucleus. The size of the signal obtained in X-ray diffraction experiments is proportional to the atomic number, Z, of an element, which is not the case for neutrons. These interactions may be compared by examining the X-ray and neutron scattering lengths, of various elements of interest in these systems. Table 2.2 summarises these values for hydrogen, deuterium, carbon, nitrogen and oxygen. A further illustration is provided in Figure 2.5, which compared the X-ray and neutron scattering cross-sections for the same elements, this time represented as circles of varying sizes. Neutrons also interact weakly with matter, and as such allow a high accuracy and reliability of quantitative modelling due to a lack of impact on the structure of the system through interaction with the probe particle.

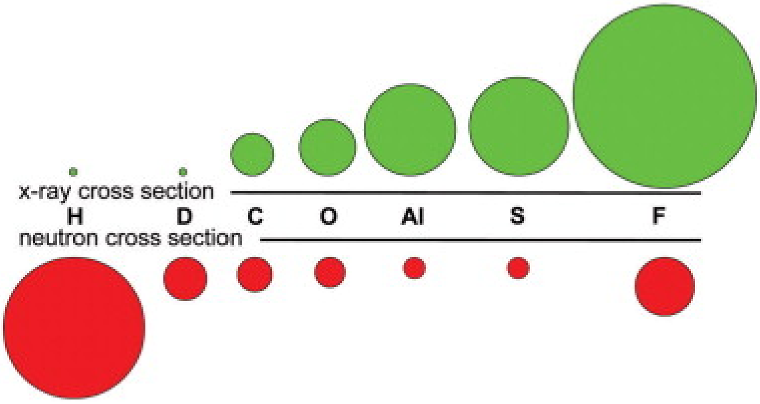

Figure 2.5: A representation of the total scattering cross-sections in the case of neutron and X-ray scattering for a range of isotopes. Reproduced from Reference [8] under a Creative Commons Attribution Licence.

From Table 2.2, it is apparent that the X-ray scattering length of hydrogen is much less than that of carbon, and many times less than that of oxygen. Hence, it can become difficult to extract meaningful information about the position and bonding of hydrogen atoms using X-ray techniques. In the case of neutrons, however, the magnitude of the scattering lengths are similar amongst the elements of interest in this thesis, so the same problem is not encountered. Additionally, the significant difference between the scattering lengths of hydrogen (^{1}H, b=-3.74) and deuterium ((^{2}H, b=6.67) something which does not occur when using X-rays as the atomic number of hydrogen and deuterium is the same. In order to resolve structures, such as a solvation layer in a micellar system using SANS, contrast variation may be used which relies on this scattering length difference. This is covered further in Chapter 4.

2.1.4 X-ray diffraction

A basic introduction to X-ray diffraction as relevant to this thesis is given here, in order to aid understanding of experimental data presented in Chapters 3 and 4.

X-ray diffraction (XRD) is a non-destructive technique which utilises X-rays to probe the structure of both crystalline and non-crystalline materials. It is termed ‘diffraction’ as it deals with the elastic scattering which results from the interaction of an incident X-ray beam with a sample. X-rays occur in the portion of the electromagnetic spectrum corresponding to wavelengths of 1 - 100 Å, and interact with the electron cloud of atoms. They are ideal to probe structures as their wavelength range is a similar distance to the spacing between atoms within a crystal structure. Although XRD also finds application in structural studies of amorphous materials, the discussion here will focus on the characterisation of crystalline materials.

X-ray diffraction is governed by Bragg’s law:

$$n\lambda = 2dsin\theta \tag{2.13}$$

where n is an integer, λ is the wavelength of the incident X-rays, and d is the spacing between atomic layers within the crystal lattice. Bragg’s law can also be illustrated by the diagram in Figure 2.6. Where the wavelength of incident radiation corresponds to the spacing between the atoms in the sample, that is, when Bragg’s law is satisfied, constructive interference occurs and a strong positive signal is obtained. In the case of single-crystal analysis, this gives rise to a diffraction pattern consisting of intense spots at certain values of θ. Throughout this project, single-crystal analysis was not used, and the pattern from powder or otherwise polycrystalline samples often containing several phases will appear as a radially averaged pattern instead of distinct points.

In a standard X-ray diffractometer, electrons are generated in a cathode ray tube, collimated and monochromated before being directed towards the sample. The detector is positioned above the sample and rotates around it, recording the number of X-rays at each angle which correspond to the counts/intensity. By convention, this scattering angle is labelled as 2θ. Where the composition of a sample is unknown, or where a sample may contain multiple phases of a compound, the experimental XRD pattern may be compared to a literature pattern obtained via a crystal structure repository in order to identify it [141]. Diffraction patterns may be further analysed to calculate parameters such as crystallite size using the Scherrer equation [142] or even fitted using a Rietveld refinement analysis [143], although neither of these techniques were used in

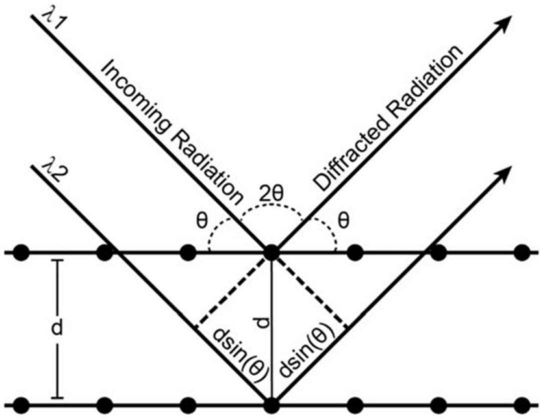

Figure 2.6: A diagram illustrating Bragg's law, showing the interaction of incoming X-ray radiation with the planes within a crystal lattice. Reproduced from Reference [9] under a Creative Commons Attribution Licence.

this thesis.

2.2 Characterisation techniques

This section will explain the theory behind the characterisation techniques used throughout this work. Further explanations regarding techniques which are specific only to single chapters will be provided in the relevant sections within those chapters.

2.2.1 Scanning electron microscopy

Scanning electron microscopy (SEM) is an imaging technique which may be used to produce high resolution images for the purposes of examining the morphology of samples. Images are obtained by scanning a sample using a fine beam of electrons and detecting the signals emitted as a result of electron interaction with the sample.

There are a variety of ways of producing electrons for use in an SEM, including passing a current through a tungsten wire or by applying a high voltage to a crystal tip. The generated electrons emitted from the electron gun are accelerated with a voltage of approximately 20 kV. Similar to many scattering instruments, these electrons then pass through a condenser and are focused via a series of lenses and scan coils before passing through an aperture and being introduced to the sample. A diagram of the instrumentation is provided below (Figure 2.7).

When these high energy electrons interact with the sample, a number of signals are produced: backscattered electrons (scattered by the sample after elastic interactions

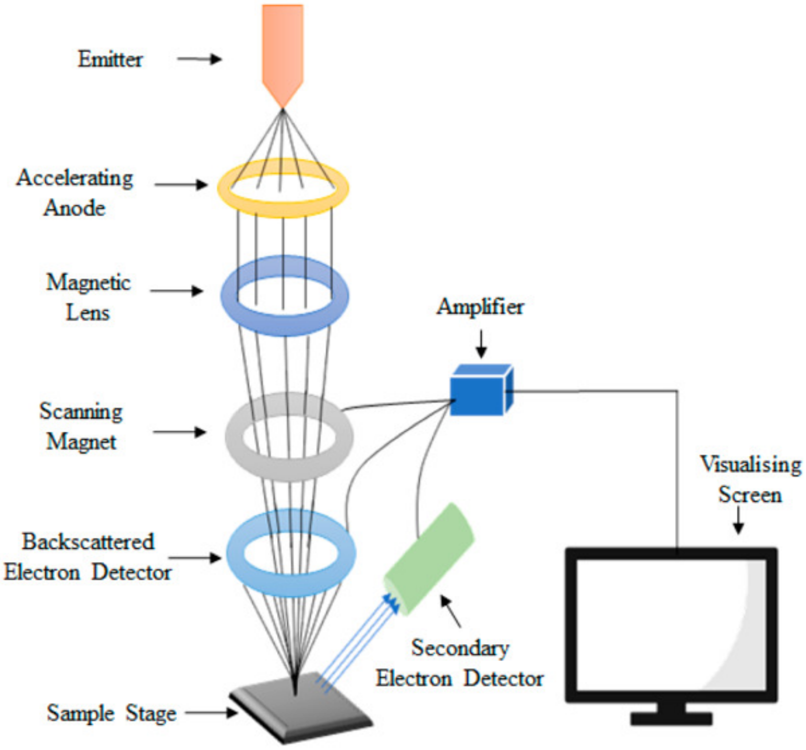

Figure 2.7: A schematic representation of the key components of a scanning electron microscope. Reproduced from Reference [10] under a Creative Commons Attribution Licence.

with the incident electrons, with only a small energy loss), secondary electrons (emitted from the atoms within the sample itself as a result of inelastic interactions between the sample and the incident electron beam, which have a much lower energy than the backscattered and incident electrons), and X-rays, which can be used to extract information about the elemental composition of the sample. Backscattered electrons originate from several microns below the sample surface and provide information about sample composition, as they are sensitive to the atomic number of the atom they are scattered by. In addition to this, they also give information about a sample's magnetic field and crystal structure, whereas secondary electrons originate from the sample surface itself (at most a few nanometres below) and give excellent information about the topography of the sample [144]. Images are produced from the signal obtained by detecting and amplifying electrons emitted by the sample. SEMs have a resolution on the order of a few nanometres, which may be adjusted by altering the size of the incident beam via control of the aperture and condenser lenses. Transmission electron microscopy (TEM) is a similar technique to SEM, but has a higher resolution (approximately 1 Å) which allows for the imaging of individual atoms.

2.3 Methods

This section will describe the synthesis and characterisation methods which are relevant to multiple results chapters within this thesis, to avoid repetition in subsequent chapters. Where experimental methods were varied as part of the investigation, or where methods apply to only one part of this PhD project, a description will be provided in the relevant chapters.

2.3.1 Preparation of deep eutectic solvents

2.3.1.1 Choline chloride-based DES

Choline chloride (99 %), urea ($\geq$99.5 %) and (where required) glycerol ($\geq$99.5 %) and ethylene glycol ($\geq$99 %) were all purchased from Merck. Due to its extremely hygroscopic nature, choline chloride was dried in a vacuum oven at 85 °C for at least 12 h immediately prior to use. All other chemicals were used directly as received.

Choline chloride:urea DES (reline) was prepared by combining the components in a molar ratio of 1:2 and stirring, with heating to temperatures up to 60 °C, until a clear, homogeneous liquid was formed. Thereafter, solvents were equilibrated at 40 °C for at least 24 h in sealed bottles. Similarly, choline chloride:ethylene glycol (ethaline) was prepared by mixing the components in the same molar ratio and stirring at 60 °C until the DES was formed.

Ternary DES comprising choline chloride, urea and glycerol were also prepared using the same method as for choline chloride:urea, for use in the the experiments discussed in Chapters 4 and 5.

2.3.1.2 Polyethylene glycol 200-based DES

Polyethylene glycol 200 (PEG-200) was purchased from Alfa Aesar. Thiourea ($\geq$99 %) was purchased from Merck. All chemicals were used as purchased.

The procedure followed was that first reported by Mu *et al.* [112]. In a typical synthesis, PEG-200 and thiourea were combined in a round bottomed flask or Schott bottle in a molar ratio of 2:1. The vessel was subsequently sealed and the mixture stirred for several hours at room temperature until a homogeneous liquid was observed.

2.3.2 Materials characterisation

2.3.2.1 X-ray diffraction

X-ray diffraction measurements were performed using a STOE STADI-P diffractometer equipped with Mythen detectors, with Cu-Kα source radiation (1.5406 Å). For powder samples (measured in transmission mode in the instrument), samples were placed between two X-ray transparent foils, sealed in the sample holder and mounted on the automatic sample changer. Film samples were mounted directly into the instrument and measured in reflection mode, with the detectors operating in Bragg-Bentano geometry. Diffraction patterns were typically collected in the range $2\theta = 20^\circ$ - 80°.

2.3.2.2 Scanning electron microscopy

Field-emission scanning electron microscopy (FESEM) imaging was carried out on a JEOL FESEM6301F instrument with an acceleration voltage of 5 keV. Powder samples were prepared by dispersion in ethanol followed by deposition onto a mica substrate. Where required, samples were sputter coated with a thin layer of gold and stored under vacuum prior to measurements. Images were acquired at a range of magnifications.

2.3.2.3 SAXS measurements

Laboratory SAXS measurements were carried out on an Anton-Paar SAXSpoint 2.0 instrument equipped with a 2-dimensional EIGER R series Hybrid Photon Counting detector. A Cu K-α source ($\lambda = 1.54$ Å) was used to produce the incident radiation. Samples were loaded into quartz capillaries of diameter 1 mm and measured with a sample-to-detector distance of 556.9 cm giving an approximate Q-range of 0.008 - 0.4 Å^{-1}. Data for each sample were collected in four frames with 300 s exposure each time, before the frames were averaged and the data processed. Depending on the sample, the temperature of the measurement was controlled using a Peltier unit. Background subtractions and data fitting were carried out using the NIST SANS data reduction and analysis macros within Igor Pro [145].

Chapter 3

Deep eutectic solvents for the synthesis of functional materials

3.1 Background

An introduction to deep eutectic solvents has already been given in Chapter 1, with some discussion of the various applications for which they have been utilised. This section will expand upon the use of DES as solvents for the synthesis of inorganic materials and in electrodeposition applications. An overview of advances in the synthesis and performance of electrocatalytic materials is also given, which provides support for the motivation behind this section of the research.

3.2 Synthesis of materials in DES

The application of DES for materials synthesis was already introduced in Chapter 1 but not expanded upon in any great detail. This section will give an overview of the use of DES in wet chemistry and solvothermal syntheses of inorganic materials, including metallic nanoparticles, porous materials and transition metal-based compounds, as well as provide a background for the solvothermal synthesis section of this chapter.

It has been shown that for materials designed for specific applications (for example catalysts or solar absorbers), control over their morphologies, structure and composition can have a great effect on their performance. Where great control is needed over the reaction, the highly tunable nature of deep eutectic solvents makes them ideal media for this type of synthesis. Ionic liquids have found extensive use in wet chemistry applications as alternative green solvents [146], but as mentioned previously in this thesis, certain advantages which DES have over ILs could make them more favourable for industrial scale-up.

The following literature review is not intended to be an exhaustive list of every material synthesised using DES, but aims to give an overview of the range of methods, morphologies and target applications in this field.

3.2.1 Open framework materials

Solvothermal and hydrothermal synthesis methods have proven popular for the synthesis of many classes of inorganic materials, offering a reproducible and relatively simple method which can be improved to include flow processes for continuous synthesis, which are relevant for industrial applications [147, 148]. Despite the convenience and relative simplicity of these methods, there is potential for improvement through exploring the use of milder synthesis conditions, or the design of systems where particle morphology can be precisely controlled by varying the composition of the reaction mixture.

In 2004, shortly after DES were first reported, Cooper *et al.* introduced a synthesis route similar to solvothermal synthesis, exploiting the ability of ILs and DES to function both as a solvent and structural directing agent within the reaction [108]. This novel method, which the authors termed an ‘ionothermal synthesis’ due to the nature of the reaction mixture, was employed to synthesise zeolite analogues (‘zeotypes’). It was suggested that by combining the solvent and template, competing solvent-framework and template-framework interactions were mitigated during the synthesis reaction. Parnham *et al.* investigated the use of DES as templating agents for the synthesis of aluminium phosphate materials (AlPOs) and cobalt aluminophosphate (CoAlPOs), with the template being introduced through the breakdown products of the DES at high temperatures during the reaction [109, 149]. It was possible to tune the structure of the product by varying the urea derivative component of the DES, and the unique synthesis method led to the synthesis of five new ALPO structures.

Besides these initial investigations, not much research exists concerning the use of DES for the fabrication of open framework materials, although a handful of studies exist using ionic liquids for this purpose [150, 151]. Lin and Huang [152] demonstrated the formation of zeolites with a high silica content such as ZSM-5, ZSM-11 and ZSM-39 in ChCl:urea, using fluoride anions as a mineralisation agent. Although the synthesis in the DES was successful, this study reported that the main source of morphology control came from the variation of the organic additives rather than through any changes in the solvent composition, and noted the longer reaction times using DES as compared to a hydrothermal synthesis. A second study by the same authors [153] to synthesise similar materials using a range of DES based on tetraalkylammonium salts did however find a change in morphology of the product.

3.2.2 Carbon-based materials

Del Monte, Gutierrez and co-workers have investigated the use of ChCl:ethylene glycol as the solvent for the resorcinol formaldehyde polycondensation for the synthesis of porous carbon materials [154]. It was also shown that resorcinol could act as the HBD component of a DES together with choline chloride, thereby forming a ternary ChCl:resorcinol:urea system. In this way, the DES functioned both as a solvent and precursor source. Mesoporous carbon structures with a narrow pore size distribution and remarkably high surface areas (approx. 600 m^2 g^{-1}) were synthesised via this route [155]. By doping the structure with nitrogen, hierarchal porous structures exhibiting good electrocatalytic activity for the oxygen reduction reaction (ORR) were obtained [156]. Similar materials have been investigated in carbon capture and storage [157] and supercapacitor applications [70].

3.2.3 Metal-based materials

Despite the promise which (in particular) the research of Cooper and Parnham showed, the use of DES for the solvothermal synthesis of compounds did not gain traction for several years, with the majority of research focus being placed on electrofinishing and separation/extraction applications. In the last decade, however, there have been a handful of publications synthesising inorganic materials via a solvothermal route (or similar) using DES for a variety of applications.

An ionothermal synthesis using ChCl:ethylene glycol was also employed for the synthesis of nickel phosphide (Ni-P) alloys comprising an amorphous core surrounded by crystalline Ni_3P shells [110]. Tuning the molar ratios of the Ni^{2+} cations and $H_2PO_2^-$ anions in the reaction mixture allowed for control over the thickness of these outer Ni_3P shells. Olivine structured $LiMnPO_4$/C nanorods, 100 - 150 nm in length were synthesised under relatively moderate conditions of heating at 130 °C for 4 h in ChCl:ethylene glycol by Wu and co-workers [158]. The obtained samples were investigated as potential cathodic materials in lithium ion batteries and showed good capacity retention (93 %) and stability under the test conditions. Furthermore, the use of a DES as the solvent as opposed to water or ILs allowed access to new morphologies for the $LiMnPO_4$ material which were previously not easily synthesised. The authors proposed that the reason for this was the solvent acting to selectively inhibit growth on certain crystal faces, so directing the structure of the products during synthesis.

The solvothermal method has also been expanded to include microwave-assisted techniques, which contributes towards designing an environmentally-friendly synthesis process by offering a low cost, low energy, rapid method of heating a reaction [159]. The rapidity of the heating can be advantageous for the production of uniform, mono-disperse nanomaterials [160]. Wu and co-workers also demonstrated the application of microwave heating, again for the synthesis of $LiMnPO_4/C$ nanorods in the ChCl:ethylene glycol DES, whereby the heating time reduced to just 30 min as compared to the 4 h required in their previous study. The same structure-directing effect of the DES was also observed in this case, with the materials exhibiting similarly high performances [111]. Also using a microwave heating method, Baker *et al.* developed a chloride-free synthesis of Ag nanoparticles. A DES comprising choline nitrate and glycerol was combined together with an Ag precursor and oleylamine (as a stabilising agent), and rapid precipitation of nanoparticles with uniform size distribution within the mixture was detected after only 30 s of heating at 100 °C [161]. The use of a DES can also favour the formation of nanoparticles as its increased viscosity can prevent rapid diffusion in solution, thus restricting the particle growth.

There have been instances where DES have themselves acted as the precursor source. Seo and co-workers reported the synthesis of an $Sn/SnO_2@C$ composite material via a pyrolysis method, at temperatures ranging from 500 °C to 800 °C by in an inert nitrogen atmosphere, using the DES formed between choline chloride and tin(II) chloride as a single source precursor [162]. The structure of the composite product comprised Sn/SnO_2 nanoparticles layered within carbon sheets. Given the range of metal chlorides which are capable of functioning as the hydrogen bond donor species within a DES, this simple pyrolysis method had the potential to be extended to a variety of metal oxide composite materials. Similarly, the direct calcination of the DES formed between various lanthanide nitrate hydrates and urea is a facile synthesis route to lanthanide oxides and hydroxides [163].

Research published by Sun *et al.* demonstrated the use of ChCl:urea as a structure-directing agent in the 'wet chemical' synthesis of gold nanoparticles for the electroreduction of hydrogen peroxide [164]. The authors showed that the use of the DES in the synthesis gave resulted in the formation of star-shaped nanoparticles with the [331] facet exposed, a morphology which was difficult to access via other synthesis routes. These particles showed higher catalytic activity under laboratory testing than alternative morphologies or polycrystalline Au samples. Similarly shaped Au nanoparticles were also reported by Krishnan and Godoy, who prepared hybrid Au/graphene oxide composites for use as a substrate surface-enhanced Raman scattering (SERS) analysis to enhance signal detection [165]. One further example is a self-assembly phenomenon reported by Raghuwanshi *et al.*, in which Au nanoparticles, synthesised onto the surface of ChCl:urea via a sputtering technique, formed an ordered structure comprising primary and secondary shells. The authors attributed this to the structure-directing nature of the DES, which may be modulated through the variation of the various ionic or neutral species within it [166].

Synthesis routes to various transition metal-based materials, whilst being carried out in non-aqueous solvent, might potentially not be considered as being purely solvothermal. In several instances, water is added to facilitate the precipitation of the product. and in such cases, the DES functions as an anti-solvent [167]. In this way, crystalline zinc oxide nanostructures with morphologies ranging from ‘nanoflowers’ to ‘rice grains’ were synthesised from a solution of ZnO powder in ChCl:urea. Structural control was obtained by adjusting the water:ethanol ratio injected into the reaction mixture to obtain the nanostructured products [113]. A later study by the same group reported the synthesis of ZnO nanosheets demonstrating catalytic activity comparable to that of TiO_2 for the degradation of methylene blue dye [168]. Gu *et al.* have demonstrated that layered double hydroxides (LDHs) of transition metals such as Co-Fe LDH [169, 170], α-$Co(OH)_2$ [170], and α-$Ni(OH)_2$ [171] may also be prepared via this water injection method. A similar approach has also been used for the synthesis of ‘spindle-like’ Fe_2O_3 particles [172], and a co-precipitation method (using potassium hydroxide solution instead of water to facilitate the formation of solid products) was used by Chen *et al.* for the synthesis of magnetic Fe_3O_4 nanoparticles [173].

Recently, George *et al.* demonstrated the synthesis of magnesium ferrite, $MgFe_2O_4$ particles in five different DES comprising choline chloride and a range of hydrogen bond donors (urea, ethylene glycol, malonic acid, oxalic acid, and fructose) [174]. The bimetallic oxides were synthesised by first combining Fe_2O_3 and MgO with the DES, followed by calcination at 500 °C. The morphology of the synthesised particles seemed to depend on the DES: cubes and spheres were obtained using DES with acid-based HBD molecules, whilst only cube-shaped particles were seen using ChCl:urea. In the case of ChCl:ethylene glycol, some spherical particles but also a great deal of aggregation was observed, and ChCl:fructose gave rise to grain-like particles. The synthesised $MgFe_2O_4$ all showed good performance in electrochemical sensing applications, with those synthesised using ChCl:fructose having the lowest detection limits and greatest sensitivity. Similarly, ternary metal oxides containing Zn, Cu and V were synthesised from a combination of binary metal oxide precursors in ChCl:urea, with the final products obtained via calcination of the reaction mixture. The structure (specifically, the number of oxygen vacancies) could be tuned through a variation of the calcination temperature [175].

A handful of other authors have also demonstrated a similar synthesis method, involving the low temperature heating of the reaction mixture to dehydrate the precursors, followed by high temperature calcination to remove the DES and form the crystalline product. Materials synthesised via this method include barium titanate [176] and superconductors such as $YBa_2Cu_3O_{7-x}$ [177] and $Bi_2Sr_2CaCu_2O_{8+x}$ [178].

Zhao *et al.* fabricated $NiCo_2O_4$-MoS_2 composite materials for use in electrochemical sensing through the calcination of a mixture of nickel/cobalt nitrates, MoS_2 in ChCl:urea [179]. A BiOCl/$BiVO_4$ heterojunction was synthesised first by using a sol-gel method in ChCl:urea [180], and later by using the ChCl:citric acid DES to precipitate the material from an aqueous precursor solition [181]. The molar ratio of the components in a DES formed between ChCl and 1,8-diaminooctane has been shown to greatly influence the structure of a series of crystalline selenidostannates with interesting properties such as thermochromism [182, 183].

Aside from metallic nanoparticles and oxide/oxyhydroxide materials, some instances of sulfide synthesis in DES have also been reported. A DES based on ChCl and thioacetamide was used for the synthesis of several binary metal sulfides, including ZnS, CdS, CuS, Ag_2S, and Bi_2S_3. In such a system, the thioacetamide functions both as a HBD molecule and as a sulfur source [184]. The effect of the DES composition was briefly investigated, with the morphology of CuS nanoparticles changing from micron-sized spheres to larger hexagonal plate structures as the molar amount of thioacetamide in the DES was increased. Similar to the theory proposed by Wu *et al.* [158], the authors of this study attributed this to the DES selectively adsorbing on the [001] crystal plane when the ratio of thioacetamide is increased, and so inhibiting crystal growth in this direction. A mixed metal nitro-sulfide material was synthesised through the direct calcination of a DES containing mixed metal chlorides and the amino acid L-cysteine [185]. Mu *et al.* [112] reported the use of a novel halide-free solvent based on polyethylene glycol (PEG) and thiourea for solvothermal synthesis. "Sea-urchin"-like particles of $NiCo_2S_4$ synthesised in this solvent using metal nitrate precursors and autoclave heating at 160 °C for 16 h showed remarkable performance as electrocatalysts for the oxygen evolution reaction (OER). The calculated overpotential was 337 mV, with a Tafel slope of 64 mV dec^{-1}, outperforming Ni and Co single metal sulfides as well as other transitional metal oxide and sulfide catalysts reported in the literature. As the function of PEG as a templating agent has been studied for many years [186], previous findings were used to propose that the growth of the nanostructures is controlled by PEG selectively adsorbing on certain crystal faces through its -OH groups, and by steric hinderance caused by the polymer chain. The same DES was further used by the group to synthesise nanosheets of Fe_3S_4 [187].

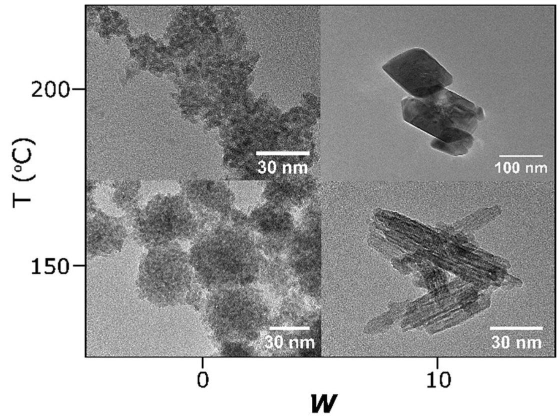

Figure 3.1: Transmission electron microscopy (TEM) images of iron oxide nanoparticles prepared by Hammond *et al.* using a microwave-assisted synthesis method, showing the variation of particle morphologies obtained by varying the synthesis temperature and water content in the DES. Reproduced from Reference [11] under a Creative Commons Attribution Licence.

Hammond *et al.* demonstrated a facile solvothermal route for the synthesis of nanostructured cerium oxide (CeO_2) [115]. In a typical synthesis, cerium nitrate was combined with ChCl:urea at various levels of water content, and heated in a stainless steel autoclave to the desired temperature and for the desired reaction time. The authors showed that at a constant synthesis temperature, increasing the water content in the DES resulted in an increase in the aspect ratio of the CeO_2 nanoparticles, showing the correlation between solvent composition and the morphology of the products. As part of this study, the authors also carried out total neutron scattering measurements on the system to gain an insight into the mechanism of particle formation and the exact role of the DES within the system (see Section 3.2.4). These CeO_2 nanoparticles were later successfully produced in flow using a continuous synthesis method by Exposito *et al.* [188], which provides great potential when considering industrial scale-up possibilities . Hammond and co-workers further reported the synthesis of iron oxide, Fe_2O_3 nanoparticles using a microwave heating method similar to those discussed above [11]. In this study, iron (III) nitrate nonahydrate was used as a precursor and both pure and hydrated ChCl:urea DES were used, such that the hydrated DES contained 10 moles of water per mole of ChCl. Reactions were carried out in a microwave reactor at temperatures between 100 °C and 200 °C with a consistent heating time of 10 min. In the pure DES, small nanoparticles of γ-Fe_2O_3 were obtained in each case with an average diameter of 2-3 nm, and were found to exhibit superparamagnetic behaviour as determined by SQUID magnetometry. In the case of the hydrated DES, reactions carried out at 150 °C produced nanoshards of γ-Fe_2O_3, which also showed this superparamagnetic behaviour, whilst those particles synthesised at 200 °C were found instead to be the α-Fe_2O_3 phase, with a large rhombohedral morphology. These observations demonstrated the control it is possible to have over particle morphology both by varying the synthesis conditions and the nature of the solvent. Photoanodes were prepared on glass coated with fluorine-doped tin oxide (FTO) by first preparing an ink from the powder and solution-casting it onto the substrate, and showed a reasonable photocurrent response.

These studies by Hammond *et al.*, in combination with several other investigation discussed in this section, demonstrate how functional materials can be developed using relatively simple synthetic methods, and how the use of a DES over an alternative solvent can give access to milder synthesis conditions, unique morphologies or morphological control. Whilst a material such as iron oxide is relevant in photocatalysis applications, the nature of this method means there is potential to extend it to include metallic oxides which are relevant in alternative applications, such as electrocatalysis. An exploration into the limitations of this method in terms of the effect of varying the metal precursor has on the products would be beneficial.

3.2.4 Mechanism of materials synthesis in DES

Whilst a variety of techniques [189] including TG-DSC, ^{1}H NMR and FTIR have been employed to study the decomposition of DES, in particular ChCl:Urea, which occurs during high temperature reactions, relatively little work has been carried out to accurately determine the mechanism of particle growth. Many studies instead contain proposed mechanisms based on previous knowledge of DES components or degradation products. It is not entirely surprising that this has not been widely studied, given that the structure of even the most widely-studied DES is complex, consisting of a wide range of intermolecular interactions, and this structure is further complicated when additives (such as reaction precursors) are present in the system [75, 190].

Kotov *et al.* investigated the mechanism of the self-assembly of PbS structures in a DES, identifying five distinct phases during formation [191]. Wide Q-range liquid-phase neutron diffraction data collected by Hammond *et al.* for a system of cerium nitrate in ChCl:Urea elucidated the mechanism of the solvothermal synthesis of ceria [115]. This data demonstrated that urea forms an extensive hydrogen-bonding network with water in the system and also acts as a ligand for cerium. These interactions facilitate its hydrolysis, with the breakdown products subsequently reacting with the cerium centres to eventually form cerium carbonate, which can be converted to the oxide via a calcination step.

The same group, building upon their study reporting on the synthesis of iron oxide [11], carried out an extensive investigation into the mechanism of particle formation in ChCl:urea during the reaction, combining several advanced experimental techniques including *in-situ* methods to elucidate the reaction pathway. The study also included the effects of water in the reaction, as in the original study the use of pure and hydrated DES gave rise to significant differences in product morphology (Section 3.2.3) [116]. The initial speciation of the Fe^{3+} ions from the precursor was explored first using extended X-ray absorption fine structure (EXAFS). Fits to this data indicated the formation of a complex wherein the Fe^{3+} ion had a coordination number of 6, with the best fits to the data obtained for a composition of $[Fe(L)_3(Cl)_3]$ (found for both pure and hydrated DES). The nature of the ligand 'L' was not easy to determine using this technique, though it was likely to be an oxygen-containing constituent of the system. This hypothesis was further supported by an analysis of neutron diffraction data. Fe^{3+} ions caused a disruption to the bulk of the structure through their coordination to various DES constituents. When the reaction was heated above 80 °C particle formation was seen to occur immediately in the hydrated DES and after approximately 5000 s in the pure DES. EXAFS data suggested the formation of oligomeric [-O-Fe-O-] species, which remain in solution until they exceed the solubility limit, at which point nanoparticles of iron oxide form directly and begin to grow. The time delay of particle nucleation in the pure DES suggested that the oligomers were more stable/soluble in the pure DES as compared to the hydrated DES. Furthermore, the inference from small-angle scattering data that a layer of choline exists at the DES/solid interface suggests that the choline also functions as a capping agent to inhibit particle growth across certain crystal faces.

Given their wide range of uses and potential for further development, it can be argued that it is imperative to carry out further systematic *in-situ* studies of material formation within the DES system to fully understand the mechanisms involved. It is important to note that, despite the examples given above, many studies have focused on the development of the synthesis route, rather than targeting a material to a desired application. However, gaining this deeper mechanistic understanding will allow for better exploitation of DES as "designer solvents" for the next generation of materials.

3.3 Metal finishing applications in DES

This section provides only a brief overview of electrodeposition using DES-based electrolytes. as this is not extensively investigated in this chapter. Several more comprehensive review articles have previously been published discussing this popular application of DES [192, 193]. Electrofinishing is widely used in industry for a variety of purposes, from corrosion protection [194] to improving electrical conductivity [195]. A number of reasons have been presented in the literature to justify the investigation of DES as an alternative solvent for these processes, both to increase the efficiency of an electrochemical process and to make the system more environmentally benign. Ionic liquids have been studied for many years as alternatives to aqueous electrolytes [196], and DES share many of the same advantages over aqueous electrolytes which make them suitable for this application.

In the first instance, aqueous electrolyte solutions can often contain toxic ions such as cyanide and heavy metal contamination, necessitating intensive treatment of waste streams [197, 198]. Many aqueous electrolytes are only stable within a narrow potential window, which limits the tunability of the deposition process - something which becomes increasingly relevant when trying to engineer the morphology and properties of the deposits to suit a certain application [199], whereas ILs and DES typically possess wider potential windows. Limitations with metal oxide solubility also hamper research progress in finding alternative metal coatings to the more toxic chromium, cadmium or nickel coatings used in industry today [199]. Although safer metallic coatings such as tungsten or aluminium are possible, the poor solubility of their respective metal oxides has hampered research progress [71]. Several metal salts, including those which are not readily soluble in water, have a high solubility in DES [200]. Several DES also display high conductivity and, at slightly elevated temperatures, their viscosity can be lowered enough to facilitate good ion transport in solution. The absence of water in an electrolyte system also allows for deposition onto substrates which are water-sensitive, such as aluminium [201] or magnesium [202].

Electrodeposition may be typically thought of as the formation of a coating or film onto a substrate via electrochemical methods. For the deposition of a metallic or alloy coating, this usually involves the use of an electrolyte solution containing the relevant metal cations, which are then deposited via an electrochemical reduction process onto substrate surface [203]. Similar to other applications, choline chloride based DES such as ChCl:Urea and ChCl:Ethylene glycol are amongst the most commonly investigated electrolytes for electrodeposition and they have been widely studied for metal coatings of Al, Cu, Ni, Zn and various alloys, typically using metal chloride precursors, some examples of which are given in this section. A eutectic mixture containing ChCl and a chromium(III) species has been shown to be a suitable alternative to the more hazardous chromium plating process from an aqueous electrolyte containing Cr(VI) ions [204, 205]. Modifications to the electrolyte, in particular through the use of additives such as LiCl can provide added control over morphology and properties of the deposits [206]. Zinc coatings are very common in industrial applications, typically used for their anti-corrosion properties. The choice of DES can have an effect on the morphology of Zn deposits (e.g. a grain-like morphology when using ChCl:urea and platelets in the case of ChCl:ethylene glycol) [207, 208]. The Abbott group used an *in-situ* atomic force microscopy (AFM) and quartz crystal microbalance (QCM) techniques to examine the electrochemical nucleation and growth of Zn coatings on a gold substrate [208]. Nucleation was found to occur via a 3-dimensional progressive growth mechanism, and the experimental techniques used demonstrated the possibility of developing a deeper understanding of the relationship between the morphology of the deposits and the nucleation mechanism, especially in the context of the potential to tailor the electrolyte composition to achieve the desired coating. Further kinetic studies, this time on nickel deposition from the same two DES has shown that both the thermodynamics and kinetic processes differ from that observed for aqueous electrolytes, with the result being altered morphologies of the coatings [209]. A variation in the deposition method, such as a potentiostatic vs. pulsed deposition has also been identified as a way to tune the morphology of the deposited nanoparticles [210].

Copper coatings are widely used in industry, and although established methods exist, changing the electrolyte may give rise to interesting properties. The electrodeposition of copper from DES such as ChCl:urea and ChCl:ethylene glycol has been shown to be an effective and efficient process [211], and mechanistic studies have found that the deposition occurs via a two-step process consisting of two separate single electron transfers, with the DES electrolyte stabilising intermediate phases. Gomez and coworkers [212] further presented evidence of a nucleation and 3D diffusion-controlled growth stage, where the DES electrolyte may actually inhibit growth compared to aqueous electrolytes. The effect of factors such as water content in the electrolyte [213, 214], halide-free alternatives to ChCl-based DES [215] and the choice of substrate has also been investigated [216]. As mentioned above, aluminium coatings are incredibly difficult to fabricate from aqueous electrolytes [196], and both ILs and DES have been explored as alternatives, with some examples being the use of a eutectic mixture of $AlCl_3$ with urea [217, 218]. Besides these commonly investigated metals which have been described so far, the deposition of other metals such as cobalt [219], silver [220], indium [221], and magnesium [222] has been explored.

DES may prove a useful alternative to aqueous electrolytes for the deposition of films where control over morphology, smaller particle sizes and minimal aggregation is an advantage. This has previously been shown true for the deposition of silver coatings, where as it was found that the presence of the DES selectively hindered vertical growth of deposited particles. Whilst a similar effect was observed in aqueous chloride electrolyte, it is conjectured that the presence of the DES leads to rounder, smaller grains being formed due to the viscosity of the DES inducing lower superficial diffusion [223].

The deposition of alloys or of compounds such as oxides or sulfides can present an additional challenge in having to consider the difference in redox potentials between the different constituents of the coating. One advantage of electrodepositing alloys using DES-based electrolytes is that these difference in redox potentials as compared to aqueous electrolytes gives access to structures and compositions which might be difficult to access via other routes. Some examples include the deposition of Zn-based anti-corrosion alloy coatings [224], including the deposition of zinc-tin alloy coatings with tunable compositions [225] and an investigation into how additives can affect the properties of the coatings [226]. A number of ternary alloys have been deposited from DES and investigated in applications such as lithium ion batteries [227] and corrosion resistance [228]. The mechanism of alloy deposition from DES has also been studied for a range of materials in order to characterise the numerous electrochemical processes which take place during the deposition [229, 230].

A natural progression to the deposition of metallic and alloy films has been to investigate the deposition of simple compounds, particularly those which are relevant to photo/electrocatalytic and sensing applications where, as mentioned above, control over the morphology of the deposits provides the ability to maximise the efficiency of the material's performance. One instance of the use of this method for the production of catalyst materials is the conversion of Cu-Ga alloys deposited from ChCl:urea to $CuGaSe_2$, which is a photoabsorber material [231]. A similar method for the conversion of deposited Ni-Co alloy to a binary metallic sulfide deposit via a solvothermal reaction in a thiourea/DES mixture has also been studied [232]. The deposition of a TiO_2 thin film from an electrolyte containing ChCl:ethylene glycol only in the presence of various additives such as LiF was reported by Pereira *et al.*, however the annealed films consist of the lesser studied brookite phase, as compared to the well-known anatase or rutile phases commonly associated with photocatalytic applications [130]. Amorphous coatings of Zn-Ni-P have been deposited using a ChCl:urea-based electrolyte, with a variation in precursor ratios and deposition current density having an effect on the morphology and corrosion resistance performance of the deposits [131]. By carrying out a potentiostatic deposition at applied potentials of -1.5 V (vs. Ag/AgCl) from an electrolyte containing ChCl:glycerol, Sakita and co-workers detected the formation of mixture of cobalt and cobalt oxides on a glassy carbon electrode [132]. Similarly, hybrid Co/CoP films have also been deposited onto nickel foam, exhibiting good electrocatalytic performance towards the hydrogen evolution reaction (HER) in alkaline solution [233].

A number of examples have been given above where electrodeposition has expanded from metallic coatings to more complex materials, however there remains great scope for electrodeposition from DES to be expanded to a vast range of materials and applications.

3.4 Theory

3.4.1 Electrochemical water splitting

3.4.1.1 Hydrogen as a renewable fuel source

Hydrogen has many advantages which make it a promising alternative fuel source [234]. It is abundant, non-toxic, produces only water as a by-product of combustion, and has the highest gravimetric energy density of any fuel [235]. Additionally, it has the ability to function both as a combustible fuel and an energy storage medium. The majority of hydrogen is produced by steam reforming of methane. Whilst this is an effective process, it still utilises fossil fuels and so alternative methods are actively being investigated. These include thermochemical, photoelectrochemical and electrochemical water splitting [236].

This section will focus mainly on hydrogen generation via the electrolysis of water, which may find commercial applications in vehicles and when used as a mechanism to convert and store excess energy from the national grid.

3.4.1.2 Theory of electrochemical water splitting

Electrochemical water splitting operates via two half-cell processes for the oxygen evolution reaction (OER) at the anode, and hydrogen evolution reaction (HER) at the cathode. The use of catalysts for both reactions is advantageous in order to increase reaction rate and lower the applied potential required for water splitting.

Water splitting may proceed in either basic or acidic electrolytes. The presence of these electrolytes promotes the separation of ions to facilitate the OER and HER. The equations for these processes are given below [236].

In the case of an acidic electrolyte, the HER may be represented by the equation:

$$2H^+ + 2e^- \leftrightarrow H_2 \tag{3.1}$$

And the OER is represented by:

$$2H_2O \rightarrow: O_2 + 4H^+ + 4e^- \tag{3.2}$$

For an alkaline electrolyte, the HER is represented by:

$$2H_2O + 2e^- \rightarrow: H_2 + 2OH^- \tag{3.3}$$

And the OER is represented by:

$$4OH^- \rightarrow O_2 + 2H_2O + 4e^- \tag{3.4}$$

A schematic illustration of an two-electrode cell for water splitting in acidic electrolyte is shown in Figure 3.2 to aid understanding of the process.

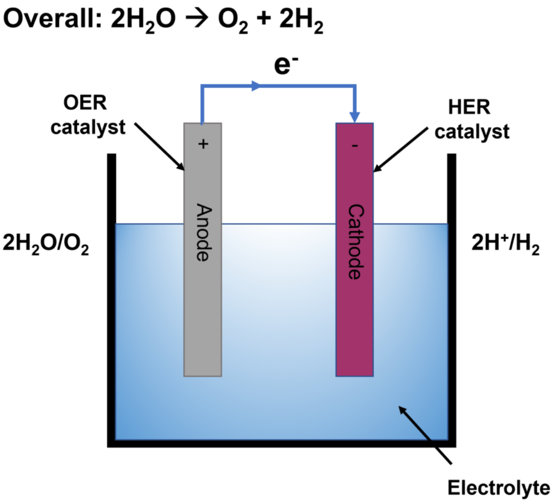

Figure 3.2: A representation of a two-electrode electrocatalytic cell for water splitting.

The minimum cell potential at which water splitting occurs is given by:

$$E^0 = E^0_{cathode} - E^0_{anode} = \frac{-\Delta G^0}{nF} \tag{3.5}$$

where ΔG is the change is Gibbs free energy of the system, n is the number of moles of electrons per mole of product and F is Faraday's constant, 96485 C mol^{-1}.

Thermodynamic calculations show the standard potential, E^0, of the HER to be 0 V vs. the reversible hydrogen electrode (RHE), and 1.23 V (vs. RHE) for the OER. However, real-life operation often requires an overpotential, η, to be applied to overcome factors such as electron/ion transfer processes, activation barriers, diffusion limitations, cell resistances and bubble formation which can lead to slow kinetics. Accounting for the ohmic potential drop, iR, Equation 3.5 may now be rewritten as:

$$E^0_{cell} = E^0_{cathode} - E^0_{anode} + \eta + iR \tag{3.6}$$

The overpotential is an important parameter in evaluating electrocatalytic performance and should be as close to 0 V possible for an optimum electrocatalyst. For electrocatalytic tests, the literature predecent has been to report the overpotential calculated for a current density of 10 mA cm^{-2}. The current generated by the electrolytic cell at a certain overpotential value η is described by the Butler-Volmer equation:

$$i = i_0 \left\{ exp\left[\frac{\alpha_{anode} nF\eta}{RT}\right] - exp\left[-\frac{\alpha_{cathode} nF\eta}{RT}\right]\right\} \tag{3.7}$$

where i_0 is the current exchange density and α is the mass transfer coefficient at the anode/cathode. If the reaction occurs far from the equilibrium potential (that is, at higher values of the overpotential), then Equation 3.7 can be further simplified to the Tafel equation:

$$\eta = a + blog(i) = -\frac{2.3RT}{\alpha nF} log(i_0) + \frac{2.3RT}{\alpha nF} log(i) \tag{3.8}$$

The Tafel slope, b, may be calculated by:

$$b = \frac{2.3RT}{\alpha nF} \tag{3.9}$$

This value, typically reported in units of mV dec^{-1} is another important parameter in reporting electrocatalytic activity, where 'dec' denotes decade, which corresponds to one order of magnitude between current values on a logarithmic scale. A low value of b indicates a large transfer coefficient, which is the proportion of the overpotential which affects the current density.

3.5 Electrocatalyst materials

Research into electrocatalysis is an extensive and wide-ranging field – as such, an in-depth critical review of electrocatalytic materials is outside the scope of this thesis. The following section highlights and briefly discusses the few key classes of materials typically employed for the hydrogen and oxygen evoution reactions (HER and OER) [237,238]. For the HER, these tend to include noble metals, chalcogenides, carbides and pnictides, whilst OER catalysts include oxides, hydroxides, perovskites and phosphates. Additionally, bifunctional catalysts capable of catalysing the HER and OER are under investigation.

3.5.1 Noble metal-based catalysts

Historically, noble metals including platinum, rhodium, iridium, ruthenium and palladium have remained the most efficient electrocatalysts for the HER reaction. Of these, platinum is the most efficient, exhibiting good stability in both alkaline and acidic media, though its high cost remains a barrier to the widespread use of electrochemical water splitting. However, a number of strategies have been employed to make its use more efficient. Strategic synthesis of the Pt catalyst to expose the highly active [110] plane allows for the material to be utilised more effectively. Alternatively, Pt can be combined with lower cost materials, either by alloying with transition metals [239,240], or through combination with transition metal-based catalysts.

Examples of this include composites with tungsten and molybdenum carbides with similar bulk electronic properties to Pt [241,242], or the deposition of transition metal hydroxides and hydr(oxy)oxides onto noble metal substrates [243,244]. Noble metal oxides, specifically IrO_2 and RuO_2 remain the most efficient catalysts for the OER, exhibiting good catalytic performance in both alkaline and acidic solution [245]. Strategies to improve their efficiency have mostly focused on modifying their preparation method.

3.5.2 Transition metal-based catalysts

Metallic particles and alloys

Metallic catalysts comprising transition metal particles have been investigated as noble metal alternatives but have previously shown poor stability and activity towards the HER. Binary and ternary metal alloys [246], in particular Ni-Mo alloys, have displayed enhanced mechanical and chemical stability in comparison to individual metallic particles in both alkaline and acidic electrolytes [247, 248]. Nanostructuring of these catalysts, in particular through the use of conductive carbonaceous supports such as graphene or carbon nanotubes (CNTs) has proved crucial to improving their performance [249]. One example includes work by Hegde *et al.*, who demonstrated that a composite or Co-Ni-graphene showed electrocatalytic activity four times higher than the Co-Ni alloy [250]. Cobalt deposited on N-doped graphene supports has shown onset overpotentials as low as 30 mV [251].

In order to enhance stability in acidic electrolytes, carbon based materials have been used to form an encapsulating shell [252–254] using a variety of techniques including chemical vapour deposition (CVD), sol-gel and microwave-assisted synthesis. Alternatively, oxides or hydroxides can be introduced into the catalyst structure to form a composite material, increasing activity by facilitating intermediate formation and activation [255].

Metal carbides

As mentioned previously, both tungsten carbide (WC, W_2C) and molybdenum carbide (Mo_xC_y) have been shown to possess a bulk electronic structure similar to that of platinum [256], and have exhibited good catalytic activity over a wide pH range [257, 258]. Nanostructured and carbon-supported (in particular through the use of reduced graphene oxide) carbides [259] have showed increased activity, with larger surface areas and lower charge transfer resistance than bulk powder samples [260, 261].

Metal chalcogenides

The investigation of transition metal chalcogenides has been a very large area of focus for research, with MoS_2 undoubtedly being the most famous of the series. Having been identified as having catalytically active sites for the HER [262], enhancement of the catalytic performance has focused on structural engineering to increase the number of S edge sites – this is most often achieved through the generation of nanosheets [263–265] or nanoparticles [266, 267]. Interestingly for this project, the use of thiourea in excess can provide a structure directing effect during synthesis of MoS_2. As thiourea is a component of a few known DES with choline chloride and PEG, there is potential for the use of these solvents in the synthesis of nanostructured MoS_2 [268].

The typically high intrinsic electrical conductivities of chalcogenide materials has led to their investigation also as OER catalysts, especially Ni and Co-based compounds, with a view to developing bifunctional catalyst materials [269]. To date, there have been several reports of metal chalcogenide catalysts exhibiting performances comparable to metal oxides. Examples from the literature include Fe-Ni and Co-Ni sulfides and selenides. Jiang *et al.* reported the synthesis of ultrathin nanosheets of $FeNiS_2$ via a simple colloidal route as a bifunctional catalyst, exhibiting HER/OER performances comparable to Pt/C and RuO_2, respectively [270]. Mu *et al.* [112] reported the synthesis of $NiCo_2S_4$ nanostructures from a DES-based solvothermal synthesis as a stable and efficient OER catalyst, with a lower onset potential compared to similar compounds and corresponding oxides and an overpotential of 337 mV at a current density of 10 mA cm^{-2}.

More recently, nanostructures grown on nickel foam substrates such as $(Ni,Co)_{0.85}Se$ nanosheets [271] and hierarchical $CoNiSe_2$ [272] have also exhibited bifunctional properties, where the use of the porous conductive substrate enhances charge transfer and catalytic performance. The high activities of metal chalcogenides can also be due to conversion to a metal oxyhydroxide during catalytic testing. This effect has been reported for samples of Ni-doped $FeSe_2$ [273], where the oxyhydroxide structure derived from the selenide was reported to have higher catalytic activity than as-prepared NiFe-LDH, suggesting the selenide acted as a conductive scaffold to facilitate charge transfer.

Nitrides

Carbonaceous materials, as well as being used as templates and supports for metal containing catalyst materials, have a range of advantageous properties such as good corrosion resistance, high conductivity, and low cost which make them suited for investigation as HER catalysts [274]. Whilst doped graphene [275] and carbon nanotubes [276] have been investigated, graphitic carbon nitride (g-C_3N_4), with a 2-D structure similar to graphene, is probably the most well know example of a carbon-based electrocatalyst [277, 278].

Phosphorus-containing compounds

A rapidly accelerating research field over the past years has been metal catalysts incorporating phosphorus. Catalysts for both the HER and OER have been synthesised in this category, with many showing good activity and stability over a wide pH range [279, 280].

Metal phosphides are often compared to the popular sulfide catalysts such as MoS_2 in the literature, but are believed to have certain advantages over sulfides, such as "metallic-like" high electrical conductivity and a greater availability of coordinatively unsaturated atoms on the structure surface due to isotropic crystal structures [281]. As such, Schaak *et al.* [282]. reported the synthesis of Ni_2P nanoparticles which outperformed unsupported MoS_2, with a Tafel slope of 46 mV dec^{-1} compared to $\tilde{9}4$ mV dec^{-1} for MoS_2 and similar to 30 mV dec^{-1} for a Pt electrode tested under the same conditions. Following this there have been a number of studies reporting nickel and cobalt phosphides with varying morphologies, with or without a porous support, which have shown high and efficient catalytic activity for the HER. Some phosphides have even shown activity towards the OER. Mixed metal phosphides comprising Ni/Co/Fe/Mn are also becoming increasingly reported in the literature [283].

The synthesis of phosphide materials can prove challenging for scale-up prospects depending on the chosen phosphorus source. Historically, organic phosphines such as trioctylphosphine (TOP) have been used, but as it is both pyrophoric and highly toxic, these reactions can only be carried out under an inert atmosphere [284]. Alternative routes using inorganic phosphorus sources have included the reduction of phosphates, a method which is facile but is often carried out at high temperatures to facilitate the breaking of the P-O bond. Hypophosphite ($H_2PO_2^-$) may also be used as a precursor in CVD [285], combination with a metal salt/oxide followed by annealing in inert atmosphere, or in an electrolyte bath for electrodeposition of thin films [286]. Most of these routes involve the synthesis of a powder or film hydroxide or oxide followed by phosphidation. Where possible, a single step synthesis would be more advantageous for scale-up.

It is worth mentioning that several P-containing materials have also been found to be catalytically active for the OER. Nanowires of Ni_2P synthesised to expose the highly active (001) phase were also found to catalyse the OER, with an overpotential of 290 mV reported at a current density of 10 mA cm^{-2} [287], however XPS analysis revealed the formation of oxides and hydroxides during catalytic testing which were thought to contribute to the overall performance of the catalyst. Cobalt phosphate was first reported in 2008 [288] as a catalyst for oxygen evolution. Since then it has been investigated extensively and is one of the most topical electrocatalyst materials [289, 290]. Additionally, it has been suggested that hybrid materials comprising chalcogenides or phosphides combined with an oxide or LDH may have a synergistic effect and generate more stable and efficient OER catalysts [291].

Oxide materials

Single and mixed transition metal oxides and hydroxides (Mn [292–294], Fe [295, 296], Co [297, 298] and Ni [299, 300]) have been the most popular materials investigated as OER catalysts, due to increased stability and decreased potential towards self-oxidation. In particular, literature has shown that Ni and Co based catalysts have the potential to exhibit catalytic performance similar to iridium-based catalysts [301].

Cobalt oxides, CoO_x, can be synthesised in a range of compositions, but research has concentrated on the spinel-structure Co_3O_4. Hydrothermal routes have been used to prepare a variety of Co_3O_4 nanostructures [302], whilst selective synthesis to expose the [111] crystal plane with a high concentration of cobalt ions has also been shown to enhance catalytic activity [303]. Cobalt oxide of the form $Co_{3-x}O_4$ was synthesised via a facile solvothermal route in glycerol [304]. The samples obtained through this engineering of cobalt defects were found to have a lower overpotential of 268 mV at 10 mA cm^{-2} than Co_3O_4 synthesised in the same study (376 mV at 10 mA cm^{-2}), with a small Tafel slope; a performance comparable to RuO_2 for the OER. Doping with other transition metals has also been found to improve catalytic activity of Co_3O_4 [305], as has combining the cobalt oxide with other catalyst materials such as nickel oxide (NiO) [306].

NiO and NiO_x catalysts for the OER have been modified to improve their activity by doping with metals such as iridium or cerium, however the mechanism of activity or identification of active sites remains unexplored [300]. Instead, focus is concentrated on nickel-based hydroxides and (oxy)hydroxides, which have historically been investigated in energy storage applications but are also active OER catalysts. Their performance may be improved by doping with heteroatoms such as Fe [307], controlling synthesis to selectively exposing active sites [308] and by combination with a carbonaceous materials such as g-C_3N_4 [309]. Additionally, layered double hydroxides (LDHs) obtained by combining Ni with Fe or Co has been a popular research direction in recent years [310]. Bimetallic oxides,146–149 in particular spinel-structured oxides (the most popular being $NiFe_2O_4$ and $CoFe_2O_4$) have high conductivities and good stability in alkaline media [311, 312]. They are typically modified by adjusting atomic ratios or through doping with cations such as Zn^{2+} [313].

3.6 Solvothermal synthesis of metal oxides

For each of the experiments discussed in this section, the ChCl:urea DES was prepared as per the method described in Section 2.3.1 and used immediately thereafter. The residual water content of the pure DES was not quantified as precise control over water content was not required for these experiments, and previous work has shown that in DES prepared using this method, the water content is around 2000 ppm [116]. The contrast in the water content between the pure and hydrated DES (typically 10 moles of water per mole of ChCl) is assumed to be great enough to be able to examine the effect of water addition on precursor speciation and particle morphology.

The applicability of the facile solvothermal method for the synthesis of nanoparticles as reported by Hammond *et al.* [11] to other transition metal oxides (Co, Ni, Mn) was investigated. Metal nitrate hydrates were initially chosen as metal precursors.

3.6.1 Solvothermal synthesis method in ChCl:urea

In a typical synthesis, 1 g of the metal nitrate precursor was dissolved in the DES with/without the appropriate molar ratio of water to a total solvent weight of 50 g. The mixture was transferred to a 150 mL capacity PTFE-lined steel autoclave and heated in an oven at a ramp rate of 5 °C min^{-1} to the desired temperature and held for several hours. Afterwards, the autoclave was allowed to cool naturally to room temperature. Following this the reaction was diluted with a 50:50 mix of deionised water and ethanol, centrifuged and washed several more times with water and ethanol. The resulting powder product was dried overnight at 60 °C under vacuum.

3.6.2 Synthesis of cobalt oxides

Cobalt oxides have perhaps been investigated more extensively than other transition metal oxides [314, 315] for their ability to catalyse both the OER and HER, and were therefore an initial choice to investigate whether this synthesis method could be easily translated to oxide materials containing metals other than iron. The synthesis of cobalt oxides was attempted with pure (unhydrated) ChCl:urea DES and with hydrated DES containing 2 or 10 molar equivalents of deionised water (relatives to the molar amount of ChCl in the DES) added. These solvent systems will be referred to as reline-0w, reline-2w and reline-10w, respectively.

3.6.2.1 Speciation of Co^{2+} in pure and hydrated DES

Upon dissolution of the metal nitrate precursor at room temperature prior to heating, an intense blue solution was formed in reline-0w and reline-2w, which indicated complexation of Co^{2+} ions with chloride from the choline chloride component in the DES, possibly resulting in the formation of the tetrahedral complex $Co(Cl)_4^{2-}$. In reline-10w, where water was included at just above 40 wt.% in the DES [316], a pink/purple solution was formed upon dissolution, which suggests that the interaction of the cobalt ions with water dominates over their interactions with chloride ions from the DES. From literature, it is suggested that this results in the formation of some intermediate in the equilibrium between the chloride complex and the hexaaquacobalt(II) complex, $[Co(H_2O)_6]^{2+}_{(aq)}$ [317]. This speciation is illustrated in Figure 3.3.

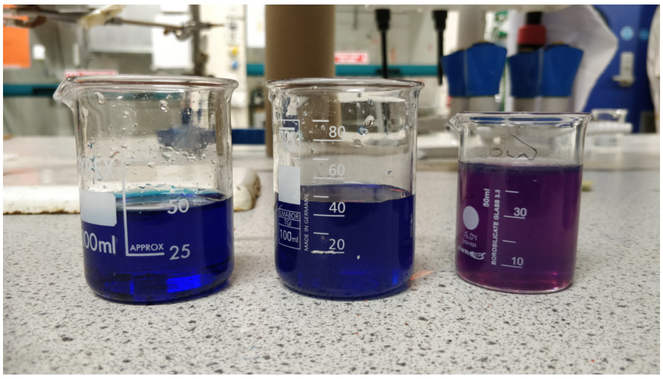

Figure 3.3: Photographs showing the speciation of cobalt(II) nitrate hexahydrate in ChCl:urea with (left to right) 0, 2 or 10 molar equivalents of water (relative to the moles of ChCl), respectively.

Attempts at synthesis were carried out at a range of temperatures (100 °C - 220 °C) and for varied lengths of time, in order to study the effect of temperature on the products with an eventual view to optimising the synthesis based on the morphology and performance of the materials. These are summarised in Table 3.1 below:

3.6.2.2 Results of solvothermal synthesis

For samples synthesised in unhydrated (reline-0w) DES, reactions carried out at 100 °C, 120 °C and 140 °C did not show a colour change following heating (which might have been expected if cobalt oxide or an intermediate material had formed), nor was it possible to immediately identify any solid material within the post-reaction mixtures. This outcome was observed irrespective of of synthesis time, and is in contrast to the synthesis of iron oxide, which proceeds readily at temperatures above 80 °C [116].

Figure 3.4: The appearance of the dried reaction mixture from cobalt(II) nitrate hexahydrate reacted in reline-0w, together with $CoCO_3$ synthesised in reline-2w and reline-10w. Black cobalt oxide powder formed following calcination at 300 °C, 30 min of the products from the reline-2w and reline-10w reactions (bottom).

Interestingly, this product appeared to have a greater viscosity than ChCl:urea at room temperature. The blue colour of the post-reaction mixtures suggest that there is still some complexation of the cobalt ions with chloride anions [317], possibly also containing other species similar to the FeL_3Cl_3 complex which was found to form when Fe^{3+} was added to ChCl:urea [116]. In the case of iron oxide formation, the Fe^{3+} further form an oligomeric species containing oxygen and the reaction and particle growth is facilitated by the thermal decomposition of the urea molecules. In the case of cobalt, there may be an additional energy barrier or competing interactions within the system which prevents the complete conversion of the material to a solid intermediate product which can be isolated.

By contrast, in the hydrated mixtures of reline-2w and reline-10w, a purple solid product was observed which could easily be isolated by washing with an ethanol/deionised water mixture and centrifugation. XRD analysis of these powder products showed the presence of several peaks which corresponded to cobalt carbonate, $CoCO_3$, rather than the oxide. These products were found to form at relatively mild synthesis conditions (100 °C and 3 h of heating). Although it was not quantified in detail, the amount of powder product recovered from the post-reaction mixtures was found to increase with increasing water content in the DES. This is possibly consistent with the observations

Table 3.1: A summary of the reactions carried out for mixtures of cobalt(II) nitrate hexahydrate in ChCl:urea, with and without water addition.

DES	Temperatures	Reaction times
Reline-0w	100 °C, 120 °C, 140 °C, 150 °C, 180 °C, 200 °C, 210 °C, 220 °C	3 h, 6 h, 8 h, 10 h, 16 h, 24 h
Reline-2w	100 °C, 120 °C, 140 °C, 150 °C, 180 °C	3 h, 6 h, 8 h, 10 h, 12 h, 16 h, 24 h
Reline-10w	100 °C, 120 °C, 140 °C, 150 °C, 180 °C	3 h, 6 h, 8 h, 10 h, 12 h, 16 h, 24 h

made by Hammond *et al.* that the water content has an effect on the rate of reaction in the DES [116]. The cobalt carbonate powders could be converted to the black cobalt oxide powders via a calcination step in air. By heating in a furnace at 300 °C for 30 min appeared sufficient to achieve conversion of the products and the use of a lower heating temperature and duration could potentially minimise the formation of large particles and aggregates through sintering of the product. A similar result was observed in the case of the synthesis of ceria (synthesised from a DES comprising cerium nitrate and urea) whereby calcination at high temperature was required to convert a cerium carbonate intermediate product to the oxide powder [115]. XRD analysis of the resulting powder products showed peaks at values of $2\theta = 31.3°$, 36.8°, 38.5°, 44.8°, 55.6°, and 59.3°, which correspond to spinel structured Co_3O_4 [318, 319] (Figure 3.5). Additionally, there appears to be an improvement in the crystallinity of the sample following calcination. The transition from the broad peaks seem in the XRD patterns for the cobalt carbonate samples to the narrower peaks seen in the patterns for the calcined oxide samples also suggests that the initial carbonate particles isolated from the reaction in DES sintered into larger particles on calcination.

Oxide samples synthesised in reline-10w at 100 °C for 3 h (followed by calcination at 300 °C 30 min) were examined using SEM in order to ascertain whether any interesting or potentially advantageous morphologies were present in the particles. Overall, particles have formed in large aggregates, several microns in diameter. Cubic structures up to 10 microns in diameter can be seen on some particles, often accompanied by flat stacked plates. Images taken at greater magnification show that these individual plates appear to be themselves made up of largely aggregated particles with no distinct

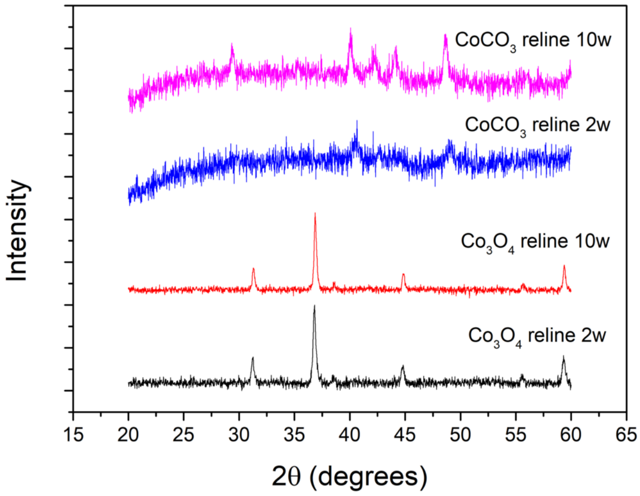

Figure 3.5: XRD patterns collected from samples of $CoCO_3$ synthesised in reline-2w (blue trace) and reline 10-w (purple trace) by solvothermal reactions at 100 °C, 10 h, together with diffraction patterns collected from Co_3O_4 samples formed by the calcination of $CoCO_3$ powders at 300 °C, 30 min (red and black traces).

morphology. Additionally, clusters of rod-like particles were also observed ranging up to several hundred nanometres in diameter. Systematic analysis would be necessary to determine whether parameters such as temperature or reaction time would significantly influence the obtained morphologies and particle size. Nevertheless, the goal of this study was to aim to extend the observations made for the synthesis of nanostructured iron oxide [11] by using similar methods to synthesised nanoparticles of oxide materials which were relevant for electrocatalysis. As it did not appear from these investigations that the formation of nanostructured oxide material was possible using the methods described above, the decision was made not to explore further samples using SEM due to it being an advanced and costly technique.

This section has described the results obtained when reactions are carried out at temperatures below 140 °C. At temperatures above this, certain key differences are seen. For reaction temperatures above 140 °C, the post-reaction mixtures had a very different appearance following cooling as compared to the mixtures from reactions at lower temperatures. The product appeared to have some phase separation within it, with a clear, colourless 'DES-like' layer on top and a brightly coloured opaque layer below. The colourless liquid was of comparable viscosity and appearance to the original DES which was used and the brightly coloured phase appeared to have a higher viscosity, resembling a gel-like substance, and was immiscible with the 'DES' phase. It was therefore easy to isolate the coloured gel simply by decanting the top layer of the

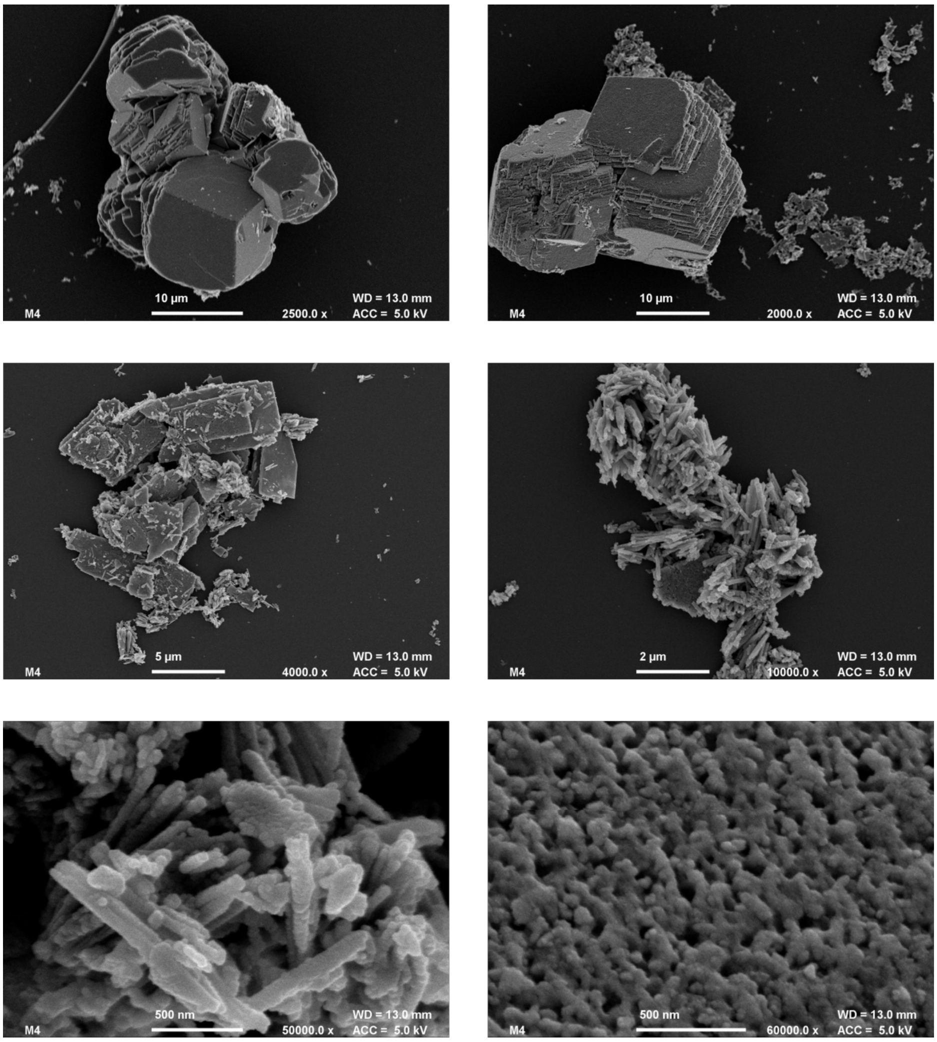

Figure 3.6: SEM micrographs for Co_3O_4 particles synthesised in the reline-10w DES by heating at 100 °C for 3 h to form $CoCO_3$ followed by heating in a furnace at 300 °C for 30 min to form the oxide material.

post-reaction mixture. This isolated phase was bright orange in colour and appeared to contain some precipitates. The residual solvent from the original reaction could be removed by repeated washing of the mixture with ethanol. When suspended in the ethanol, the isolated precipitates resembled orange crystals, and whilst these were not analysed further, a reasonable suggestion is that the species is a complex containing the cobalt cations, chloride anions and some products from the thermal hydrolysis of urea, such as hexamminecobalt chloride, $[Co(NH_3)_6]Cl_3$ [320, 321]. This is further evidenced by the fact that the product appeared to readily oxidise to blue-purple crystals in air [322]. Furthermore, on addition to water, a deep brown solution was formed,

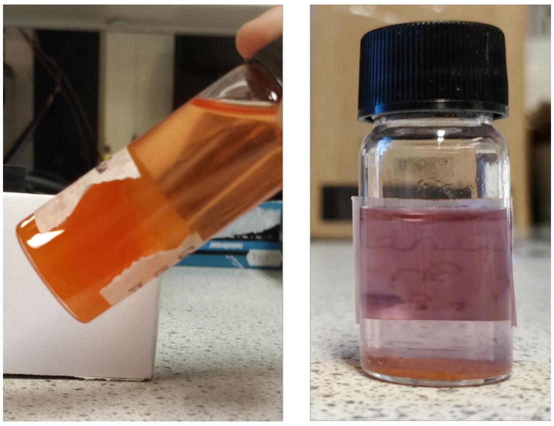

Figure 3.7: Post-reaction appearance of cobalt(II) nitrate hexahydrate reacted in reline-0w at 150 °C, 10 h (left) and the solid isolated from the mixture by ethanol addition (right).

which is suggestive of oxidised form of a cobalt complex with ammonia in solution. Further confirmation would involve characterisation of the product through methods such as XRD or UV-vis absorption spectroscopy.

These observations again suggest the formation of an intermediate species which is stable enough within the reaction mixture to not react further to form an oxide material. This is in contrast to the synthesis of iron oxide, where the reaction occurs readily above the degradation temperature of urea in the DES. This is an indication that extending the facile solvothermal synthesis method is not at all trivial, and alternative methods would have to be explored for the synthesis of electrocatalyst materials with the same unique morphologies (and potentially enhanced catalytic performances) using DES.

3.6.2.3 Alternative metal precursors

Briefly, to determine whether the limitations of the synthesis method also applied to other metal salts, a similar synthetic route was also attempted for nickel-based materials. A summary of these reactions in reline-0w is given below. For a reaction of nickel(II) nitrate hexahydrate or nickel(II) chloride in reline-0w, bright purple crystals were obtained each time irrespective of the reaction time or temperature, whereas a dark coloured solid would be expected if successful conversion to nickel oxide had been achieved. These purple crystals could be isolated in a similar manner to the crystals from the reactions of cobalt(II) nitrates in DES described above by washing with ethanol and it was possible to dry them at low temperatures in air. XRD analysis (Fig 3.8) of the precipitates identified peaks mainly corresponding to hexammine nickel chloride, $[Ni(NH_3)_6]Cl_2$ with some peaks suggesting the presence of $NiCl_2$ [323]. This tendency for nickel to form stable complexes in similar environments was also observed by Ge *et al.* [324].

Table 3.2: A summary of the reactions carried out for mixtures of Ni- and Mn-based presursors in ChCl:urea, with and without water addition.

DES	Ni/Mn precursor	Temperatures	Reaction times
Reline-0w	Nickel(II) nitrate hexahydrate	100 °C, 120 °C, 150 °C, 180 °C, 200 °C, 210 °C, 220 °C	3 h, 6 h, 8 h, 10 h, 12 h, 16 h, 24 h, 36 h
Reline-0w	Nickel(II) chloride	100 °C, 120 °C, 140 °C, 150 °C, 180 °C	3 h, 6 h, 8 h, 12 h, 16 h, 24 h
Reline-0w	Manganese(II) nitrate tetrahydrate	100 °C, 120 °C, 140 °C, 150 °C, 180 °C, 200 °C, 210 °C, 220 °C	3 h, 6 h, 8 h, 10 h, 12 h, 16 h, 24 h, 36 h
Reline-10w	Manganese(II) nitrate tetrahydrate	100 °C, 120 °C, 150 °C, 180 °C	3 h, 6 h, 8 h, 12 h, 16 h

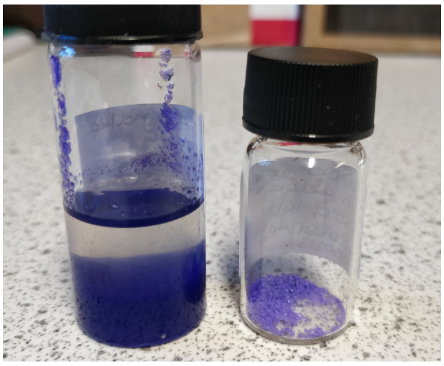

Figure 3.8: Post-reaction appearance of nickel(II) nitrate hexahydrate reacted in reline-0w at 150 °C, 10 h (left) and the solid isolated from the mixture by ethanol addition (right).

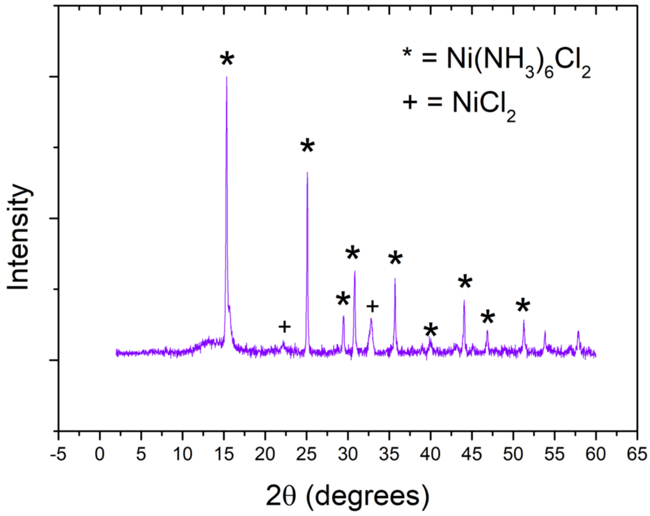

Figure 3.9: XRD pattern of the isolated product of the reaction of nickel(II) nitrate hexahydrate in reline-0w. The peaks corresponding to the suggested species present are labelled.

Similar reactions using manganese-based precursors also yielded similar results (Table 3.2). In the case of reactions in reline-0w, no precipitates were observed irrespective of the heating temperature and time, whilst reactions carried out in hydrated DES produced only manganese carbonates which would have to be converted to oxides via a further high temperature heating step as described in the previous section. One further interesting observation is the products obtained when Fe-based precursors were combined with the Co, Ni or Mn-based precursors used in this chapter with binary metal oxides (e.g. $NiFe_2O_4$) as the target materials. For reactions in reline-0w, the only powder product formed was Fe_2O_3 in each case, whilst the colour of the residual DES indicated that the second metal remained as as a stable complex in solution. This shows the strong preference of the reaction pathway for iron-based materials which does not occur when a different metal precursor is used.

Table 3.3: A summary of the reactions carried out for mixtures of transition metal nitrates, reline-0w, as an attempt to synthesised mixed metal oxides via a solvothermal process. The reactions are described relative to the two metal precursors used and the molar ratio in which they were combined in the reaction mixture.

Target material	Precursor A	Precursor B	Molar ratio	Temperatures	Reaction times
$NiFe_2O_4$	Nickel(II) nitrate hexahydrate	Iron(III) nitrate nonahydrate	1:2	100 °C, 120 °C, 150 °C, 180 °C, 200 °C	3 h, 8 h, 12 h, 16 h
$CoFe_2O_4$	Cobalt(II) nitrate hexahydrate	Iron(III) nitrate nonahydrate	1:2	120 °C, 150 °C, 180 °C, 200 °C	3 h, 8 h, 10 h, 12 h, 16 h
$MnFe_2O_4$	Manganese(II) nitrate hexahydrate	Iron(III) nitrate nonahydrate	1:2	120 °C, 150 °C, 180 °C, 200 °C	3 h, 8 h, 10 h, 12 h, 16 h

Due to difficulties in achieving the intended outcome of the project, which was to apply a solvothermal synthesis method reported for the formation of iron oxide [11] to form other nanostructured oxide materials, as well as circumstantial changes involving supervision, the synthesis of metal oxides was not pursued further during this PhD project. The work presented here has nevertheless introduced some of the limitations of the solvothermal method in terms of its applicability to the synthesis of alternative transition metal oxides. It is important to note that since these experiments were carried out, several studies have been published which use alternative methods to synthesise similar target compounds [325, 326]. The use of DES as solvents to form intermediate species from transition metal precursors has however been reported several times [327] and several methods have been discussed in the literature review of this section. Nevertheless, the main focus of this section of the project was to explore facile synthetic methods in order to determine whether the presence of the DES unlocked any morphologies or special properties in the products which were not easily accessible via synthesis routes. The next section describes an alternative approach to synthesising electrocatalyst materials.

3.7 Synthesis in PEG200:thiourea

3.7.1 Motivation for experiments

In the previous section, several attempts made at a facile solvothermal synthesis of metal oxide materials have been presented and the drawbacks of this method have been discussed. As it was not possible to achieve the initial aim of these experiments, which was to extend the synthesis method beyond iron oxide, it seemed prudent to explore other electrocatalytic materials as potential target compounds, especially if they would also be synthesised via a similar solvothermal method. Investigation into sulfide electrocatalysts is also widespread, and some examples have already been given in Section 3.5.

To design an appropriate DES-based solvothermal synthesis, it was necessary to modify the previous method to incorporate a sulfur source either in the reaction mixture or as part of the DES itself. As the choline chloride:urea DES was used in the initial investigations, choline chloride:thiourea seemed a logical starting point, as the thiourea component would have provided a sulfur source and its thermal decomposition may have driven the synthesis via a similar route to the reaction using urea. Although several attempts were made to synthesise a DES containing choline chloride and thiourea using a literature procedure [328], a stable liquid was never formed despite exploring other ratios and synthesis conditions. It was therefore necessary to either incorporate thiourea as a precursor, or to explore the use of an alternative DES which would allow the reaction to proceed via a similar mechanism as for metal oxides.

In 2017, a novel DES comprising polyethylene glycol-200 (PEG200) and thiourea (PEG200:TU) was reported by Mu *et al.* [112], and used in the solvothermal synthesis of nanostructured nickel cobalt sulfide, $NiCo_2S_4$, which proved to be a stable and efficient electrocatalyst for the OER. This DES can be prepared very easily by combining the components in a 2:1 ratio and stirring for several minutes at room temperature. The same group later characterised the physiochemical properties of these DES, termed ‘PEGylated’ solvents by the authors [329]. Due to the ratio of the components and the relatively high molecular weight of PEG-200 compared to thiourea (72.06 g mol^{-1}), there is only a small amount of thiourea in the DES as compared to PEG, however it still remains in excess in the eventual reaction mixture.

As iron oxide was the initial focus of the experiments using reline and could be synthesised readily, iron sulfides seemed a good starting point for these experiments. FeS_2 is not typically considered a good or popular electrocatalytic material as compared to its nickel- or cobalt-based counterparts, however a few studies have suggested that the incorporation of a small amount of dopants such as cobalt ions into the Fe-S lattice could improve electrocatalytic activity and stability [330]. In these experiments, the synthesis of Co-doped iron sulfide was investigated using the PEG200:thiourea DES and iron/cobalt nitrate precursors. The ratio of the iron and cobalt nitrates in the reaction mixture was varied to see if this was reflected in the composition of the product, with a view to optimising the electrocatalytic performance of the binary sulfide material. Additionally, we wanted to investigate whether the use of the DES specifically in comparison to other synthesis methods would introduce any interesting structural features which could also enhance performance.

3.7.2 Synthesis method in PEG200:thiourea

In a typical synthesis, cobalt(II) nitrate hexahydrate ($Co(NO_3)_2{\cdot}6H_2O$) and iron(III) nitrate nonahydrate, ($Fe(NO_3)_3{\cdot}9H_2O$) in the desired Co:Fe molar ratio were added to PEG200:thiourea DES (50 g). The total mass of solid metal precursor used for each synthesis was approximately 1.3 g. The reaction mixture was homogenised with stirring before being transferred to a 150 mL capacity PTFE-lined steel autoclave. The sealed reaction vessel was heated in an oven at 140 °C for 10 h, with a heating ramp rate of 5 °C min^{-1} before being allowed to cool to room temperature naturally. The resulting products were diluted with deionised water and centrifuged at 4500 rpm for 20 min to remove as much of the remaining DES as possible. After this, the mixture was filtered and washed with several portions of water and ethanol. The recovered powder product was then dried under vacuum overnight at 60 °C.

3.7.3 Electrocatalytic testing

3.7.3.1 Electrode preparation

In order to facilitate electrocatalytic testing of the sulfide powders, samples first had to be immobilised on a glassy carbon electrode (GCE) of diameter 12 mm. The surface of the GCE was prepared by sanding on wetted fine grit sanding paper before being cleaned with isopropanol to remove surface imperfections. To enhance adhesion of the electrocatalyst powder onto the GCE, a suspension of Vulcan XC 72R carbon black together with Nafion (5 wt.% mixture) in isopropanol was prepared [331], in a carbon:Nafion ratio of 50:50 µg cm^{-3}. The electrocatalyst ink was subsequently prepared by sonification of the catalyst powder in isopropanol such that 0.05 mL of the suspension contained approximately 50 µg of catalyst powder. To prepare the sample for testing, 0.05 mL of the Nafion/carbon suspension was placed onto the GCE followed by 0.1 mL of the catalyst ink. Following thorough drying of the electrode under an infra-red heating lamp, a further 0.05 mL of Nafion/carbon suspension was added to ensure adhesion of the catalyst powder.

3.7.3.2 Electrochemical measurements

Electrochemical measurements were using an Origatrod three-electrode electrolytic cell setup (Origalys), comprising an Ag/AgCl reference electrode (RE), platinum wire counter electrode (CE) and a rotating disc electrode containing the glassy carbon disk with immobilised electrocatalyst powder, which functioned as the working electrode (WE). In order to induce sufficient flux over the WE [332], the RDE was rotated at a speed of 2000 rpm during measurements. For HER measurements, sulfuric acid (0.5 M) was used as the electrolyte.

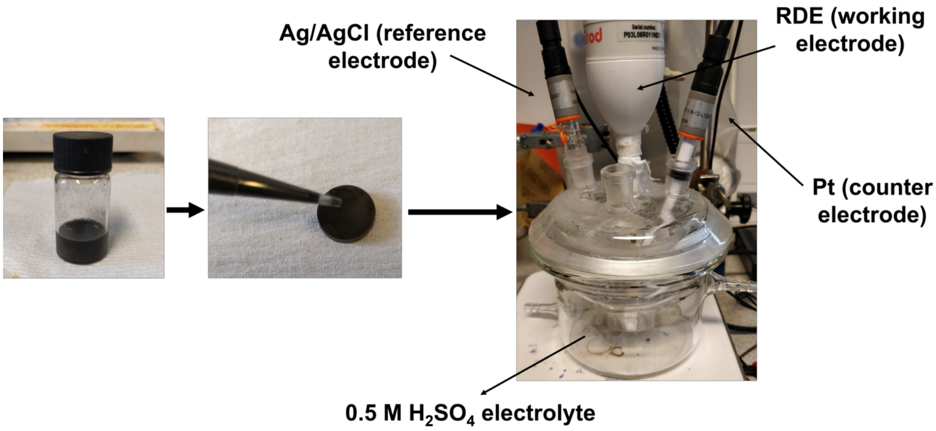

Figure 3.10: A schematic showing the catalyst ink, deposition onto the glassy carbon electrode and the 3-electrode electrolytic cell setup.

The electrochemical performance of the samples was evaluated using linear sweep voltammetry (LSV). Measurements were taken at a scan rate of 5 mV s^{-1} in a potential range of 0 - -1.8 V.

Potentials were measured relative to the Ag/AgCl reference electrode. These were subsequently calibrated to the reversible hydrogen electrode (RHE) using a modified version of the Nernst equation:

$$E_{RHE} = E_{Ag/AgCl} + 0.059pH + E^0_{Ag/AgCl} \tag{3.10}$$

where $E^0_{Ag/AgCl}$ is the standard potential of the reference electrode at 25 °C, $E_{Ag/AgCl}$ is the measured potential relative to the reference electrode and the pH is that of the electrolyte solution. Further conversion of current to current density in mA cm^{-2} allowed for the plotting of polarisation curves. Tafel slopes were plotted as per Equation 3.9.

3.7.4 Results of solvothermal synthesis of sulfide samples

Samples of mixed Co-Fe sulfides were synthesised according to the method already described. The ratio of cobalt- and iron nitrate precursors within each mixture was varied in order to examine the effects of the Co:Fe ratio on catalytic performance. In this section, samples are described in terms of their expected compositions given the ratio of their precursors rather than their exact composition following analysis of the powder product.

In contrast to the synthesis using the ChCl:urea DES discussed in the previous section, it was more difficult when preparing the solvothermal mixtures to obtain complete dissolution of the nitrate precursors, requiring several hours of stirring at slightly elevated temperatures (40 °C) prior to transferring to the steel autoclaves. All reactions were carried out in Teflon-lined steel autoclaves at 140 °C for 10 h.

Initially, it was difficult to obtain loose powder product from the reaction, as the sulfides were isolated by washing with water and centrifuging a few times. This led to the product appearing more as a black paste following drying under vacuum rather than a powder. This was most likely due to remaining solvent residue within the product, which prevented proper isolation of the sulfide powder. The problem was resolved by repeated washing and centrifugation of with both ethanol and water to remove this residue and in this way a loose, fluffy black powder was obtained for all samples.

The powder samples were analysed using PXRD (Figure 3.11). Peaks were obtained in the diffraction pattern in all cases, although they were not well defined and the noise in the pattern suggested that the samples either did not pose a high degree of crystallinity or that the particle size was small. Peaks were observed in the positions $2\theta = 33.0°$, $37.0°$, $40.6°$, $43.5°$, $47.3°$ and $56.1°$. By comparison to literature patterns, the presence of mixed Co-Fe sulfide material was confirmed, however there did not appear to be a discernible trend in the XRD patterns which corresponded to the precursor ratio in the reaction mixture.

Two samples, $Co_{0.2}Fe_{0.8}S_2$ and $Co_{0.5}Fe_{0.5}S_2$ were selected for imaging using field-emission SEM to both examine particle size and aggregation, and to determine whether interesting morphologies and microstructures of particles were present. Both samples showed the formation of large aggregated particles several microns in diameter,

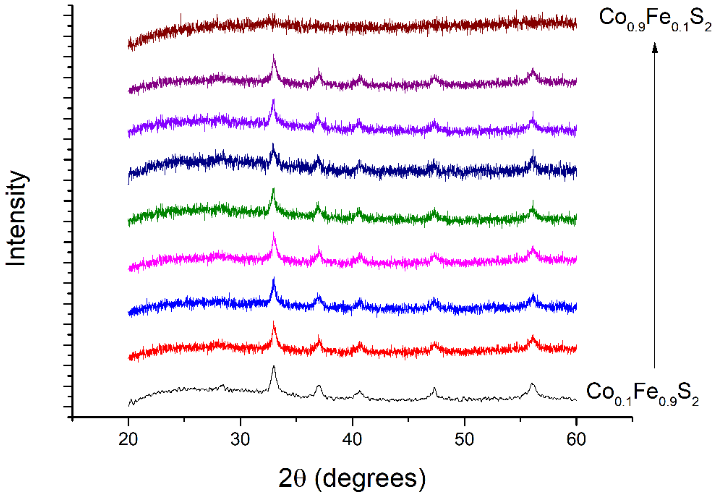

Figure 3.11: XRD patterns of mixed Co-Fe sulfides, labelled from lowest Co precursor content (bottom) to highest (top). Note that samples are labelled according to the relative ratios of the metal precursors included in the reaction mixture and not necessarily as their true composition.

although these aggregates appeared to have the same morphology. In the case of $Co_{0.2}Fe_{0.8}S_2$, a distinct 'desert-rose'-like formation can be seen, with large micron-sized particles. Similar structures have previously been reported in the literature [333]. There is an indication that this same morphology is beginning to form in the $Co_{0.5}Fe_{0.5}S_2$ sample, as it can be seen in the image but is significantly less distinct and clearly defined. Further imaging would be required to determine whether this is present in all samples. Additionally, it appears that some solvent residue may still be present in the $Co_{0.5}Fe_{0.5}S_2$ sample due to the appearance of smeared areas in the images.

3.7.5 Electrocatalytic testing of Co-Fe mixed sulfide samples

Following synthesis, the mixed Co-Fe sulfide samples were tested for electrocatalytic activity towards the hydrogen evolution reaction, both to determine their overall catalytic activity and to investigate whether the Co-Fe ratio had an effect on catalytic performance (to see whether any trends are present). Prior to analysis, samples were immobilised onto a glassy carbon electrode (GCE) following the method explained in Section 3.7.3.2. It must be noted that the use of a GCE as a catalyst support is not considered to enhance catalytic activity, unlike supports such as nickel foam which are used in other studies. Hence, the results presented here may not be directly comparable

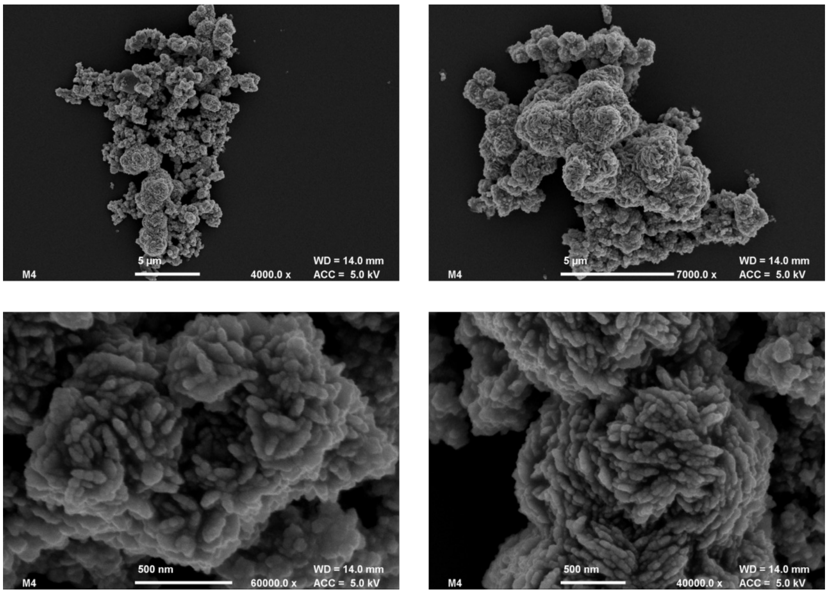

Figure 3.12: SEM micrographs of $Co_{0.2}Fe_{0.8}S_2$ powder.

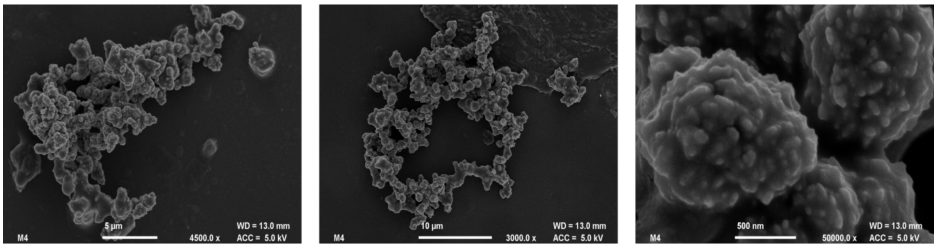

Figure 3.13: SEM micrographs of $Co_{0.5}Fe_{0.5}S_2$ powder.

to the performance of other supported or composite materials.

The electrocatalytic activity of the Co-Fe sulfide samples was evaluated using linear sweep voltammetry (LSV) in a potential range of 0 V - -1.8 V (vs. the Ag/AgCl reference electrode) at a scan rate of 5 mV s^{-1}, with 0.5 M H_2SO_4 as an electrolyte. For all samples, polarisation curves of the potential (in V) vs. the measured current density (in mA cm^{-2}, calculated by considering the measured current and the area of the working electrode) were plotted together with identical data recorded for the bare glassy carbon electrode (GCE) and a platinum benchmark catalyst. Constructing a polarisation curve can provide information on the capability of an electrocatalyst material towards charge adsorption/desorption. This can be evaluated by determining the applied potential at which a noticeable change (drop) in the current density occurs. At this value of the overpotential, a drop in current density marks a lower resistance to the flow of charge on the electrode surface. Compared to the bare carbon electrode, all samples demonstrated some catalytic activity towards the HER, as seen from the onset of the slope of the polarisation curve occurring at potential values closer to 0. Tafel plots were constructed in the manner described in Section 3.4. The Tafel slopes for selected samples together with comparison data from the platinum and GCE are displayed in Figure 3.15. A summary of the slope gradients for all of the samples is also presented in Table 3.4. Samples are labelled according to the amount of cobalt precursor used as compared to the amount of iron precursor.

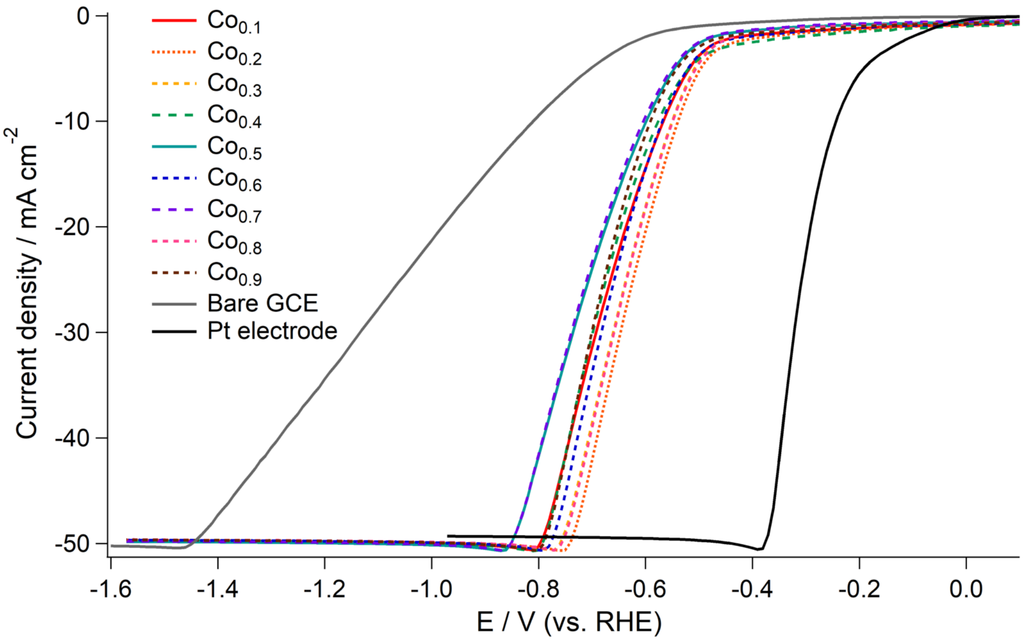

Figure 3.14: Polarisation curves plotted for the mixed Co-Fe sulfide samples, together with comparison data for a Pt benchmark catalyst and the bare glassy carbon electrode.

There appeared to be no discernible trend in the electrocatalytic activity of the samples with respect to the Co:Fe ratio. These initial tests do appear to show that $Co_{0.8}Fe_{0.2}S_2$ exhibited the highest electrocatalytic activity for the HER with overpotentials of 550 mV at 10 mA cm^{-2} current density. Despite this, all of the measured values of the overpotential are relatively high as compared to those values reported in the literature for high performing electrocatalyst materials. For example, hybrid Co-FeS_2/CoS_2 samples synthesised by Wang and co-workers exhibited an overpotential value of 278 mV under similar testing conditions [334], whilst the incorporation of carbon into a similar structure resulted in an overpotential of just 88 mV [335]. Although these represent only a couple of examples out of the vast number of publications concerning electrocatalysts, the higher values obtained in this project therefore suggest that a great deal of optimisation of the catalyst material, for example through

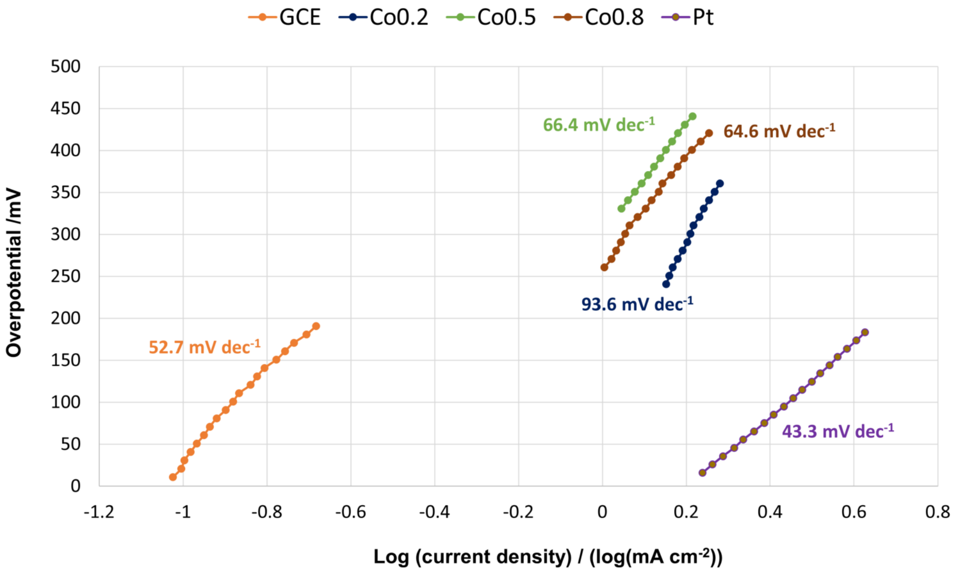

Figure 3.15: Tafel slopes constructed for various mixed Co/Fe sulfide samples, together with comparison data obtained for the bare Pt and glassy carbon electrode.

exploring different synthesis methods or through the fabrication of a thin film rather than a suspension of powder product is required to improve catalyst performance. In addition to determining the overpotentials for the samples, calculated Tafel slopes for all samples were in the range 64.6 - 99.3 mV dec^{-1} (Table 3.4). In comparison to the Pt benchmark catalyst, which had a calculated Tafel slope value of 43.3 mV dec^{-1}, the higher values obtained for the sulfide powders suggest lower charge transfer coefficients for these materials, which would inhibit their catalytic performance.

Table 3.4: The values of the gradient of the Tafel slope (b) estimate for all Co-Fe sulfide samples.

Sample	Tafel slope (b)/mV dec^{-1}
$Co_{0.1}Fe_{0.9}S_2$	99.3
$Co_{0.2}Fe_{0.8}S_2$	93.6
$Co_{0.3}Fe_{0.7}S_2$	70.3
$Co_{0.4}Fe_{0.6}S_2$	83.8
$Co_{0.5}Fe_{0.5}S_2$	66.4
$Co_{0.6}Fe_{0.4}S_2$	83.1
$Co_{0.7}Fe_{0.3}S_2$	65.7
$Co_{0.8}Fe_{0.2}S_2$	64.6
$Co_{0.9}Fe_{0.1}S_2$	96.9

Whilst these results are significant enough to merit further investigation, there is not enough evidence for this finding to be conclusive. Variations in data could arise from a number of factors such as mass loading. This is especially likely due to the fact that the differences in the activities of the various samples are minimal. In order to verify whether there truly is any difference in sample performance it would be necessary to carry out repeat measurements and error calculations.

3.8 Conclusions

Deep eutectic solvents (DES) possess a wide range of properties which have led them to be described as an ideal alternative 'green' solvent, as a replacement for organic solvents commonly used in industry today. In addition to this, the use of a DES over other solvents may give access to morphologies and properties in products which are not easily obtained using other methods, and may further allow a tuning of properties through a variation of DES composition.

In the first part of this work, the solvothermal synthesis of various transition metal oxides was attempted in order to extend a facile method previously demonstrated for the synthesis of iron oxide nanoparticles [11]. Synthesis in ChCl:urea (reline) using cobalt-based precursors was initially explored. Cobalt oxide, Co_3O_4 could be produced only via the calcination of cobalt carbonate samples synthesised in hydrated DES (reline-2w and reline-10w), and it was not possible to isolate a suitable powder product from the unhydrated systems. Additionally, a temperature dependence on the post-reaction mixture was observed in the case of the unhydrated DES, whereby reactions above 140 °C resulted in an orange solid, possibly hexamminecobalt chloride. The replacement of cobalt-based precursors with nickel alternatives also did not produce an oxide product, but a purple crystalline solid could be isolated which showed evidence of containing hexammine nickel chloride. Although the mechanism of the reaction is not defined, it was suggested that complexation of the metal species by chloride ions limits the reaction pathway. The results from this study have begun to define the limitations of expanding this synthetic route to all transition metal oxides. Further characterisation of cobalt oxide samples would be needed to determine if water addition and reaction conditions effect particle morphology and activity, however this synthesis was not explored further during the course of this project.

It is possible to take the principles of the solvothermal synthesis method and apply it to other materials, which may be synthesised via a similar route. Samples of mixed Co/Fe sulfides were synthesised using a PEG200:thiourea DES, in which the thiourea

DES component acted as the sulfur source. Initial electrocatalytic tests showed some activity towards the HER. $Co_{0.3}Fe_{0.7}S_2$ and $Co_{0.8}Fe_{0.2}S_2$ exhibited the highest activities with an overpotential of approximately 550 mV at 10 mA cm^{-2}, although there was no discernible trend relating performance to sample composition.

3.9 Further work

Even though the results presented in this chapter have given some insight into the possibilities of using DES for the deposition of various metal-based materials, it is clear that these experiments are greatly underdeveloped and far more work would be needed in order to fully explore their potential for this application. One aspect of investigation which will be critical to the future development of the work will be carrying out characterisation of the intermediate states observed during the initial synthesis experiments. These were presumed to be metal complexes and suggestions were made as to their composition based on their appearance and by comparison to the literature. Where the formation of any solid matter could not be determined in the post-reaction mixture, techniques such as small-angle X-ray scattering could be carried out in order to determine whether any particles were present. For both the post-reaction mixtures in DES and for the isolated particles, the nature of the metal complexes should be characterised using techniques such as elemental analysis, thermal analyses (e.g. thermal gravimetric analysis, TGA), or through spectroscopic techniques such as atomic absorption or UV-visible spectroscopy. A thorough understanding of the composition and nature of these metal-ligand complexes will aid in forming an explanation of the differing behaviour of various metal precursors within the solvothermal reaction, and in defining the limits of the synthesis method.

Another area of exploration is the synthesis method itself. For example, the synthesis of Co, Ni and Mn oxides via an intermediate could be further investigated, and a characterisation of the effect of synthesis conditions in this case could be carried out, particularly in relation to the electrocatalytic activity of the samples. Alternative synthesis methods could also be used, as have since been demonstrated in the literature such such as direct calcination of a reaction mixture to form oxide powders [336].

Aside from extending the investigation into the solvothermal synthesis, alternative directions could include exploring ways to introduce additional functionality into the materials which may enhance their electrochemical properties. One example of this would be increased surface area through the fabrication of porous oxide samples, which could be achieved via surfactant templating methods. The ChCl:urea DES was not capable of supporting the self-assembly of typical soft-templates such as the cationic C_nTAB surfactants [13], however it was possible to modify the system to facilitate micellisation of these molecules and carry out trial synthesis reactions. This process is discussed in the following chapter.

Whilst the synthesis work on mixed metallic sulfides is still in its initial stages, there is potential to carry out further tests on the already synthesised samples and expand its scope. The mixed Co-Fe sulfides could be further characterised using SEM and complementary techniques such as energy-dispersive X-ray analysis (EDX) to determine more details on the sample morphology and composition. Initial results on catalytic performance could be verified by further sample synthesis and catalytic testing. The effect of varying synthesis conditions such as heating time and temperature to determine the effect on electrocatalytic activity could also be investigated. Additionally, the catalysts could be tested for their performance towards the OER, in accordance with recent literature reports of sulfides active as bifunctional or OER catalysts [337].

The literature review section of this chapter has described how the use of DES as electrolytes for electrodeposition may may contribute to the growth of smaller particles and have a structural directing effect on obtained films. Although the deposition of metallic films using such electrolytes has been extensively studied, research on the deposition materials such as metal sulfides and phosphides remains limited. One alternative synthesis method which was briefly explored was using DES-based electrolytes to deposit films of metal sulfides and phosphides, using substrates such as fluorine-doped tin oxide (FTO) coated glass and nickel foam. This was not investigated extensively enough to be discussed within this chapter, however initial results are presented further in on in this thesis as part of the Summary and Future Outlook of the project.

Chapter 4

Investigating the self-assembly of surfactant molecules in ternary DES

A significant portion of the results presented in Sections 1.5 - 1.8.4 within this chapter are adapted from the publication:

Ria S. Atri, Adrian Sanchez-Fernandez, Oliver S. Hammond, Iva Manasi, James Doutch, James P. Tellam and Karen J. Edler. Morphology modulation of ionic surfactant micelles in ternary deep eutectic solvents. *The Journal of Physical Chemistry B*, 124(28):6004-6014, 2020.

The author contributions towards this work are as follows:

As the first author, Ria Atri carried out all physical characterisation measurements (except for density measurements) and analysis on the ternary deep eutectic solvents, all fitting of SANS data for the systems containing 130 mM C_{16}TAB and wrote the manuscript. Density measurements were performed by Iva Manasi. Fitting for the 25 mM C_{16}TAB/DES solutions was originally carried out by Adrian Sanchez-Fernandez for the publication however all fitting presented in this thesis was carried out by Ria Atri. James Doutch and James P. Tellam were the instrument scientists during the ZOOM and LOQ experiments at ISIS Muon and Neutron Source, respectively. SANS experiments were carried out by Ria Atri and Iva Manasi (130 mM C_{16}TAB data, ZOOM) during experiment RB1910484, and by Adrian Sanchez-Fernandez and Oliver S. Hammond (25 mM C_{16}TAB, LOQ). Ria Atri was supervised by Karen J. Edler, who assisted with the experiment concept and design, and with the writing of the manuscript. All authors gave approval to the final version of the manuscript. Any reproduced material is used with permission from Reference [13]. Copyright 2020, American Chemical Society. Further permissions related to any material excerpted should be directed to the ACS.

4.1 Introduction

In the last chapter, a series of experiments which attempted to synthesise metal oxide and sulfide electrocatalyst materials was discussed. Although several materials were investigated with a range of reaction parameters, it was not possible to synthesise nanoparticles with enhanced electrocatalytic activity via a solvothermal DES-based synthesis. A different direction which may enable the introduction of certain functionality into materials synthesised in DES would be the use of a soft template, such as a surfactant to introduce porosity and increase a material's surface area.

Over the last decade, DES have been increasingly investigated for their ability to support self-assembly, including the micellisation of amphiphilic molecules. Understanding the factors which influence this self-assembly with respect to the interaction of the surfactant molecules with the DES components. A knowledge of the factors which influence micelle morphology has the potential to allow researchers to tailor the micelle shape and size and hence possibly influence the pore structure of the resulting material.

In this chapter, a three component DES comprising choline chloride, urea and glycerol is investigated primarily for its ability to support the micellisation of cationic surfactants. The properties of this DES and the effect on micelle morphology of varying the hydrogen bond donor ratio in the solvent, together with the effect of additives such as water and metal ions into the system are characterised. Finally, some preliminary results are discussed where the synthesis of metal oxide materials from these surfactant/DES mixtures was explored.

The following sections comprise an introduction to surfactants, a literature review of self-assembly in ILs and DES, and provides the relevant theoretical background for the experimental techniques.

4.2 Introduction to surfactants

Surfactants, or 'surface active agents' are molecules which possess both a hydrophobic (lyophobic, 'solvent-fearing') and hydrophilic (lyophilic, 'solvent-loving') region. This has led to them being referred to as amphiphilic molecules (illustrated in Figure 4.1). Surfactants are typically classed according to the nature of their headgroup:

- Non-ionic surfactants, where headgroups are uncharged but polar.
- Ionic surfactants, which have permanently charged headgroups and may further be separated into cationic (e.g. quaternary ammonium surfactants) or anionic (e.g. sodium dodecyl sulfate) surfactants.
- Zwitterionic or 'amphoteric' surfactants, which have headgroups which contain both a cation and an anion, and as such have no formal charge.

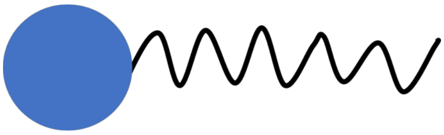

Figure 4.1: A representation of a typical surfactant molecule, showing the hydrophilic head region (blue) and the hydrophobic tail (black).

Probably the most notable feature of surfactants is their ability to self-assemble spontaneously under certain conditions. This is a property they share with other molecules such as certain polymers, alcohols and biological components such as most proteins, enzymes, and fatty acids. The formation of these aggregates is driven by the nature of the surfactant molecules (i.e. their lyophobic and lyophilic moieties). When micelles are formed, the lyophilic portion of the molecule will remain in contact with the (typically polar) solvent environment and shield the hydrophobic part from solvation. The specific nature of the surfactant determines its interactions with solvents. In the case of ionic surfactants, the lyophilic component consists of a charged headgroup and an ionic component bound to it electrostatically. This headgroup region, and specifically the electrostatic interactions between the headgroups on different surfactant molecules often direct the micellisation process. The packing of surfactants at the micelle interface (Section 4.3) is also modulated through the condensation of counterions and their interaction with the headgroups.

4.2.1 Critical micelle concentration

This formation of supramolecular aggregates is observed when the surfactant molecules are in solution in sufficient concentration, known as the critical micelle concentration (CMC). At the CMC, a certain property of the system (most commonly the surface tension, but may also be other parameters such as the conductivity, osmotic coefficient, or turbidity) experiences a sharp change. At low concentrations, surfactant molecules will adsorb at an interface, typically an air-water interface.

Gradually, as more surfactant is added, the surfactant concentration of the bulk reaches a stage where the formation of micelles is more energetically favourable than disrupting the hydrogen-bond network of the solvent. At this point, surfactant molecules will preferentially begin to self-assemble into and form micelles, and the surface tension at the interface becomes a constant. This is illustrated diagrammatically in Figure 4.2.

There are many factors which influence the CMC of a particular surfactant in a solvent. The nature of the head and tail portions of the surfactant can influence its solubility and so the CMC. An increase in the hydrophilicity (or lyophilicity) of the headgroup can increase solubility and so increase the CMC. An increase in the size of the lyophobic group can decrease the CMC due to an increase in the solvophobicity of the surfactant, and furthermore contribute to an increase in micellar size due to an increase in occupied volume of the surfactant tail within the micelle. The association of the counterions with the surfactant headgroup has been found to result in a lowering of the CMC [338]. Aside from the nature of the surfactants themselves, the use of additives such as simple salts (e.g. NaBr) can alter the electrostatic interactions within the system and cause a decrease in the CMC [339]. This effect has been seen for non-ionic and zwitterionic surfactants as well as the expected ionic surfactants, though admittedly to a lesser degree. Lastly, experimental conditions such as temperature must be taken into account, especially in the case of non-ionic surfactants as an increase in the Brownian motion of the surfactant monomers with increasing temperature (until the cloud point of the solution is reached) can decrease the CMC. This effect is less pronounced in the case of ionic surfactants, though it is still important to take into account both the cloud point [340] and the Krafft temperature (the temperature at which the CMC and solubility of the surfactant are identical) [341] when carrying out measurements.

In addition to water soluble surfactants, where the phase behaviour of the surfactants can be described and measured using the methods described above, there are also surfactants which are insoluble in water, such as phospholipids (which are important components of biological systems). Similar to water soluble surfactants, these will also adsorb at an air-water interface and the change in surface properties may be analysed via the compression of a monolayer and the measurement of a Langmuir (pressure-area) isotherm [342]. These surfactants will not be discussed in this chapter.

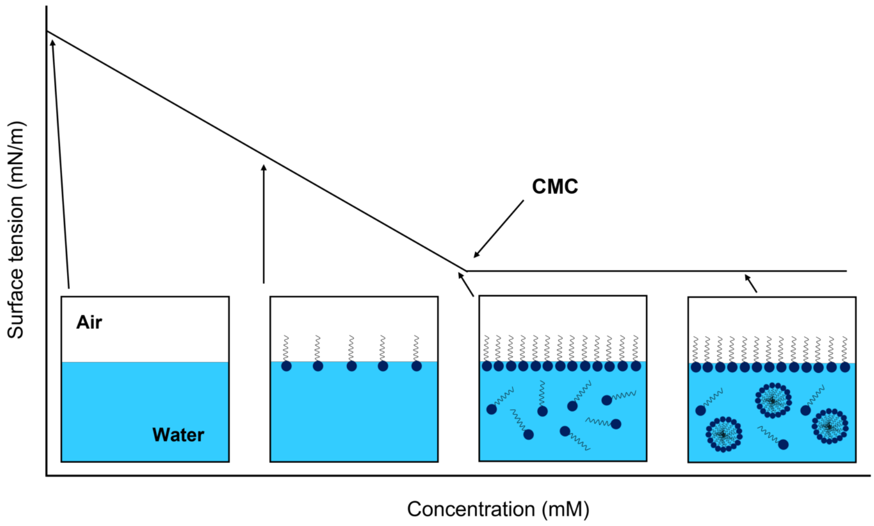

Figure 4.2: A diagram showing the interaction of surfactant molecules with the air/water interface at various concentrations above and below the CMC.

4.3 Self-assembly

Micellisation is promoted by the preference for hydrophobic/lyophobic moeities in solution to self-associate and form aggregates instead of interacting with the solvent molecules. As such this, 'solvophobic effect' is responsible for micelle formation above the CMC and promoting micelle growth, wherein the micelle core is typically thought of as a hydro/flurocarbon fluid environment which does not interact with the solvent. Conversely, interactions between the polar headgroups of the molecules are thought to limit micelle growth through repulsion interactions, and so have a profound effect on the micellisation process and micelle morphology.

Tanford first demonstrated that the imposition of geometric constraints upon a system suggested the presence of micelles within a system which adopted shapes other than spherical, which introduced the idea that consideration of the aggregation number could be used to predict micelle shape [25]. A short while later, Israelachvili and colleagues developed the concept of the 'packing parameter' [343] to describe the various morphologies adopted by micelles, and defined this in the following way:

$$Critical\ packing\ parameter = \frac{v}{a_0 l_c} \tag{4.1}$$

where v is the calculated average volume of the hydrophobic core of the aggregate, a_0 is the calculated headgroup area and l_c is defined as the surfactant tail length. The values of the packing parameter can be used to predict the shape of micelles obtained in a particular system. The constraints upon the equation may be imposed by considering the radius of the micelle (R), the aggregation number (N_{agg}), and the volume and surface area of the core (V_{core} and A_{core}, respectively). For a spherical micelle of radius R, $V_{core} = N_{\mathrm{agg}}v = 4\pi R^3/3$ and $A_{\mathrm{core}} = N_{\mathrm{agg}}a_0 = 4\pi R^2$.

A derivation using these equations can yield the relationship $R = 3v/a$, and considering that R cannot be greater than the extended tail length l_0 of the surfactant, it is calculated that the packing parameter for spherical micelles must be between 0 and 1/3 [344]. A summary of the predicted aggregate morphologies obtained for various values of the packing parameter is provided in Table 4.1.

Table 4.1: Micelle shapes predicted by various calculated values of the packing parameter. [24]

Packing parameter	Micelle shape
$< 1/3$	Spherical micelles
1/3 - 1/2	Worm-like micelles
1/2 - 1	Vesicles
$\sim$1	Planar bilayers
> 1	Inverse micelles

Although the tail length and volume of a particular surfactant will not vary between systems, the equilibrium area per monomer (effective headgroup area, a_0) is greatly affected by changes in the local environment which cause changes in headgroup interactions. These interactions between the headgroups, therefore, can be said to direct micelle morphology. For example, the addition of salts and other electrolytes to a solution can alter the repulsion between surfactant headgroups through the introduction of a charge-screening effect and so alter micelle elongation.

4.3.1 Solvents for self-assembly

Whilst studying the morphology and other properties of the assembled structures is important, equally crucial is understanding how the properties and structure of chosen media drive the self-assembly process. Examining the physical properties of the solvents such as surface tension, viscosity, ionic strength and polarity can provide the ability to predict whether self-assembly will be supported, and the morphology of the resulting aggregates.

Although water may be the solvent which is immediately connected with amphiphile self-assembly, a range of solvents has been investigated as suitable non-aqueous media. These include, but are not limited to, glycerol [345], ethylene glycol [346], other alcohols [347] and even supercritical CO_2 [348]. Analogous to the hydrophobic effect, the term 'solvophobic effect' was coined to describe the driving force behind self-assembly in these solvents. Whilst research into these non-aqueous systems has been carried out for several decades, more detailed understanding as to the mechanism and influencing factors of this process is continually required.

A comprehensive discussion of self-assembly in non-aqueous solvents is outside the scope of this thesis. A brief description of micellisation in ILs is given below, in order to give context and comparison to the more detailed discussion of micellisation in deep eutectic solvents which follows.

4.3.2 Ionic liquids for self-assembly

By contrast to other non-aqueous solvents, which are comprised of uncharged molecules, ILs are made up of ions bonded largely through strong ionic interactions and secondary forces such as hydrogen bonds, as introduced in Section 1.2. Greaves and Drummond estimated that prior to the discovery that ILs were also capable of supporting self-assembly, fewer than 20 molecular solvents had been investigated for this purpose, such that the addition of ILs to this list greatly expanded the number of available media for aggregate formation [349]. The nature and behaviour of ILs provides an interesting opportunity to study the self-assembly of a wide range of molecules. For example, many ILs are capable of forming a segregated nanostructure comprising both polar and non-polar regions, which can provide an ideal environment for the solvation of the hydrocarbon chain of surfactant molecules [350].

As early as the 1980s, micelle formation in ethylammonium nitrate was observed by Evans *et al.*, who determined the CMCs of a series of the cationic alkyltrimethylammonuim bromide, C_nTAB, and cetylpyridinium bromide, C_nPBr surfactants in this solvent [351]. Through the use of a combination of experimental techniques (viscometry, interfacial tension analysis and calorimetry) and a careful choice of amphiphiles, the effect of the headgroup, counterion and surfactant tail length was explored. Furthermore, the authors compared the behaviour of the solvent to that of water, introducing the idea of a 'solvophobic' effect similar to the hydrophobic effect, highlighting that both solvents possessed the capability to form extensive hydrogen-bonded networks. Subsequent experimental work comparing micellisation in ILs and water has proposed that surfactant monomers are more soluble in ILs than in water, leading to higher CMC values observed in these systems [352].

Further studies have found a range of structures formed with cationic surfactants, from spheres and ellipsoidal micelles [353] to lyotropic phases [354, 355] in cases where the surfactant molecules have been added in sufficient concentration (far above the micellar region). Although the high ionic strength of the solvent could potentially alter the micelle shape significantly compared to that observed in water through charge-screening effects (similar to salt addition to aqueous systems), studies have found that this is not the case, although it is thought to cause a great reduction in interaction between micelles [353, 356]. Factors which have been investigated for their effect on micellisation include the degree of headgroup solvation by the IL [356], and in this case it was found that self-assembly was determined by the short-range hydrogen bonding interactions between the a protic ionic liquid (PIL) and the surfactant molecules.

With their tunable nature, variation of both the cationic and anionic components of the IL can induce changes in aggregate morphology. The degree of micellisation seen in mixtures of non-ionic surfactants (dodecyl poly(ethylene oxide)) in PILs was correlated to the nature of the solvent cation [357]. Varying the length or substituents in the hydrocarbon chain of the IL cation can lead to variations in the non-polar regions of the solvent, which affected its ability to support aggregation through the 'solvophobic effect' mechanism [357]. Applying these same principles, altering the hydrophobicity of the anion in the IL can similarly affect the forces driving micellisation [358]. The same group [359] demonstrated that careful solvent selection and in particular the mixing of two ILs with which the dodecyl poly(ethylene oxide) non-ionic surfactant molecules interacted in opposite manners (they were highly soluble and no aggregation observed in 1-hexyl-3-methylimidazolium tetrafluoroborates (hmimBF_4), but did not mix at all with 1-ethyl- and 1-ethyl-3-methylimidazolium tetrafluoroborates (emimBF_4). Combining the two ILs however facilitated the micellisation of the surfactant molecules. This highlighted the possibility of controlling self-assembly through an understanding of solvent properties and careful choice of solvent composition.

Some self-assembly may also be observed in ionic liquids in cases where one component of the solvent is itself amphiphilic, i.e. where the component has polar and non-polar domains. One example of this is the a study carried out by Bruce and co-workers, who investigated structuring both in the bulk and at the surface of mixtures of ILs [360]. A range of experimental (X-ray and neutron scattering, fluorescence) and theoretical (MD simulations) were used to characterise the behaviour of a mixture of ILs synthesised from the combination of 1-ethyl-3-methylimidazolium and 1-dodecyl-3-methylimidazolium with bis(trifluoromethylsulfonyl)imide(to form [C_2mim][Tf_2N] and [C_{12}mim][Tf_2N]). In this study, the aggregation of C_{12} were observed, with the coalescence of these increasing with the concentration of [C_{12}mim][Tf2N]. This coalescence results in the formation of networks of segregated polar and non-polar domains, somewhat similar to those observed in the solvent nanostructure of pure ILs. Whilst a full discussion of this is outside the scope of this thesis, it is nevertheless an interesting phenomenon, particularly as several aspects of these observations have also been seen in DES. Long- and short-chain ILs have been shown to self-assemble in ChCl-based DES [361, 362]. Similar nanostructuring to that observed by Bruce *et al.* has recently been observed in DES, through the use of an HBD molecule which is amphiphilic [363, 364]. The structure of DES is further discussed in Chapter 5.

It has been highlighted in the literature that an understanding of the the solvent nanostructure, especially in so complex a system as an IL, was crucial to identifying the factors which controlled self-aggregation. Many computational [365] and advanced experimental techniques such as X-ray [366] and neutron diffraction [367, 368] and even quasi-elastic neutron scattering (QENS) [369] have been used to further understanding of this.

Aside from surfactants, other molecules which are relevant to biological systems have been investigated in ILs. For example, Bryant *et al.* investigated vesicle formation by phospholipids in protic ILs, relating their observations to the solvent nanostructure [370]. Other molecules investigated for self-aggregation are proteins [371–373], and DNA [374, 375].

4.3.3 Self-assembly in deep eutectic solvents

Whilst the previous section has highlighted a broad body of work dedicated to investigating the self-assembly of molecules in ILs which dates back several decades, the number of studies which concerned self-assembly in DES was limited until the last five years, when the field began to expand. An introduction to DES has already been given in Chapter 1, with a discussion of their main properties and applications. As tunable solvents, capable of displaying a wide range of physiochemical properties through the variation of their composition, there is a potential opportunity to control aggregate morphology and tailor it to a number of applications. In addition to this, certain properties of DES make amphiphile self-assembly favourable. For example, the dipolarity-polarisability parameter ($\pi*$), taken from the Kamlet-Taft solvatochromic paramaters [376] are reported to be higher for several ChCl-based DES than for water [377, 378]. It is suggested that an increase in solvent polarity should promote the formation of micelles in DES, potentially at lower CMCs than observed for water due to this. The following section will review the available literature on amphiphile self-assembly within these unique systems.

Although DES were investigated for a number of years in for the same applications as ILs, it was not until the last few years until they were considered as alternative media for self-assembly. Early investigations began in 2014 [379], when Rengstl *et al.* explored the structuring of choline-based surfactants (namely choline dodecyl sulfate, choline hexadecyl sulfate and choline oleate) in various DES based on ChCl. The surfactant/DES mixtures were characterised using SAXS and WAXS and the presence of aggregates of choline dodecyl sulfate in a mixture of choline-based DES was confirmed. As the object of the study was to combine DES to form systems with low melting transition points, the morphology of the aggregates was not characterised, though the authors did recognise the need for advanced scattering experiments to properly characterise these structures.

The first dedicated research into surfactant self-assembly in DES was carried out in the same year by Pal *et al.*, who tested the solubilities of ionic and non-ionic surfactants in ChCl:urea [380]. They determined that both the non-ionic (Triton X-100, Brij-35, and Tween-80) and cationic alkyltrimethylammonium bromide surfactants (dodecyltrimethylammonium bromide, $\mathrm{C_{12}TAB}$, and hexadecyltrimethylammonium bromide, $\mathrm{C_{16}TAB}$) were insoluble in the DES, but that sodium dodecyl sulfate (SDS) dissolved readily. The group subsequently reported the existence of well-defined structures in both the pure and hydrated DES with varying water content. As before, no extensive morphological characterisation of the aggregates was performed, but surfactant/DES mixtures were examined using surface tension and fluorescence spectroscopy techniques. Dynamic light scattering (DLS) and small-angle X-ray scattering (SAXS) data were presented as evidence of aggregate formation, but these measurements were not accompanied by any structural characterisation.

Similarly, the micellisation of alkyltrimethylammonium ($\mathrm{C_nTAB}$) surfactants with varying tail lengths (n = 10, 12, 14, 16 and 18) were reported by the same group, this time in ChCl:glycerol [381]. The CMCs of the surfactants in DES and DES/water mixtures in both of these studies were estimated using surface tension and fluorescence spectroscopy and were found to be approximately one order of magnitude higher than for the surfactants in water. Estimates obtained through SAXS measurements suggested the formation of globular micelles by $\mathrm{C_{16}TAB}$ with a radius of gyration (R_g) of around 2 nm, however these measurements did not allow for a detailed characterisation of aggregate morphology. Alongside this, the authors also presented some thermodynamic analysis of the system, reporting that micellisation in DES was less favourable than in water, evidenced by a less negative $\Delta G^0_{\mathrm{agg}}$ and lower $\Delta S^0_{\mathrm{agg}}$, possibly due to a weaker solvophobic effect in the surfactant/DES systems.

Research in this field was greatly advanced through a series of studies carried out by Sanchez-Fernandez and co-workers, who published a series of papers which presented several aspects of the self-assembly of surfactants and proteins in DES, alongside detailed structural characterisation of the micelle morphology using advanced scattering techniques. The group's work began with an investigation of SDS in ChCl:urea [21], as Pal *et al.* had demonstrated the formation of micelles in this system [380]. Using surface tension analysis, the CMC was estimated to be 2 ± 1 mM. The micelle morphology was characterised using small-angle neutron scattering (SANS) and reflectivity techniques. SDS is capable of forming a variety of self-assembled structures, including spherical or cylindrical micelles or lamellar phase dependent on the solvent and conditions such as temperature. In contrast to the spherical micelles formed in water, highly elongated cylindrical micelles up to a certain concentration (17 mM) [382] were observed which could be fitted to a cylinder geometric model. This elongation is similar to that observed when salt is added to SDS/water mixtures [383,384]. In the case of the DES, the cholinium cations would bind to the negatively charged SO_4^- headgroup, and the charge screening effect would allow the headgroups in the micelle to pack closer together, resulting in elongation. The limitation on this elongation results from the availability of choline cations within the DES; at a certain concentration of SDS the shielding effect on the sulfate headgroups decreases and the resulting lowered packing parameter causes a reduction in micelle elongation.

The CMCs of the C_nTAB surfactants in the ChCl:glycerol DES were found to be comparable to $C_{16}TAB$ or slightly higher ($C_{12}TAB$, $C_{14}TAB$) than values obtained for aqueous mixtures [14]. These values (e.g. $CMC_{C_{16}TAB} = 0.9$ mM), obtained through surface tension measurements, disagreed with those previously reported by Pal *et al.* [381], who used fluorescence spectroscopy ($CMC_{C_{16}TAB} = 16.1$ mM) in their study. Discrepancies in the values obtained for the CMC of the surfactants in these systems could be due to differences in the method used or simply attributed to a variation in the water content of the highly hygroscopic DES, which is difficult to control when solvent handling is necessary. The calculated aggregation number did not appear to vary in these systems with surfactant concentration, though at higher concentrations (greater than in water), intermicellar interactions could be characterised [14]. The increased ionic strength in the DES as compared to water could be the reason for the contribution to the structure factor not being apparent at lower concentrations, as this could have given rise to charge shielding in the system.

To assess the effect which altering DES composition could have on surfactant behaviour, the group also studied the micellisation of these same surfactants in the ChCl:malonic acid DES, this time also introducing water into the system to compare self-assembly in the dry and hydrated DES [385]. The surface tension in this system initially decreases with the addition of water up to 5 mole equivalents (per mole ChCl), after which it begins to increase again until 10 mole equivalents of water results in a surface tension greater than that of the neat DES, which denotes an increase in the cohesive forces within the system at high water contents. Unlike their previous observations, in this DES the micelle morphology was seen to be dependent on a number of factors. The length of the surfactant tail altered the degree of variation in micelle shape; for shorter alkyl chain lengths i.e. in the case of C_{12}TAB, the micelles remained globular with little variation in dimension, whilst C_{16}TAB was affected to a greater degree by changes in concentration and solvent environment. On increasing the concentration of C_{16}TAB in the solution, a clear transition from a globular to elongated micelle shape was observed. This is especially interesting as in pure water, C_nTAB surfactants typically form globular micelles, and introduced the idea of strong interactions between the surfactant headgroups with DES component (in this case, the malonate ions) leading to micelle elongation. Conversely, increasing the water content of the system resulted in a shortening of the micelles. A few reasons were proposed for this, such as an increase in solvent polarity and acid deprotonation, or the decrease in solvent screening effects within the aqueous systems as compared to the dry DES, though the authors noted the need for these complex interactions to be further characterised.

Some interesting micelle morphologies have been reported by Li *et al.* [386], who observed the transformation of cetylpyridinium bromide (CPyBr) from micelles (concentrations below 40 %), to hexagonal phases, to a bicontinuous cubic phase and finally to the lamellar phase (at high temperatures, above 80 °C) with increasing surfactant concentration in ChCl:glycerol and ChCl:ethylene glycol. The behaviour of CPyBr was also analysed in water and ethylammonium nitrate in order to see how the presence of the DES might affect self-assembly. The surfactant was found to behave similarly in DES as it did in water, and the group attributed this to the strong cohesive forces within the DES.

We have already seen several factors which can influence micellisation in DES, including the surfactant tail length, concentration, the water content of the system, temperature, and the DES components. Yet another factor which has proven to influence micelle formation and morphology is the surfactant counterion [338]. Sanchez-Fernandez *et al.* built on their previous work by exploring investigating the micellisation of dodecylsulfate surfactants with a variety of counterions, from single metallic cations (e.g. Li^+, Cs^+) to larger ions such as [1-ethyl-3-methylimidazolium]$^+$ or [1-butyl-3-methylimidazolium]$^+$, which are common components of ILs. Consistent with previous results, the CMCs for all but one of the surfactants were lower in ChCl:urea and ChCl:glycerol than previously reported in water. The binding of the counterion to the surfactant headgroup has previously been shown to cause a decrease in CMC values in aqueous solution [387], and the surfactant/DES mixtures showed a similar trend. This observation is especially interesting as it might be assumed that due to the number of ions present in the solvent in the case of both ILs [351] and DES, the surfactant counterions would have a negligible effect on the behaviour of the system. Instead of the cylindrical model used in previous studies, SANS data were instead fitted to a prolate ellipsoid model to allow the aspect ratios (the ratio between the polar and equatorial radii) to be compared directly. In ChCl:urea, highly elongated micelles were observed which the degree of elongation following a trend from the strongest to the most weakly solvated cation, indicating that the binding of the counterion to the micelle surface causes a change in the packing of the surfactant headgroups, and so to the micelle shape. In ChCl:glycerol, micelles tended to be globular rather than elongated with less variation in the elongation, which suggested a greater degree of solvation of the counterions in this DES leading to fewer counterions remaining close to the micelle surface.

Although non-ionic surfactants were found to be insoluble in ChCl:urea [380], later studies have found systems where they are capable of forming micelles. Poly(ethylene oxide), PEO surfactants were found to be soluble in DES formed from ethyl/butylammonium bromide combined with either ethylene glycol or glycerol [388]. The solubility of the PEO was reported to improve when the alkyl chain length of the HBA increased, and when ethylene glycol was used in the DES instead of glycerol. These observations were attributed to the change in the hydrogen bonding environment which are introduced when the DES composition is varied, a hypothesis which was supported by computational work carried out by Stefanovic *et al.*, who suggested similar changes in the hydrogen bond network within ChCl-based DES, achieved by changing the HBD, would alter the PEO solubility [389].

Most recently, a halide-free type IV DES comprising cerium nitrate and urea combined in a 1:3.5 ratio was shown by Manasi and co-workers to be capable of solubilising cationic (C_{12}TAB, $C_{12}TANO_3$), anionic (SDS) and non-ionic surfactants (hexa- and octoethylene glycol monododecyl ether - $C_{12}EO_6$ and $C_{12}EO_6$, respectively) [390]. The hybrid inorganic/organic nature of this DES as compared to the commonly investigated organic type III DES, together with its high Gordon parameter is thought to contribute to the low CMCs of the non-ionic surfactants (e.g. 1.2 ± 0.2 mM for $C_{12}EO_6$). The micelle morphologies obtained were consistent with those which would be expected in water or choline-based DES, with a micelle size smaller than has been measured in aqueous systems, but comparable to those obtained in ILs. This similar spherical morphology was observed for cationic surfactants $C_{12}TAB$ and $C_{12}TANO_3$. By contrast, SDS forms cylindrical micelles with a degree of elongation far greater than observed in other solvents (a length of over 400 nm), which has been attributed to a 'salting out' effect which occurs due to the high ionic strength of the solvent.

Aside from the surfactants discussed above, the self-assembly of ILs [361], proteins [391], dye molecule aggregates [392,393], and amphiphiles which frequently form components of biological systems have also been explored. The last of these applications is summarised briefly below.

Several years before the first studies concerning anionic and cationic surfactant micellisation in DES were being published, Gutierrez *et al.* reported that the formation of vesicle dispersions of 1,2-dimyristoyl-*sn*-glycero-3-phosphocholine (DMPC) had been achieved by the lyophilisation of aqueous solutions which contained the ChCl:urea or ChCl:thiourea DES [69]. The same group subsequently used the same preparation method to describe the incorporation of bacteria in DES [394], highlighting the potential for other biocatalytic transformations to be carried out in these solvents. However, the authors did not determine the role of the DES in supporting self-assembly in either of these studies. Subsequently, Bryant *et al.* showed that phospholipid molecules could be dissolved directly into ChCl:urea without needing any water addition or lyophilisation steps, and that the molecules spontaneously self-assembled into lamellar phases [395]. Over time, these transformed into vesicles, which is analogous to their behaviour in water. It was further demonstrated that the stability of the bilayer phase depends on the nanostructure of the DES itself, which was not the case for molecular solvents [396].

Sanchez-Fernandez *et al.* investigated the self-assembly of zwitterionic phosphocholine and sulfobetaine surfactant molecules in ChCl:glycerol [397]. The surfactants used in the study were selected such that the effect of both the headgroups and surfactant tails could be examined, and both were found to have an effect on the CMC and micellar shape. SANS analysis showed the formation of globular micelles of varying dimensions, influenced by differences in the nature of the headgroup and the tail length. It was found that the phosphocholine surfactant had a lower CMC than a sulfobetaine surfactant with the same alkyl chain length, and when the two sulfobetaine surfactants were compared, the C_{14} surfactant had a lower CMC than the C_{12} tail length. This behaviour is similar to that exhibited by these molecules in water. When the systems were analysed using neutron reflectivity, however, it was determined that the systems display the opposite behaviour to what is observed in water. The surface excess concentration was calculated to be higher for the phosphocholine than for the sulfobetaines, whilst the opposite was true for the area per surfactant molecule. At higher concentrations, intermicellar interactions could be seen in the SANS data, which is an unusual observation for zwitterionic surfactants. A few reasons were suggested to account for the variations in these interactions across different systems; a difference in the long-range electrostatic interactions in the system which are not completely screened by the DES and differences in ion binding to the headgroups, or a restructuring of the solvent in the local environment of the aggregates, similar to that observed for nanoparticles in DES [398].

From the summary of the literature we can see that there are many factors which influence micellisation in DES and the nature of the aggregate morphologies. This can be seen by the simple fact that surfactant molecules which are virtually insoluble in one DES may be solubilised just by changing one component [14]. Where the use of surfactants to design synthetic methods is concerned, these need to be taken into consideration, together with factors such as limitations induced by the degradation of surfactant molecules or DES components at elevated temperatures. For alternative applications, limitations imposed by the factors such as the viscosity of the system and how it may affect solvent handling will need to be considered.

Although the use of soft templates for the synthesis of porous materials such as mesoporous silica (SiO_2) [399] and titania (TiO_2) [400] has been researched for several decades [399], surfactant templating has not been explored to any great extent in DES. Chen *et al.* reported the application of SDS as a templating agent for the synthesis of hierarchical ZIF-8 particles via a facile solvothermal method [114]. Moreover, the porosity of the product could be controlled by varying in the water content and amount of SDS in the reaction mixture. This is an interesting result, as it had previously been reported by Hammond *et al.* that the use of SDS in the synthesis of cerium oxide resulted either in the formation of bulk powder with negligible porosity, or in surfactant pyrolysis at high temperatures with unfavourable degradation products [115]. Manasi *et al.* reported the successful synthesis of porous cerium oxide powder from a DES comprising cerium nitrate and urea with the addition of various surfactants. Here, the morphology of the powders and the nature of their porosity was tunable via variation of the surfactant [336].

Whilst it is true that only a small number of studies have been published concerning surfactant-templated synthesis in DES, both the use of surfactants for functional materials synthesis and of DES as a solvent for materials synthesis have been investigated separately for several years. Therefore, there is a good argument for exploring the design of surfactant/DES systems in which the synthesis of templated materials may be possible. This would be especially advantageous given the tunable nature of DES and the ability to influence product morphology through varying the solvent composition, which is relevant for the synthesis of functional materials for applications such as catalysis. Naturally, in order to gain a thorough understanding of any synthesis procedure, it is important to investigate the micellisation process itself, characterise aggregate morphologies and explore the interactions of these mixtures with precursor molecules.

The work presented in this chapter is partly taken from a publication by Atri *et al.* [13] which includes and follows on from the work presented by Sanchez-Fernandez and coworkers, exploring how surfactant molecules which are particularly useful in synthesis self-assembly in a ternary DES comprising ChCl, urea and glycerol. Although comparison data for systems containing SDS and C_{12}TAB as reported in the paper are presented here to aid the discussion of how these ternary DES support and influence self-assembly and aggregate morphology, this chapter will mainly discuss data collected for systems containing C_{16}TAB.

4.4 Theory of small-angle neutron scattering

The following section will dicuss neutron scattering theory as it applies to small-angle neutron scattering (SANS) experiments. A more general discussion of X-ray and neutron scattering theory has already been given in Chapter 2. The theory presented here is largely adapted from *Introduction to the Theory of Small-Angle Neutron Scattering and Neutron Reflectometry* by A.J. Jackson, 2008 [133].

SANS is an elastic scattering technique which measures scattering at angles close to the original beam trajectory (0.1 - 10 °) in order to probe the averaged structure of larger scatterers. It is typically quoted as capable of accessing a mesoscopic length scale of 1 - 100 nm. Examples of systems which SANS has been used to probe include (but are not limited to) polymers [401], nanocomposites [402], colloidal suspensions [403], biomolecules [404], semiconductors [405], liquid crystals [406] and glasses [407]. At these length scales, it is helpful to consider the whole system rather than treating each atom individually. To do this, a bulk property called the scattering length density is used which is defined as the average scattering length contributions from n atoms in a volume V. For clarity, the equation for the SLD for neutron scattering is repeated below:

$$SLD = \frac{\sum_i^n b_i}{V} \tag{4.2}$$

where b is the bound coherent scattering length and V corresponds to the volume which is occupied by n atoms[3].

The instrumentation for SANS measurements is similar to that of most scattering experiments, involving the generation, monochromation and collimation of an incident beam, which is then scattered by a sample and the scattered intensity detected. The experimental setup of a typical SANS experiment is illustrated in Figure 4.3. The intensity of the scattered radiation is recorded by the detector within the desired q-range.

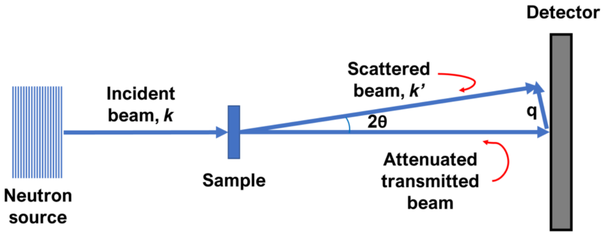

Figure 4.3: A schematic representation of the typical setup of a small-angle scattering experiment. Adapted from Reference [12] under a Creative Commons Attribution Licence.

The scattered intensity, $I(\lambda, q)$ from the interaction of an incident beam with intensity I_0 with a sample is given by:

$$I(\lambda, q) = I_0(\lambda) d\Omega \eta(\lambda) T_s \frac{d\Sigma}{d\Omega}(q) \tag{4.3}$$

where a detector which subtends an angle $d\Omega$ relative to the sample has an efficiency of $\eta(\lambda)$, and T_s is the sample transmission. These terms depend on the instrument itself and are not related to the sample. The final term, $\frac{d\Sigma}{d\Omega}$ is the macroscopic cross-section and is related to the differential cross-section, $\frac{d\sigma}{d\Omega}$ by integrating the equation:

$$\frac{d\sigma}{d\Omega}(\mathbf{q}) = \frac{1}{N} \left| \sum_{i=1}^{N} b_i e^{i\mathbf{q}\cdot\mathbf{r}} \right|^2 \tag{4.4}$$

using the scattering length density distribution across the sample, and then normalising it to the sample volume, to obtain the Rayleigh-Gans equation:

$$\frac{d\Sigma}{d\Omega}(\mathbf{q}) = \frac{N}{V}\frac{d\sigma}{d\Omega}(\mathbf{q}) = \frac{1}{V}\left|\int_V \rho(\mathbf{r})e^{i\mathbf{q}\cdot\mathbf{r}}d\mathbf{r}\right|^2 \tag{4.5}$$

As already discussed in Chapter 2, the macroscopic cross-section is the sum of the coherent, incoherent and absorption cross-sections. Incoherent scattering is independent of the scattering vector q and gives rise to an increase in sample background, especially in hydrogenous samples (due to the relatively high incoherent scattering cross-section of hydrogen). The absorption component also does not give useful information for the purposes of this thesis. For SANS measurements therefore only the information which can be obtained from the coherent contribution to the scattering cross-section is considered.

Equation 4.5 shows that small-angle scattering is observed as a result of inhomogeneities in the SLD within the system. However, in contrast to techniques such as microscopy, SAS measurements are carried out in reciprocal (Fourier) space and only the magnitude of the scattering cross-section and not its phase are measured, leading to phase information being lost during the experiment. This 'phase problem' means that it is not possible to perform a direct Fourier inversion of the data to produce an image of the structure in real space. Considering a two-phase system with a scatterer and solvent, coherent scattering will be observed from the system due to a difference in SLDs, but according to Babinet's principle this would be indistinguishable from a system where the SLD of the solvent and scatterer were swapped.

Although many systems may contain enough 'naturally occurring' inhomogeneities in the SLD in order to provide contrast within the system and hence a strong scattering signal, this can be enhanced by the use of the contrast variation technique. This is especially useful for complex systems with multiple phases, in order to reduce the number of distinct scattering phases observed in the scattering pattern. The technique of contrast variation for soft matter research relies on the significant difference in the coherent neutron scattering lengths of hydrogen (-3.74 x 10^{-5}Å) and deuterium (6.67 x 10^{-5}Å), and causes minimal disruption to the interactions and chemical behaviour of the system. By selectively deuterating certain components of the system, the scattering length densities of multiple phases can be matched to each other, thus allowing scattering from only part of the system to be observed due to the remaining inhomogeneities. This is illustrated by Figure 4.4, which shows a core-shell structure with various parts of the system highlighted through the means of selective deuteration.

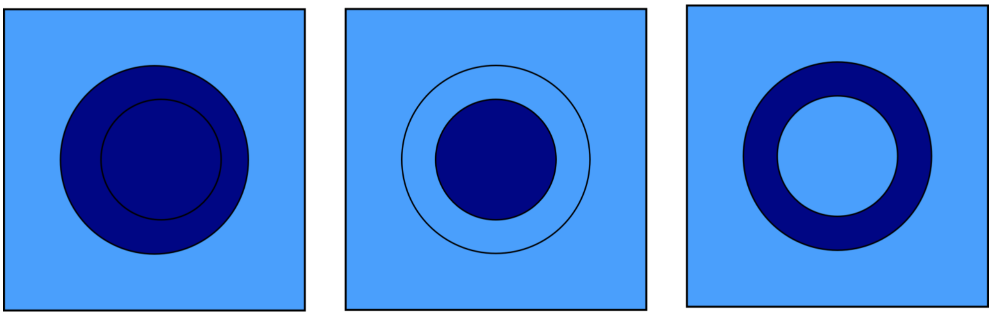

Figure 4.4: A representation of the contrast variation technique used for a core-shell system. The left panel shows deuteration of the core+shell, the middle panel shows selective core deuteration and the right hand panel shows selective shell deuteration.

In the case of soft matter systems as studied in this chapter, which show isotropic scattering, the intensities of the scattered radiation recorded by the detector during a SANS experiment are averaged to obtain the macroscopic cross-section as a function of q (on an absolute scale). As explained above, this does not automatically provide the structure of the scatterer(s), but the data can be analysed in a number of ways to gain structural information. This include model-dependent and -independent data analysis and constructing mathematical models of the scattering length density profiles of the system. Those methods which are relevant to the experiments in this chapter are discussed below.

4.4.1 Model independent data analysis

Model independent data analysis may be used in the case of systems which are too complex to describe to a great degree of accuracy using a geometric model. In the case of the experiments in this chapter, however, this method of analysis has been used to estimate the size of the scattering object in highly dilute surfactant/DES mixtures. At low concentrations, intermicellar interactions can be assumed to be negligible. The Guinier approximation considers the scattering measured at low-q values (in contrast to Porod analysis, which concerns the high-q region). The scattering intensity may be approximated as:

$$I(q) = I(0)\exp\left(-\frac{(qR_g)^2}{3}\right) \tag{4.6}$$

This allows the radius of gyration, R_g, to be extracted from the slope of a plot of $\ln(I(q))$ vs. q^2, as:

$$\ln(I(q)) = \ln(I(0)) - \frac{(R_g)^2}{3}q^2 \tag{4.7}$$

This approximation is valid for values of q where $q \leq 1/R_g$.

4.4.2 Model dependent data analysis

The scattered intensity, $I(q)$ of a system of monodisperse, isotropic, centrosymmetric particles may be described by the equation:

$$I(q) = NV^2(\Delta\rho)^2 P(q)S(q) + B \tag{4.8}$$

where N is the number of particles and V the volume of the particles. $\Delta\rho$ is the difference between the scattering length densities of the scatterer and dispersant. $P(q)$ and $S(q)$ refer to the form factor and structure factor, respectively, and B is the incoherent background scattering. The form factor describes the scattering within the particle and therefore gives information on the particle shape, and the structure factor relates to the interaction between particles in the system, although at low concentrations the particles are often considered to be disperse enough that the structure factor is considered to be negligible. At higher concentrations, however, it is important to account for interparticle interactions, which in particular affects the apparently scattered intensity at low q values.

The form factors used in data analysis in this chapter were the ellipsoid and cylinder model and their core-shell modifications, contained within and implemented using the SasView fitting program [408].

Ellipsoid model

The ellipsoid model considers an ellipsoidal body with a uniform scattering length density. It contains geometric parameters for the polar and equatorial radii (r_{po} and r_{eq}, respectively). For the micellar systems examined in this chapter, a prolate ellipsoid was considered as shown in Figure 4.5. [135]

The scattering intensity for an ellipsoid form factor, $P(q)$, is given by [135, 409, 410]:

$$P(q,\alpha) = \frac{scale}{V}F^2(q,\alpha) \tag{4.9}$$

where α is the angle between q and the axis of the ellipsoid, and V is the ellipsoid

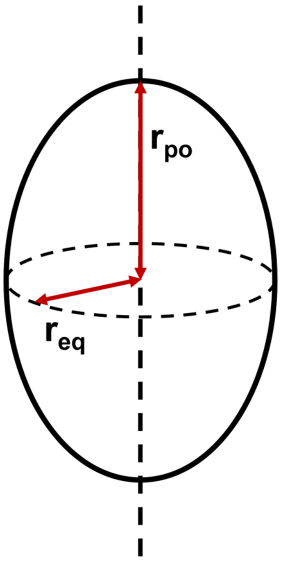

Figure 4.5: A representation of a prolate ellipsoid oriented about the polar (z) axis, defining the positions of the equatorial and polar radii.

volume, calculated by considering the values of the polar and equatorial radii. $F(q,\alpha)$ is the amplitude of the form factor of a uniform sphere. For an ellipsoid, this expression becomes:

$$F(q,\alpha) = \Delta\rho V \frac{3(\sin qr - qr\cos qr)}{(qr)^3} \tag{4.10}$$

where $\Delta\rho$ is the difference in scattering length density between the scatterer and the solvent. The value of r is given by:

$$r = [r_{eq}^2 \sin^2\alpha + r_{po}^2 \cos^2\alpha]^2 \tag{4.11}$$

Cylinder model

The cylinder model calculated the form factor of a cylinder with uniform scattering length density and contains parameters for the cylinder radius R and length L [411,412]. The scattering intensity for a cylinder may be described as:

$$P(q,\alpha) = \frac{F^2(q\alpha)\sin(\alpha)}{V} \tag{4.12}$$

where

$$F(q,\alpha) = 2(\Delta\rho)V\frac{\sin(\frac{1}{2}qL\cos(\alpha))}{\frac{1}{2}qL\cos(\alpha)}\frac{J_1(qR\sin\alpha)}{qR\sin\alpha} \tag{4.13}$$

In this case, α is now the angle between q and the cylinder axis, V is the cylinder volume, and J_1 is the first order Bessel function.

4.5 Methods

4.5.1 Materials

Deuterated forms of each DES component were required in order to carry out the neutron scattering experiments. Choline chloride-d9 (d-ChCl, 99% atom, 99% D), urea-d4 (d-U, 99% atom, 98% D) and glycerol-d8 (d-Gly, 99% atom, 99% D) were purchased from Cambridge Isotope Laboratories. For simplicity, this chapter refers to a 'fully deuterated solvent' as being d-ChCl:d-U:d-Gly, though the d-ChCl component actually refers to the partially deuterated compound $(CD_3)_3NC_2H_4OHCl$.

The surfactants hexadecyltrimethylammonium bromide, (C_{16}TAB, $\geq$ 99%), dodecyltrimethylammonium bromide, (C_{12}TAB, $\geq$ 99%), and sodium dodecyl sulfate (SDS, $\geq$ 99%) were purchased from Sigma Aldrich and used as received. Isotopically labelled C_{16}TAB with both the head and tail deuterated (d-C_{16}TAB) was provided by the STFC ISIS Deuteration Facility. Similar to h-choline chloride, it was necessary to dry d9-choline chloride under vacuum at 80 °C for at least 12 h immediately prior to use, to minimise water content in the DES.

4.5.2 Preparation of ternary DES

The ternary DES comprising ChCl, urea and glycerol were prepared in three different molar ratios (ChCl:U:Gly = 1:1.5:0.5, 1:1:1, and 1:0.5:1.5). The components were combined in the appropriate molar ratio and heated, with stirring, at 60 °C until a homogeneous liquid was formed, and subsequently equilibrated overnight in an oven at 40 °C in sealed vessels. For the SANS experiments, deuterated forms of these DES (d-ChCl:d-U:d-Gly) were also prepared using the same method.

4.5.3 Preparation of DES/surfactant mixtures

Solutions containing the cationic C_{16}TAB surfactants were prepared by mixing an appropriate amount of surfactant in the DES and equilibrating at 60 °C in an oven due to their low solubilities and high Krafft points in the DES. Further samples containing metal ions were prepared by the addition of $FeCl_3$ or $ZnCl_2$ to the DES/surfactant mixtures at a concentration of 0.25 mol kg^{-1} and 0.375 mol kg^{-1}, respectively. Dissolution of the metal chloride was facilitated by stirring the solutions at 60 °C for several hours.

4.5.4 Characterisation methods for ternary DES

4.5.4.1 Density

The densities of the ternary DES at 30 °C were determined using a triplicate average of measurements on an Anton Paar DMA 4500 M.

4.5.4.2 Surface tension

Surface tension measurements were carried out on the neat solvents using an Attension Sigma 700 force tensiometer, using the du Noüy ring method, which involves submerging a ring formed of a thin platinum wire below the surface of a liquid and slowly lowering the container where the liquid is held, such that the ring is gradually pulled up, raising the meniscus of the liquid surface until it finally breaks away. The interfacial tension is calculated by considering the maximum force measured as the ring is lifted through the air-liquid interface [413].

4.5.4.3 Differential scanning calorimetry

Differential scanning calorimetry (DSC) measurements on the DES were performed using a TA Instruments DSC-Q20 differential scanning calorimeter, in order to try to determine the glass transition temperature of each system. The sample was first equilibrated to 50 °C and held for one minute, cooled to -75 °C at a ramp rate of 10 °C min^{-1} and held for 10 min, before heating to 30 °C at a ramp rate of 5 °C min^{-1}.

4.5.4.4 Viscosity

The viscosity of the solvents was measured using a TA Instruments HR-3 Discovery Hybrid Rheometer operating in flat plate geometry with Peltier temperature control. Viscosity data was obtained in a temperature range of 20 °C - 85 °C. The DES were measured as prepared, with a seal of mineral oil to prevent any interaction of the solvent with the atmosphere during the measurement [13]. Although Kadhom *et al.* [414] suggested that the ternary DES exhibited non-Newtonian behaviour, this was not observed in the measured temperature range during these experiments, and so measurements were performed at a fixed shear rate of 1 s^{-1}.

4.5.4.5 Solubility tests

The solubility of the salt sodium bromide, NaBr, in the DES was estimated by gradual addition of known quantities of the solid to a known mass of DES with continuous stirring at room temperature [13].

4.5.4.6 Critical micelle concentration

There are many methods for determining the critical micelle concentration of a surfactant solutions, and the system to be studied is one of the crucial things to consider when choosing an appropriate technique. The most commonly used method in the literature is an analysis of the surface tensions of a concentration series of surfactant solutions, typically using the pendant drop method. In certain instances, such as those where the solution needs to be kept at elevated temperatures, or where a drop of surfactant solution is difficult to stabilise for long enough to capture an image, then alternative surface tension methods such as the du Noüy ring or the Wilhelmy plate might be more suitable.

In this work, it was not possible to use tensiometry to analyse the surfactant/DES mixtures, as the cationic surfactant mixtures in particular required heating to remain in the liquid state during measurement, and it was not possible to control this using the pendant drop method, nor was it easy to stabilise droplets suspended from the needle long enough to obtain a measurement. Although other interfacial tension methods may have overcome this drawback, it would have necessitated the preparation of a very large volume of DES. As such, the critical micelle concentrations of the surfactants in DES were estimated using the pyrene fluorescence method [415]. A brief explanation of this method is given below.

A typical emission spectrum of pyrene comprises five distinct peaks. The ratio of the intensities of the first and third vibronic bands, labelled I_1 and I_3, respectively, may be used to determine point at which micelles begin to form within the medium. The first vibronic band is promoted to the polar region, whereas the third band is not sensitive to changes in polarity. The ratio remains fairly consistent at concentrations below the CMC, however upon reaching the CMC, the pyrene molecules move from the polar solvent medium into the non-polar environment of the micelle core - this change in polarity results in a drop in the I_1/I_3 ratio [416,417]. The inflection point of the graph, that is, the intersection of the gradients of the lines before and after this transition is commonly used to define the value of the CMC.

It is important to note that whilst tracking the $\mathrm{I}_1/\mathrm{I}_3$ ratio over a concentration series is

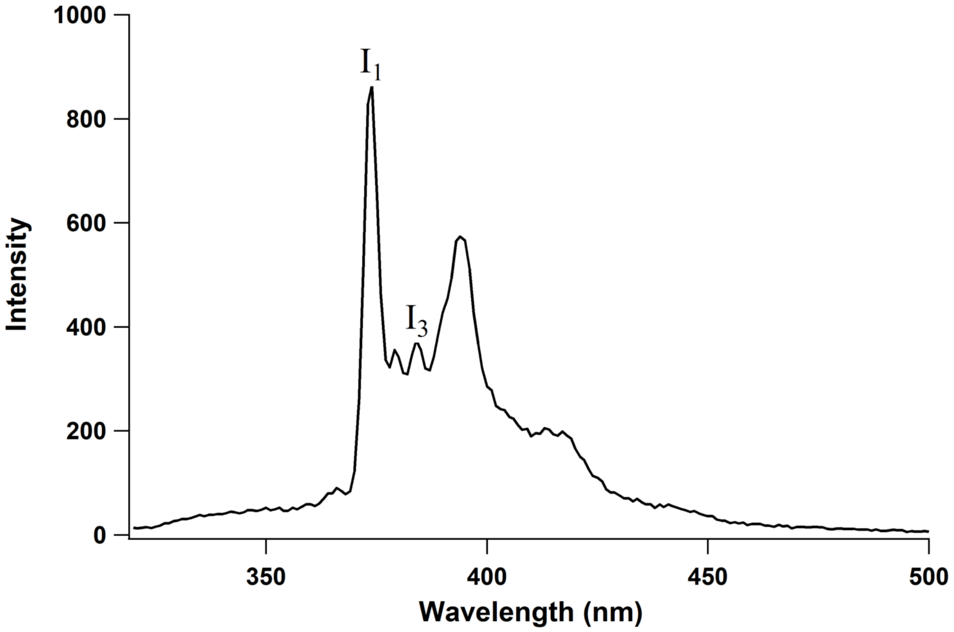

Figure 4.6: A typical fluorescence emission spectrum of pyrene, measured from a solution of pyrene in dodecane as part of this project.

the most commonly reported method of using pyrene fluorescence for CMC determination, the robustness of the method has previously been called into question [418]. However, for the purposes of this thesis, where a comparison between the estimated CMC values is important, and given the lack of practicality of the other available methods, we believe using pyrene fluorescence is an appropriate choice for these measurements.

Surfactant/DES solutions were first prepared by incorporating the pyrene into the ternary DES, and subsequently introducing the surfactant to form a concentration series. The CMCs of SDS, C_{12}TAB and C_{16}TAB were estimated in the DES with a urea:glycerol ratio of 1.5:0.5 in order to provide a comparison across the three surfactants, whilst for the urea:glycerol ratios of 1:1 and 0.5:1.5, only the CMC of C_{16}TAB was estimated.

An approximate concentration of 1 µM of pyrene in DES was chosen by consideration of the literature and in order to minimise interaction of the probe with surfactant molecules [415]. Such a low concentration was difficult to prepare directly with the laboratory equipment available, as obtaining a reasonable level of precision would necessitate the use of large volumes of DES. In order to circumvent this, a more concentrated 1 mM solution of pyrene in ethanol was first prepared. Approximately 0.1 mL of this solution was pipetted into a flask and the ethanol evaporated using a gentle stream of nitrogen gas. Freshly prepared ChCl:U:Gly DES was then added in order to obtain the desired concentration of approximately 1 µM. The flask was covered with foil to minimise exposure of the pyrene to light and stirred overnight. It was not necessary for the concentration of pyrene in DES to be accurate, but it was important that it was consistent throughout the samples to improve the reliability of the measurements. A sample of solution was tested using the fluorimeter in order to see whether this method resulted in the successful incorporation of pyrene into the DES, and a spectral response was obtained which confirmed that the mixture was suitable for further use.

The 'stock solution' of pyrene in DES was used immediately following preparation to prepare the surfactant solutions. For SDS and C_{16}TAB, a 1 wt.% concentrated solution was prepared first, whilst for C_{12}TAB, this was a 5 wt.% solution. A series of dilutions were next prepared by diluting the previous concentration by 50 % with the DES/pyrene solution. Intermediate concentrations were prepared by mixing two diluted samples together. Each sample was thoroughly mixed with vigorous stirring for at least 30 min before the next sample was prepared.

Samples were kept in a water bath at an appropriate temperature (between 40 °C and 50 °C) in order to maintain them in the liquid state during measurements. Fluorescence measurements were carried out on an Agilent Cary Eclipse fluorescence spectrophotometer equipped with Peltier temperature control. Samples were measured in a 10 mm path length quartz cuvette at 50 °C. Measurements were carried out using a photomultiplier tube (PMT) voltage of 700 V in the wavelength range of 320 - 500 nm. The excitation wavelength was set to 310 nm, and the excitation and emission slit widths were set to 5 nm and 2.5 nm, respectively.

4.5.5 Nitrogen adsorption isotherms

Nitrogen adsorption analysis was carried out using an Autosorb-iQ-C by Quantachrome Anton Paar at 77 K. Prior to measurement, the sample was degassed under vacuum at 90 °C for 1 h, and subsequently at 200 °C for 5 h. The BET specific surface area was calculated from the adsorption branch of the isotherm using the HK method in the Quantachrome ASiQWin software, provided by the instrument manufacturer.

4.5.6 Small-angle X-ray scattering experiments

Laboratory SAXS measurements were carried out on an Anton-Paar SAXSpoint 2.0 instrument equipped with a 2-dimensional EIGER R series Hybrid Photon Counting detector. A Cu K-α source ($\lambda = 1.54$ Å) was used to produce the incident radiation. Samples were loaded into quartz capillaries of diameter 1 mm and measured with a sample-to-detector distance of 556.9 cm giving an approximate Q-range of 0.008 - 0.4 Å^{-1}. Data for each sample were collected in four frames with 300 s exposure each time, before the frames were averaged and the data processed. The temperature of the measurement was 70 °C; this was controlled using a Peltier unit. Background subtractions were carried out using the NIST SANS reduction macros within Igor Pro [145].

4.5.7 Small-angle neutron scattering measurements

Small-angle neutron scattering (SANS) measurements for 130 mM mixtures of C_{16}TAB in DES were carried out on the ZOOM instrument at ISIS Pulsed Neutron and Muon Source, UK, under experiment number RB1910484. ZOOM is a time-of-flight instrument capable of accessing a Q-range of 0.0045 - 0.85 Å^{-1} when operating with a sample-to-detector distance of 4 m. Data for 25 mM mixtures of C_{16}TAB were collected on the LOQ instrument at the same facility under experiment number RB1720289. LOQ is a fixed-geometry time-of-flight instrument with two detectors positioned at 0.5 m and 4 m from the sample and utilises neutron wavelengths of 2.2 - 10 Å to provide a Q-range of 0.008 - 1.6 Å^{-1} [13].

For all experiments, samples were sealed in quartz cuvettes with a path length of 1 mm (Hellma GmbH) and loaded onto an automatic sample changer within the instrument. A measurement of 70 °C was chosen in order to maintain the mixtures containing cationic surfactants in the liquid state, and also because this was closer to the reaction temperature required for a templated solvothermal synthesis whilst remaining below the degradation threshold for urea, which in DES has been shown to be *ca.* 80 °C [419].

Data reduction was subsequently performed following the standard procedures on each instrument using the routines within Mantid [420]. The data were normalised to the sample transmission, calibrated to absolute units using a polymer standard and corrected for detector efficiencies before subtracting the scattering from the empty cell. The resulting output was converted to absolute units of the scattering intensity, ($I(q)$, cm^{-1}) vs. the momentum transfer (q, Å^{-1}). The scattering from the pure solvents was subtracted afterwards using the NCNR SANS analysis macros within the Igor Pro software [145] to account for the incoherent contribution to each sample [13].

Surfactant in DES mixtures were prepared at concentrations of 25 mM and 130 mM. Various isotopic mixtures were used in order to aid in resolving the micelle structure. Deuterated surfactant in fully protonated DES (h-ChCl:h-U:h-Gly) and protonated surfactant in fully deuterated solvent (d-ChCl:d-U:d-Gly) provided structural information about the micelle core, as the scattering is dominated by the scattering length density correlation between the micelle core and the solvent.

4.5.8 Analysis of SANS data

For the low concentration C_{16}/DES solutions, the Guinier approximation was used to examine the data at low-q. This allowed for an analysis of the density distribution of the longest dimension of the structure and hence give an insight into how micelle elongation varied with solvent composition. This analysis allows the determination of the radius of gyration, R_g, of the scatterer, which quantifies the scattering length density (SLD) distribution of an object from its centre of mass. At low concentrations, colloidal interactions are negligible and hence an approximate micelle size may be calculated by analysing the low-q region of the data (Section 4.4). Thereafter a systematic, model-based approach was used to fit all of the data sets and the relevant form factors have also been described in Section 4.4. For most datasets, a uniform ellipsoid or cylinder model was used to fit the data, however for those datasets which were sufficiently constrained were fitted to core-shell models in order to resolve the structure of the headgroup regions of the micelles. In each case, two contrasts (protiated surfactant in d-ChCl:d-U:d-Gly and deuterated surfactant in h-ChCl:h-U:h-Gly) were fitted simultaneously in order to achieve the best description of the data.

4.5.9 Solvothermal synthesis in surfactant/DES mixtures

C_{16}TAB in DES mixtures were prepared according to the method above. An appropriate amount of iron(III) chloride ($FeCl_3$) or zinc(II) chloride ($ZnCl_2$) was dissolved into the mixture, with stirring, at 60 °C. The reaction mixtures were transferred to PTFE-lined steel autoclaves and reacted in an oven at a range of temperatures between 80 °C and 180 °C before being allowed to cool to room temperature naturally. In some cases, the reacted or unreacted mixtures were placed into a porcelain crucible and calcined in a furnace at temperatures above 450 °C at a ramp rate of 10 °C min^{-1} before cooling naturally to room temperature. Where possible, powder material was recovered from the post-reaction mixtures by diluting them with a 50:50 mixture of deionised water and ethanol and centrifuging to remove the residual DES and surfactant. The recovered solid was dried in air at 60 °C in an oven. In order to be able to assess the effects of adding the surfactant to the synthesis, reactions were carried out using these same methods in pure and hydrated ternary DES without the addition of any templating agent. Recovered powder product and samples of the post-reaction mixture were characterised according to the methods described in Chapter 2.

4.6 Properties of the ternary DES

Overall, all three ternary DES formed readily at relatively low temperatures, but as expected, those with a higher glycerol content formed faster and remained stable in the liquid state at room temperature for a longer period of time. This is due to mixing of the DES components being far easier when there is a greater amount of liquid and because the freezing point of glycerol is very low (ca. -40 °C). Before introducing any surfactants into the DES, the properties of these solvents were characterised. This was carried out in part because they had previously not been characterised extensively in the literature by Kadhom and co-workers [414], but also to see if any variation in properties with solvent composition could be used to rationalise observations of varying micelle morphology.

DSC measurements carried out of the DES at various urea:glycerol ratios are presented in Appendix 6. Although a wide temperature range (-75 °C - 30 °C) was investigated, it was not possible to discern a glass transition temperature from this data. As previously examined in the literature, this could arise from limitations of the instrument or from confinement or supercooling effects, as both are factors which make it difficult to accurately observe a glass transition temperature in DES [190].

Table 4.2 provides a summary of the experimentally measured densities, average molar masses and molar volumes of the three ratios of ternary DES considered in this chapter, together with literature data for relevant DES and other species for comparison. The average molar mass for a DES may be calculated by taking into account the molar masses each DES component and the ratio of components in the ternary DES. Molar volumes were calculated by considering the average molar mass of each sample and the measured densities.

The Gordon parameter [424], G, may be calculated from surface tension data using the following equation:

$$G = \frac{\gamma}{{V_m}^{1/3}} \tag{4.14}$$

This parameter is considered a description of the 'solvophobicity' of a solvent and is comparable to quantifying the hydrophobic effect in water [425]. It provides a measure of the cohesiveness of solvent molecules and may therefore be used to predict the capability of a solvent to promote the self-assembly of amphiphilic molecules [349,426]. The measured physical properties of viscosity, surface tensions and calculated Gordon parameter for the ternary DES and relevant comparison data are summarised in Table

Table 4.2: The densities, average molar masses and calculated molar volumes of the ternary DES used in this chapter together with literature data for relevant systems. Reprinted with permission from Reference [13]. Copyright 2020, American Chemical Society.

System	Density at 30 °C(g cm^{-3})	Average molar mass (g mol^{-1})	Molar volume (cm^3 mol^{-1})
Water	0.997	18.02	18.0
1:2 ChCl:urea [21]	1.15	86.6	75.3
1:1.5:0.5 ChCl:U:Gly	1.1970 ± 0.0001	91.9	76.8
1:1:1 ChCl:U:Gly	1.1957 ± 0.0003	97.3	81.3
1:0.5:1.5 ChCl:U:Gly	1.1945 ± 0.0001	102.6	85.9
1:2 ChCl:glycerol [421, 422]	1.19	107.9	90.7
Glycerol [423]	1.26	92.1	73.1

4.3 Reprinted with permission from Reference [13]. Copyright 2020, American Chemical Society.

The density values obtained for these DES vary little with solvent composition, though as expected they decrease very slightly as the glycerol content in the DES is increased. The measured surface tensions of the ternary DES are all slightly higher than the reported values of the binary ChCl:urea and ChCl:glycerol DES. Although small differences in these measurements may arise from the use of different techniques (in this study, the du Noüy ring method was used, but others have used the pendant drop method), the results presented here allow for a comparison between the surface tension values across the ternary DES with varying component ratios. However, they do not appear to display a trend which correlated with solvent composition, and indeed the values overlap when considering their associated errors.

Interestingly, a study by Hammond and co-workers showed that in the case of the 1:1 ChCl:malic acid DES, the addition of one mole equivalent of water resulted in an increase in the surface tension of the system by 12 mN m^{-1} (from 65 to 77 mN m^{-1}).

Table 4.3: The surface tensions, calculated Gordon parameter and viscosity of the ternary DES used in this chapter together with literature data for relevant systems.

System	Surface tension, γ (mN m^{-1})	Gordon parameter, G (J m^{-3})	Viscosity at 25 °C (Pa s)
Water	71.99 [427]	2.743 - 2.750 [428]	8.9 x 10^{-4} [423]
1:2 ChCl:urea [21]	66 ± 1	1.57 ± 0.02	1.57 [429]
1:1.5:0.5 ChCl:U:Gly	69.3 ± 0.7	1.63 ± 0.02	0.70 ± 0.2
1:1:1 ChCl:U:Gly	70.1 ± 0.6	1.62 ± 0.01	0.56 ± 0.1
1:0.5:1.5 ChCl:U:Gly	68.2 ± 0.5	1.55 ± 0.01	0.46 ± 0.1
1:2 ChCl:glycerol	63.5 ± 0.5 [14]	1.41 ± 0.01	0.26 [430]
Glycerol	62.5 [431]	1.51 [428]	0.91 [432]

The addition of 2 mole equivalents of water was found to have no further effect on the measurement [433]. In the study, this increase was attributed to changes in the hydrogen bond network and a resulting increase in cohesive interactions in the DES. Whilst the change in surface tension might be caused by the saturation of species at the DES surface, this is not likely for a couple of reasons. Firstly, the quantity of water added was low, and water molecules are known to interact strongly with the DES. As such, they would not be expected to assemble preferentially at the air/liquid interface and so cause an increase in the surface tension. A surface excess of the other species would not change the observed surface tension compared to the dry DES, as the interface would still be made up of the mixed DES components. Therefore, it may be suggested that water in the system functions similar to a hydrogen bond donor. Applying this to the ternary DES system, the addition of a second hydrogen bond donor (for example, adding glycerol to ChCl:urea) may result in a rearrangement of the solvent structure allowing formation of a greater number of hydrogen bonds than in the relatively constrained binary systems. As such, the resulting structure may be more cohesive and therefore show a higher surface tension at the interface. However, after initial glycerol addition the surface tensions appear to rapidly saturate, and there is little variation between values for the three ternary DES, although all values are below the surface tension of water and higher than that of glycerol [13].

The differences in the calculated molar volumes shown in Table 4.2 mean that the values of the Gordon parameter calculated from the surface tension values show a small decreasing trend with added glycerol content. These values are, however, still similar across the three DES compositions. It may be assumed that they contain comparable hydrogen-bonding interactions. Although this parameter has been used to predict the ability of a solvent to support self-assembly, the similarities between the calculated values mean that any observed differences in micelle morphology discussed in subsequent parts of this chapter cannot be attributed to a significant variation in hydrogen bonding across solvent compositions. Further work discussing the hydrogen bonding network in the ChCl:U:Gly DES is presented in Chapter 5.

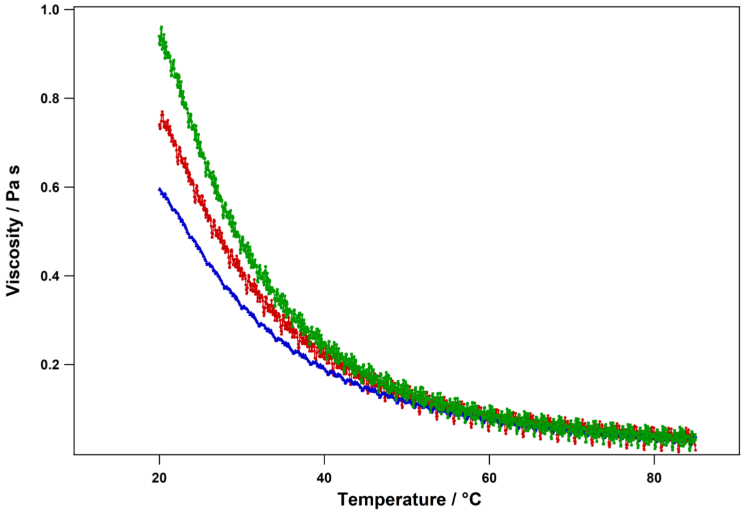

Figure 4.7: Viscosity measurements for the ChCl:U:Gly DES with urea:glycerol ratios of 1.5:0.5 (green), 1:1 (red) and 0.5:1.5 (blue), measured at a constant shear rate of 1 s^{-1} across a temperature range of 20 °C - 85 °C. Reprinted with permission from Reference [13]. Copyright 2020, American Chemical Society.

It is interesting to note that whilst ChCl:glycerol has a lower viscosity than pure glycerol, the addition of urea increases the viscosity of the ChCl:U:Gly DES. When looking at the viscosity measurements obtained for the ternary DES (Figure 4.7), we can see that the variation in viscosity is most apparent at low temperatures, and the DES with the highest urea content also has the highest viscosity. In every case, the data could be fitted following an exponential decay as per the Arrhenius equation (with R^2 values > 0.99). Above 50 °C, the viscosity values of all three DES become very similar. At 70 °C the temperature chosen for the SANS measurements, the difference in viscosities is negligible and therefore is unlikely to significantly influence self-assembly. At this temperature, it is expected that surfactant species will be equally free to move within all three DES compositions to find thermodynamically favoured structures.

4.7 Preliminary investigations of surfactant/DES solutions

Although the majority of this chapter will concentrate on the cationic C_nTAB surfactants, solutions containing the anionic SDS were also initially prepared in order to compare the solubility of a range of surfactants in the ternary DES. During this work, it became apparent that the surfactants did not readily solubilise in the DES in high concentrations at room temperature. Gentle heat was already required in the case of DES with a higher urea content to overcome viscosity issues and facilitate better mixing, but in the case of the cationic C_nTAB surfactants, several hours of heating at temperatures up to 60 °C and frequent agitation was required to solubilise the surfactants up to concentrations above 1 wt.%. As expected for the cationic surfactants, which are insoluble in ChCl:urea, an increase in the glycerol content in the ternary DES resulted in a higher solubility of the surfactants. Once the surfactants/DES mixtures were formed, it was required to heat them to at least 50 °C during any handling and measurement to keep them in the liquid state. By contrast, SDS, which mixes readily with ChCl:urea, was much easier to solubilise and only required heating and equilibrating at 40 °C.

SDS has been shown to both solubilise and form micelles in both ChCl:urea [21, 382] and ChCl:glycerol [338], albeit with differing micelle morphologies. It was expected therefore that micelles would form in the ternary DES, and the mixtures were not investigated extensively prior prior to SANS experiments being carried out. The dependence of the morphology of SDS micelles on the urea:glycerol ratio within the ternary DES has been covered in the publication from which many of the results in this chapter are drawn [13] but will not be discussed in detail in this thesis.

Before any advanced characterisation could be carried out on these mixtures, it was first necessary to determine whether micelle formation could be observed to assess whether these systems merited further investigation. In order to do this, data from small-angle X-ray scattering (SAXS) were first collected on an in-house instrument. Although it was possible to form solutions containing $C_{12}TAB$, at the concentrations prepared (below 5 wt.% surfactant), no scattering characteristic of micelle formation in these systems was detected using SAXS. Evidence of micellisation in the $C_{12}TAB$/DES mixtures was later confirmed using SANS techniques and the relevant data is again published in the same study on which many results in this chapter are based, however, this will also not be discussed here [13]. In the case of $C_{16}TAB$, the obtained SAXS data showed

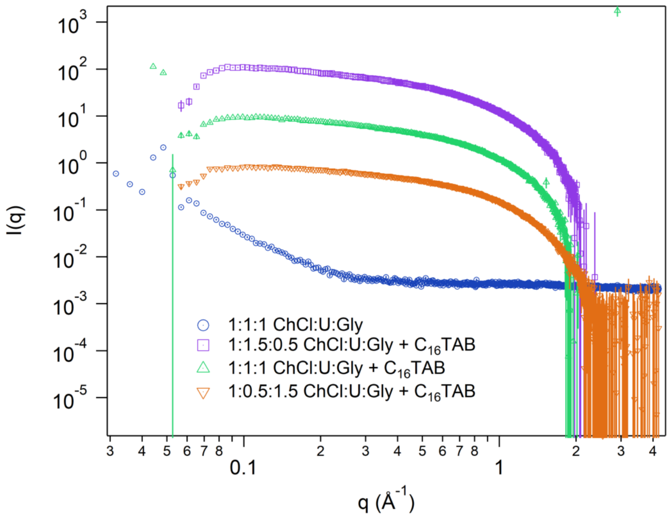

Figure 4.8: Corrected SAXS data collected for solutions of h-C_{16}TAB in h-ChCl:h-U:h-Gly with component ratios of 1:1.5:0.5 (purple markers), 1:1:1 (green markers), and 1:0.5:1.5 (orange markers), shown together with data for the 1:1:1 neat DES.

the formation of micelles in the case of all surfactant/DES mixtures. This is especially interesting given that this surfactant is insoluble in ChCl:urea, but formed aggregates even in the ternary DES with the lowest glycerol content (urea:glycerol = 1.5:0.5). The SAXS patterns in Figure 4.8 show the corrected scattering data obtained from C_{16}TAB/DES solutions at various component ratios, along with the scattering from the pure DES with component ratios of 1:1.5:0.5 plotted for comparison. Although extensive characterisation was not carried out on the data, the formation of aggregates which were globular or ellipsoidal in nature was suggested, although there was not enough resolution in the data to determine whether the micelle morphology varied with varying solvent ratio. In order to characterise this morphology further, small-angle neutron scattering experiments were carried out on a series of C_{16}TAB/DES mixtures, and the results from this study are presented in Section 4.8.

The CMC values of some of the surfactant/DES mixtures were estimated using the pyrene fluorescence method (Section 4.7.1). Subsequently, and given the above observations, a detailed study of C_{16}TAB mixtures in ChCl:urea:glycerol DES was carried out using small-angle neutron scattering techniques, with a view to exploring how changing the composition of the solvent can affect surfactant behaviour. An understanding of how the morphology of the obtained micelles can be related to the urea:glycerol ratio in the DES could provide a way to tune the structure of any materials synthesised via surfactant-templating methods in the DES. Additionally, some characterisation was also carried out using the same techniques on C_{16}TAB/DES mixtures containing water or metal ions (Fe^{3+} and Zn^{2+}) to also investigate the effects of these additives on micelle morphology. The results from these investigations are presented in Section 4.8.

4.7.1 Measurements of the critical micelle concentration

As mentioned in Section 4.5, fluorescence spectroscopy using pyrene as the fluorescence probe was chosen as a suitable method for estimating the CMCs. In order to compare values across DES ratios, the CMC of C_{16}TAB in all three DES was measured. To provide comparison between different surfactant molecules, further sets of fluorescence measurements were obtained for SDS and C_{12}TAB mixtures in the 1:1.5:0.5 DES. The values of the CMC calculated from the point of inflection of the I_1/I_3 graph (Section 4.5.4.6) are tabulated below (Table 4.4). Data plots are for all systems are provided in Appendix 6.

Table 4.4: Values of the critical micelle concentration obtained using the pyrene fluorescence method for various surfactant/DES mixtures.

ChCl:U:Gly ratio	Surfactant	CMC
1:1.5:0.5	SDS	3.1 ± 1.6 mM
1:1.5:0.5	C_{12}TAB	25 ± 2 mM
1:1.5:0.5	C_{16}TAB	2.05 ± 0.6 mM
1:1:1	C_{16}TAB	1.6 ± 0.4 mM
1:0.5:1.5	C_{16}TAB	1.1 ± 0.6 mM

The CMC values obtained in this work are more congruous with those values obtained by using tensiometry for C_nTAB surfactants in ChCl:glycerol reported by Sanchez-Fernandez *et al.* [14] than the values obtained previously by Pal *et al.* using fluorescence spectroscopy, which were an order of magnitude higher [381]. The values of CMC estimated for C_{16}TAB show a slight downward trend as the glycerol content in the DES is increased, however the errors of these values do overlap. The trend is continued with the literature value for the CMC of C_{16}TAB in ChCl:glycerol, which was reported as 0.9 ± 0.1 mM [14]. This observation is interesting, and perhaps contradictory to what would be expected. As the glycerol content in the DES increases, it would be assumed that the solubility of the cationic surfactant would increase too, thus leading to higher CMC values, but this does not appear to be the case.

The comparatively high CMC of C_{12}TAB is also notable, being approximately a factor of 10 higher than the CMC determined for C_{16}TAB. Again, this is in agreement with the observations made by Sanchez-Fernandez *et al.* (CMC of C_{12}TAB in ChCl:glycerol = 22 ± 2 mM) [14]. In their study, the authors suggested that the surfactants with shorter tail lengths would have greater monomer solubility in the DES, as is seen for other polar solvents, and the value presented in this work would appear to agree with this. As already described, the accuracy of the pyrene fluorescence method has been debated. Previous work has suggested that the length of time a sample is kept for after preparation does not have much of an effect on the measurements [415]. Although in that study, Li and co-workers only tested samples up to 24 h after preparation and so did not determine the long-term stability of the samples, their observations were considered sufficient for this surfactant/DES mixtures in this project. No surfactant/DES mixtures with added pyrene were kept standing for this length of time before measurement, and all concentrations for a single CMC determination were measured consecutively to allow for as little error as possible between samples. The same study by Li and co-workers also found that at low concentrations of pyrene, similar to those used in these experiments, the pyrene concentration did not influence the CMC [415]. Scholz *et al.* [434] have suggested that the error in similar CMC measurements is approx. 0.4 mM; the findings from this thesis suggest that it is slightly higher given the difficulty in determining accurately the intersection of the two gradient lines. However, taking into account these nuances, we believe the method is accurate enough to provide an estimate of the CMC for these systems, especially where a comparison between values is important.

For more accurate data, a method such as tensiometry would be needed, which is a well tested method for the determination of the critical micelle concentration and would allow for the averaging of several data points during data collection, however due to restrictions on laboratory time and the practical difficulties of stabilising droplets of surfactant/DES solutions which crystallised rapidly at temperatures below 40 °C (for some mixtures), this method was not deemed suitable in this case, not least because it would not be applicable to every DES/surfactant mixture. Future work would include using tensiometry for one system where the mixture remains in the liquid state at room temperature at the desired surfactant concentrations, and comparing it to those results obtained using the pyrene fluorescence method in order whether to determine whether both methods were able to give consistent results.

4.8 SANS data from surfactant/DES mixtures

4.8.1 Approach to data analysis

The data fitting presented in this chapter was carried out using the form factors provided within the relevant models contained within the NCNR SANS analysis macros [435] in the Igor Pro software [436] and in the SasView program [408].

The extended tail lengths, volumes, neutron scattering lengths and SLD values of individual constituents of the system are listed in Appendix 6 (Table A.1). Neutron scattering lengths were calculated as the sum of the coherent neutron scattering lengths of the individual atoms in each unit. Extended lengths for surfactants were taken from a previous publication (Ref [14]), and were originally calculated by those authors from Tanford equations [25]. The calculated SLDs for each DES, obtained by considering the neutron scattering lengths of the individual components together with their mole fractions in each DES, are given in the Appendix 6 (Table A.2).

Data obtained for the 25 mM solutions of C_{16}TAB in the ternary DES were initially fitted using the Guinier approximation to determine the radius of gyration (R_g). This was possible when the surfactant was at sufficiently low concentration as the particles are considered sufficiently disperse for intermicellar interactions to not contribute to the scattering intensity, such that an analysis of the low-q region of the scattering curve can give an approximate size of the scatterer.

Following this, the data were fitted to geometric models. Details of the various models primarily investigated as potential best fits to the SANS data for the DES/surfactant mixtures are presented in Figure 4.9 together with the associated reduced X^2 values from the best fit it was possible to obtain from each model, whilst maintaining physically realistic parameters for the micelle morphology (Table 4.5). Note that a Schulz-radius distribution was applied to the sphere form factor during the fitting trials, in line with previous studies on surfactant/DES systems [14, 382].

Table 4.5: Reduced X^2 values obtained from the best fits to the data of various geometric models explored in the fitting process.

Model	X^2 value
Core-shell sphere	3659
Sphere	1558
Core-shell cylinder	168
Cylinder	132

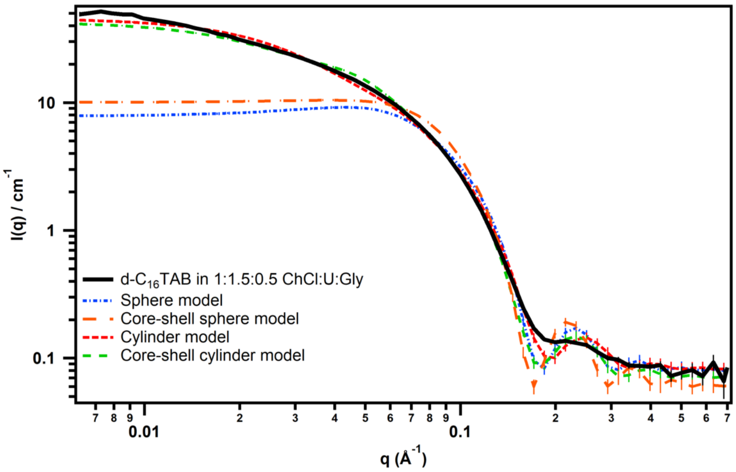

Figure 4.9: A representation of various geometric models tested for a mixture of d-C_{16}TAB in fully protonated ChCl:U:Gly DES with a urea:glycerol ratio of 1.5:0.5. Reprinted with permission from Reference [13]. Copyright 2020, American Chemical Society.

Although the sphere model was suitable to fit the data from globular micelles and the cylinder model provided a good fit for elongated micelles, an ellipsoidal model was ultimately chosen to fit all of the data as it is capable of fitting a wide range of aspect ratios and allowed for a direct comparison of the outputted dimensions of the micelles. Data from the 25 mM concentration mixtures was fitted to a uniform prolate ellipsoid model (as described in Section 4.4.2), with the equatorial radius oriented through the rotational axis of the spheroid. This would allow for some characterisation of the overall shape of the micelles. Given the observation that amphiphile aggregates in DES adopt a core-shell density distrubution, with the surfactant tails forming the micelle core the the partially-solvated micelle headgroups forming the shell [14,382], a core-shell model was used to fit the data from the 130 mM mixtures, where sufficient contrast was seen to resolve the shell structure. The SLD of the tail was fixed, as solvent penetration into the lyophobic region is considered minimal, whilst the SLD of the shell was allowed to vary during the fitting procedure to account for partial solvation by the DES.

In the higher concentration surfactant/DES mixtures, intermicellar interactions can no longer be assumed to be negligible, and must be accounted for by the use of a structure factor in the data fitting. For these highly charged systems, there is no structure factor which is entirely descriptive of the system. Although the Hayter mean spherical approximation [437] may seem suitable as it is used for highly charged systems, it requires the knowledge of parameters such as the dielectric constant, which it is not possible to determine for the DES. As such, a modified Percus-Yevick hard sphere structure factor [438] was used to fit the data instead. This structure factor comprises two parameters, the interaction radius (r_{eff}) and the effective volume fraction (Φ_{S_q}). The value of r_{eff} was calculated as the radius of a sphere with the same second virial coefficient as the micelle, such that $r_{\text{eff}} = (r_{\text{po}} {r_{\text{eq}}}^2)^3$. This approach was identical to that used by Sanchez-Fernandez *et al.* in several previous studies concerning surfactant self-assembly in DES and allowed for a consistent approach to data analysis across similar systems [14, 382, 385]. The effective volume fraction was not constrained to the form factor volume fraction and was therefore determined through fitting the data.

4.8.2 Micelle morphology at low concentration

Reported values of the radius of gyration (R_g) for micelles formed by C_{16}TAB determined through fitting the low-q region in the three ChCl:urea:glycerol DES are shown below in Table 4.6, together with comparison data obtained from literature for values in water and the IL ethylammonium nitrate. The SANS data together with the best fits from the Guinier analysis, as well as a plot of the R_g values are shown below in Figure 4.10.

Table 4.6: Values of the radius of gyration reported for globular C_{16} micelles in a range in solvents.

Solvent	R_g (Å)	Reference
Water	25.4 Å	[439]
Ethylammonium nitrate	15.5 Å	[14]
1:1.5:0.5 ChCl:urea:glycerol	111 ± 8 Å	This work
1:1:1 ChCl:urea:glycerol	59.4 ± 4.5 Å	This work
1:0.5:1.5 ChCl:urea:glycerol	23.2± 1.2 Å	This work
ChCl:glycerol	26.1 ± 1.2 Å	[14]

In the first instance, the data from the SANS experiment confirms what was observed using the laboratory SAXS instrument, and C_{16}TAB does form micelles in all three ternary DES, even at higher urea concentrations (urea:glycerol = 1.5:0.5). A similar result was also observed for C_{12}TAB [13]. As discussed previously, this is especially interesting given that these cationic surfactants are virtually immiscible with ChCl:urea, so the presence of even a small amount of glycerol in the system has a profound effect on solubility. The values of R_g obtained for C_{16}TAB in the 1:1.5:0.5 and 1:1:1 DES (111 Å and 59.4 Å, respectively) are higher than the value obtained for water (25.4 Å), in which the surfactant forms globular micelles with strong intermicellar interactions [14, 440], whilst the R_g determined for the 1:0.5:1.5 solvent is slightly lower. In the case of simi-

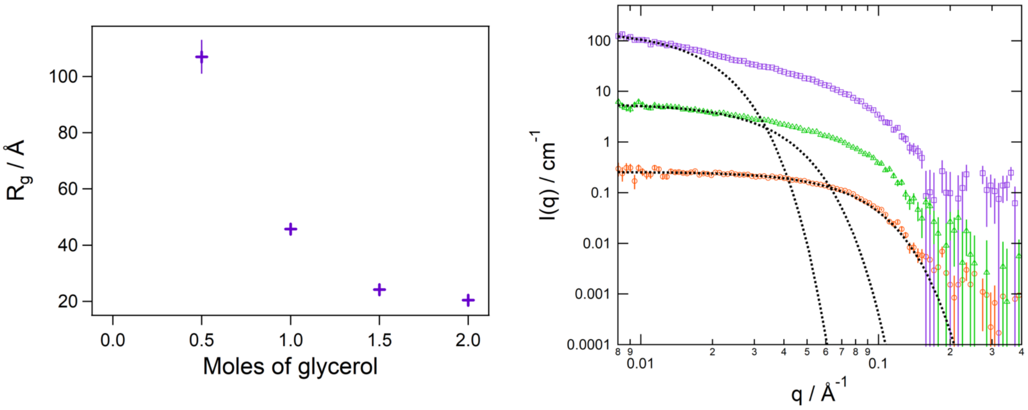

Figure 4.10: (Left): A representation of the values of R_g determined through fitting the low-q region of SANS data from 25 mM solutions of $C_{16}TAB$ in ChCl:urea:glycerol DES with urea:glycerol ratios of 1.5:0.5, 1:1 and 1.5:0.5, plotted relative to glycerol content in the DES. Error bars are obtained by averaging fits from multiple contrasts of the same mixture. Data for a solution of $C_{16}TAB$ in ChCl:glycerol, taken from Reference [14] is included for comparison. (Right): SANS data (coloured markers) and best fits (black dashed lines) for 25 mM solutions of d-$C_{16}TAB$ in h-ChCl:h-U:h-Gly DES with U:Gly ratios of 1.5:0.5 (purple squares), 1:1 (green triangles) and 1.5:0.5 (orange circles) from the Guinier analysis to determine R_g values.

lar systems containing SDS or $C_{12}TAB$, the values of R_g were consistently higher than determined for aqueous mixtures [13]. Previous work has explained this difference as the presence of ions in the DES providing a slight charge neutralisation effect, and the strong cohesive effects of water [382]. Overall, $C_{16}TAB$ forms larger aggregates than those formed by SDS or $C_{12}TAB$, with $C_{12}TAB$ forming the smallest assemblies of the three surfactants which have previously been characterised in this DES [13].

The Guinier region at low-q values, shown in the right hand panel of Figure 4.10, can clearly be seen to gradually shift towards the left hand side of the graph (lower-q values) as the urea content in the DES is increased, which is an indication that the micelles become more elongated. A further indication is given by the fact that the gradient of this region increases steadily across the three patterns (from lowest to highest urea content), which also indicates a transition from globular to more elongated structures.

The SANS data from the 25 mM solutions were next fitted to a uniform ellipsoid model. The fitted parameters are reported in Table 4.7 with the best fits to the data shown in Figure (4.11). As interactions between micelles are assumed to be negligible in this dilute regime, no structure factor was used in the fitting procedure. Little variation is seen in the values for the equatorial radius, r_{eq}; there is no discernible trend across

Table 4.7: Fitted parameters for the 25 mM solutions of $C_{16}TAB$ in ChCl:urea:glycerol DES with urea:glycerol ratios of 1.5:0.5, 1:1 and 1.5:0.5, determined from co-fitting protiated and deuterated contrasts to a uniform ellipsoid model. Scattering length density values are presented in the Appendix.

Solvent	r_{eq} (Å)	r_{po} (Å)
1:1.5:0.5 ChCl:urea:glycerol	22.2 ± 1.5	248 ± 12
1:1:1 ChCl:urea:glycerol	20.9 ± 1.6	89.4 ± 10.8
1:0.5:1.5 ChCl:urea:glycerol	22.9 ± 1.7	40.7 ± 6.2

the DES compositions and there is overlap between the errors in the measurements. Conversely, the fitted values obtained for the polar radius, r_{po}, oriented about the rotational axis of the micelle, show a great deal of variation with DES composition. This is to be expected given the elongation observed both from the scattering patterns themselves and the fitted values of R_{g}. At high urea contents (low glycerol contents), $C_{16}TAB$ forms highly elongated micelles, and the degree of elongation decreases non-linearly as the glycerol content in the DES is increased.

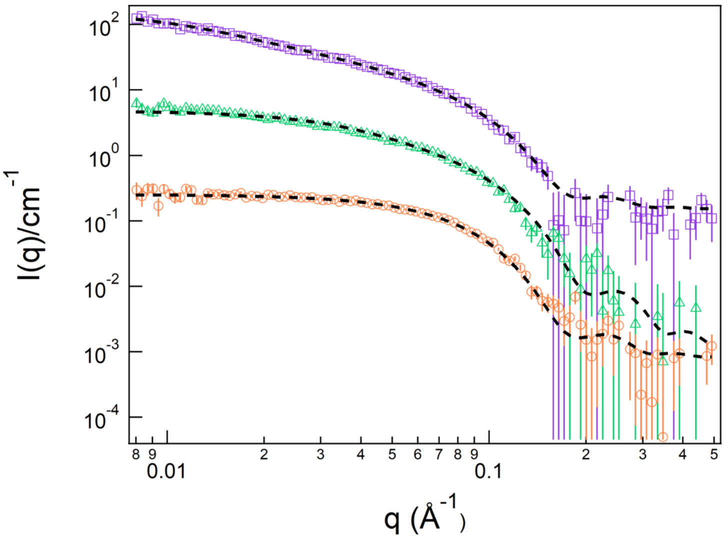

Figure 4.11: SANS data (coloured markers) and best fits (black dashed lines) for 25 mM solutions of d-$C_{16}TAB$ in h-ChCl:h-U:h-Gly DES with U:Gly ratios of 1.5:0.5 (purple squares), 1:1 (green triangles) and 1.5:0.5 (orange circles) from fits to a uniform ellipsoid model. Best fits were obtained through co-refinement of two contrasts.

In the DES with the lowest urea content (urea:glycerol = 0.5:1.5), the dimensions of the micelles clearly indicate a shift to a globular morphology instead of highly elongated.

Even so, these micelles appear to be marginally more elongated than those observed in the ChCl:glycerol DES (a similarly low concentration of C_{16}TAB in this DES had an estimated r_{po} value of approximately 41 Å) [14]. Similar observations were made in the case of SDS and C_{12}TAB [13], though the effect was more pronounced for SDS than for C_{12}TAB, where the micelles showed little variation in dimension along their polar axis (elongation decreasing from 32.6 Å to 30.5 Å as glycerol content in DES increased).

The aggregates in the DES are more elongated than those formed by C_{16}TAB in water (where $r_{\mathrm{po}} \sim 37$ Å) [441], and the peak in the SANS patterns which appears in the surfactant/water mixtures at similar concentrations due to strong intermicellar interactions is not evident in the surfactant/DES data, which suggests that long-range electrostatic interactions are not present in this system due to the relatively low permittivity of the DES compared to water.

4.8.3 Micelle morphology at higher concentration

At higher concentrations of C_{16}TAB in DES, intermicellar interactions can no longer be assumed to be negligible and therefore affect the scattering pattern. In order to account for these interactions, data from 130 mM mixtures were fitted to a uniform ellipsoid model combined with a hard-sphere structure factor. The best fits to the data for the three surfactant/DES mixtures are shown in Figure 4.12 and the fitting parameters are presented in Table 4.8.

Table 4.8: Fitted parameters for the 130 mM solutions of C_{16}TAB in ChCl:urea:glycerol DES with urea:glycerol ratios of 1.5:0.5, 1:1 and 1.5:0.5, determined from co-fitting protiated and deuterated contrasts to a uniform ellipsoid model. Scattering length density (SLD) values for the relevant DES and surfactant components are presented in the Appendix.

Solvent	r_{eq} (Å)	r_{po} (Å)	$\Phi_{S_{(q)}}$ (x10^{-2})
1:1.5:0.5 ChCl:urea:glycerol	21.7 ± 1.6	171.7± 6.7	5.2 ± 0.02
1:1:1 ChCl:urea:glycerol	21.5 ± 1.4	139.1 ± 5.8	5.5 ± 0.04
1:0.5:1.5 ChCl:urea:glycerol	20.5 ± 1.2	72.1 ± 3.6	5.4 ± 0.04

The initial observations as regards the changes in micelle morphology with varying DES composition which were seen in the SANS data from the dilute regime are also evident here, even though contributions to the structure factor alter the scattering pattern. The fitted parameters show again that there is little variation in the values of the equatorial radii, whereas the polar radii vary significantly and following the same

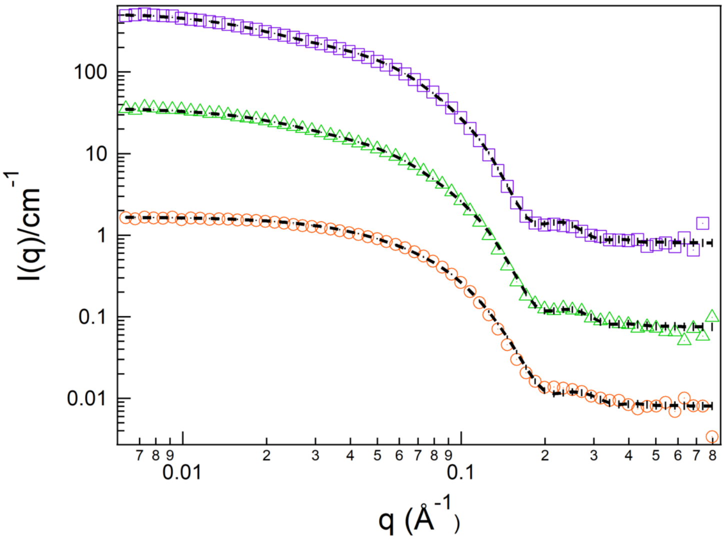

Figure 4.12: SANS data (coloured markers) and best fits (black dashed lines) 130 mM solutions of d-C_{16}TAB in h-ChCl:h-U:h-Gly DES with U:Gly ratios of 1.5:0.5 (purple squares), 1:1 (green triangles) and 1.5:0.5 (orange circles) from fits to a uniform ellipsoid model. The fitting procedure included a modified hard-sphere structure factor, as discussed above. Best fits were obtained through co-refinement of two contrasts.

trend previously observed.

The micelles formed by C_{16}TAB had slightly larger cross-sections than reported in the literature for the dodecyl surfactants SDS and C_{12}TAB [13], which is consistent with the behaviour seen in equivalent surfactant/water mixtures [441, 442]. A slight coiling of the hydrophobic moeities is suggested by the fact that fitted values of r_{eq} are lower than the calculated extended tail length for C_{16}TAB (Table A.1 in the Appendix), but this tail length lies within the errors of the fitted value of r_{eq}.

Although there were small variations in the fitted values of the micelle volume fraction $\Phi_{P_{(\mathrm{q})}}$ in the dilute regime and when the structure factor was not introduced, these can be explained by small differences in monomer solubility in the DES or in variations in solution concentration arising from inaccuracies during sample preparation. Such observations have previously been made for anionic surfactants in DES [338]. The values of fitted effective volume fractions, $\Phi_{S_{(\mathrm{q})}}$ when the structure factor was introduced were consistently higher than the bare micelle volume fraction - an observation which can be attributed to short-range repulsive electrostatic interactions occurring between charged micelles. The result of this is that the effective excluded volume is slightly larger than the physical volume occupied by the aggregates. These intermicellar interactions were found to be higher than those observed in the ChCl:malonic acid DES [385], where the presence of the acid is thought to provide an increased charge-screening effect, but comparable to the interactions within the ChCl:glycerol DES [14]. Additionally, intermicellar interactions have been reported in the literature to increase with decreasing micelle tail length in the case of cationic surfactants. The effect has been observed both in DES [14] and in water [443]. This may arise from a lower degree of counterion condensation in systems containing surfactants with shorter tail lengths. This would explain the observation that C_{12}TAB tends to form globular aggregates in the DES even when C_{16}TAB has formed highly elongated structures [13].

In order to further understand the micelle shape and resolve the structure of the headgroup layer, SANS data obtained from 130 mM solutions of C_{16}TAB in ChCl:U:Gly DES were fitted to a core-shell ellipsoid model. When investigating systems where the surfactant is not varied, the difference in micelle morphology must be explained by the difference in interactions of the micelle headgroups as the DES composition varies. The surfactant tails, which form the micelle core, are assumed not to affect micelle morphology significantly as solvent penetration into this lyophobic region would be minimal. The core-shell model contains the fitting parameters for the polar and equatorial radii as per the uniform ellipsoid model, but additionally contains a parameter for the shell thickness, T_{shell}. The ratio of shell thickness between the polar and equatorial axes was fixed to 1 during the fitting, as the micelle headgroup size should be similar along all axes. The SLD of the micelle core was fixed as the SLD of the surfactant tail (Table A.1 in the Appendix), whilst the SLD of the shell (made up of the surfactant headgroups) was allowed to vary to account for solvent penetration into this region. Both the polar and equatorial radii were fitted, and the shell thickness was allowed to vary between 4 - 10 Å this range was determined from previous studies [14]. The data were fitted simultaneously to two contrasts: d-C_{16}TAB in h-ChCl:h-U:h-Gly and h-C_{16}TAB in d-ChCl:d-U:d-Gly. The parameters from this fitting are shown in Table 4.9, whilst the plots of the data and best fits are shown in Figure 4.13.

Table 4.9: Fitted parameters for the 130 mM solutions of C_{16}TAB in ChCl:urea:glycerol DES with urea:glycerol ratios of 1.5:0.5, 1:1 and 1.5:0.5, determined from co-fitting protiated and deuterated contrasts to a core-shell ellipsoid model. The parameter $\mathrm{SLD}_{\mathrm{shell}}$ is reported as (1) h-C_{16}TAB in deuterated DES and (2) d-C_{16}TAB in protiated DES. Adapted from Reference [13]. Copyright 2020, American Chemical Society.

DES ratio	r_{eq} (Å)	r_{po} (Å)	T_{shell} (Å)	$\mathrm{SLD}_{\mathrm{shell}}$ (x10^{-6} Å^{-2})	$\Phi_{S_{(q)}}$ (x10^{-2})
1:1.5:0.5	17.5 ± 0.5	138.2 ± 5.2	4.6 ± 0.8	(1) 7.1±0.2, (2) 0.18±0.3	5.3±0.04
1:1:1	16.2 ± 0.8	111.8 ± 3.4	4.5 ± 0.8	(1) 7.0±0.4, (2) 0.2±0.2	5.2±0.02
1:0.5:1.5	16.4 ± 0.7	50.8 ± 2.6	4.7 ± 0.7	(1) 6.34±0.3, (2) 1.3±0.2	5.5±0.03

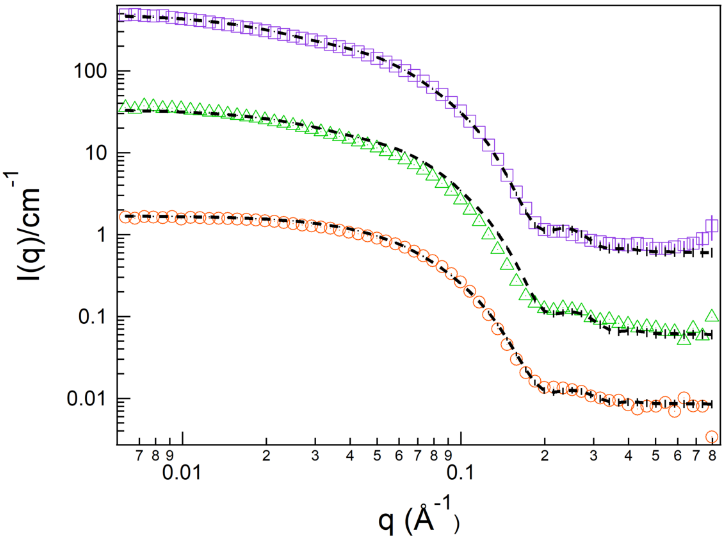

Figure 4.13: SANS data (coloured markers) and best fits (black dashed lines) 130 mM solutions of d-C_{16}TAB in h-ChCl:h-U:h-Gly DES with U:Gly ratios of 1.5:0.5 (purple squares), 1:1 (green triangles) and 1.5:0.5 (orange circles) from fits to a core-shell ellipsoid model. The fitting procedure included a modified hard-sphere structure factor, as discussed above. Best fits were obtained through co-refinement of two contrasts.

The parameters for the best fits obtained using the core-shell model agree with the results obtained using the uniform ellipsoid model, and again show the clear trend towards micelle elongation with decreasing glycerol content in the DES. The degree of elongation observed in these mixtures may be linked to either or both the interaction of the headgroups and the counterion with the solvent. The fitted SLD values for the shell do not vary greatly from the expected values for the deuterated and protiated headgroups (7.12 x 10^{-6}Å^{-2} and 0.18 x 10^{-6}Å^{-2}, respectively), and the apparent headgroup thicknesses (T_{shell}) are also close to expected results.

There is a greater deviation observed in the shell SLD in the DES with the highest glycerol content (urea:glycerol = 0.5:1.5), and so it can be assumed that solvent penetration is greatest into the micelle shell occurs to the greatest extent in this system. When similar structural parameters were obtained for 130 mM mixtures of SDS in the ternary DES, an additional partially deuterated contrast, where the hydrogen bond donors (urea and glycerol) were deuterated allowed for further insight into the local environment around the micelle. It was suggested that the solvent components within the DES were segregated and that an excess of hydrogen bond donor molecules preferentially sit around the micelle headgroup and direct the solvation mechanism [13].

The discussion and subsequent proposed explanation of the elongation observed in the micelles formed in surfactant/DES mixtures measured in this chapter must build upon previous studies and conclusions formed from the body of work summarised in the literature review, which explored the self-assembly of ionic surfactants in ChCl-based DES. It has been observed in the case of surfactant/IL solutions that the surfactant counterions can be incorporated into the hydrogen bond network of the solvent. In the case of the micellisation of SDS in DES, it was proposed that a similar effect might be happening [382]. Anionic SDS forms highly elongated cylindrical micelles in both ChCl:urea [21] and ChCl:glycerol [338], and it was proposed that interactions in the micelle headgroup region between the negatively charged surfactant headgroups and choline cations from the DES provided a charge-screening effect. This lowered repulsion between headgroups led to altered molecular packing and the formation of elongated aggregates. Also in this system, it was observed that as the concentration of SDS (and so the ratio of sulfate to choline) was increased, micelles transitioned to more globular morphologies. In this case, it was assigned to a lower availability of choline counterions and so increased repulsion between sulfate headgroups. Whilst this same mechanism is not anticipated in the C_{16}TAB/DES mixtures, a larger concentration series would be needed to investigate the exact effect of varying the amount of surfactant in these systems.

A similar effect was also reported in the case of the micellisation of C_nTAB surfactants in ChCl:malonic acid, where a transition to elongated micelles was observed. This was attributed to a mechanism whereby malonate ions formed through deprotonation of malonic acid could provide a charge-screening effect, similar to that observed for the micellisation of cationic surfactants in aqueous solutions containing carboxylic acids [444]. This behaviour was not seen in the case of the micellisation of C_nTAB surfactants, where globular micelles were observed in ChCl-based DES [14] and it was suggested therefore that similar mechanisms do not control micelle morphology in these solvents. As such, it is likely that there is another explanation for the observed elongation of the C_{16}TAB micelles discussed in this chapter.

For SDS in ChCl-based DES, it was proposed that the addition of surfactants to a DES would disrupt the solvent nanostructure, largely governed by a hydrogen bond network, by competing for interaction with the choline cation [382]. Furthermore, the addition of water was found to also affect micelle morphology and this was attributed to the substantial modification of the competing interactions between the solvent hydrogen bond network and the micelle interface. For the C_{16}TAB/DES mixtures studied in this chapter, especially in the case of the ammonium headgroups of the C_{16}TAB micelles, there is potential for competing hydrogen bonding interactions to disrupt the solvent network, and preferential bonding with certain components of the DES could have an effect on the solvent nanostructure and so the environment of the headgroup region and close to the micelle surface.

Although the introduction of any species into the hydrogen-bonded DES network is sure to have an effect on the interactions between components and their most statistically likely configurations, the SANS data obtained during the experiments presented in this chapter do not allow conclusions to be drawn as to the specific nature of this. Advances in techniques such as neutron diffraction, which has been used extensively to characterise the hydrogen bonding within DES, have been made to include approaches such as coarse-graining in their analysis routines, which has been used to characterise micelles [445]. It is possible in future that applying similar techniques to the systems under study in this chapter will allow for the determination of the overall 'molecular picture' of the system and the interelation between of both the surfactant and the DES.

The presence of counterions near the headgroup region, and so the degree of dissociation of counterions within the solution has been demonstrated to affect the charge density and so the morphology of the micelle [446]. The degree to which the surfactant counterion interacts with the micelle headgroup has been shown to affect the CMC of aqueous surfactant mixtures, where a greater interaction results in a lowering of the CMC analogous to a 'salting out' effect [387, 447]. The surfactant counterion has previously been shown to affect micelle morphology both in water [448] and in DES [338]. By varying the counterion on dodecyl sulfate anionic surfactants, Sanchez-Fernandez *et al.* determined that the micelle elongation along the rotational axis varied with different counterions, with counterion binding to the surface facilitated by a poorer solubility of the surfactant counterions in the DES as compared to in water. This is especially interesting given that the ChCl-based DES do themselves already contain choline cations and chloride anions, making the solvent environment very different from aqueous solutions. The results obtained in this study suggest that the same effect is occurring in these systems.

Where the surfactant is not varied, the micelle morphology must depend on the DES composition. In order to explain the reasons for different structures being observed in different DES compositions, both charge-screening within the system and the counterion solubility in the DES must be considered. The effect of salt addition to aqueous surfactant solutions has already been discussed (Section 4.3.3), whereby the presence of an increased number of charged particles results in charge-screening effects on the micelle surface and a partial charge neutralisation within the solvent [383]. At high salt concentrations, the effect on micelle morphology can be profound, with previously spherical structures forming worm-like micelles [384]. In the case of the surfactant/DES mixtures, counterion condensation on the surface (in addition to the ions already present within the DES, such as chloride anions) would have a similar effect, screening the charge on the surfactant headgroups and therefore reducing the apparent headgroup area. This would allow for a tighter packing of the headgroups (Section 4.3) which would result in the formation of elongated structures [13].

Another factor which must be considered is the solubility of small ions in the DES. The solubility of sodium bromide, NaBr (a salt which contains the Br^- counterion of C_{16}TAB and also Na^+ which is the counterion of many anionic surfactants) in the ternary DES was estimated. The obtained values were 50, 58 and 65 g kg^{-1} in the DES with urea:glycerol ratios of 1.5:0.5, 1:1, and 0.5:1.5, respectively. These values are relatively low, especially considering that by contrast the solubility of NaBr in glycerol is 387 g kg^{-1} [449] and 943 g kg^{-1} in water [450]). The values of solubility increase steadily with increasing glycerol content in the DES. In DES with lower glycerol contents, the decreased solubility would therefore result in a tighter binding of the surfactant counterions to the micelle surface, and inducing the charge-screening effect already described above [13].

By looking at the slight deviations in the fitted values of the shell SLDs from their calculated values, it has already been suggested that glycerol might penetrate into the solvent shell and therefore the cationic headgroups may interact more with this component of the DES. The structure of ChCl:glycerol has been shown to be dominated by a hydrogen-bonded glycerol network, with ChCl occupying voids within the structure. This is most evident at DES compositions with a higher glycerol content (e.g. ChCl:glycerol = 1:2). These structural investigations are discussed at length in Chapter 5. In such a regime, counterions with a greater solubility in glycerol would have the potential to also occupy these voids and hence be dissociated from the micelle surface. As no SANS measurements were made for the C_{16}TAB/DES mixtures in which only one DES component was selectively deuterated, it is impossible to draw further conclusions as to the exact interactions occurring between the micelles and various DES components. This will form a key part of future work in order to examine further the full range of molecular interactions occurring within the system.

4.8.4 Effect of changes to system composition

Whilst the main focus of the SANS experiments discussed in this chapter was the collection of data for mixtures of C_{16}TAB in the ternary DES, a few select measurements were also made to explore the effect of changing other aspects of the system composition besides the urea:glycerol ratio in the solvent. First, the effect of a change in the counterion species from Br^- to NO_3^- was investigated. In order to prepare these samples, $C_{16}TANO_3$ was used, which had previously been synthesised via an ion-exchange method from C_{16}TAB, as published by Manasi *et al.* [390]. The remainder of the procedure including preparation of the surfactant/DES mixture and data collection was carried out as discussed in Section 4.5. The SANS data for a mixture of 130 mM $C_{16}TANO_3$ in the ternary DES with a urea:glycerol ratio of 1.5:0.5 (micelles in this DES showed the greatest degree of elongation) is shown in Figure 4.14. As the scattering pattern closely resembled that obtained from the C_{16}TAB mixture, a core-shell model with a hard-sphere structure factor was again chosen to fit the data. The fitted parameters are presented in Table 4.10. A full record of the fitted parameters and the relevant scattering length density values are presented in Appendix 6.

Table 4.10: Fitted parameters for the 130 mM solutions of d-$C_{16}TANO_3$ in h-ChCl:h-U:h-Gly DES, and d-C_{16}TAB in h-ChCl:h-U:h-Gly:H_2O with component ratios of 1:1.5:0.5:10. Best fits to a core-shell ellipsoid model were determined by co-fitting the two contrasts.

Dataset	r_{eq} (Å)	r_{po} (Å)	T_{shell} (Å)	SLD_{shell} (x10^{-6} Å^{-2})	$\Phi_{S_{(\text{q})}}$ (x10^{-2})
$C_{16}TANO_3$/DES	17.1 ± 1.8	131.7 ± 4.6	4.5 ± 0.4	6.9 ± 0.2	5.4 ± 0.5
C_{16}TAB/DES/H_2O	17.7 ± 1.7	155.9 ± 5.4	4.6 ± 0.4	5.9 ± 0.3	5.7 ± 0.4

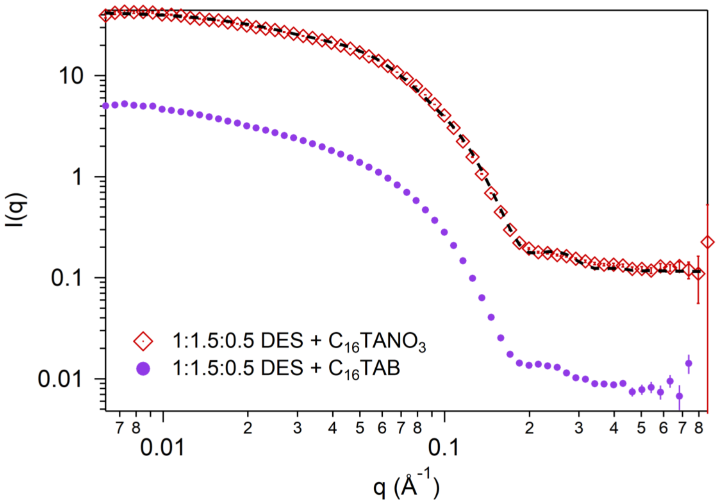

Figure 4.14: SANS data (red squares) and best fits (black dashed line) of a 130 mM solution of d-$C_{16}TANO_3$ in h-ChCl:h-U:h-Gly DES with a component ratio of 1:1.5:0.5. The best fit presented was obtained through co-refinement of two contrasts to a core-shell ellipsoid model with a modified hard-sphere structure factor. SANS data for the scattering from a mixture $C_{16}TAB$ in the same DES (purple markers) is provided for comparison. A record of the fitting parameters from this analysis is given in Table 4.10.

By comparison of the fitted values for the $C_{16}TANO_3$/DES mixture to those reported in Table 4.8 for the $C_{16}TAB$/DES mixtures, it is several parameters are quite similar, and indeed often have overalapping errors. For example, $r_{\mathrm{eq}} = 17.5$ Å for both the $C_{16}TAB$/DES and $C_{16}TANO_3$, which is expected as both surfactants have a C_{16} tail. The values for the micelle elongation (r_{po}) were fitted as 138.2 Å and 131.7 Å, respectively. The apparent headgroup area thickness (shell thickness) also did not vary by much across the two samples. There was a slight decrease in the SLD values of the micelle shell region from 7.13 to 6.9, however here the errors overlap and as measurements were not made in DES with varying urea:glycerol ratios for $C_{16}TANO_3$, it is not possible to draw any significant conclusions from this. The fact that the fitted parameters are similar for the $C_{16}TAB$/DES and $C_{16}TANO_3$/DES are so similar is not wholly unpredictable, especially given the hypothesis that it is the condensation of the counterion on the micelle surface which gives rise to the micelle elongation. The two surfactant counterions, Br^- and NO_3^- are adjacent to each other in the Hofmeister series [451] and as there was no variation in the DES composition, we can assume that their actions in the mixture are relatively equivalent. This is similar to observations made in aqueous solution [452] and also other DES [390], albeit the DES in the referenced study was a 'Type IV' DES comprising cerium nitrate and urea, as compared to the 'Type III' DES used in this study which contain only organic components. As no other counterions were studied, and furthermore samples were only prepared in one ratio of the ternary DES, there is not sufficient evidence to draw significant conclusions from these initial data. Further work would include the analysis of a wider range of samples (counterions and DES ratios) and in conducting appropriate solubility tests similar to those carried out for NaBr in the ternary DES.

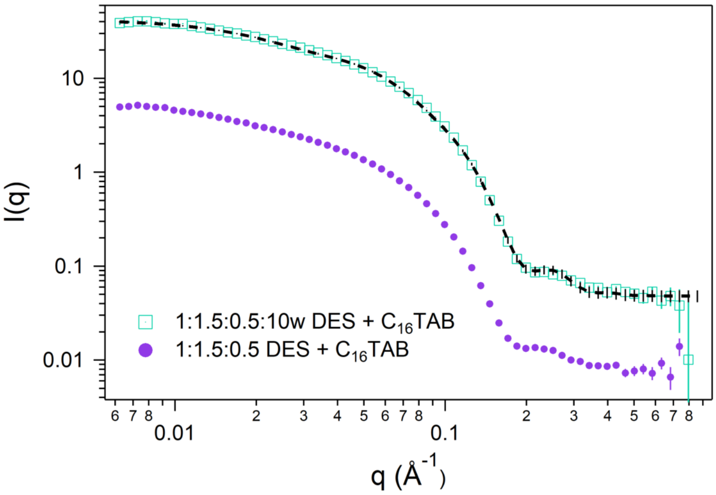

Figure 4.15: SANS data (blue squares) and best fits (black dashed line) of a 130 mM solution of d-C_{16}TAB in h-ChCl:h-U:h-Gly:H_2O with component ratios of 1:1.5:0.5:10. The best fit was obtained through co-refinement of different contrasts to a core-shell ellipsoid model with a modified Percus-Yevick hard sphere structure factor. SANS data for the scattering from a mixture C_{16}TAB in the same DES (purple markers) is provided for comparison. A record of the fitting parameters from this analysis is given in Table 4.10.

The effect of water addition to the DES was also briefly examined, although again, this was not the primary focus of this study. A hydrated ternary DES (urea:glycerol = 1.5:0.5) was prepared such that 10 moles of water were added for every mole of ChCl. As compared to the pure (unhydrated) DES, where prolonged mixing at elevated temperatures (60 °C) was required to prepare the C_{16}TAB solutions, the mixtures containing hydrated DES were far easier to form, requiring only gentle heating to 35 °C. This is expected given that C_{16}TAB is highly soluble in water at ambient temperatures [453]. As already mentioned in this chapter, C_{16}TAB forms spherical micelles in water [454].

It has been demonstrated in the literature that the addition of water to surfactant/DES systems results in a shortening of the micelle length, such that transition from elongated/cylindrical micelles to globular micelles is seen. Sanchez-Fernandez and co-workers observed this in the case of SDS in ChCl:urea [382] and C_nTAB surfactants in the ChCl:malonic acid DES [385]. In the former study, ChCl:urea:water mixtures were prepared up until the addition of 4 mole equivalents of water (per mole of ChCl). Through the use of neutron diffraction techniques, Hammond and co-workers have investigated the liquid structure of hydrated ChCl:urea. The threshold until which the DES nanostructure was retained was identified as the addition of 15 mole equivalents of water (1:2:15), whereas the addition of further quantities of water resulted in a structural transition to an aqueous solution. It is likely therefore that in the mixtures of SDS in hydrated ChCl:urea measured by Sanchez-Fernandez *et al.* [382], the structure of the solvent was largely DES-like, but the presence of water in the system still had a noticeable effect on the micelle morphology.

In the case of ChCl:malic acid, a carboxylic acid-based DES not unlike ChCl:malonic acid, the addition of water (2 mole equivalents per mole of ChCl) was found to result largely in a retention of the DES nanostructure rather than the formation of an aqueous solution, in which the water molecules acted as a second hydrogen bond donor [190]. The change in nanostructure on addition of further quantities of water is unclear, and as the hydrated ChCl:malonic acid DES investigated by Sanchez-Fernandez *et al.* included water up to 20 mole equivalents [385], the exact nature of the solvent at these high hydration levels cannot be known. Again, the observations of a contraction in the micelle length with increasing hydration level in this case indicates the presence of an intermediate solvent environment when water is added to the DES, with the micelle morphology lying between the two extremes.

As the ternary ChCl:urea:glycerol DES is different still from both ChCl:urea and ChCl:malonic acid, the exact effect of water addition and its interaction with the DES components cannot be determined accurately. On looking at the SLD profile of the micelles in the hydrated ChCl:urea:glycerol DES in Figure 4.15, however, it is apparent that the micelles formed are elongated in nature, with the scattering pattern closely resembling that obtained from the unhydrated surfactant/DES solutions. In order provide a direct comparison between the hydrated and unhydrated regimes, the scattering data from the hydrated $C_{16}TAB$/DES mixtures were fitted to a core-shell ellipsoid model. Data from two contrasts (h-$C_{16}TAB$ in d-ChCl:d-U:d-Gly:D_2O and d-$C_{16}TAB$ in h-ChCl:h-U:h-Gly:H_2O were co-fitted in order to give the best description of the data. The fitted parameters are reported in Table 4.10 alongside those for the mixture containing $C_{16}TANO_3$. A full record of the relevant scattering length density values are presented in Appendix 6.

Overall, the cross-section of the micelles showed little variation, with both the equatorial radii and the shell thickness being comparable between the hydrated and unhydrated mixtures. The fitted values for the shell SLD (5.9 ± 0.3 x10^{-6} Å^{-2}) was lower than the calculated value of 7.13 for the trimethylammonium headgroup (in the case of the deuterated surfactant in protiated solvent), whereas the fitted values obtained for the unhydrated mixture did not deviate much from the calculated SLDs. This is indicative of a greater level of solvation of the deuterated headgroups by protiated components from the solvent; this could be water molecules, however as no data was collected for samples containing partially deuterated DES (with specific components selectively deuterated), it is not possible to accurately determine the nature of the solvent environment in the micelle headgroup region or immediately beyond the micelle surface. In the case of SDS micelles in unhydrated ChCl:urea:glycerol at similar concentrations, a slight increase in the shell SLD was observed in partially deuterated DES, where the deuterated components were hydrogen bond donors (HBDs), leading to a hypothesis that a degree of component segregation takes place within the system, with HBD components preferentially sitting around the micelle headgroup [13].

The most interesting fitted parameter was the value of the polar radius, r_{po}, which describes the micelle elongation. In the unhydrated DES mixture, this value was fitted to be 138.2 ± 5.2 Å, whereas for the hydrated mixture it was fitted as 155.9 ± 5.4 Å. This observation contradicts the hypothesis above, as it appears the presence of water causes further elongation of the micelles rather than a contraction. One explanation for this could be that the ionic strength of the solvent is not lowered by the addition of water as might be expected, and so the resulting charge-screening effect which contributes to micelle elongation might not reduce accordingly.

It has recently been demonstrated that long-range electrostatic interactions between micelles persist in cholinium-based DES even at high calculated salt concentrations, within regimes where a high level of charge screening would be expected [455]. This observation can be rationalised by comparison of the system to ILs, where interactions between oppositely-charged ions in the bulk structure lead to a reduced contribution from these ions to the total ionic strength of the solvent [456]. In a surfactant/DES mixture, this could lead to both an increase in long-range correlations between aggregates and lower charge-screening effect between micelle headgroups than might otherwise be predicted by Debye-Hückel theory. If similar ion-ion interactions were occurring in a surfactant/DES mixture, the addition of a large quantity of water could potentially result in increased ion-water interactions diminishing the reduction in ionic strength facilitated by ion-ion interactions. This increase of ‘free’ ions in the system caused by the addition of water could therefore increase the measured ionic strength of the solvent, and potentially explain the differences seen in the degree of micelle elongation between the hydrated and unhydrated regimes.

The addition of water has previously been shown to affect the bulk nanostructure of DES. It has been demonstrated in the literature through a variety of experimental and computational techniques that the DES nanostructure is largely retained even at significant hydration levels (for example, in ChCl:urea, the disruption of the solvent structure and transition to an aqueous solutions was only observed at a water content of 51 wt.%/81 mol%) [75]. Before this transition point is reached, however a series of structural 'states' has previously been proposed to characterise the nature of DES-water mixtures at low water contents. These states range from the incorporation of water molecules into the DES nanostructure with some hydrated species, to a 'hydration-dominated' regime, where DES components become increasingly dissociated as they form hydrated species [457]. The nanostructure and interactions between components in DES, including the effect of the addition of water, is discussed further in the literature review in Chapter 5. For the purposes of this discussion, the structural observations made when adding water to DES suggest that the presence of water within the structure, and the resulting ion-water interactions has the potential to disrupt interactions between both DES components and other ions in the system. This can in turn have an effect on the differences observed in the micelle morphologies between the hydrated and unhydrated systems.

The fact that the elongation seen in the hydrated DES/surfactant system was not previously seen in the literature could potentially be due to the differences in the water quantities added in each case. In the case of the micellisation of SDS in ChCl:urea, water was added to the solvent up to a maximum of approximately 20 wt.% [382], whereas in the present study the hydration level was close to 40 wt.% (with small variations due to isotopic substitution between samples). As mentioned previously however, the affinity of the DES components in the ChCl:urea:glycerol DES has not been characterised and therefore no conclusions can actually be drawn about the nature of the solvent structure in DES/water mixtures in this thesis.

The differences between this DES and literature data from other surfactant/DES mixtures could also be due to the nature of the hydrogen bond donor species within the solvents, however as only one surfactant/hydrated DES mixture was measured during this study, it is not possible to correctly identify the nature of the interactions within the solvent or the environment around the micelle headgroup region. In order to determine the effect which the addition of water has on the liquid structure and interactions between components in the three-component DES, structural studies using techniques such as neutron diffraction would need to be carried out on DES/water mixtures at varying levels of hydration. This would allow the determination of the extent to which the bulk nanostructure solvent is retained upon addition of different quantities of water, and the balance of interactions between DES components and water. This could then combined with SANS measurements of hydrated surfactant/DES mixtures with varying surfactant concentration and hydration levels in order to build a thorough picture of how micelle morphology is affected by the presence of water.

4.8.5 Effect of metal ions on micelle morphology

As has been mentioned in previous chapters, ChCl:urea has been used for the solvothermal synthesis of several materials [11,115], and as C_nTAB is an appropriate and widely used soft template [458,459], the addition of glycerol to the DES allows the design of a system which promotes the self-assembly of these surfactants, whilst retaining the urea functionality (which is essential to the solvothermal mechanism). To this end, surfactant/DES mixtures containing Fe^{3+} and Zn^{2+} ions were also prepared in order to examine the effect of the metal ions on the micelle structure. The synthesis of iron-based materials has been investigated previously, both in this thesis and in published literature concerning DES [11,116], so an investigation into iron oxide synthesis in the ternary DES and the interaction of Fe^{3+} ions with surfactant molecules will provide a good comparison. Studying the behaviour of Zn^{2+} provided a comparison to Fe^{3+}, and Zn-based materials remain under-investigated with respect to DES. Porous zinc oxide (which has previously found application in fields such as photocatalysis [460]) synthesised from such a method could obviate the need for complex syntheses and additives such as polymers and provide control over particle morphology through variation of the composition of the surfactant/DES mixture [461–463].

As the surfactant/DES mixtures containing $C_{16}TAB$ had to be prepared at elevated temperatures and often (especially in the case of higher urea contents in the DES) only remained in the liquid state at temperatures above 60 °C, the mixtures containing metal chlorides were also prepared at this temperature. In the case of iron oxide, it is known that the precursors do not react in reline at these temperatures, as the thermal decomposition of urea which drives the reaction only occurs above 80 °C [116]. Iron(III) chloride and zinc(II) chloride were dissolved into the DES/surfactant mixtures with constant stirring in concentrations of 0.25 mol kg^{-1} (iron) and 0.375 mol kg^{-1} (zinc) relative to the molar amount of ChCl in the DES. The mixtures formed containing $FeCl_3$ dissolved readily in the surfactant/DES mixtures at all component ratios, whilst

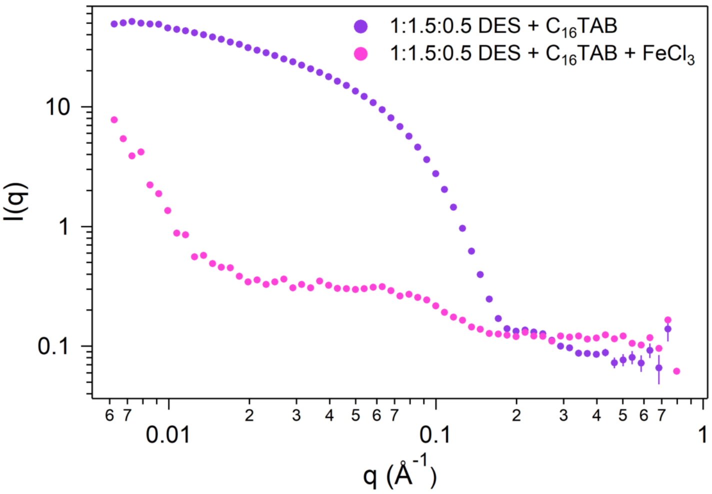

Figure 4.16: SANS data measured for a 130 mM solution of d-C_{16}TAB in h-ChCl:h-U:h-Gly (U:Gly = 1.5:0.5) with (pink markers) and without (purple markers) added $FeCl_3$ at a concentration of 0.25 mol kg^{-1}.

those containing $ZnCl_2$ took several hours of constant stirring before a homogeneous mixture was formed.

Similar to the samples in the previous sections, these solutions were investigated briefly using SANS following the experimental protocol described in Section 4.5.7. Some example data for the scattering from C_{16}TAB in DES (urea:glycerol ratio of 1.5:0.5) containing $FeCl_3$ are presented in Figure 4.16. The scattering curve from the DES/C_{16}TAB solution (with no Fe^{3+}) is also presented in each figure in order to provide a comparison. Even without carrying out any fitting procedures on the corrected data, it is clear from a visual inspection that the presence of Fe^{3+} ions causes significant disruption to the micelle structure, to the point where no evidence of the formation of micelles is apparent in the scattering pattern. This same observation could be made irrespective of the component ratio within the DES. The origin of this disruption is unclear, but one potential explanation is the nature interaction of the Fe^{3+} with those DES components which stabilise micellisation leads to the self-assembly not being supported. Further investigation into the structure and bonding of the ternary DES and how the $FeCl_3$ addition affects this would be required in order to verify this.

Further characterisation of the exact speciation of the Fe^{3+} ions when $FeCl_3$ is added to the surfactant/DES mixtures could also provide valuable insight into the observed loss of the micelle structure. In the case of a solution of $FeCl_3$ in ChCl:urea, the Fe^{3+} ion was determined to have a coordination number of 6, resulting in the formation of an octahedral complex of the type [Fe(L)$_3$(Cl)$_3$] (previously discussed in Section 3.2.4) [116]. In a system which contains an additional hydrogen bond donor (glycerol), the charged headgroup and counterion of the ionic surfactant molecules, and likely small quantities of water, the speciation of FeCl$_3$ has the potential to be complex. One species which may form is FeX$_4^-$ salts due to the presence of halide ions from the solvent, FeCl$_3$ and bromide surfactant counterions. Though the experimental data presented in this chapter allows no specific conclusions to be drawn about this, it should nevertheless remain an important factor when considering the reason why the addition FeCl$_3$ would destabilise micelle formation in the surfactant/DES mixtures and be a focus of future work.

In the case of mixtures containing zinc(II) chloride, a complete loss of the micellar structure was not observed, however the micelle morphology appeared to be noticeably altered. In the case of a low-urea regime (ChCl:urea:glycerol = 1:0.5:1.5), the form factor is characteristic of highly elongated structures which are cylindrical in nature. This is in stark contrast to the globular micelles observed at this DES component ratio in the surfactant/DES mixtures without added ZnCl$_2$ (Figure 4.17).

Although the use of an ellipsoidal form factor would have provided the greatest direct comparison between datasets, it was not possible to achieve a good enough fit to the data using this model, and a uniform cylinder was ultimately chosen, which would still allow some comparison between the degrees of elongation of the micelles in each system. This model contains parameters for the radius (r) and length (l) of the micelles, and the fitted values are presented in Table 4.11. Additionally a hard-sphere structure factor was used during the fitting; the effective volume fraction was fitted, whilst the value of the interaction radius had the constraint $P(q)xS(q)$ applied to produce an approach analogous to the modified structure factor used for the C$_{16}$TAB/DES mixtures fitted to ellipsoidal form factors in previous sections [464]. The dimension of the micelle cross-sections remained comparable to those of the pure C$_{16}$TAB/DES mixtures (fitted to a uniform ellipsoid, to encompass the cross-section of the micelle core and shell), whilst the elongation increased dramatically from 74 ± 1.2 Å to 1549 ± 25 Å. The fitted value of the volume fraction, $\Phi_{\mathrm{S}_{(\mathrm{q})}}$ is lower than the calculated value, which suggests that not all of the C$_{16}$TAB molecules are in the measured micelles. The significant increase observed in the micelle elongation could simply be due to the presence of more ions in the system, causing an increase in the charge-screening effect, or due to a markedly decreased solubility of the Br$^-$ counterion, leading to more condensation on the surface. Further datasets would need to be collected, in particular involving the use of specific head or tail deuteration of the surfactant molecules or selective deuteration of the DES

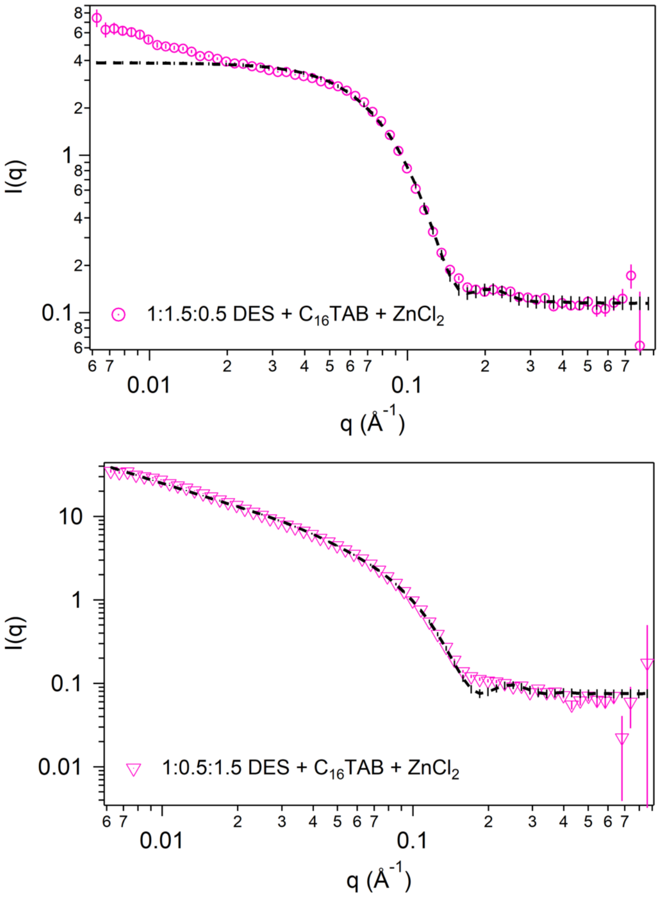

Figure 4.17: SANS data and best fits for 130 mM solutions of d-C_{16}TAB with added $ZnCl_2$ (0.375 mol kg^{-1}) in h-ChCl:h-U:h-Gly at component ratios of 1:1.5:0.5 (top) and 1:0.5:1.5 (bottom). The best fits to the data were obtained through co-refinement of two contrasts to a uniform ellipsoid (top) or uniform cylinder (bottom) model with a modified hard sphere structure factor. A record of the fitting parameters is given in Table 4.11.

components in order to better resolve the micelle structure and the solvent environment immediately beyond the micelle surface.

The form factor of the scattering curve from a high-urea regime (ChCl:urea:glycerol = 1:1.5:0.5) presents an even more complex problem. Whilst the form factor is not completely characteristic of highly elongated micelles, the slope at low-q values suggests the presence of elongated structures within the mixture. Fitting the gradient of this slope determined that in this region, $I(q) \propto q^{-1}$ which confirmed this initial observation. However, it was not possible to fit all of the datapoints in the scattering curve to a single geometric model. Originally, a fit to a cylinder model was also

Table 4.11: Fitted parameters for the 130 mM solutions of d-C_{16}TAB in h-ChCl:h-U:h-Gly DES with U:Gly ratios of 1.5:0.5 and 0.5:1.5 with added $ZnCl_2$ (0.375 mol kg^{-1}). Samples in the DES with U:Gly ratios of 1.5:0.5 were fitted to a uniform ellipsoid model, and samples in the DES with U:Gly ratios of 0.5:1.5 were fitted to a uniform cylinder model. The column headings for the micelle radius and elongation refer to the values of the equatorial radius r_{eq} and polar radius r_{po} (uniform ellipsoid model) and the radius r and length l (cylinder model), respectively. Best fits to the data were determined from simultaneous fitting of two contrasts.

DES component ratio	Radius (Å)	Elongation (Å)	$\Phi_{S_{(\mathrm{q})}}$ (x10^{-2})
1:1.5:0.5	22.6 ± 1.6	51 ± 3.1	0.23 ± 0.02
1:0.5:1.5	20.4 ± 2.2	1549 ± 25	1.6 ± 0.04

attempted, however ultimately the slope of the curve and the data points at higher q values could be best fit to a uniform ellipsoid model, which still allowed for some comparison between the degree of micelle elongation in the two regimes studied here. The equatorial radius was found to be comparable to the low-urea mixture, whilst the value of the polar radius was estimated to be 51 ± 3.1 Å, which is lower still than the elongation observed for the shortest micelles in pure C_{16}TAB/DES mixtures. This suggests that those surfactant molecules which did self-assemble are in an environment which does not result in a charge-screening effect or significant counterion condensation on the micelle surface. The fitted volume fraction, $\Phi_{S_{(\mathrm{q})}}$ was significantly lower than the calculated volume fraction (and lower still than the value obtained for the low-urea system), which again suggests that very few of the C_{16}TAB actually participate in the self-assembly measured in the bulk solution during the SANS experiment.

A peculiar observation was made when the SANS data for the C_{16}TAB/DES mixtures containing Zn^{2+} were first collected. On removing the sample cell from the instrument following measurement, some phase separation was observed in certain mixtures. This is likely to have only been noticed during the SANS experiment and not during laboratory handling of the mixtures due to the samples remaining on the automatic sample changer within the instrument at elevated temperatures for several hours whilst measurements were carried out. In order to verify this phase separation, similar mixtures were subsequently prepared in larger volumes ($>$ 20 mL) and left to stand in vials in an oil bath at 70 °C for several hours in order to simulate the conditions within the SANS instrument (Figure 4.18). With a sufficient sample volume, it was possible to separate enough of the upper phase to analyse using SAXS.

The gradient of the low-q region of the scattering curve from the SAXS data was deter-

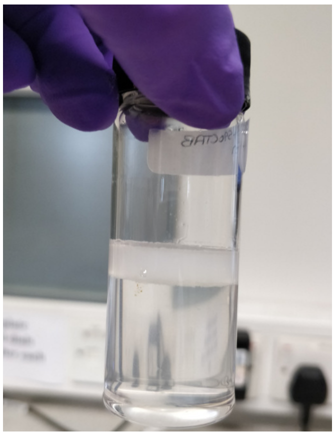

Figure 4.18: A photograph of the phase separation observed when $ZnCl_2$ is added to C_{16}TAB/DES (urea:glycerol = 1.5:0.5). Samples were prepared by allowing the solutions to stand in an oil bath at 70 °C for several hours.

mined (by fitting to an exponential function) and showed that the scattered intensity appeared to be proportional to q^{-2}, which is in contrast to a similar analysis of the SANS data for the same sample, where $I(q) \propto q^{-1}$. The observation of this phase separation however means it is unclear exactly how much of either phase was measured during the SANS experiment. The appearance of the scattering pattern also suggests the presence of a concentrated surfactant phase, by the observation of strong structure factor correlations. A slope of -2 typically suggests the presence of flat structures such as lamellae, which could be expected in this phase if the majority of the surfactant molecules had preferentially assembled within it and hence the concentration would be far higher than originally calculated for the solution. This phase separation was especially evident in the mixtures where the DES had a higher urea content, but not observed in the mixture where urea:glycerol = 0.5:1.5. The presence of two distinct liquid phases within the mixture where urea:glycerol = 1.5:0.5 could explain the apparent presence of two types of structure with differing dimensions seen in the scattering curve. $ZnCl_2$ is capable of forming a DES with urea in a component ratio of 1:3.5, so it is possible that in the high-urea regime, strong associations between these two components leads to the formation of a separate phase. C_{16}TAB is soluble up to at least 20 wt.% in similar DES comprising metal salts and urea [336], and hence the surfactant molecules might have a greater affinity for this phase than for the ternary DES. This would account for the significantly lower volume fraction of the globular micelles, whilst the increased number of ions in the $ZnCl_2$/urea-containing phase could lead to greater charge screening effects, giving rise to the highly elongated structures detected in the SANS data. The fact that this is not observed in the low-urea regime

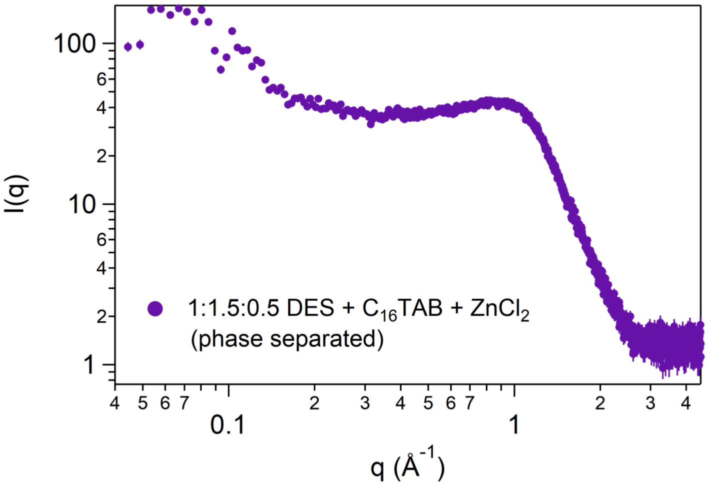

Figure 4.19: SAXS data collected at 70 °C for the top layer (see Figure 4.18) of the phase separated mixture of $ZnCl_2$ in $C_{16}TAB$/DES (urea:glycerol = 1.5:0.5).

could potentially simply be due to there being insufficient urea to allow this complexation and subsequent phase separation to occur, especially given the relatively high molar amount of urea required to form the metal salt-based DES. It is worth noting that $FeCl_3$ is capable of forming a DES (albeit most typically with ChCl rather than urea) [465] and some phase separation was also seen within these mixtures, however the differences in effects on micelle structure observed between the two types of metal ion warrants further investigation before any further conclusions can be drawn as to why micelles are still observed in the case of Zn^{2+} ions and not in the case of Fe-containing mixtures. Further work would include thorough compositional analysis on of both layers of the phase-separated mixtures. This work would also take into account again the potential speciation of the Zn^{2+} ions in the surfactant/DES mixtures and the formation of any salts with halide ions, as discussed above in the case of $FeCl_3$ addition. An understanding of any differences in the speciation of Zn^{2+} and Fe^{3+} could also help to explain the interactions of the metal ions with the DES components and the differences in the effects on micelle morphology in each case.

4.8.6 Synthesis of metal oxides from surfactant/DES mixtures

Synthesis using $FeCl_3$

Alongside understanding micelle formation in these ternary DES, a secondary objective of this study was to explore the possibilities of using these surfactant/DES mixtures in the synthesis of porous materials, employing similar methods as those already published for synthesis in DES [116]. Even though the SANS data presented in the previous section clearly show that the micelle structure is significantly disrupted, and even lost completely when $FeCl_3$ is added to mixtures of $C_{16}TAB$ in the ternary DES, this system was investigated initially as both previous literature [11] and some of the work presented in Chapter 3 has shown, iron (III) oxide (Fe_2O_3) forms readily in ChCl:urea, and it would be of interest to investigate the effect both the glycerol and the presence of surfactant molecules had upon the synthesis.

In the first instance, solvothermal reactions in six systems were investigated. In each case, $FeCl_3$ was added in a concentration of 0.25 mol kg^{-1} relative to the amount of ChCl, and $C_{16}TAB$ was incorporated at 130 mM in the ternary DES in all three urea:glycerol ratios, with or without 10 molar equivalents of water (relative to the number of moles of ChCl). The surfactant/DES mixtures were prepared and complete dissolution of the $C_{16}TAB$ was ensured before the addition of the $FeCl_3$. Following this, the reaction mixtures were transferred into Teflon-lined stainless steel reaction vessels and heated at the desired temperature and length of time, before being allowed to cool to room temperature naturally. It has been shown in the literature that the thermal degradation of the urea component of ChCl:urea is the driving force of the solvothermal reaction to form iron oxide nanoparticles, and that this degradation in the DES begins at 80 °C [419]. At this temperature, Fe_2O_3 particles also begin to form in this DES [116]. Trial reactions for the six systems described above were carried out at initially at 100 °C with a heating time of 3 h.

A noticeable difference was seen in the post-reaction mixtures as the glycerol and water contents in the DES were varied. In the case of all three compositions of the hydrated DES, the clear formation of red-brown iron oxide particles was observed, however the same was only seen in the pure DES in the high-urea system (urea:glycerol = 1.5:0.5). For the other two compositions of the unhydrated DES (urea:glycerol ratios of 1:1 and 0.5:1.5) the recovered mixtures were highly viscous and yellow-green in colour, which indicated the formation of a hydrated iron (III) or iron (II) chloride (see Figure 4.20). Even though the synthesis was repeated at higher temperatures (up to 180 °C) and with reaction times of up to 16 h, this same result was obtained each time.

Figure 4.20: Photographs of post-synthesis mixtures obtained from the reaction of $FeCl_3$ in unhydrated C_{16}TAB/DES mixtures with lower urea content (left) and in hydrated C_{16}TAB/DES or unhydrated high-urea DES (right). The reactions were carried out at 180 °C for 16 h in each case.

It is likely that in the hydrated and high-urea ternary DES, a similar octahedral iron complex ($[Fe(L)_3(Cl)_3]$) which is observed in reactions in ChCl:urea (both dry and hydrated) is also formed in this case, however it has been shown that the onset of nanoparticle nucleation and growth is determined by the rate of thermal hydrolysis of the urea molecules and the diffusion of these hydrolysis products. A faster rate of thermal hydrolysis/diffusion results in spontaneous nucleation and growth of the iron oxide nanoparticles, and the viscosity and hydration level (where increased hydration also lowers viscosity) affect these two parameters. It was expected therefore that Fe_2O_3 would form readily in the hydrated mixtures and in the high-urea system, which does not differ greatly from ChCl:urea. In the unhydrated DES, there was still evidence of urea degradation due to an ammoniacal odour which was observed upon opening the reaction vessel, but diffusion limitations or some energy barrier might exist which prevents the formation of the oxide product. One other explanation could simply be that urea was not in sufficient excess to drive the reaction mechanism through the formation of [-O-Fe-O-] oligomers [116].

For the reactions where the formation of Fe_2O_3 was likely, the powder products were isolated by repeated washing and centrifugation with ethanol and deionised water to remove any residual solvent, before drying overnight in air at 60 °C. A comparison of the X-ray diffraction patterns of the dried powders obtained through reaction in the pure and hydrated ternary DES (urea:glycerol = 1.5:0.5) shows that there is a significant amount of noise in each pattern (Figure 4.21). In the iron oxide produced from reaction in the pure DES, some peaks are noticeable, which by comparison to literature data were found to correspond to hematite, Fe_2O_3 (as expected). For the powder synthesised in the hydrated DES, no distinct peaks were discernible in the diffraction pattern. This was also observed by Hammond *et al.* in the synthesis of iron oxide in hydrated ChCl:urea, where the incredibly small particle size did not give rise to sharp peaks when analysed by XRD. Further analysis such as EDX (to characterise composition) or TEM (to visualise particle morphology) would be required in order to fully characterise the nature of the products, however this was not carried out in this case as it was not expected that the templating of porous iron oxide would be successful using this solvothermal method.

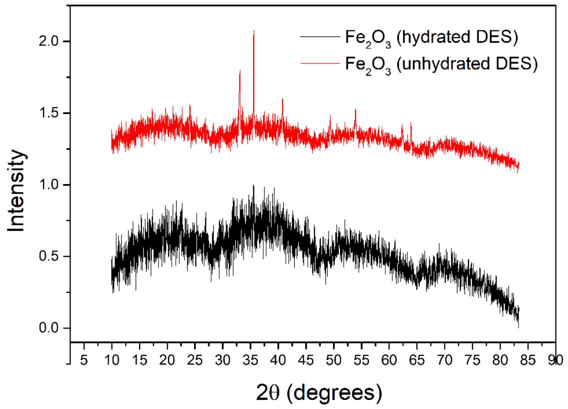

Figure 4.21: X-ray diffraction patterns collected for samples of Fe_2O_3 synthesised in ternary DES (urea:glycerol = 1.5:0.5) with 130mM C_{16}TAB, with (bottom) and without (top) water addition. Samples were synthesised by heating at 100 °C for 3 h.

Synthesis using $ZnCl_2$

The synthesis of zinc oxides from using the surfactant/DES mixtures was also investigated briefly, as the micellar structure was found to be retained when $ZnCl_2$ was added to the system, albeit with some interesting observations regarding changes in morphology and phase separation. Solvothermal reaction in this case were only carried out in the unhydrated high-urea C_{16}TAB/DES mixture (urea:glycerol = 1.5:0.5), as this showed the most promise for a successful synthesis. Initially, the reaction mixtures were prepared in a similar way those those described in the previous subsection, and reactions were carried out in stainless steel pressure vessels under similar conditions to those using $FeCl_3$. In these cases, the post-reaction mixture appeared to be a cloudy, viscous liquid from which it was not possible to isolate particles by washing with a DI water/ethanol mixture and centrifugation. The synthesis time was lengthened to 72 h and 120 h in order to account for any slow nucleation and growth of particles, however it was still not possible to isolate a powder product using this procedure.

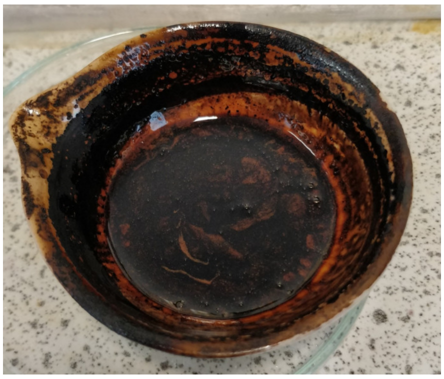

Figure 4.22: A image of the mixture obtained from the direct calcination of a solution of $ZnCl_2$ in C_{16}TAB/DES (urea:glycerol = 1.5:0.5) at 450 °C, 4h.

As an alternative method, the prepared mixture of $ZnCl_2$ in the C_{16}TAB/DES was calcined directly in order to remove the solvent and surfactant and directly obtain the powder product. A similar approach has been used for the synthesis of porous ceria (albeit in a DES comprising cerium nitrate and urea) [336]. In the first attempt to directly calcine the reaction mixture, the calcination was carried out at a lower temperature of 400 °C for 3 h. During the initial temperature ramp, a strong smell of ammonia and gas evolution was observed from the furnace and the product following a natural cooling to room temperature resembled a viscous black liquid (Figure 4.22). It is most likely that the temperature was not high enough to efficiently remove the organic matter from the reaction mixture. The procedure was repeated at a higher calcination temperature of 600 °C for 3 h, and in this case a powder product was successfully obtained, however it was dark in colour and not the expected off-white which would have been expected for ZnO. This could be the result of excess carbon or other component thermolysis products remaining on the surface of the product. The XRD patterns for the two samples are however remarkably similar, with sharp peaks at values of $2\theta = 31.6°$, 34.4°, 36.5°, 47.4°, 56.4°, 62.9°, 66.4°, 67.8° and 69.0°. By comparison to literature patterns [466], this indicates the presence of zinc oxide within each sample, although the very narrow peaks would suggest that the samples comprised large particles. Additionally, in the sample synthesised by direct calcination of the reaction mixture, there is a very noticeable broad, diffuse peak at low values of 2θ, which could indicate a large quantity of amorphous material or be characteristic of carbon/leftover DES on the material. This could potentially indicate that complete removal of the DES/C_{16}TAB and complete conversion of the precursor material into the oxide was not achieved. Further analysis would include an estimation of the crystallite size either from the diffraction pattern (using the Scherrer equation) or by fitting small-angle scattering data.

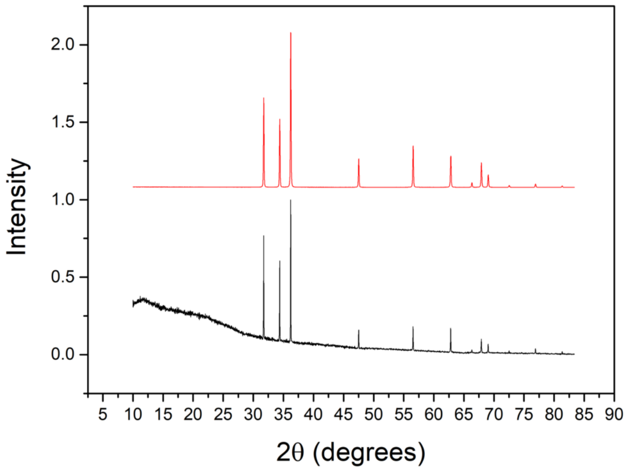

Figure 4.23: X-ray diffraction patterns measured for powder products synthesised from (bottom) direct calcination of the $ZnCl_2$/C_{16}TAB/DES reaction mixture at 600 °C for 3 h and (top) heating of the $ZnCl_2$/C_{16}TAB/DES reaction mixture at 100 °C for 96 h, followed by calcination at 600 °C for 3 h.

The N_2 adsorption isotherm (at 77 K) of the ZnO sample synthesised from heating of $ZnCl_2$/C_{16}TAB/DES reaction mixture at 100 °C for 96 h, followed by calcination at 600 °C for 3 h is plotted in Figure 4.24. The plot is characteristic of a Type II isotherm, which denotes a non-porous or macroporous material. The BET specific surface area of the sample was calculated to be 3 m^2 g, which is consistent with limited porosity

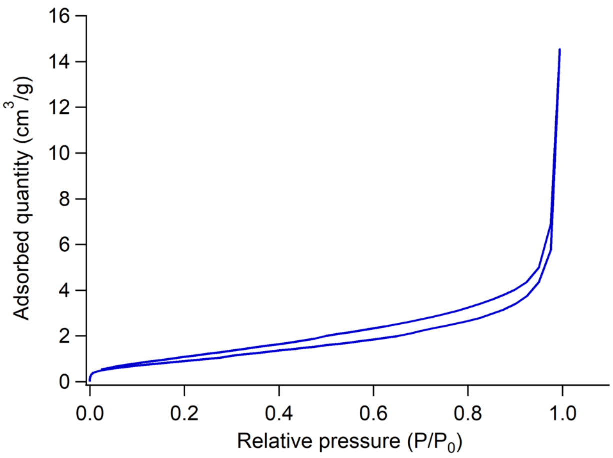

Figure 4.24: The nitrogen adsorption/desorption isotherm at 77 K measured for a sample of ZnO synthesised from heating of $ZnCl_2$/C_{16}TAB/DES reaction mixture at 100 °C for 96 h, followed by calcination at 600 °C for 3 h.

in the sample. This suggests that the surfactant/DES mixture and the methods used in this chapter are not resulting in the successful synthesis of a porous product and further method development will be required to explore this application.

4.9 Conclusions

The main objectives of this study were to study the self-assembly of the cationic C_{16}TAB surfactant in a three component DES (ChCl:urea:glycerol), to examine the effect of varying the component ratio of the solvent. Surfactant behaviour differs greatly between ChCl:urea and ChCl:glycerol, so micellisation in a mixed environment between these two extremes could be used to tune micelle morphology. Ternary DES comprising ChCl, urea and glycerol were prepared in component ratios of 1:1.5:0.5, 1:1:1 and 1:0.5:1.5. Preliminary data collected for the physiochemical properties of the DES show that the values of the surface tension, viscosity, density and Gordon parameter do not vary by much across the various solvent compositions. The CMCs of C_{16}TAB in the ternary DES combined with those of C_{12}TAB and SDS in one DES component ratio (to provide a comparison between surfactants) were estimated using pyrene fluorescence data.

C_{16}TAB was found to form micelles in the ternary DES at all component ratios. Interestingly, the inclusion of even a small quantity of glycerol in the DES enabled the solubilisation of C_{16}TAB, which is otherwise insoluble in ChCl:urea. The morphology of the micelles could be altered through varying the ratio of the HBD molecules (urea:glycerol) within the DES. At low urea contents, globular aggregates are formed, whilst in a DES with higher urea content, highly elongated structures were observed.

The explanation of this of this elongation was formed by consideration of previous studies carried out examining the micellisation of both cationic and anionic surfactants in DES. The addition of C_{16}TAB to the ChCl:urea:glycerol DES will almost certainly cause a change in the hydrogen bond network of the DES, especially as the ammonium headgroups are capable of interacting with DES components in this way. It was suggested due to the degree of solvent penetration into the micelle headgroup region increasing as the glycerol content of the DES was increased, that the headgroups might preferentially interact with glycerol molecules. As no SANS measurements were made of contrasts where certain DES components were selectively deuterated in order to determine their contribution to the system and any preferential interaction with the micelles, further work will be needed in order to elucidate the favoured interactions within the surfactant/DES mixtures. Ultimately, it was proposed that the elongation observed in the micelles is a result of a degree of solvation of the micelle headgroup, and also due to counterion condensation on the micelle surface. Estimations of the solubility of the salt NaBr showed that it is highly insoluble in the DES compared to solvents such as water and glycerol. The estimated solubilities showed a slight variation across the three DES compositions according to the glycerol content. This observation suggests that the bromide counterion from C_{16}TAB is more likely to bind to the micelle surface in those DES where it is least soluble, screening the neutralising the headgroup charges and allowing elongation of the micelles through closer packing of the headgroups. Although further characterisation would be needed in order to elucidate the exact nature of the solvent environment around the micelles, the results provided further insight into the mechanism of micellisation and the factors which must be thoroughly investigated in order to be able to control self-assembly in these solvents.

As a secondary objective, the effect of metal ions and other changes to the system such as water addition or varying the nature of the surfactant cation were investigated. Varying the surfactant counterion was found to have a negligible effect on micelle morphology and the same mechanism is likely to occur in this system. Interestingly, the addition of water to the DES composition which already gave rise to the longest micelles caused even further elongation, when it would be expected (by comparison to literature) that an intermediate solvent environment might cause a contraction in the micelle length. Some discussion was provided as to a possible explanation for this, however further experiments would be needed in order to fully investigate these observations. Further interesting effects on the micelle morphology were obtained through the addition of metal ions; the addition of $FeCl_3$ to the C_{16}TAB/DES mixtures caused a significant disruption of the micelle structure, and no evidence of self-assembly was seen in the SANS data. The addition of Zn appeared to cause extreme micelle elongation in the DES with lowest urea content (in which C_{16}TAB was found to form globular aggregates), and in the DES with highest urea content it was determined that both globular and elongated structures exist within the mixture. Some discussion was given as to the reasons for these varying observations, relating to the interaction of the Zn^{2+} ions with the DES components and the phase separation which was seen in the samples. Additionally, the speciation of the metal ions in the surfactant/DES mixtures and the resulting effects on various system components and the stabilisation of micelles would need to be characterised in order to build a better picture of the interactions within the system.

Finally, the synthesis of oxide materials in these DES was briefly investigated. It was found that iron oxide only formed via a solvothermal reaction in hydrated DES or in DES with low glycerol content. Zinc oxide could not easily be synthesised by a solvothermal reaction along, but the addition of a calcination step at high temperature produced the target material. However, analysis of the porosity and surface area of the oxide material suggested that the synthesis method had not successfully produced a porous sample, and further synthetic work is therefore needed to fully understand this application. Whilst more understanding of both the factors influencing the micellisation and the mechanism of synthesis is needed, these initial investigations present interesting opportunities for further developing methods to produce functional materials.

4.10 Future work

The experimental techniques used in this chapter, in particular small-angle neutron scattering, have allowed a detailed insight into micelle morphology which would not have been possible using equipment available in a university laboratory setting. However, there are still certain aspects of the work which can be improved and investigated further to provide a better insight into the properties of the surfactant/DES solutions and the mechanism of micellisation. In the first instance, the measurements of the CMC obtained from fluorescence spectroscopy could be compared to data obtained from surface tension measurements (hanging drop method), which would give the ability to calculate datapoints from an average of several drops, and provide a way to directly compare the CMCs of surfactants in other DES which were determined using this method.

The use of more complex geometric models such the core-shell ellipsoid model to fit SANS data gave some resolution of the solvent environment immediately surrounding the micelle headgroup region. Further understanding could be achieved by measuring contrasts which make use of selective deuteration of the surfactant (head or tail deuteration) and/or DES components, such that the role of each constituent of the system could be elucidated. Further neutron scattering experiments, in particular using wider angles, would be beneficial in order to probe the length scales corresponding to the interactions between components of the system, to allow a better molecular picture of the system to be formed.

In the case of water addition to the system, this approach could also be combined with varying the hydration level of the DES to determine if there is a transition point in the micelle morphology where aggregates tend to longer/shorter dimensions. The effect of metal ion inclusion in the surfactant/DES mixtures, particularly in the case of Zn^{2+}, could be further studied by exploring the effect of varying the metal ion concentration on the micelles in solution. Additionally, compositional analysis should be carried out on surfactant/DES mixtures containing Fe^{3+} and Zn^{2+} ions in order to explore the speciation and potential for salt formation on addition of the metal chlorides. It would be of particular interest to determine the compositions of both layers of the phase separated mixture observed in the case of $ZnCl_2$ addition to surfactant/DES mixtures to characterise the species present in each case.

Certain promising results were also found in trial synthesis experiments in the ternary DES/surfactant mixtures, particular in the case of ZnO synthesis. These experiments were carried out toward the end of this project, and as such there was not sufficient time to fully explore the effect of adjusting several synthesis conditions on the success of the method or the nature of the final product. Further work could involve the use of a series of different temperatures and heating times for the reaction, or varying the precursors and calcination temperature/time. A comparison could also be made between sealing the reaction mixture and heating at lower temperatures for a greater length of time ($\geq$ 72 hrs) before calcining, or directly calcining the reaction mixture to achieve a one-step synthesis procedure. If these experiments showed promising results then the opportunity would exist to expand the most successful method to materials containing metal ions which remain relatively unexplored in DES. An additional development, although somewhat outside the original focus of this chapter, could include an investigation into self-assembly in Zn-based DES and the potential for the synthesis of oxide materials directly from this system, similar to the method which has recently been demonstrated for ceria [336].

Chapter 5

Exploring the liquid structure of ternary DES using neutron diffraction

5.1 Introduction

Chapter 4 introduced a three-component DES comprising choline chloride, urea and glycerol, which can form in urea:glycerol ratios of 1.5:0.5, 1:1 and 0.5:1.5. Some characterisation of the physiochemical properties of these DES such as viscosity, surface tension and the Gordon parameter was carried out, and the interesting behaviour of surfactant molecules in the solvents was investigated. Additionally, the effect of the presence of metal ions on the micelle morphology was also briefly discussed. In the case of Fe^{3+} ions in the system, significant disruption was caused to the micelle structure, whilst this effect was less pronounced in the case of Zn^{2+}, although the shape of the micelles still appeared to be altered significantly. This effect was seen irrespective of the nature of the anion in the metal compound. It appears, therefore, that the addition of metal ions into the system induces a change in the structure and bonding within the system which gives rise to these observations.

In order to gain insight both into the structure of a DES comprising three components (where one component is not water), and into the effects on the system of introducing metal ions, it is crucial to resolve the structure of the system. Extensive structural characterisation, both in the form of computational and experimental studies using advanced techniques such as total neutron scattering have already been carried out on the ChCl:urea and ChCl:glycerol DES by multiple groups. The findings, in particular as they relate to the hydrogen bonding present within the system, may be used to form the basis of an investigation into the structure of the ternary DES. In this chapter, the structure of the ChCl:urea:glycerol DES in three compositions is resolved using total neutron scattering techniques and data refinement. Additionally, the effect of the addition of $FeCl_3$ to 1:1:1 DES was investigated for comparison to the structure of the pure DES, and some preliminary results are presented at the end of this chapter.

It is now well understood that the structure of ChCl:urea involves the formation of complex clusters through competing hydrogen bonding interactions between components [75], whilst ChCl:glycerol (in the 1:2 eutectic ratio) comprises an extended hydrogen-bonded glycerol network with choline and chloride occupying voids within the structure. An investigation into a system comprising all three of these components and the variance of the urea:glycerol ratio will give an insight into whether the structures lie between the two regimes or adopt another configuration altogether. The following sections present a literature review of DES structure and a discussion surrounding theoretical/experimental techniques for elucidating the structure of liquids.

5.2 Literature review - structural studies of DES

This section will discuss the existing literature surrounding the liquid structure of DES, with particular emphasis given to the study of those systems which are relevant to this chapter. DES are typically thought of as binary mixtures, often stable in the liquid state at room temperature and formed (though not always) from solid components. Like many liquids, they have been shown to possess distinct and ordered structure which persists over several length scales. Previous chapters within this thesis have already discussed the unique properties which DES possess, and compared and contrasted them with alternative systems such as molecular solvents and ILs. In contrast to both of these solvent classes, different DES may possess varying degrees of ionicity and accordingly vary vastly in their structure and behaviour. The implication of this is that in contrast to ILs, where the structure is dominated by interactions between the ionic species in the solvent, the structure within DES are dictated by hydrogen bonding between largely molecular components [467, 468].

DES have been shown to have complex solvent structures, both in the bulk and at interfaces, which consist of a number of inter- and intramolecular interactions such as van der Waals forces, Coulombic interactions and hydrogen bonds. This structure within DES has been found to dictate their properties, as has been the case for ILs. The differences in the bulk nanostructure however often further highlights the significant differences between the two classes of solvent, even though DES are often defined as a sub-category of ILs [469]. Although this fundamental research area has not progressed at the same rate as research into physiochemical properties or various DES applications, there is now a significant enough body of work to merit the publication of a number of reviews discussing the progress of experimental and computational research into the liquid structure of DES [470–472]. As DES were novel solvents and only reported in the literature within the last two decades, their unique behaviour was for many years not understood. More specifically, the rapid growth of the range of applications for which they were investigated was not matched by the progress of research into accurately determining the nature of their structure and bonding. However, it now appears clear that, as with similar solvents such as ILs, a greater understanding of the liquid structure of DES can aid in understanding their behaviour and interactions within a system. The nature of the DES components will determine its structure and behaviour, such that even a small change in the DES composition may have a profound effect on its physiochemical properties and interaction with other compounds. This allows a solvent to be tailored even more specifically through correlating its properties with its structure.

Although some commonalities exist between the liquid structures of various DES, the sheer number of combinations of hydrogen bond donors and hydrogen bond acceptors which might be used as DES components [51] means that it is impossible to determine one ‘structure of a DES’. This fundamental research has instead been limited to the investigation of the more popular DES in the literature. Many of these are choline-chloride based, though a handful of studies exist concerning non-choline based DES. Additionally, there is a body of work concerning the interaction of water molecules with DES and the degree of disruption which the incorporation of water causes to the solvent structure. An overview of these research topics is given in this section.

It has already been mentioned that structuring and order within DES can occur over a range of length scales. At the shortest of these length scales, interactions between atoms in a DES component molecule/ion or between species such as water with a DES can prove complicated to characterise. At longer length scales, interactions between clusters of molecules, and finally long range heterogeneous liquid ordering may be observed. The following sections attempt to describe the evolution of the structural understanding of deep eutectic solvents, from early experimental work to the more recent use of advanced experimental techniques and computational modelling methods.

Early comments on DES structure presented in the literature involved inferences made from experimental data gathered using techniques which were not capable of directly measuring structure. The earliest example of this was seen in the work of Abbott *et al.* [48]. When describing DES components it is common to refer to the combination of a hydrogen bond acceptor (HBA) with a hydrogen bond donor (HBD) molecule. This description originates from early experimental results presented by the group, who analysed NMR spectroscopy data (^{1}H-^{19}F HOESY 2D experiments) for a model choline fluoride:urea DES, and hypothesised that charge delocalisation of the F^{-} ions from the choline fluoride occurred, resulting in the formation of a 'complex ion' between the halide anion and urea [48]. Mass spectrometry data collected by subjecting the DES sample to fast atom bombardment (FAB) further suggested this charge delocalisation effect through the identification of fragments which can be assigned to ion clusters consisting of urea and the halide anion. The idea that a DES is formed from the complexation of a HBA and HBD species introduces a fundamental difference between the structure of DES as compared to the nanostructure within ILs.

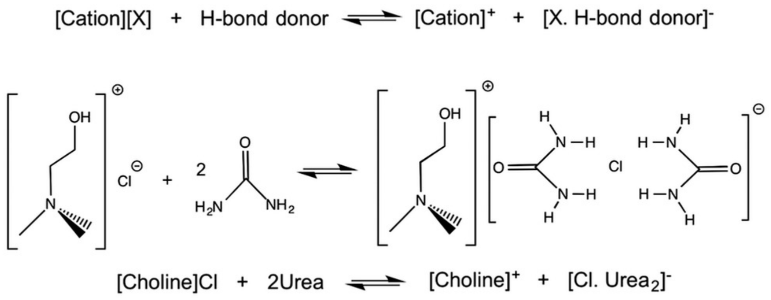

Figure 5.1: A schematic representing the complex-ion model of DES structure in ChCl:urea in a molar ratio of 1:2. Reproduced from Reference [15] with permission from the PCCP Owner Societies.

NMR spectroscopy work was also carried out several years later by D'Agostino *et al.* in collaboration with the Abbott group [473], which aimed to characterise any microscopic properties of several ChCl-based DES, in contrast to the widely studied macroscopic properties such as viscosity and surface tension. The authors argued that a solid understanding of the diffusion properties of the DES components was key to explaining the equilibrium within the systems, which involved the ionic components, complexing agent (HBD) and the resulting complex ions. By using pulsed field gradient (PFG) NMR techniques, the group were able to obtain self-diffusion data for four DES. In the case of ChCl combined with glycerol, ethylene glycol and urea, the choline ion was found to diffuse at a slower speed than the HBD molecules, which was thought to correlate with the degree of hydrogen bonding in the system. In the case of ChCl:malonic acid, the opposite effect was reported, thought in part to be due to dimerisation of the malonic acid. Whilst these results were promising, the technique was limited by the low sensitivity of the technique towards the chloride anion within ChCl, and the method remains reliant on significant inferences made from the experimental data.

Following on from these initial studies, research which sought to provide detailed structural characterisation of various DES took the approach of more advanced experimental techniques and computational modelling. Gradually, as the understanding of interactions and bonding between DES components began to improve, the previous 'complex-ion' model of DES structure expanded to include description of the hydrogen bonding network within the solvent.

There are a number of studies which use computational simulation techniques to propose structures for ChCl-based DES. Whilst investigating the interaction of copper and copper oxide with the ChCl:urea DES using quantum chemical simulations, Rimsza and René Corrales investigated the possibility of the formation urea anions in terms of proton transfer processes within the DES [474]. The study reported that the solvent mainly consisted of molecular urea rather than anions. The effect of the composition on the bonding within ChCl/urea mixtures was investigated by Sun *et al.* using MD simulation techniques [475]. The highest hydrogen bond strength calculated was that formed by the interaction of the choline species with the chloride ion through the choline hydroxyl ion. This bond also had the longest lifetime, and in the 1:2 eutectic ratio, the interaction energies between choline-chloride and urea-chloride were balanced. These observations are in contrast to the theory behind the complex ion model, as they suggest several more competing interactions with in the DES which ultimately define its structure.

MD simulations were combined with infrared spectroscopy measurements of ChCl:urea by Perkins, Painter and Colina [476], looking mainly at the interactions between the urea molecule and the chloride anions through the bonding between the amine hydrogens and Cl^{-}. The chloride anion was found to interact preferentially with the hydrogens which were *trans* to the carbonyl group in order to maximise the hydrogen bonds formed in the system. As the 1:2 (ChCl:urea) eutectic ratio is approached, the disappearance of the evidence of the carbonyl bond in spectroscopy measurements suggests an increase in the interactions between the -NH_2 or -OH hydrogens with the carbonyl group, whilst at lower concentrations of urea the interactions between -NH_2 groups dominate. The same authors further studied ChCl-based DES with a dicarboxylic acid (malonic acid) or polyol (ethylene glycol and glycerol) HBD molecules [477]. Good agreement was seen in the self-diffusion coefficients in ChCl:glycerol and ChCl:ethylene glycol. The experimental values obtained for ChCl:malonic acid were orders of magnitude lower than obtained for the other two DES, and not confirmed using MD simulations due to computational limitations. Similar to ChCl:urea, the Cl^--HBD interaction was particularly significant, and furthermore HBD-HBD interactions were also a major contribution to the structure in all DES except ChCl:malonic acid. The authors noted that the split bands observed in the spectral region for carbonyl groups in ChCl:malonic acid could be assigned to the presence of C=O groups from the HBD which were hydrogen bonded, and C=O groups from the carboxyl functional groups which were 'liberated' as a result of the -OH component forming hydrogen bonds.

Findings by Garcia and co-workers may have contributed to an explanation of the strong associations and cluster formation between the chloride anion with the choline cation/HBD in ChCl-based DES [478]. The models built for the DFT simulation in this publication were based on clusters formed between various constituents in the DES, and showed a linear relationship between the melting points of the DES and the bonding within the DES when modelled in this configuration. The publication further highlighted the link between the bulk nanostructure of the solvent and its influence on physical properties, noting the need to thoroughly understand solvent structure in order to truly be able to design task-specific DES.

The common consensus from many of the studies presented thus far has been that the structure of the solvent is dominated by interactions between the hydrogen bond donor molecules (e.g. urea, glycerol) and the chloride anion, though there have been some contradictions to this. Studies by Ferreira *et al.* [479] and Zekhenov *et al.* have suggested that other interactions are just as, if not more important in certain DES [480]. In the latter investigation, the choice of DES components appeared to influence the dominant interactions, as analysed using MD simulations. The interaction of the chloride ion with the HBD molecule were much stronger in ChCl:ethylene glycol and ChCl:glycerol DES than in the case of the ChCl:urea DES, and furthermore the authors reported that the strength of this interaction in ChCl:urea was similar to the competing choline-chloride and choline-urea interactions [480]. Comparing the same 3 DES, Stefanovic and co-workers determined that the urea component of ChCl:urea had a greater effect on the electrostatic interactions between the choline cation and chloride anion, whilst this same disruption was not caused by the HBD in ChCl:ethylene glycol. The increased size of the ethylene glycol molecule could lead to the formation of hydrogen bonds which are linear and preserve the ethylene glycol network. A similar effect was also observed for ChCl:glycerol, where the extended glycerol network largely persisted in the DES [467].

Ashworth and co-workers [15] provided a comprehensive analysis of the possible struc-

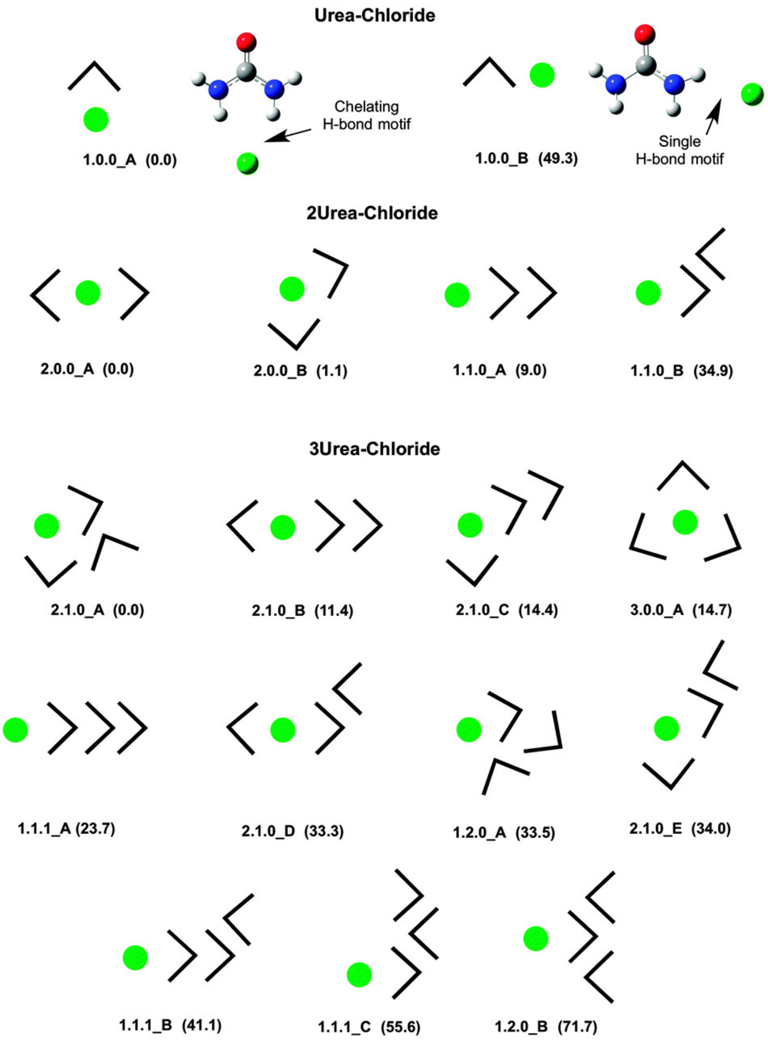

Figure 5.2: A simplified representation of the various urea-chloride clusters analysed by Ashworth and co-workers. The urea molecules (specifically, the N-C-N backbone) are represented by the black chevrons, whilst the green circles represent chloride anions. The calculated relative energies (in units of kJ mol^{-1}) are given alongside each cluster. Reproduced from Reference [15] with permission from the PCCP Owner Societies.

tures which might be formed in ChCl:urea, obtained using quantum chemical simulations, with an original aim to investigate the nature of doubly ionic hydrogen bonds, which are underinvestigated as compared to their neutral or ionic counterparts. A total of 172 potential hydrogen bonds were analysed and classified, with the conclusion that the DES contains an ‘alphabet soup’ of many types of these, including OH$\cdots$NH, OH$\cdots$Cl$^-$, NH$\cdots$C=O, amongst several others. Additionally, the strength of these bonds varies significantly between types and competition between stronger and weaker

H-bonds appears evident from the formation of a range of low energy conformers. This presented a distinct contract to molecular solvents, in which the number of hydrogen bond types is limited. The increased entropy of the system which would arise from a greater range of hydrogen bonds forming could promote the formation of the eutectic mixtures. Another conclusion drawn from this work is that the formation of the complex ion $[\mathrm{Cl(urea)_2}]^-$ might not be the most favourable, and instead the interaction with the competing species $\mathrm{urea[Ch]}^+$ could result in the formation of a charge diffuse complex between $\mathrm{urea[Cl]}^-$ and $\mathrm{urea[Ch]}^+$. These observations are in agreement with results presented further in this section [75, 481].

Given the insights, and indeed contradictions, seen from the early experimental and later the computational data, it can be argued that the use of advanced experimental techniques combined with data modelling/refinement routines can yield an even more accurate picture of DES structure. The remainder of the section will now focus on these studies before introducing the motivation behind the experimental work carried out in this chapter.

Wagle and co-workers carried out a quasielastic neutron scattering (QENS) study on the ChCl:glycerol DES, to investigate the rate of diffusion of the DES components. Of the three distinct species present, chloride was found to have the slowest diffusion, followed by glycerol, whilst choline was found to have the fastest rate over length scales up to 1 nm [481]. These observations were the opposite of those observed by D'Agostino *et al.* discussed above [473] where it was suggested that the slowest long-range diffusion was observed for choline as the largest ion in the system. The rationale proposed by Wagle *et al.* for their observations was that on shorter length scales, competing interactions of the choline and glycerol with the chloride ion formed a dynamic cage, with the glycerol forming a stronger hydrogen-bonded network with the chloride. This would in turn allow choline to have more freedom of movement throughout the DES structure, and hence faster diffusion rates.

Hammond *et al.* carried out the first dedicated experimental study using total neutron scattering combined with an iterative computational data refinement procedure to directly measure the structure of DES. In this case, the authors chose to study the ChCl:urea solvent [75]. The results from this study determined the presence of a three-dimensional nanostructure within the solvent, with strong urea-chloride and choline-chloride interactions, but weaker interactions between choline and urea. A 'cage'-like structure, centred around chloride ions with competing hydrogen bonding from the urea and choline species was proposed, with the preferential position for the chloride ion being between the ammonium and -OH regions of the choline species, with a second preferred position for the Cl^- ion at the positively charged end of the choline ion. There also exists a hydrogen-bonded network formed through interactions between urea molecules. These results have also been supported by purely computational research, such as the first-principles MD simulations carried out by Fetisov *et al.*, who suggested a similar structure with urea-chloride interactions dominating the structure [482].

The same group further investigated the structure of ChCl:malic acid using QENS and the total neutron scattering techniques described above. In this case, the self-association between the HBD molecules was less evident than the authors found for ChCl:urea, however the inherent differences in the structures of urea and malic acid, in addition to the DES composition (HBA:HBD ratio for ChCl:urea is 1:2 and 1:1 for ChCl:malic acid) might explain this [190]. Instead, it was proposed that strong interactions through hydrogen bonding of both the choline and malic acid with the chloride anion resulted in the formation of ion clusters.

Gontrani *et al.* conducted the first study combining energy dispersive X-ray diffraction with MD simulations techniques to examine the structure of the ChCl:oxalic acid DES, comparing the anhydrous and hydrated forms of the acid [483]. The results of the structural study were discussed in the context of the physiochemical properties also reported in the study, such as conductivity, viscosity and density. The high number of intermolecular interactions within the DES structure was thought to lower the crystallisation temperature, which was also reflected in the measured density values. The hypothesis proposed from conductivity and viscosity data was that in the case of hydrated oxalic acid, the waters of crystallisation remain partially ‘frozen’ within the DES structure, leading to weaker complexation between the acid/choline and chloride moeities. Qualitatively, X-ray diffraction data showed a difference in the structures of the between the dry and hydrated DES. Patterns were compared to those obtained using MD simulations, and a comparison of the partial RDFs from the dry DES showed that the oxalic acid-chloride interactions are found at shorter distances compared to the hydrated system. Additionally, the water-water interaction show a single, broad peak, which suggests that competing interactions involving other components mediate the bulk water structure. This observation that the water molecules play a large role in the DES structure is in direct contrast to the study of Hammond *et al.*, where water was not found to significantly affect the nanostructure of the ChCl:malic acid DES [190] despite there being more water in the system overall.

Gilmore *et al.* reported on the structure of DES at elevated temperatures, carrying out neutron diffraction experiments on ChCl:urea and ChCl:oxalic acid at 65 °C. Under these conditions, ChCl:urea undergoes a structural rearrangement as compared to its behaviour at room temperature [75]. In the case of ChCl:urea, the dominant interaction is that of hydrogen bonds formed between urea molecules through the N-H$\cdots$N mode (as compared to bonding between the N-H group and O at room temperature), whilst the bond between choline hydroxyl group and the chloride anion lengthens significantly from 2.1 Å to 2.8 Å, indicating a weakening of this interaction. In the ChCl:oxalic acid DES, a strong interaction between the Cl^- and the oxalic acid was observed, similar to that seen in malic acid by Hammond *et al.* [190], with little self-association between oxalic acid molecules. These observations were thought to arise from a lower number of sites capable of hydrogen bonding in the oxalic acid compared to urea (oxalic acid contains two hydroxyl groups, whilst urea has four amine hydrogens through which it may form hydrogen bonds).

In their recent work examining the structure of the ChCl:glycerol DES, Turner and Holbrey carried out neutron diffraction measurements at elevated temperatures (60 °C) and carried out subsequent modelling and refinement of the data using the Empirical Potential Structure Refinement (EPSR) technique [16]. Similar studies carried out on the structure of pure liquid glycerol have revealed that it has an extensive hydrogen bond network with intramolecular hydrogen bonding forming the dominant contributions to the liquid structure [484]. In industry and laboratory settings, glycerol is used as a cryoprotectant because this extensive network is largely unaffected by the presence of other molecules which are also capable of forming strong hydrogen bond networks, such as water or other guest molecules. It was found that this glycerol-glycerol extended network largely persists in the DES when the components are in a 1:2 molar ratio (ChCl:glycerol), and the choline cations were found to be situated in interstitial voids within the glycerol network. In the 1:1 eutectic mixture, the increased mole fraction of ChCl in the system induced a more significant structural rearrangement to the liquid network, and a shift from a structure dominated by glycerol-glycerol interactions to one where glycerol clusters exist within a wider ChCl 'ionic' environment. The ChCl:glycerol DES has a viscosity three times lower than that of pure glycerol, possibly due to this disruption of the glycerol network when ChCl is added. This explanation is in direct contrast to results previously obtained for similar DES such as ChCl:ethylene glycol [485], however the authors' findings align with those reported by Stefanovic *et al.* [467]. An study conducted by Faraone *et al.* using neutron spin-echo and dialectric spectroscopy of the ChCl:glycerol DES provided further evidence of this [486]. Controlling a physical property such as viscosity through variation of the solvent composition in this manner, especially with a thorough understanding of the origin of these changes allows for the use of a DES which is far easier to manipulate under mild conditions than glycerol, and opens the possibility for its use in those applications where glycerol is a useful but not always practical choice.

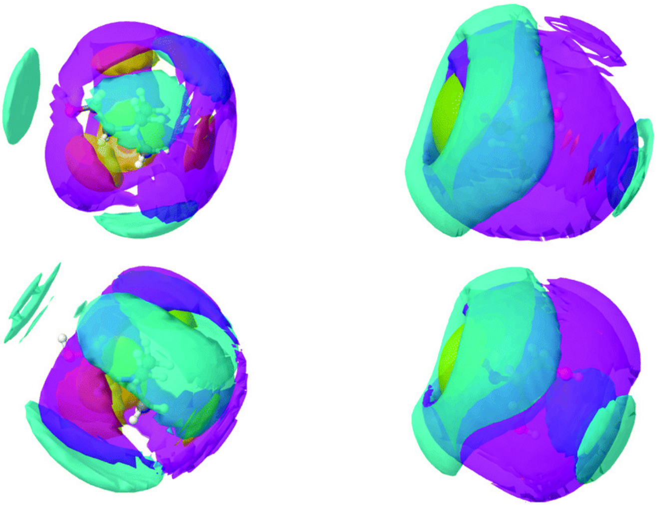

Figure 5.3: Spatial density function (SDF) plots derived from EPSR analysis of neutron diffraction data collected for ChCl:glycerol, showing the probable distributions of choline (blue), chloride (yellow) and glycerol (purple) around a central choline ion (left) or glycerol molecules (right). The top two plots are for the component ratio 1:2 and the bottom two are from the 1:1 DES. Reproduced from Reference [16] with permission from the PCCP Owner Societies.

5.2.1 Structure of DES not based on choline chloride

Research interest in DES which do not contain ChCl is growing rapidly, especially in applications where hydrophobic DES are suitable [67]. Despite this, the number of structural studies carried out on these DES is relatively low compared to those concerning ChCl-based DES, although this is likely to increase in the future.

Atkin *et al.* carried out detailed studies using neutron diffraction and EPSR analysis to investigate the liquid structure of DES formed between alkylammonium bromides and either urea or glycerol. Ternary DES formed using these components, which comprised urea and a mixture of ethyl- and butylammonium bromide, had lower eutectic temperatures than the binary mixtures. The DES were shown to have a nanostructure which was amphiphilic in nature, akin to the PILs briefly discussed in Section 4.3.2. The polar regions of this nanostructure are governed by hydrogen bonding and electrostatic interactions between components, whilst a solvophobic effect forms the apolar domain within the solvent. The size of this apolar domain can be tuned by varying the alkyl chain length of the alkylammonium bromide in the DES. The degree of polar/apolar segregation was less pronounced in the case of the DES containing urea as compared to those formed with glycerol, thought to arise from stronger interactions between the HBA and HBD molecules in the former DES as compared to the latter, where glycerol preferentially self-associates and forms extensive hydrogen bonded networks.

The segregation into polar/apolar domains was not observed for alkylamide-based DES, formed by combining various acetamide and propionamide with lithium perchlorate, though some evidence of structuring was observed using X-ray and neutron scattering techniques and MD simulations [487]. As expected, hydrogen bonding and electrostatic interactions were thought to be responsible for the structuring which was observed. It had previously been observed using MD simulations and spectroscopy techinques that varying the alkyl chain length within the alkylamide component of the DES, and the use of different lithium-based ionic species affected the microstructure within the solvent [488].

Hammond *et al.* demonstrated the formation of a series of lanthanide-based DES through complexation of various lanthanide (Ce, Pr, Nd) nitrate hydrates with urea in a molar ratio of 1:3.5 [163]. By contrast to the systems which are dominated by hydrogen bonding interactions, as seen in many ChCl-based DES, the pseudophase formed by ionic interactions in these DES governs the liquid structure, whilst the secondary pseudophase was formed through the hydrogen bonding interactions between urea and water. This unique structure gave rise to remarkable physical properties, such as low viscosities, and high surface tension and density values.

Aside from these publications, there have been a few isolated studies carried out on unusual systems, although more work would be required in order to build a proper structural description of these DES. Coutinho *et al.* briefly investigated the structure of hydrophobic deep eutectic solvents, though this was within a study which largely aimed to characterise their physiochemical properties [489]. Malik and Kashyap also investigated the hydrophobic DES based on DL-menthol using simulated SAXS patterns obtained from atomistic MD simulations [490]. The analysis of the SAXS pre-peak region suggested that the solvent structure consists of a largely apolar environment populated by DL-menthol and the nonpolar alkyl tails of the HBD molecules, with small segregated polar regions within this space.

5.2.2 Interaction of DES with water

In addition to studying dry (or 'pure') DES, a number of studies have also been carried out looking at DES/water mixtures. On a basic level, the influence of water on DES structure and properties cannot be ignored especially in the case of ChCl-based DES, where the ChCl itself is extremely hygroscopic such that many experimental samples will still contain a small residual amount of water even though careful preparation methods were used [316]. In industrial 'real-world' applications, it is likely that this will be even more pronounced. Additionally, a detailed understanding of the interaction of water molecules with DES and how this impacts their structure and properties adds yet another method by which DES composition might be tuned further to suit specific applications.

It has already been shown that water content can have a significant impact on the physiochemical properties of many DES [429, 491]. For example, water addition to a DES results in lower viscosity and may make the DES easier to handle for industrial applications. In the case of ChCl:urea, the original determined eutectic point of 12 °C [48] is now believed to be inaccurate due to a lack of control of water content in the initial studies, with the true value for the dry solvent being nearer 25 °C [56].

Ma and co-workers published a review of the effect of water on both DES and ILs, analysing six commonly studied water/solvent mixtures in addition to collating the physiochemical properties of several other systems [457]. In this work, the authors suggested that DES-water mixtures could exist in four structural 'states', which were determined by their water content. Whilst the authors did not imply that there were defined compositions at which structural transitions would occur, they proposed that the addition of small quantities of water to a neat DES would result in the water molecules being incorporated into the DES structure, with some species hydrated. At increased water contents, the structure would instead resemble a 'hydration domination' regime, where the DES components are almost completely dissociated and the equilibrium between association and hydration shifts towards hydration. Finally, at high water contents, the DES structure would be disrupted significantly, with the components being completely hydrated and behaving essentially as solutes in an aqueous solution.

Several studies which have been published which attempt to characterise the degree of structural disruption observed when water is added to a DES, though many of these disagree with respect to the water contents which result in a loss of the nanostructure within the solvent. This is not unsurprising, given that the tolerance of the DES structure to water addition is strongly dependent on the interaction of the components with water molecules. In a similar fashion to early structural inferences made from NMR data, Gutierrez *et al.* looked at interactions between the HBD molecule and anions within the DES with the addition of water [69]. Their findings suggested that at lower water contents (14 wt.%), the structure of the DES was altered, but that on addition of more water the DES structure was completely lost, as these HBD-anion interactions were no longer visible. Although the results were limited, they introduced the concept that the DES nanostructure is retained at far higher hydration levels than might otherwise be assumed, and that the addition of water to a DES containing water-soluble components does merely lead to the formation of an aqueous solution containing the component species.

Using neutron diffraction and EPSR analysis on hydrated mixtures containing the ChCl:urea DES at different water contents, a study by Hammond *et al.* showed that the majority of the DES nanostructure was retained at high water contents, up to 40 wt.% [316]. At 51.wt.% water content, the disruption of the DES structure and therefore the transition to an aqueous solution was observed. Given that this water content translates to over 80 mol.%, it is remarkable that an aqueous solution would only be formed at such high concentrations. Other experimental studies carried out using spectroscopic techniques estimated the transition point as much lower, around 15-20 wt.% [492]. Yadav and Pandey proposed similar behaviour to the results reported by Hammond *et al.*, where the excess logarithmic viscosities of water-reline mixtures were found to be negative, attributed to the water molecules being incorporated into the hydrogen-bonded DES network at several concentrations [493]. Further work by Hammond *et al.* combining neutron diffraction with quasi-elastic neutron scattering (QENS) techniques showed that the nanostructure of the ChCl:malic acid DES was mostly retained with water addition, albeit at lower water contents (up to 12 wt.%) [190]. In this system, the water molecules function as hydrogen bond donors akin to urea and are able to sit within the DES structure without causing significant disruption. Clustering between water molecules and the formation of worm-like aggregates was also suggested.

Pure computational work using MD simulations has determined values from 25 up to 41 wt.% as the point where DES-water mixtures become aqueous solutions, as reported by various authors [494, 495]. Some studies have suggested structural disruptions may occur as low at 5 wt.% [480]. Gao *et al.* modelled a regime whereby the choline and chloride ions within reline were hydrated in DES-water mixtures, with a transition point close to 20 wt.%. A recent study by Sapir and Harries [496] proposed that very low water contents caused changes in the nanostructure of the ChCl:urea DES, and further presented evidence of two competing nanostructures at lower concentrations (below 30 wt.% water), the first in which water molecules are incorporated into the DES and steadily replace urea molecules in solvating the chloride anion, and one consisting of a linear network of water-chloride aggregates. At higher water contents, a dilute aqueous solution was observed, in which both the choline and chloride ions were solvated.

The range of values estimated for the tolerance of the DES structure to water addition could be due to the use of different experimental techniques (for example, spectroscopic techniques as compared to advanced scattering experiments and data refinement), and in the case of computational work arise from the definition of parameters within the model and constraints placed upon the system. Some studies, however, also suggest that there is no 'onset' concentration of water whereupon this structural transition occurs [378, 497]. For example, in their work focusing on the ChCl:glycerol DES, Weng and Toner proposed a system by which the choline and glycerol simply became increasingly hydrated as the water content was increased, through the formation of more hydrogen bonds [497]. This is consistent with the work of Turner and Holbrey [16] discussed in the previous section, which determined that the unhydrated ChCl:glycerol DES was formed mostly of a glycerol hydrogen-bonded network, as compared to a DES such as ChCl:urea where many competing interactions with varying natures exist in the system.

As expected, the majority of the work described above focuses on the most commonly investigated DES, namely ChCl combined with urea, glycerol or ethylene glycol. Other DES, not based on ChCl have also been studied, though as with non-hydrated DES, research into this remains limited. Rumyantsev *et al.* investigated, amongst others, aqueous mixtures containing the betaine:urea DES using quantum chemical calculations and spectroscopic techniques. Their study suggested that the strong interactions of betaine with water molecules formed betaine-water complexes in the DES, resulting in the formation of segregated domains. Analysis of the supramolecular structure of several NADES-water mixtures (such as those DES formed by the combination of various sugars or carboxylic acids with ChCl, or those including amino acids) has also been carried out using ^{1}H-^{1}H nuclear Overhauser effect spectroscopy (NOESY) [491]. The results from this study suggested that the strong hydrogen bonding between the NADES components broke down at approximately 50 % water addition (by volume). By measuring the physiochemical properties of the DES, the authors showed that even the addition of a small amount of water greatly reduced viscosity and increased conductivity of the solvents, which further highlighted the effect of the interaction of water molecules with DES components and the potential for using water to tailor DES structure precisely to suit certain applications.

5.3 Determining the structure of disordered materials

The following section provides an overview of the various challenges encountered when determining the structure of a liquid, as well as an introduction into the experimental and computational methods which are commonly used in this field. Finally, the theory behind the Empirical Structural Potential Refinement (EPSR) method, which is used in this chapter, is presented.

5.3.1 The liquid state

Liquids are commonly defined as the intermediate state between a solid and a gas, and share properties with both. They have densities comparable to those of solids, but exhibit particle motion similar to a gas. Solids which are crystalline in nature have a well-defined structure with atoms in specific positions, and exhibit long-range order. Amorphous solids, such as glasses do not exhibit this order, and in theory the structures of amorphous solids and liquids are comparable. The problem arises in the time-scale of particle motion, which is much faster in liquids and makes their structure complex to define. The 'true' structure of a liquid is a combination both of particle position and dynamics, but most experiments or simulations do not accurately capture both of these types of structuring. Furthermore, whilst the idea of an ordered crystalline material is relatively easy to visualise and compare to 'real-life' examples, the structure of a liquid presents a challenge for scientists to conceptualise and describe.

The persistent opinion within the research area is that liquids exhibit some degree of order on small length scales, but are more disordered as the length scales are increased. One common description used for the structure of a liquid, which also allows for a comparison between solid, liquid and gaseous states is the use of a statistical function known as the radial distribution function (RDF). This is also known as the pair correlation function or the pair distribution function. Strictly speaking, the RDF $G(r)$ is the ensemble average of the pair correlation functions across all directions of the vector $\mathbf{r}$ [498]. In calculating this quantity, directional information is lost.

$$G(r) = \langle G(\mathbf{r}) \rangle_{\Omega} \tag{5.1}$$

Equation 5.1 is valid for isotropic, atomic liquids at distances away from boundaries, where the directional dependence of $\mathbf{r}$ may be ignored, however for anisotropic molecular liquids, $G(r) \neq G(\mathbf{r})$. $G(\mathbf{r})$ does not actually refer to the probability of atoms a and b being separated by a distance $\mathbf{r}$, but instead describes the local number density of an atom of type j. The number density, $n(\mathbf{r})$ of an atom j is described using its position, R_j by:

$$n(\mathbf{r}) = \sum_j \delta(\mathbf{r} - \mathbf{R_j}) \tag{5.2}$$

Crystalline solids with a repeating unit cell have well-defined density fluctuations over their structure, which is not the case for disordered materials, where fluctuations in the density can be lost due to the lack of long-range order within the structure. Instead, the random distribution of atoms is all that can be observed. An autocorrelation can be performed on the density distribution in order to better describe the arrangement of atoms within the liquid structure. Considering atom types i and j, this autocorrelation separates terms where $i = j$ from terms where $j \neq i$ to eventually define $G(\mathbf{r})$ in terms of correlations between atoms of the same type and those between atoms of different types. This yields an equation which is considered to be the formal definition of $G(\mathbf{r})$:

$$\begin{aligned} G(\mathbf{r}) &= \delta(r) + \frac{1}{N}\sum_{i \neq j} \delta(r + R_j + R_i) \\ &= \delta(r) + \rho G(r) \end{aligned} \tag{5.3}$$

where ρ is the average atomic number density, expressed in units of Å^3. Briefly, this describes all of the atoms at a displacement $\mathbf{r}$ from a particular atom, expressing this number as a local density averaged across all atoms in the system. Although $G(\mathbf{r})$ typically refers to the correlation between two atoms at positions $\mathbf{r_1}$ and $\mathbf{r_2}$, the correlation between three atoms can also be expressed as $g_3(\mathbf{r_1}, \mathbf{r_2}, \mathbf{r_3})$. This approach often leaves room for error, as it introduces the possibility that several $g_3(\mathbf{r_1}, \mathbf{r_2}, \mathbf{r_3})$ might be resolved to give the same $g_2(\mathbf{r_1}, \mathbf{r_2})$ function, resulting in inaccurate information about the local order within the system.

Figure 5.4 shows a series of examples of simulated 2-dimensional pair correlation functions of liquid aluminium. At a values close to $r = 0$ relative to the position of one atom, the value of the distribution function is also zero, as two atoms cannot occupy the same space, however at increasing distances we observe the ripple-like pattern which begins to emerge as the result of close-range repulsive potentials between atoms. At greater values of r, the radial distribution function eventually tends to 1 as the increasingly random distribution of atoms tends towards uniform atomic distribution within the system.

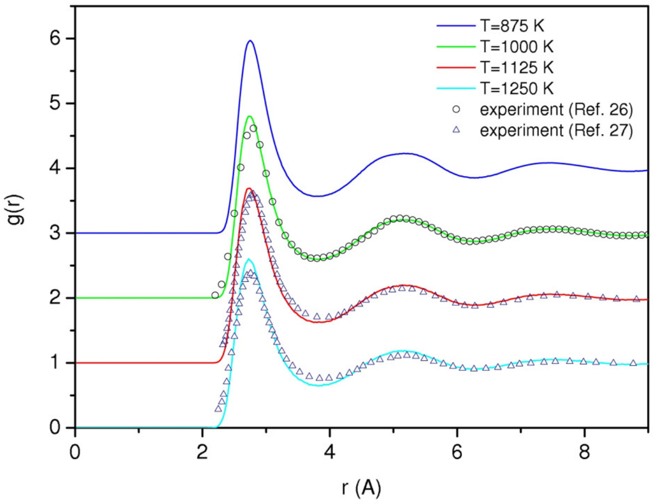

Figure 5.4: Pair correlation functions plotted for liquid aluminium at various temperatures, obtained from MD simulations. Reproduced from Reference [17] under a Creative Commons Attribution licence. Note that the image also contains experimental data added by the authors of the study, which was obtained from [18] and [19].

So far, the description provided applies to atomic systems, however all of the experiments carried out in this project concern samples which are molecular in nature. In such systems, it is preferable to examine a series of partial pair correlation functions, calculated between different types of atoms in the system. The pair correlation function then becomes the sum of all the partial pair (site-site) correlation functions within the system:

$$G(\mathbf{r}) = \sum_{i} c_i \delta(\mathbf{r}) + \rho \sum_{i,j \geq i} (2 - \delta_{ij} c_i c_j g_{ij}(\mathbf{r})) \tag{5.4}$$

where ρ_i would denote the number density of atom type i, $c_i = \frac{\rho_i}{\rho}$, and δ_{ij} is the Kronecker delta, which in this case is included to avoid pairs of atoms of the same type being counted twice.

The coordination number, N$_{ij}$ is defined as the number of atoms which coordinate a central atom or point of interest (e.g. the calculated centre of mass of a molecule) relative to a particular distance range (between r_{max} and r_{min}). As such, this value can be calculated by the integrating the partial RDF over all directions of $\mathbf{r}$ from the onset of the first peak until its first minimum, such that:

$$N_{ij} = 4\pi \rho c_j \int_{r_{min}}^{r_{max}} r^2 g_{ij}(r) dr \tag{5.5}$$

5.3.2 Techniques for measuring liquid structure

As might be expected, many of the experimental and computational techniques which are used to study liquid structure have been used to investigate DES, and as such are mentioned in the literature review (Section 5.2). This section does not aim to provide a comprehensive theoretical background to any of these techniques, and instead a brief summary of the various approaches is provided.

Experimental methods have largely been separated into three categories; observation of certain physical properties, spectroscopic techniques, and scattering analysis. In the first instance, conclusions on the bonding present within DES have been studied by the measurement of physical properties such as density and viscosity in DES with different component ratios and at various temperatures [422], or through the calculation of quantities such as excess molar volumes [499]. Interactions within a sample may be examined using various forms of spectroscopy, including NMR, FTIR and fluorescence. Indeed, the earliest explorations of DES structure which formed the basis of the complex ion model involved inferences made from detailed spectroscopic measurements about the molecular-scale interactions present within the system [48, 473]. Diffraction/scattering experiments also probe the interaction of radiation with the atoms in a sample, using the relation between the angles of the incident and scattered radiation to determine the positions of atoms within the structure. The theory behind X-ray and neutron scattering has already been discussed in Chapters 2 and 4, and the diffraction techniques relevant to this Chapter will be summarised in further sections.

When referring to computational modelling in this context, it refers to constructing a purely computational representation of a liquid/disordered material, in which a force field may be constructed through the combination of the interactions potentials between various components in the system. The calculation of the interaction potentials varies according to the type of simulation. In the case of classical simulations, empirical force fields are used, whereas in *ab-initio* simulations, the force field is determined by quantum mechanical calculations using fundamental principles. For complex systems, it is possible to use coarse-graining in order to simplify the system and obviate the need to assign empirical potentials individually to every atom, however increasing computational capabilities has made it possible for even complex systems to be analysed using individual potentials, which allows for all atomic interactions to be investigated.

In a Monte-Carlo simulation, which is relevant to the structural refinement technique used in this project, certain moves are attempted to alter the system, such as a translation or molecular rotation. Moves are accepted or rejected depending on whether or not they result in a lowering of the potential energy of the system [500]. This method does not yield information about the dynamics of the system. Conversely, molecular dynamics (MD) simulations determine the time-dependant movement of the particles/components within a system through obtaining numerical solutions to Newton's laws of motion [501]. The former method has been used to study properties such as the vapour pressures and vapour phase compositions of DES [502] and more pertinently plays a crucial role in EPSR analysis of diffraction data, whilst the latter remains the most popular technique in purely computational structural studies on these systems. Examples of empirical force-fields which have been used include the AMBER [476], the OPLS-AA [475] and the MMFF force-fields [494].

Analysing such complex systems as DES computationally can have certain advantages, such as giving researchers the ability to investigate the system under conditions which are difficult to achieve experimentally, or (as is particularly relevant for DES) access regions within a phase diagram which cannot be easily replicated experimentally. However, it is important to note that the accuracy of the simulation and any data about the properties of the system which are extracted from it are only as good as the potentials which are assigned to the atoms in the system. This necessitates an accurate method of determining the interaction potentials which make up the force field, something which has been shown in the literature to not be a trivial task even for simple systems such as water [503]. Whilst a discussion of most of these methods is outside the scope of this thesis, the following section introduces total neutron scattering and EPSR, which was the data refinement process used in this project.

5.3.3 Total neutron scattering

Chapter 2 has already provided an introduction into scattering theory, including the generation of high energy X-rays and neutrons for scattering experiments. Chapter 4 expanded on this, providing the background to small-angle neutron scattering (SANS) and presented results from experiments using this technique. However, all of the techniques discussed heretofore have been limited to only examining a small portion of the total Q-range in order to analyse either small-scale or large-scale structures.

In Section 2.1, the case was made for the choice of neutrons over X-rays to examine structure and self-assembly in ternary DES. Whilst SANS was an appropriate technique for the experiments conducted in Chapter 4, for experiments to elucidate the structure of the ternary DES, it is important to study interactions such as hydrogen bonding, which oscillates around a length scale of approximately 1.8 Å. This value is below the minimum length scales achievable by the SANS instruments at neutron facilities such as ISIS Neutron and Muon Source. Additionally, the interactions or structural features of interest within the system may be present on several different length scales. In order to facilitate this, a technique called total (neutron) scattering has become increasingly popular for probing such systems, as it involves designing instruments to operate over a wide Q-range. It is important to note that, particularly in the case of this technique, 'neutron scattering' and 'neutron diffraction' are often used interchangeably in the literature. The two are not distinctly different processes, but neutron diffraction describes coherent, elastic scattering which is typically measured during these experiments.

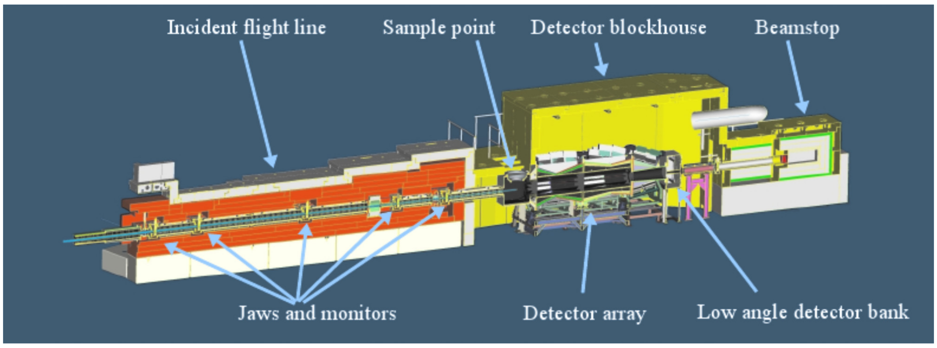

Figure 5.5: A diagram of the NIMROD total neutron scattering instrument at ISIS Neutron and Muon Source (UK), highlighting its main components. Reproduced from Reference [20] with permission from the American Institute of Physics.

Figure 5.5 shows a diagram of the layout of the NIMROD instrument at ISIS Neutron and Muon Source, including the path of the incident beam, sample position, and detector blockhouse [20]. On an instrument such as NIMROD, capable of accessing a wide Q-range, such measurements are made possible by the use of modern instrument design, detector arrays, and data acquisition electronics. Data are therefore collected simultaneously in the small-angle range and also at high-Q values more typical of neutron diffraction experiments [20]. The underlying principles behind the experiment are the same as the SANS measurements carried out in Chapter 4, however even for systems such as colloidal mixtures which would typically be associated with small-angle scattering techniques, the collection of data over the wider Q-range allows for the observation of structural features such as intermolecular interactions which would otherwise not be measured due to instrumental limitations [504].

As described in Section 2.1, the quantity measured during a scattering experiment is the the differential cross-section, $\frac{d\sigma}{d\Omega}$ of neutrons scattered through the solid angle $d\Omega$. The total scattering cross-section can further be divided into the 'self' and 'distinct' cross-sections. The former consists of a background signal in the scattering pattern, whilst the latter quantity contains the description of the structure factor of the system.

The differential scattering cross-section is normalised by considering the number of atoms in the system and calibrated using a standard. For solid samples, a static approximation can sometimes be used whereby $\frac{d\sigma}{d\Omega}$ is simply considered to be equal to the elastic differential scattering cross-section as the atomic structure is considered as fixed. In the case of liquid samples, as in this project, the data must be corrected to account for attenuation, multiple scattering, inelastic scattering (arising from light elements such as hydrogen) and the instrument background to yield the total structure factor, $F(Q)$, of the system [498]:

$$F(Q) = \sum_i c_i b_i^2 + \sum_{j \geq i} (2 - \delta_{ij}) c_i c_j b_i b_j S_{ij}(Q) - 1 \tag{5.6}$$

where $S_{ij}(Q)$ denotes the partial structure factors in the system, c is the concentration of the relevant species in the system, and b is the scattering length of the of i and j. The partial structure factors are derived from the partial pair distribution functions described in Section 5.3.1 through a Fourier transform:

$$S_{ij}(Q) = 1 + 4\pi\rho \int_0^\infty (g_{ij}(r) - 1) \frac{\sin Qr}{Qr} dr \tag{5.7}$$

where again, ρ is the atomic number density of the system, r is the radial distance and g_{ij} the radial distribution function.

In the case of SANS experiments (Chapter 4), the best signal is observed when maximum contrast is achieved between components in the system, and so common samples include a deuterated scatterer in a protiated dispersant, and vice versa. This is also the case for total scattering experiments, achieving this contrast becomes markedly more complicated, as the length scales involved (higher Q-values than SANS experiments), mean that H/D substitutions also affect correlations between atoms and the structure factors cannot be considered to be identical. As with small-angle scattering experiments, the selective deuteration of certain components is the most common isotopic substitution used in sample preparation, though other substitutions have been used where the relevant samples could be synthesised [505].

Theoretically, it would be possible to use this substitution method to highlight every site-site interaction and therefore extract all the partial structure factors within the system. In reality, however, it is not always possible to achieve complete deuteration of a system component, and there are many atoms such as carbon and oxygen, which are abundant in many liquids, for which isotopic substitutes cannot be easily be prepared. Isotopically substituted samples, or ‘contrasts’ may instead be carefully chosen in order to maximise the contributions to the scattering intensity of interactions of interest. This experimental data can then be combined with various constraints such as potentials and sample density in order to refine against a computational model, hence obtaining the best description possible of the structure of the system. In the next section, the method for achieving this which was used in this project is discussed.

5.3.4 Empirical Potential Structure Refinement (EPSR)

This section aims to summarise the key concepts and processes involved in the Empirical Structural Potential Refinement (EPSR) modelling method, in order to provide a foundation for the remainder of the chapter. A fully detailed account of EPSR is however beyond the scope of this thesis.

EPSR is a method designed primarily by Alan Soper, with contributions from the Disordered Materials Group at ISIS, to analyse data from total scattering experiments [506]. EPSR has its roots in the Reverse Monte Carlo (RMC) method, and whilst both methods introduce experimental data against which the model is refined, some key differences remain. In RMC, hard-sphere potentials are used, and moves are either accepted or rejected based on whether a particular move has improved the fit of the model to the data. EPSR however uses a ”reference potential” which is derived from Lennard-Jones potentials defined through the molecular components used to create the simulation box [507].

Initially, atomic or molecular components are created and combined to generate a simulation box, and the physiochemical properties of the system under study, such as the density and chemical composition are used to constrain the data further. A classical Monte Carlo simulation then produces a theoretical model of the system and calculates the structure factors, which are compared and iteratively refined to the experimental data until the closest fit is achieved. Further analysis routines may then be performed on the model in order to extract key parameters, such as coordination numbers, which provide information about the bonding and interactions within the system.

In EPSR analysis, the total potential energy of the system is modelled as the sum of the reference and empirical potentials:

$$U_{tot} = U_{ref} + U_{emp} \tag{5.8}$$

The reference potential of the system, which is first calculated and refined before the experimental data is introduced to the model, may be defined as the sum of the intra- and intermolecular potentials:

$$U_{ref} = U_{intra} + U_{inter} \tag{5.9}$$

The intramolecular potential, U_{intra}, between two particles i and j of type α and β, as a function of the radial distance r_{ij} may be defined as [508]:

$$U_{intra}(r_{ij}) = C \sum_{i} \sum_{\alpha\beta \neq \alpha} \frac{(r_{\alpha_i\beta_i - d_{\alpha\beta}})^2}{2w_{\alpha\beta}^2} \tag{5.10}$$

where C is a constant, $r_{\alpha_i\beta_i}$ is the separation between the two atoms and $d_{\alpha\beta}$ is their average separation. The expression $w_{\alpha\beta}^2$ is a broadening function derived from the average separation and the reduced mass of the atom pair.

The intermolecular potential, derived from a combination of the Lennard-Jones 12-6 potentials and Coulomb terms, for these same particles i and j is defined as:

$$U_{inter}(r_{ij}) = 4\epsilon_{\alpha\beta} \left[\left(\frac{\sigma_{\alpha\beta}}{r_{ij}} \right)^{12} - \left(\frac{\sigma_{\alpha\beta}}{r_{ij}} \right)^{6} \right] + \frac{q_\alpha q_\beta}{4\pi\epsilon_0 r_{ij}} \tag{5.11}$$

where $\sigma_{\alpha\beta}$ is the distance between two atoms at which the potential is 0, $\epsilon_{\alpha\beta}$ is the distance at which the potential is at a minimum value between the two atoms, q_α and q_β are the charges on atoms α and β, respectively, and ϵ_0 is the permittivity of free space [508].

Lorentz-Berthelot mixing rules are used to combine the Lennard-Jones well depth, $\epsilon_{\alpha\beta}$ and range parameters $\sigma_{\alpha\beta}$. EPSR also imposes periodic boundary conditions upon the simulation, where a particle will re-enter the simulation box on the opposite side if it leaves. As mentioned above, the simulation proceeds via the standard Monte Carlo process to bring the simulation to equilibrium without the data being introduced [508].

Once the system has reached equilibrium and the simulated structure factors have been calculated, the model has been refined as much as possible using the reference potential alone. The empirical potential, U_{emp}, must now be introduced to account for the difference between structure factors from the simulated and experimental data. This potential is introduced via a series of power law exponential functions in order to ensure that it accounts only for the residuals between the modelled and experimentally measured data, without compensating for artefacts within the diffraction data. These power exponential (Poisson) functions are represented by:

$$U_{emp}(r) = kT \sum_{i} C_k p_{n_k}(r, \sigma_r) \tag{5.12}$$

where k is an integer between 0 and i, T is the temperature of the system, C_k are constants which may be estimated directly from the diffraction data due to the fact that the derivation of p_{n_k} has a 3-D Fourier transform in Q-space [509]. The following series is therefore fitted to the residuals between the simulated and experimentally measured data:

$$U_{emp}(Q) = \sum_{i} C_k p_{n_i}(Q, \sigma_Q) \tag{5.13}$$

Moves are accepted based on the change in the potential energy, (U), of the system, with a probability (based on the Boltzmann factor) of:

$$exp\left[\left\{\Delta U_{intra} + \frac{1}{k_B T}(\Delta U_{ref} + \Delta U_{emp})\right\}\right] \tag{5.14}$$

Eventually, the simulation reaches a point where the best fit has been obtained and the model has equilibrated to $U_{ref} + U_{emp}$ and the empirical potential will not vary further, which makes it possible to calculate radial distribution functions (RDFs) from the ensemble-averaged data. At this point, the software provides several auxiliary analysis routines which may be used to extract several pieces of information about the physical structure of the system, including coordination numbers, molecular cluster sizes, and angles between various atoms in the system. These analyses are further discussed later in the chapter.

5.4 Methods

As mentioned previously, those methods which are common to several chapters are detailed in Section 2.3. In this section, methods specific to the neutron diffraction experiments carried out on the DES are detailed.

5.4.1 Materials

Protiated components of the ChCl:urea:glycerol DES were purchased from Merck as described in Section 2.3. Iron(III) chloride, (anhydrous, $FeCl_3$, $\geq$99.99 %) was also purchased from Merck. Deuterated forms of each DES component were required in order to prepare the various H/D contrasts required for the neutron diffraction experiments. Choline chloride-d9 (d-ChCl, 99% atom, 99% D), urea-d4 (d-U, 99% atom, 98% D) and glycerol-d8 (d-Gly, 99% atom, 99% D) were purchased from Cambridge Isotope Laboratories. For simplicity, this chapter refers to a 'fully deuterated contrast' (D:D:D) as being the DES d-ChCl:d-U:d-Gly, though the d-ChCl component actually refers to the partially deuterated compound $(CD_3)_3NC_2H_4OHCl$.

5.4.2 Preparation of DES samples for neutron diffraction experiments

Choline chloride:urea:glycerol DES were prepared according to the method detailed in Section 2.3.1 in component ratios of 1:1.5:0.5, 1:1:1 and 1:0.5:1.5. Isotopically substituted DES were prepared in several contrasts, as summarised in Table 5.1 to make a total of 21 samples of pure DES for the initial diffraction experiments. For these measurements care must be taken over the preparation of the isotopic contrasts, as a knowledge of the exact composition of each sample is necessary for accurate data reduction. The samples containing $FeCl_3$ were prepared following this first experiment and included the same contrasts, so these are not listed separately here.

Table 5.1: A list of DES samples prepared using a mixture of protiated and deuterated components for neutron diffraction experiments. The 'component ratio' refers to the ratio of ChCl:urea:glycerol in the DES. 'HD' for any component listed in the table below denotes a 50:50 mixture of the relevant protiated and deuterated components.

Component ratio	Contrasts
1:1.5:0.5	D:D:D, HD:HD:HD, H:H:H, HD:D:D, H:D:D, D:HD:D, D:H:D
1:1:1	D:D:D, HD:HD:HD, H:H:H, HD:D:D, H:D:D, D:HD:D, D:H:D, D:D:HD, D:D:H
1:0.5:1.5	D:D:D, HD:HD:HD, H:H:H, HD:D:D, H:D:D

Following the first experiment which involved only the pure DES, water was added to the samples in order to carry out neutron diffraction experiments on the hydrated DES. These measurements are not part of the work in this project and will not be analysed here. Following this, the hydrated samples of the 1:1:1 DES were recovered from the cans, and the water removed by freeze-drying of the samples for a minimum of

48 h. As glycerol is used extensively as a cryoprotectant, the recovered DES samples, especially those with a higher content of glycerol, were frozen at -80 °C prior to being loaded into the freeze drier. Even with the use of a low temperature freezer, the DES did not remain in the solid state for almost all of the lyophilisation process. In order to assess whether successful removal of water from the system had occurred, several samples were selected for analysis using Karl-Fischer titration, which showed a residual water content in the DES of below 2 wt.% which was deemed sufficient. In addition to the DES, a glycerol/water mixture was also lyophilised under the same conditions to determine whether any glycerol would evaporate under vacuum conditions, but by a comparison of both the mass and the water content (again by Karl-Fischer titration) it was determined that only the water had been lost. Following these two measurements, the samples of dried DES were deemed suitable for use in the next stage of sample preparation.

For the second experiment which is discussed in this chapter, the effect on the structure Fe^{3+} ions in the 1:1:1 DES was investigated. Fe^{3+} was introduced to the system via the addition of anhydrous iron(III) chloride, $FeCl_3$, in a concentration of 0.25 mol kg^{-1} relative to the molar amount of ChCl in the DES. $FeCl_3$ was dissolved, with stirring, into each of the freeze-dried DES samples until clear, yellow-coloured solutions were formed.

5.4.3 Neutron diffraction experiments

Samples containing pure DES were measured on the NIMROD instrument, located within Target Station 2 at ISIS Pulsed Neutron and Muon Source, UK. NIMROD is a total scattering instrument with an operational Q-range of 0.02 - 50 Å^{-1}, allowing access of length scales up to 300 Å. Samples of DES with added $FeCl_3$ were measured on SANDALS, located within Target Station 1 of the same facility. SANDALS is capable of accessing a Q-range of 0.1 - 50 Å^{-1}. The instrument is optimised for the study of light elements due to the minimisation of inelastic scattering effects and is ideal for structural studies on disordered liquids. The use of a single analysis routine for the entire Q-range allows for collection of small-angle and wide-angle data and allows for simultaneous analysis of interatomic and mesoscale interactions within a system.

For both sets of experiments, approximately 2 g of sample was transferred (with gentle heating to 40 °C, where required to overcome the viscosity of the DES) into flat-plate, null-scattering titanium-zirconium ($Ti_{0.68}Zr_{0.32}$) containers which give a sample thickness also of 1 mm. The filled cans were sealed tightly and vacuum tested to confirm that no leakage from the container would occur during measurements.The filled TiZr cans were then loaded onto the automatic sample changer and measured over the available Q-range of 0.02 - 50 Å^{-1} (NIMROD) or 0.1 - 50 Å^{-1} (SANDALS). Samples on NIMROD were measured for an approximate counting time of 2 h per sample, whilst samples on SANDALS were measured for approximately 6 h each, with some variation in counting time according to the isotopic composition of the sample. A single measurement temperature of 30 °C was chosen for all experiments, maintained by a Julabo circulating heater. Additional measurements were required to aid in data processing and instrument calibration. The consisted of the empty instrument, empty sample cells and a 3mm thick vanadium standard measured under the same conditions as the samples.

5.4.4 Data processing

After collection, the raw data must be processed in such a way that the structure factor, $F(Q)$ and partial structure factors, $S_{\alpha\beta}(Q)$ are calculated. Processing of the experimental data is conducted using the GudrunN software, which is based on the widely used ATLAS software package designed to correct raw data from total neutron scattering experiments [498]. Data must be corrected such that unwanted contributions to the signal from the empty TiZr cans and inelastic scattering can be removed and the data normalised.

The datasets are first processed to remove the effects of faulty detectors using a *'Purge'* routine. Using further routines within the GudrunN software, data are corrected for the sample background, attenuation and multiple scattering, before normalisation using the vanadium standard to give the data in units of barns atom^{-1} sr^{-1}. An automatically calculated, iterative correction is then made for the inelastic scattering which arises from light elements in the system (i.e. hydrogen). The final outputs are datasets containing merged differential scattering cross-sections consistent with the isotopic composition of each sample, which are suitable for analysis using EPSR [509].

5.4.5 Data modelling using EPSR

Separate simulations were set up in order to model the datasets; three for the pure DES and one for the DES in the 1:1:1 ratio with added $FeCl_3$. For each simulation, molecules were first constructed using the software *Jmol* to impose physical constraints on the system by defining interatomic distances (bond lengths and bond angles), with distinct (uniquely labelled) atomic components for each molecule. Figure 5.6 shows these molecules with their atom number and type labels. Table B.2 in the Appendix gives the assigned bond lengths within the system.

Whilst the bond lengths and bond angles were assigned by the software as part of the process of generating the molecular structures, it was necessary to assign further parameters of atomic mass, charge and Lennard-Jones values (σ and ϵ) to each defined atom type in the system. Parameters used for choline and chloride were derived from previous work on the ChCl:urea DES [75], parameters for urea were derived from those presented by Rousseau *et al.* for urea in its crystal phase [510], whilst parameters for glycerol were derived from those previously assigned by Towey *et al.* in their analysis of the liquid structure of glycerol [484]. In the case of the analysis of the samples containing $FeCl_3$, the parameters for Fe were taken from the work of Hammond et al [116], originally derived through an iterative refinement of literature values. A full account of these parameters is given in Appendix B. Additionally, in order to better model the rotational freedom of the molecules, the dihedral angles assigned by the program when constructing the models were replaced with rotational axes between carbon atoms along the backbone and other atoms.

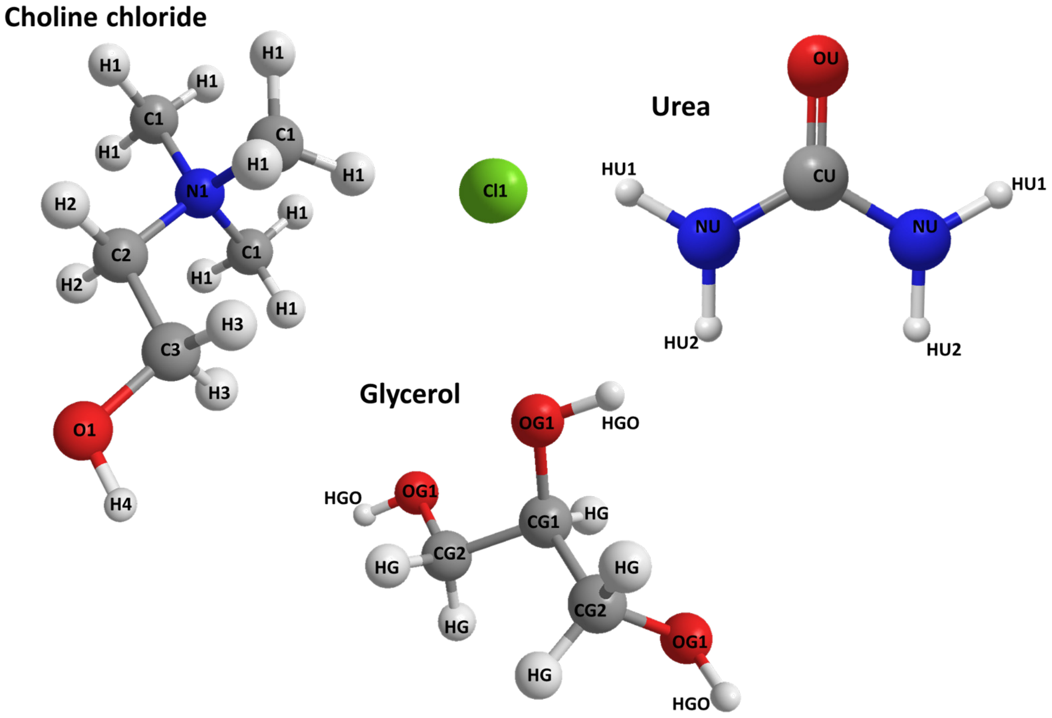

Figure 5.6: Molecules used to create the simulation box within the EPSR software, labelled with the atom types assigned to each environment.

Next, it was necessary to combine these molecules to create a simulation box to model each dataset. The exact number of molecules of each DES component included in the box vary as the ratio of DES components vary across the datasets, but each simulation contained 300 molecules of ChCl, with an average box side length of approximately 49 Å. For the simulation which included $FeCl_3$, the number of Fe^{3+} and Cl^- ions was calculated such that the correct molar ratio of 0.25 mol kg^{-1} was maintained relative to the amount of ChCl in the simulation box. The side length of the simulation box therefore allows for the resolution of structures up to approximately half this dimension, in this case 24.5 Å. The densities of the DES were measured at 30 °C in units of g cm^{-3}, which was converted to an atomic number density in units of atoms $Å^{-3}$ by the software through consideration of the system constituents. Full details of the composition of each simulation box, experimental density and box size are given in Tables 5.2 and 5.3.

Table 5.2: Details of the composition of each simulation box, given as the number of molecules of each DES component included.

DES	Ch^+	Cl^-	Urea	Gly	Fe^{3+}	Cl^- ($FeCl_3$)
1:1.5:0.5	300	300	450	150	0	0
1:1:1	300	300	300	300	0	0
1:0.5:1.5	300	300	150	450	0	0
1:1:1 + Fe	300	300	300	300	43	129

Table 5.3: Total number of atoms, box size and box densities used in each EPSR simulation.

DES	Total atoms	Box size (Å)	Box density (atoms $Å^{-3}$)
1:1.5:0.5	12300	48.5962	0.107176
1:1:1	13200	49.5353	0.1086
1:0.5:1.5	14100	50.5001	0.109842
1:1:1 + Fe	13372	50.0749	0.106497

A disordered starting configuration for the model is achieved next by placing the molecules within the simulation box in randomised positions. Initially, the experimental data was not introduced into the model. Next, the input files for each EPSR simulation were set up and in each case the empirical potentials were set to 0. In each case, the simulation box was expanded to 20 times its size to minimise molecular overlap and allowed to decline in size gradually (by 10% per iteration) until the experimentally determined density was reached. The simulations were then run for several thousand iterations until the energy of the system plateaued, at which point they had equilibrated as much as possible without refining against the experimental data. Next, the neutron diffraction data, against which simulation could refine, were introduced into the model. For each data file which was included in the simulation, a scattering weights file was then made which reflects the isotopic composition of each sample. Alongside this, it was necessary to introduce the empirical potential (EP) into the simulation.

Attempts were made to determine the best value of this for each simulation using two different methods. Firstly, a range of values was specified and the simulation was run with the potential value increasing incrementally, and secondly the value of the EP was varied manually, the simulation allowed to run and the effect on the quality of fit examined each time. Ultimately, the quality of fit did not vary much with different values of the EP, and was instead oscillating around values $\leqslant$0.01 (this is discussed further in the following section). Nevertheless, a value of 10 was found to give some improvement to the fits and was therefore chosen for the refinement.

In each case, the simulations were accumulated for at least 10000 iterations. Each refinement cycle within EPSR consists of five Monte Carlo cycles and the subsequent recalculation of the EP. The accumulated statistics were then used to extract structural information from the model, including molecular-centred, partial radial distribution functions, and coordination numbers.

5.5 Results - EPSR analysis of pure DES

5.5.1 Fits to the data

The experimental diffraction patterns, together with the simulated patterns obtained through refinement of the EPSR model for each simulation are shown as a function of Q space and real space (Figure 5.7). For every simulation, relatively good agreement was seen in the peak positions of the modelled data as compared to the experimental diffraction patterns, which suggested that the parameters and constraints imposed on the molecular components and simulation box reflected the experimental system well. However, a few discrepancies can still clearly be observed. In some contrasts, the simulated data has more peaks than the experimental pattern, which suggests that the model has assumed the system has greater degrees of freedom than is reflected by the experimental data. As some restriction in the freedom of the molecules in the simulation box has already been imposed by replacing the dihedral angles of each molecule with select rotational axes, it would be unrealistic to constrain the molecules further in order to produce a better fit. Furthermore, the majority of these inconsistencies occur at low values of Q, below 2 Å^{-1}, where the inelastic scattering of hydrogen is known to affect the data. As fully deuterated ChCl cannot be obtained for use in the samples, it is always possible in refinement of similar data that inaccuracies can arise in the subtraction of this inelastic scattering during the data reduction process. This has previously been well documented in the literature, and is a known challenge when analysing neutron diffraction data [511].

The peak intensities of the simulated diffraction patterns when plotted both in Q-space and r-space is slightly higher than the peak intensities in the experimental data. This often more pronounced for those contrasts which have a mix of protiated and deuterated components in the DES. This observation could suggest that there is more hydrogen in the system in some of these samples than expected, and as such the sample composition used during the data reduction process (using GudrunN) is not completely accurate. This could arise from inconsistencies in measuring the components when preparing the DES samples, or perhaps even from the presence of small quantities of water absorbed by the sample during preparation, storage, or transfer into TiZr containers prior to measurement. In order to attempt a correction for this deviation, it would be possible to adjust the raw data by using a tweak factor when reducing the data, however as it is not possible to determine the exact source of the inconsistencies, and as this correction would have little effect on the structural information extracted from the simulations, it was decided that the original data reduction routine should be followed.

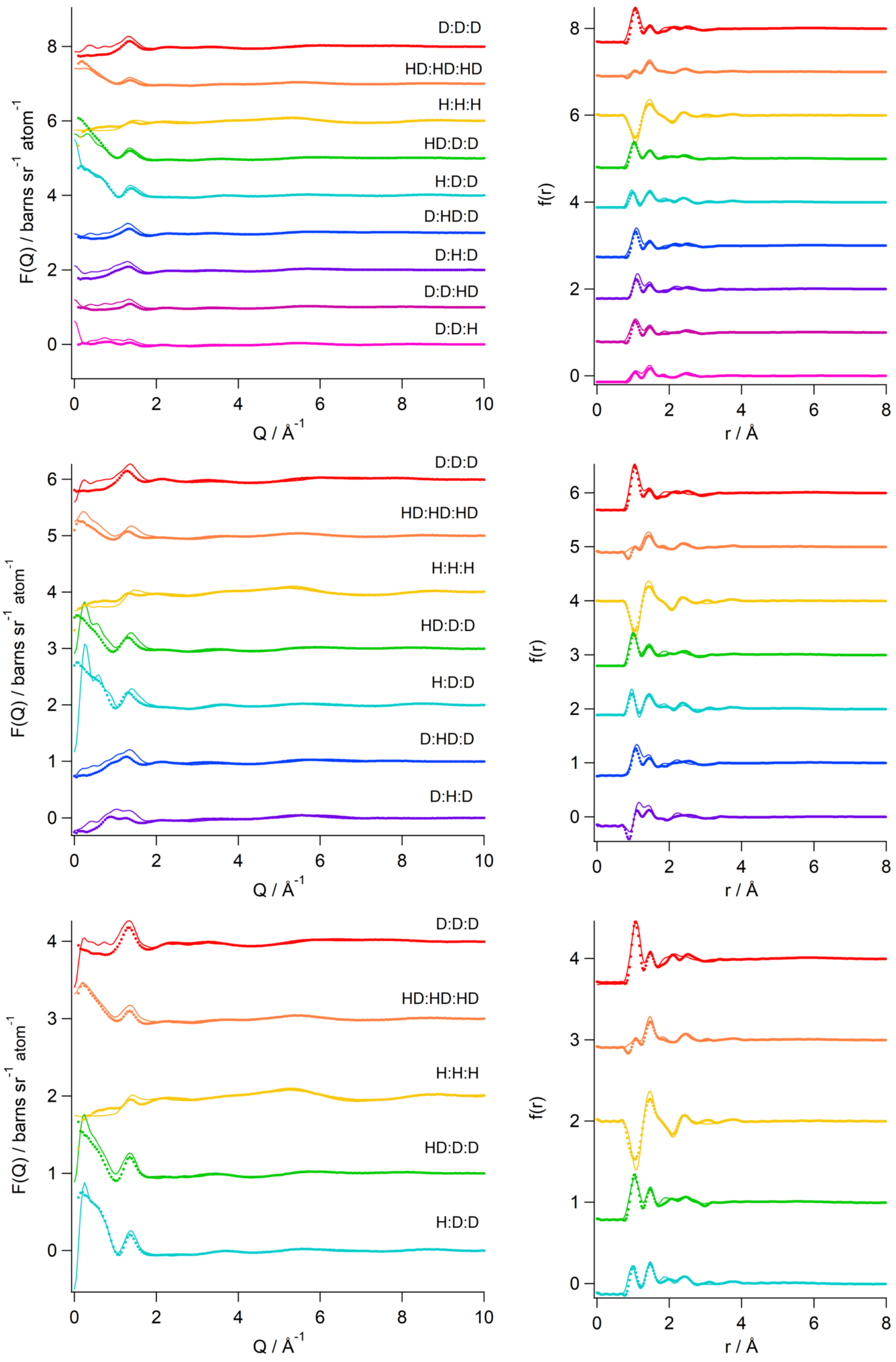

Figure 5.7: Best fits obtained using EPSR (solid lines) to the total neutron scattering profiles (coloured markers) from multiple isotopic contrasts of ChCl:urea:glycerol = 1:1:1 (top), 1:1.5:0.5 (middle) and 1:0.5:1.5 (bottom). The data and fits are plotted as a function of Q (left) and r (right) space.

An extra indication of the quality of the fit is obtained by looking at the R-factor which is calculated as part of the EPSR refinement, a lower value of which indicates a better fit. For these simulations, the mean R-factors over at least 10000 accumulated iterations for each simulation are summarised in Table 5.4. All of them have relatively low values, comparable to or below those obtained when analysing neutron diffraction data from other DES [75], which indicates that despite the discrepancies described above, the refined models have achieved a good fit to the data and can be assumed to represent the structure of the DES as accurately as possible whilst retaining realistic parameters.

Table 5.4: A summary of the values of the R-factors determined when the best fits to the data for each simulation were achieved, which reflect the quality of fit of each model.

DES	R-factor
1:1.5:0.5	0.0045
1:1:1	0.006
1:0.5:1.5	0.0038
1:1:1 + Fe	0.0055

A further point can be noted when discussing the methods of fitting data from experiments such as small-angle neutron scattering (SANS) as compared to total neutron scattering. In SANS experiments, data is collected over a narrow Q-range, whilst total neutron scattering instruments operate over a much wider range of values. This creates a challenge for any modelling of total scattering data due to the number of interactions and length scales which must be accounted for. Furthermore, a typical model-based analysis of SANS data, as presented in Chapter 4, involves altering the parameters of a structural model until it produces the best fit to the experimental data, which is an entirely different method compared to EPSR and therefore fits may visually appear to be more accurate. As such, in modelling the structure of a whole system, some allowances must be made for the challenges of accurately reflecting the experimental data. The parameters extracted from the refined model, together with the inferences about the DES structure and how it is affected by component ratio and the addition of Fe^{3+} made from these are now discussed in the following sections.

5.5.2 Molecular-centred radial distribution functions

Although centres of mass for each molecule in a system may be calculated using spherical harmonics, and routines for performing this exist within the EPSR modelling software, for many molecules this is not strictly required. A good approximation can be obtained by choosing an atom within the molecule to act as the molecular centre. For the three molecules in this system, the atoms chosen were N1 (ChCl), CU (urea) and CG1 (glycerol), as can be seen in Figure 5.6, which shows the molecular structures and atom labels used in data analysis. Long-range structural order was not observed beyond interatomic distances of 16 Å, which is evidenced by the RDFs all converging close to this value. Consequently, the data presented in Figures 5.8, 5.9 and 5.10 have been truncated accordingly.

Whilst studies will typically display all molecular-centred RDFs on the same graph in order to allow for a direct visual comparison, the number of components in the DES in this project results in a complex graph where individual correlations cannot be easily examined due to the number of overlaps with other traces. For clarity, in this section the RDFs are presented relative to interactions involving each of choline, urea and glycerol, which necessitates some repetition of traces between the figures, but allows the reader to better follow the data overall (Figures 5.8, 5.9 and 5.10). Chloride-chloride interactions are further included within the plot for choline interactions. For clarity and to allow direct comparison between DES ratios, Table 5.5 presents the values of mean radii determined from the plots of the molecular-centred RDFs, whilst Table 5.6 presents the calculated coordination numbers derived from these same plots.

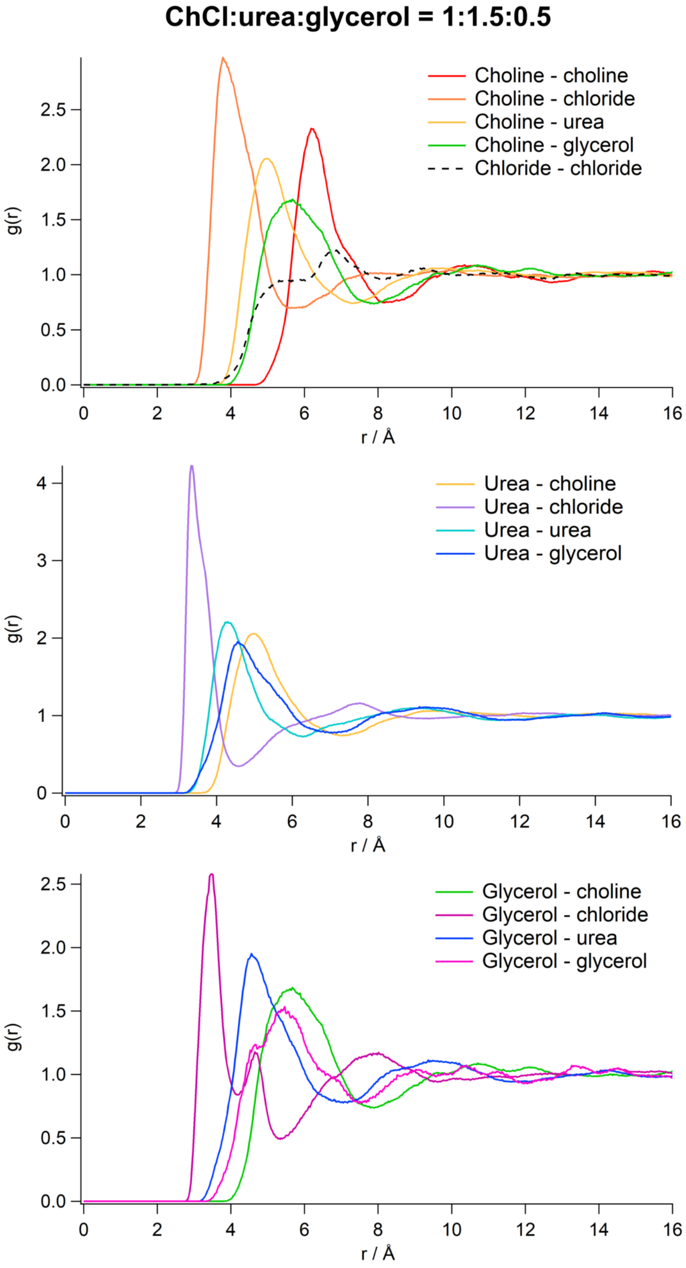

Figure 5.8: Molecular centred radial distribution functions (RDFs) between the various constituents of the DES with component ratio of 1:1.5:0.5. The plots correspond to interactions centred on each of cholinium, urea and glycerol. Note that the chloride-chloride RDF is included in the plot for choline interactions. Molecular centres in this case were approximated as the N1 atom of choline, CU atom of urea and CG1 atom of glycerol.

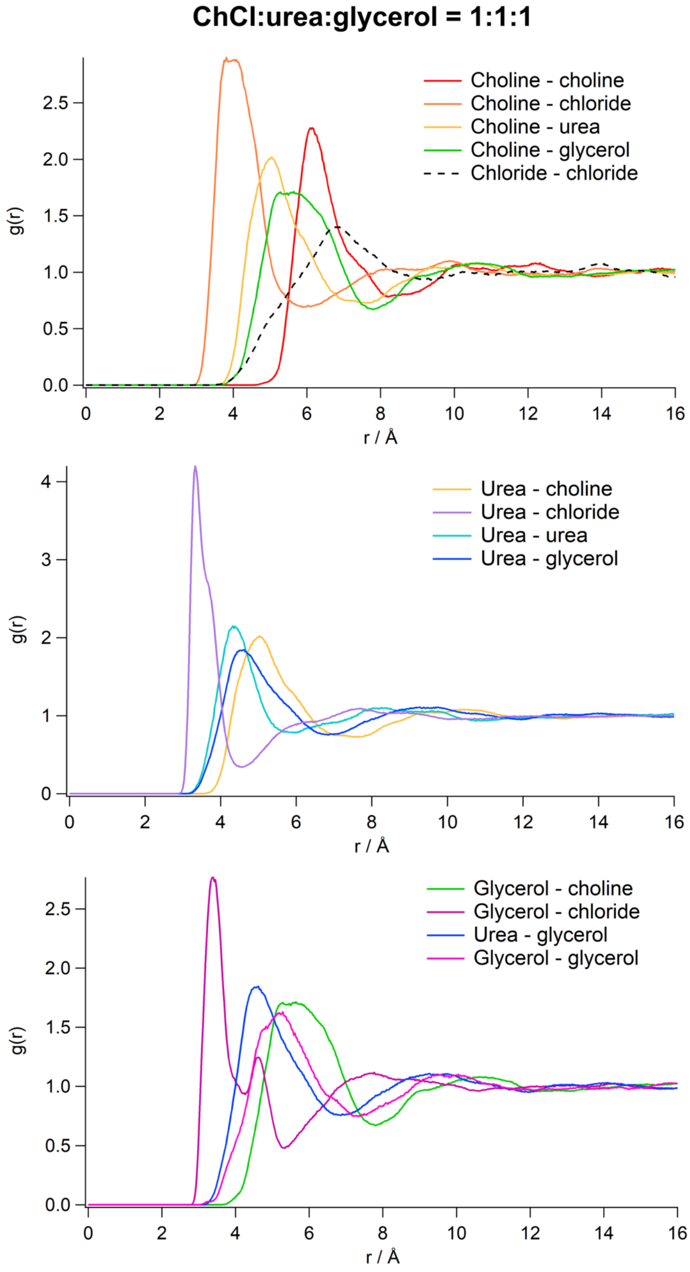

Figure 5.9: Molecular centred radial distribution functions (RDFs) between the various constituents of the DES with component ratio of 1:1:1. The plots correspond to interactions centred on each of cholinium, urea and glycerol. Note that the chloride-chloride RDF is included in the plot for choline interactions. Molecular centres in this case were approximated as the N1 atom of choline, CU atom of urea and CG1 atom of glycerol.

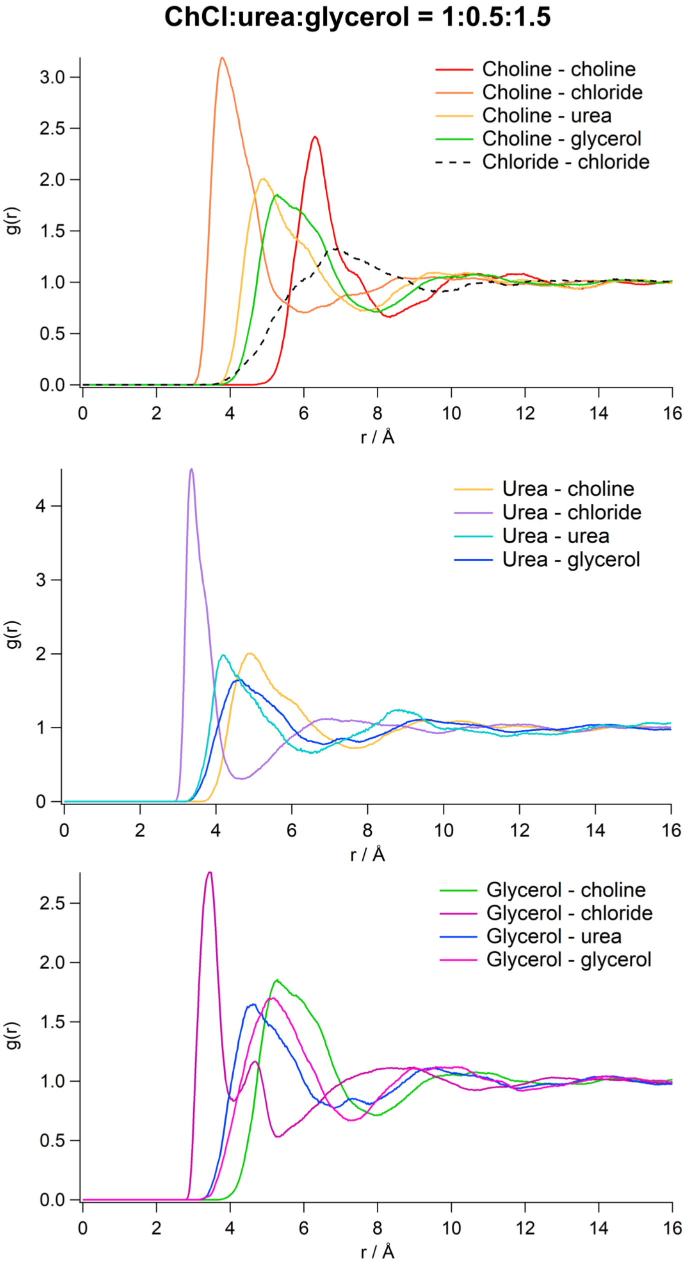

Figure 5.10: Molecular centred radial distribution functions (RDFs) between the various constituents of the DES with component ratio of 1:0.5:1.5. The plots correspond to interactions centred on each of cholinium, urea and glycerol. Note that the chloride-chloride RDF is included in the plot for choline interactions. Molecular centres in this case were approximated as the N1 atom of choline, CU atom of urea and CG1 atom of glycerol.

Table 5.5: Positions of the maxima (r_{max}) and minima (r_{min}) of the primary correlation peaks in the molecular-centred radial distribution functions of the ChCl:urea:glycerol DES with component ratios of 1:1.5:0.5, 1:1:1 and 1:0.5:1.5. The DES are described in the table with respect to the molar content of urea, such that n_{urea}=1.5 denotes the 1:1.5:0.5 system. The atoms N1 (choline), Cl1 (chloride), CU (urea) and CG1 (glycerol) were used as effective molecular centres for these correlations.

		$r_{\text{max}}(r_{\text{min}})$ / Å	
RDF	n_{urea}=1.5	n_{urea}=1	n_{urea}=0.5
Choline - choline	6.32 (8.11)	6.13 (8.19)	6.32 (8.32)
Choline - chloride	3.80 (5.68)	3.93 (5.94)	3.80 (6.03)
Choline - urea	4.99 (7.30)	5.06 (7.03)	4.88 (7.54)
Choline - glycerol	5.66 (7.87)	5.51 (7.78)	5.28 (7.99)
Urea - urea	4.32 (6.31)	4.38 (5.94)	4.20 (6.49)
Urea - chloride	3.34 (4.56)	3.32 (4.54)	3.36 (4.68)
Urea - glycerol	4.59 (7.06)	4.57 (6.89)	4.60 (6.85)
Glycerol - glycerol	5.44 (7.54)	5.21 (7.30)	5.14 (7.30)
Glycerol - chloride	3.47 (4.15)	3.40 (4.24)	3.44 (4.09)

In general, good agreement was seen between both the position of the peaks in the molecular-centred RDFs and the calculated coordination numbers and previous data published for ChCl:urea [75] and ChCl:glycerol [16]. The data from the studies by Hammond *et al.* (ChCl:urea, molar ratio 1:2) and Turner and Holbrey (ChCl:glycerol, molar ratios of 1:2 and 1:1) will be referenced frequently within this discussion, so it is prudent to mention that the neutron diffraction data for ChCl:urea was collected at 30 °C (the same as the ternary DES in this thesis), whilst the data for ChCl:glycerol was collected at elevated temperatures of 60 °C. Although the individual values of the peak maxima/minima and calculated coordination numbers vary across the three DES compositions, the ordering of the RDFs remains same in each case. This is indicative of the local structure and ordering within the DES not undergoing any major transition as the urea:glycerol ratio is varied.

Strong, well-defined correlations are observed in each case between choline and chloride, which shows that anion-cation ordering is present in this DES, but whilst the coordination numbers vary slightly across the three compositions, there is no discernible trend in peak positions. It is interesting however that this correlation occurs at slightly longer distances in the 1:1:1 solvent. This strong interaction between the two components is expected due to the likelihood of hydrogen bonding between Cl^- and the -OH group of choline. The maxima of the primary correlation peaks appear at slightly shorter

Table 5.6: Mean coordination numbers (N_{coord}) calculated for the molecular centred radial distribution functions of the ChCl:urea:glycerol DES with component ratios of 1:1.5:0.5, 1:1:1 and 1:0.5:1.5. Values are obtained by integrating the relevant RDF from the onset of the first correlation peak up until its first minimum. The DES are described in the table with respect to the molar content of urea, such that n_{urea}=1.5 denotes the 1:1.5:0.5 system. The atoms N1 (choline), Cl1 (chloride), CU (urea) and CG1 (glycerol) were used as effective molecular centres for these correlations.

	N_{coord}		
RDF	n_{urea}=1.5	n_{urea}=1	n_{urea}=0.5
Choline - choline	5.64	5.43	5.15
Choline - chloride	2.54	2.75	2.68
Choline - urea	6.30	3.67	2.13
Choline - glycerol	2.57	4.87	7.43
Urea - urea	4.10	2.14	1.25
Urea - chloride	1.25	1.12	1.17
Urea - glycerol	1.92	3.34	4.50
Glycerol - glycerol	2.19	3.82	5.46
Glycerol - chloride	0.80	0.88	0.70

distances in the ternary DES as compared to ChCl:urea (where r_{max}=4.2 Å) [75] and ChCl:glycerol (r_{max}=4.1 Å), though each choline has on average fewer chloride ions associated with it. These shorter bond distances indicate the possibility of stronger hydrogen bonds in the ternary DES as compared to ChCl:urea, whereas the temperature difference between the measurements for the ternary DES (30 °C) and ChCl:glycerol (60 °C) might explain the observation of longer bonds in that solvent. By contrast to the observations made for ChCl:urea and ChCl:glycerol, no obvious secondary interaction peak was discernible in the RDFs for the ternary DES.

The first correlation peak for choline-choline interactions appears at a greater distance, with the closest of these being 6.1 Å (n_{urea}=1) and the furthest being 6.3 Å (n_{urea}=0.5 and n_{urea}=1.5) which suggest that these are secondary shell interactions (since the interactions between other species corresponding to the primary solvation shell appear at closer distances). Again, these values do not follow a distinct trend, but in this case the interaction in the 1:1:1 solvent occurs at a slightly decreased distance compared to the RDFs for the other solvents. The estimated coordination number does increase gradually from 5.1 to 5.6 with increasing urea content in the DES, and increases further still to 6.74 in the case of ChCl:urea [75]. This indicates that, on average, choline is solvated by fewer other choline ions as the glycerol content in the DES is increased. For the same interaction in ChCl:glycerol at 60 °C, however, N_{coord}=3.5±1.1 at a molar ratio of 1:1, which suggests that the presence of urea within the three component DES affects the preferential interactions of the choline cations, even when the relative molar amounts of glycerol and ChCl are the same (1:1, as seen in the 1:1:1 ChCl:U:Gly solvent) as in the binary DES. Furthermore, there is a shoulder in the choline-choline RDFs at all three DES compositions appearing at 7.3 Å in each case, suggesting an additional interaction between choline ions beyond the expected length scale for hydrogen bonding.

The choline-urea interaction also appears as a well-defined peak in each case, which reduces slightly in intensity as the glycerol content in the DES is increased. An increase in the glycerol content also gives rise to a shoulder in the RDF at approximately 5.8 Å becoming more apparent. Whilst there is little variation in the peak position (albeit the interaction in the 1:1:1 solvent occurs at the greatest distance), there is a marked difference between the calculated coordination numbers, as they rise from 2.1, to 3.7 and finally to 6.3 as the urea content increases to n_{urea}=1.5. This observation is somewhat expected given the strong potential for hydrogen bonding between the hydroxyl group on the choline ions and the urea N-H groups. The urea-chloride interactions give rise to very intense, sharp peaks at an average radius of 3.3 Å in each DES composition, which is again not surprising as strong hydrogen bonding interactions are expected between these two components. Additionally, a second broader and much less intense peak at approximately 7.6 Å suggests the presence of a second solvation shell. Urea-urea interactions are also evident in all three DES, though these become broader and weaker as the urea content in the DES decreases. The estimated coordination number also drops markedly from 4.1 in the high urea regime to 1.25 in the low urea system. As the RDFs presented here were calculated using an atom from the middle of the molecule as an effective molecular centre, the length scale of these interactions suggests hydrogen bonding between choline, chloride and urea persists in the ternary DES.

In the case of interactions involving glycerol molecules, the choline-glycerol interaction appears as a broad peak in all three DES compositions and is shortest in the DES with the highest glycerol content (5.3 Å) and longest in the DES where the glycerol content is lowest (5.7 Å). Predictably, the choline ions become increasingly solvated by glycerol ions as the glycerol content in the system increases, and the coordination number increases significantly across the three compositions. The coordination number was determined to be higher still (8.4) in ChCl:glycerol (component ratio = 1:2) [16]. The self-association between glycerol molecules also rises accordingly. Interestingly, the glycerol-chloride interaction presents as two sharp peaks with maxima at 3.4 Å and

4.6 Å both at shorter distances than observed for ChCl:glycerol [16]. As discussed above however, this observation could again be due to the effects of the higher temperature used in the ChCl:glycerol study [16]. Finally, the interactions between urea and glycerol molecules are apparent at all DES compositions and are most intense at higher urea contents. The peak positions, centred on average around 4.6 Å again suggest that hydrogen bonding occurs between these two components. The estimated coordination numbers show that urea becomes increasingly solvated by glycerol molecules as the proportion of urea:glycerol in the DES increases.

It should be noted that the length scales of the molecular correlation peaks do not always follow a trend across the three DES compositions. The choline-choline interaction is slightly contracted in the 1:1:1 solvent. This suggests that choline ions, on average, sit closer together in the 1:1:1 solvent and these interactions are slightly favoured here, which could increase the cohesion between these components. By contrast, the choline-chloride, choline-urea and urea-urea interactions occur at the longest distances in the 1:1:1 solvent, indicating slightly less preferential interactions between these components at this ratio. This could occur at this ratio as a result of the balance between urea/glycerol contents leading to enough disruption of the glycerol network to allow choline ions to sit closer together, and a low enough urea content such that choline-urea interactions are slightly diminished. Further evidence for this is seen from the choline-urea interactions, where the primary interaction in the 1:1:1 solvent is marginally extended. As the choline molar amount is not varied across the solvents, this balance in the interactions could arise mainly from correlations between the other components at this ratio. In the case of urea-chloride, urea-glycerol and glycerol - chloride, there appears to be negligible variation in the distances at which the primary correlation peaks appear, whilst the glycerol-glycerol interactions occur at shorter distances as the glycerol content of the DES is increased. This last trend is expected, given the tendency of glycerol molecules within the DES to form hydrogen-bonded networks and the increased glycerol concentration, giving rise to closer correlations between molecules.

Hydrogen bonding between species is apparent given the length scales of the interactions seen in the molecular-centred RDFs. Some ordering of the species is also evident given the observation of multiple shell correlations in RDFs such as urea-chloride, choline-choline, and glycerol-chlorde (amongst others). An interesting observation was made in Chapter 4 when the surface tensions of the three component DES were measured. Figure 5.11 shows that a distribution resembling a curve can be seen in the surface tension measurements, with the highest value measured for the DES with component ratio 1:1:1. This could imply that the greatest number of cohesive interactions occur within this solvent, which contribute to the increased surface tension at the 1:1:1 component ratio.

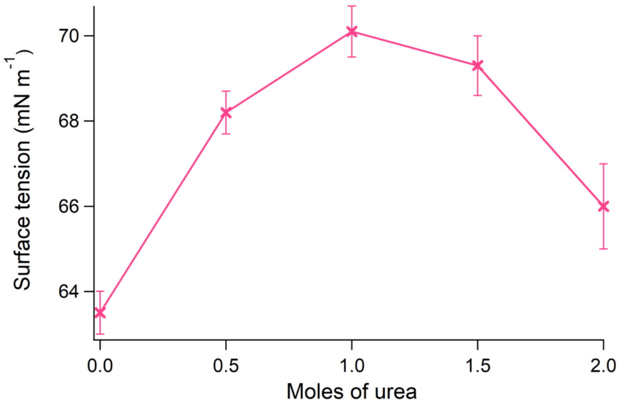

Figure 5.11: A graph showing the values of the surface tension for the three component DES, together with comparison literature data for ChCl:urea [21] and ChCl:glycerol [14]. Numerical values have previously been tabulated in Table 4.3. Data are reported relative to the mole fraction of urea in the DES.

5.5.3 Partial radial distribution functions

Partial (site-site) radial distribution functions, which describe the interactions between individual atoms within the system, allow for even more insight into the structure and bonding within the system. For example, EPSR calculates 210 partial RDFs for the pure DES. Those p-RDFs which are most useful for extracting structural information are presented and discussed here, with tables and figures again separated for easy viewing. Figures 5.12 and 5.13 plot the relevant site-site interactions for the 1:1:1 DES composition, with corresponding plots for the 1:1.5:0.5 and 1:0.5:1.5 compositions presented in the Appendix. Tables 5.7, 5.8 and 5.9 list the positions of the primary correlation peaks and their first minima, together with calculated coordination numbers for interactions involving choline, urea and glycerol, respectively. Examining all of the site-site interactions can quickly become overwhelming, however this section will attempt to condense these by systematically summarising the main preferential ordering and correlations between system constituents, as well as discussing the effect of varying the DES components has on the ordering or strength of these interactions.

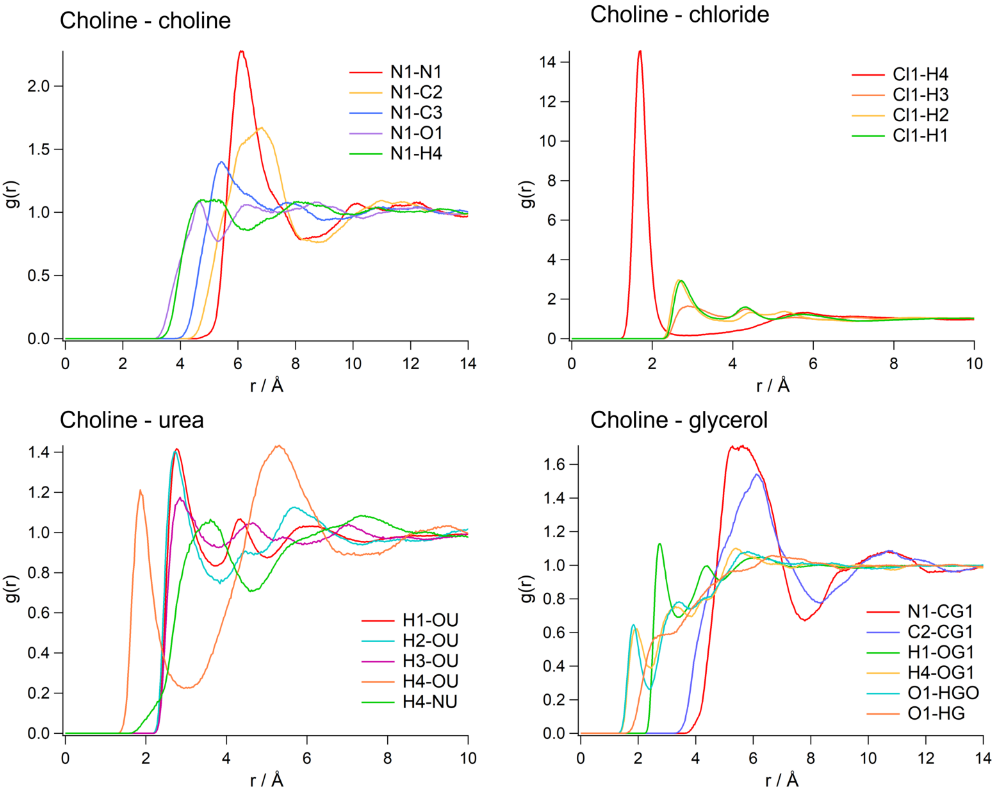

Figure 5.12: Partial (site-site) radial distribution functions for various species included in the EPSR refinement of diffraction data from the 1:1:1 ChCl:U:Gly DES, centred on choline. For clarity, the p-RDFs presented in this figure are those centred on the interactions which provide the most structural information about the systems. Corresponding data for the 1:1.5:0.5 and 1:0.5:1.5 compositions are presented in the Appendix.

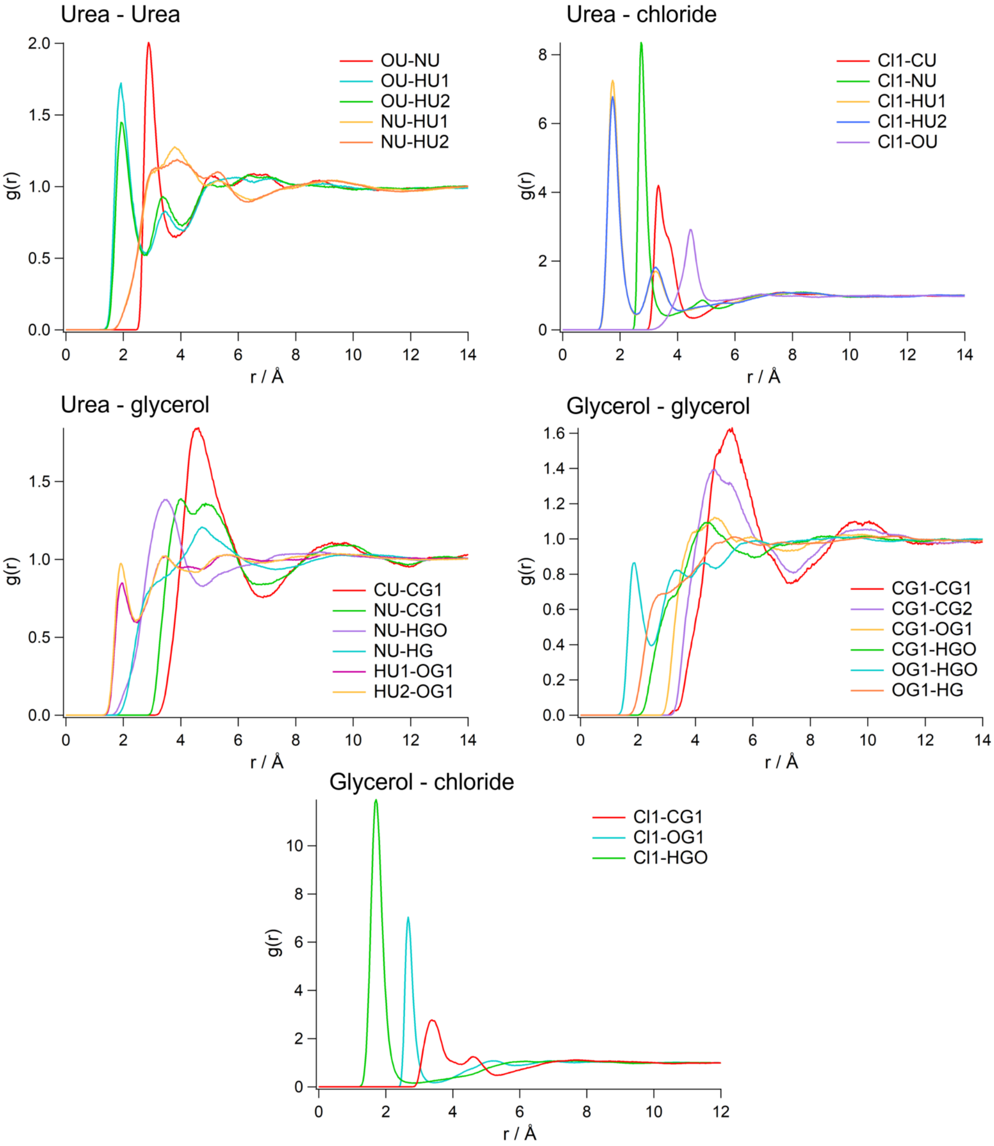

Figure 5.13: Partial (site-site) radial distribution functions for various species included in the EPSR refinement of diffraction data from the 1:1:1 ChCl:U:Gly DES, centred on urea and glycerol. For clarity, the p-RDFs presented in this figure are those centred on the interactions which provide the most structural information about the systems. Corresponding data for the 1:1.5:0.5 and 1:0.5:1.5 compositions are presented in the Appendix.

Table 5.7: Coordination numbers (N_{coord}) calculated for select partial (site-site) RDFs involving choline ions, as shown in Figure 5.12. Coordination numbers were determined by integrating the RDF up until the first minimum (r_{min}) which followed the primary correlation peak (r_{max}). The DES are described in the table with respect to the molar content of urea, such that n_{urea}=1.5 denotes the 1:1.5:0.5 system. Atom labels are given in Figure 5.6.

	n_{urea}=1.5		n_{urea}=1		n_{urea}=0.5	
p-RDF	$r_{\mathrm{max}}(r_{\mathrm{min}})$	N_{coord}	$r_{\mathrm{max}}(r_{\mathrm{min}})$	N_{coord}	$r_{\mathrm{max}}(r_{\mathrm{min}})$	N_{coord}
Ch - Cl						
Cl1-H4	1.68(2.92)	0.6	1.68(2.65)	0.6	1.69(2.98)	0.6
Cl1-H3	2.95(3.85)	1.3	2.87(3.87)	1.2	2.90(3.69)	0.9
Cl1-H2	2.65(3.72)	1.2	2.65(3.96)	1.4	2.64(3.63)	1.0
Cl1-H1	2.76(3.77)	6.0	2.76(3.70)	5.7	2.76(3.72)	5.6
Ch - Ch						
N1-N1	6.20(8.11)	5.6	6.13(8.17)	5.4	6.29(8.30)	5.1
N1-C2	6.60(8.39)	6.3	6.83(8.61)	6.3	6.62(8.52)	5.1
N1-C3	5.42(7.30)	3.7	5.45(7.14)	3.2	5.45(7.22)	3.1
N1-O1	4.67(5.46)	1.2	4.68(5.27)	0.9	4.66(5.36)	0.9
N1-H4	4.78(6.08)	1.8	5.07(6.32)	2.0	4.86(6.05)	1.6
Ch - Urea						
H1-OU	2.74(3.72)	0.7	2.80(3.68)	0.4	2.77(3.75)	0.2
H2-OU	2.69(3.91)	0.7	2.74(3.82)	0.4	2.67(3.81)	0.2
H3-OU	2.87(3.69)	0.5	2.84(3.70)	0.4	2.99(3.95)	0.3
H4-OU	1.82(2.95)	0.2	1.80(3.02)	0.1	1.82(2.87)	0.05
H4-NU	3.55(4.70)	2.6	3.57(4.65)	1.5	3.47(4.71)	0.7
Ch - Gly						
N1-CG1	5.65(7.90)	2.6	5.60(7.77)	4.9	5.28(7.96)	7.4
C2-CG1	5.93(8.50)	3.1	6.10(8.36)	5.8	5.98(8.30)	8.2
H1-OG1	2.79(3.53)	0.4	2.79(3.46)	0.7	2.73(3.32)	0.8
H4-OG1	1.86(2.49)	0.09	1.95(2.45)	0.18	1.87(2.44)	0.2
O1-HGO	1.80(2.35)	0.07	1.84(2.63)	0.2	1.91(2.39)	0.2

Table 5.8: Coordination numbers (N_{coord}) calculated for select partial (site-site) RDFs involving urea, as shown in Figure 5.13. Coordination numbers were determined by integrating the RDF up until the first minimum (r_{min}) which followed the primary correlation peak (r_{max}). The DES are described in the table with respect to the molar content of urea, such that n_{urea}=1.5 denotes the 1:1.5:0.5 system. Atom labels are given in Figure 5.6.

	n_{urea}=1.5		n_{urea}=1		n_{urea}=0.5	
p-RDF	$r_{\text{max}}(r_{\text{min}})$	N_{coord}	$r_{\text{max}}(r_{\text{min}})$	N_{coord}	$r_{\text{max}}(r_{\text{min}})$	N_{coord}
Urea - Urea						
OU-NU	2.90(3.75)	1.3	2.90(3.87)	0.9	2.90(3.81)	0.4
OU-HU1	1.97(2.79)	0.5	1.90(2.87)	0.4	1.96(2.76)	0.1
OU-HU2	1.95(2.77)	0.5	1.94(2.74)	0.3	1.90(2.81)	0.2
NU-HU1	3.74(4.78)	3.7	3.82(4.90)	2.5	3.81(6.10)	2.2
NU-HU2	3.69(4.83)	3.9	3.87(4.84)	2.3	3.08(4.80)	1.1
Urea - Cl						
Cl1-CU	3.37(4.59)	1.9	3.29(4.57)	1.1	3.33(4.63)	0.6
Cl1-NU	2.74(3.62)	2.7	2.77(3.70)	1.4	2.79(3.58)	0.8
Cl1-HU1	1.72(2.60)	1.2	1.72(2.57)	0.8	1.73(2.5)	0.4
Cl1-HU2	1.77(2.55)	1.2	1.74(2.57)	0.7	1.70(0.57)	0.4
Cl1-OU	4.45(5.57)	2.9	4.46(5.27)	1.5	4.43(5.20)	0.7
Urea - Gly						
CU-CG1	4.56(7.06)	1.9	4.60(6.87)	3.2	4.63(6.85)	4.5
NU-CG1	4.54(7.06)	1.9	3.98(6.67)	3.1	4.12(4.88)	5.2
NU-HGO	3.50(4.83)	1.7	3.43(4.76)	3.1	3.47(4.91)	4.7
NU-HG	4.72(7.33)	10.8	4.71(7.28)	17.7	4.77(7.44)	27.8
HU1-OG1	1.94(2.38)	0.1	1.91(2.48)	0.2	1.99(2.47)	0.3
HU2-OG1	1.94(2.45)	0.1	1.90(2.42)	0.2	1.93(2.42)	0.2
OU-HGO	1.86(3.00)	0.27	1.84(2.93)	0.45	1.86(3.04)	0.71

Table 5.9: Coordination numbers (N_{coord}) calculated for select partial (site-site) RDFs involving glycerol, as shown in Figure 5.13. Coordination numbers were determined by integrating the RDF up until the first minimum (r_{min}) which followed the primary correlation peak (r_{max}). Note that for the OG1-HG correlation, it was not possible to discern the values of r_{max} and r_{min} except for the 1:0.5:1.5 solvent. The DES are described in the table with respect to the molar content of urea, such that n_{urea}=1.5 denotes the 1:1.5:0.5 system. Atom labels are given in Figure 5.6.

	n_{urea}=1.5		n_{urea}=1		n_{urea}=0.5	
p-RDF	$r_{\mathrm{max}}(r_{\mathrm{min}})$	N_{coord}	$r_{\mathrm{max}}(r_{\mathrm{min}})$	N_{coord}	$r_{\mathrm{max}}(r_{\mathrm{min}})$	N_{coord}
Gly - Cl						
Cl1-CG1	3.47(4.15)	0.4	3.37(4.26)	0.9	3.43(4.12)	1.1
Cl1-OG1	2.68(3.44)	0.8	2.66(3.48)	1.5	2.68(3.46)	2.1
Cl1-HGO	1.72(2.84)	0.8	1.70(2.81)	1.5	1.70(2.78)	2.1
Gly - Gly						
CG1-CG1	5.44(7.49)	2.2	5.21(7.25)	3.7	5.14(7.33)	5.6
CG1-CG2	4.72(7.32)	4.0	4.68(7.42)	7.8	4.49(7.10)	10.0
CG1-OG1	4.62(5.22)	1.1	4.71(5.43)	4.2	4.74(5.45)	6.1
CG1-HGO	4.07(5.19)	1.9	4.43(6.05)	5.9	4.23(5.94)	8.3
OG1-HGO	1.86(2.49)	0.1	1.84(2.48)	0.2	1.85(2.5)	0.3
OG1-HG	-	-	-	-	2.61(3.2)	1.3

The choline-chloride interaction was analysed by considering the interactions of the chloride anions with each of the choline hydrogen environments (H1 - H4). The site-site RDFs described in Table 5.7 suggest a great degree of ordering is present between the two components across all three DES ratios, with an intense peak appearing at an average distance of 1.68 Å (Figure 5.12) for the interaction between Cl^{-} and the -OH hydrogen from choline (H4) and an estimated coordination number of approximately 0.60 Å. This strong hydrogen-bonding correlation between the two atoms varies little as the glycerol content in the DES is increased, and the coordination number is calculated as 0.60 in each case, but these values are overall smaller than those determined for the same interaction in ChCl:urea (30 °C) [75] and ChCl:glycerol (60 °C) [16]. The interactions of the remaining hydrogens (H1, H2 and H3) with chloride are noticeably much weaker and occur at longer length scales (in the range of 2.6 Å - 2.9 Å). Whilst at distances of 2 Å - 4 Å there seems to be a slight preference for chloride interactions with the methyl hydrogens (H1) and the hydrogens on the carbon immediately adjacent to the nitrogen atom (H2), at longer distances ($\geq$ 4 Å) there seems to be no preferential chloride-hydrogen interactions. Although these interactions in the binary DES were assigned as the origin of the shoulder peaks in the choline-chloride RDFs, in the ternary DES this shoulder peak was not as pronounced (see e.g. Figure 5.9). It is apparent therefore that the main association between choline and chloride is through hydrogen bonds formed between the chloride ions and the hydroxyl -OH, with rotational capability of the latter group allowing the chloride to exist in numerous favoured configurations around the choline.

The molecular-centred RDFs between choline ions (assuming the N1 nitrogen as an effective centre of mass) showed that the interactions occurred over greater length scales than seen for other correlations and could therefore be assigned to second shell correlations. Predictably, this is also evident in the case of the site-site correlations and furthermore several of these interactions are relatively low in intensity. The presence of a shoulder implying a secondary correlation between the nitrogen atoms in two choline molecules can be seen at all three DES ratios, with coordination numbers decreasing slightly from 5.64 to 5.08 as the urea content in the DES decreases. This is not surprising, given that repulsion between two choline ions with like-charges would be expected. Although the N1-N1 interaction is the most pronounced, the N1-C2 interaction also shows a high coordination number, with the highest (6.325) determined for the 1:1:1 DES. In both cases, these values are higher than calculated for pure ChCl:glycerol (even at higher concentrations of ChCl) and ChCl:urea [16,75]. On average, the N1-C3 correlation appears at a shorter distance than the N1-C2 correlation, and the N1-O1 correlation at a shorter distance still. This is in contrast to the interatomic distances within choline and implies that the choline ions which coordinate to a central choline are oriented with the -OH in the opposite direction to the hydroxyl of the original choline molecule. The calculated coordination number of the N1-O1 correlation was found to drop significantly between the 1:1.5:0.5 DES (N_{coord}=1.181) and the 1:0.5:1.5 DES (N_{coord}=0.90). The opposite is seen in the case of the N1-H4 interaction, where N_{coord} is greatest in the 1:1:1 DES. Although this is only slightly increased compared to the other DES compositions, this could imply a greater degree of hydrogen bonding is permitted at this molar ratio due to the balance of interactions between solvent components.

Interactions between choline and urea were primarily examined through assessing the hydrogen bonding capabilities of the choline hydrogens to the oxygen (OU)and nitrogen (NU) atoms on urea. The intensities of all correlations are relatively weak. The shortest interaction in each case occurs between the hydroxyl hydrogen on choline (H4) and OU, with a primary correlation peak appearing on average at 1.8 Å across the three DES composition. The intensity of this peak increases slightly as the urea content in the DES increases, although given that similar correlations in ChCl:urea are also relatively weak it is not surprising that the strength of this interaction does not increase by much [75].

A broad peak for a secondary H4-OU interaction also appears in all three DES. The estimated coordination numbers for this interaction are very low by comparison to other interactions within the system, declining from 0.204 in the high urea regime to 0.05 in the high glycerol regime, at which point they become almost negligible. This indicates that the H4-OU is not the primary interaction between the two molecules in the ternary DES. Greater coordination is seen in the H4-NU interaction, and it is likely that the majority of the correlation between choline and urea occurs through hydrogen bonding via this mode, though this also sees a decline in coordination number as the urea content is decreased. Structuring arising from the interactions of H1, H2 and H3 with the urea oxygen appear to have a primary correlation peak at roughly the same distance, with a slightly increased preference for the H1-OU interaction becoming apparent as the urea content in the DES decreases. These interactions are likely to provide secondary structuring effects in the choline-urea association.

Urea molecules appear to have a weaker self-association within the ternary DES, which is similar to observations made of the ChCl:urea DES and also determined by Soper and co-workers in the case of aqueous solutions of urea [512]. Hydrogen bonding is observed between both amine protons and the OU oxygen. There is initially a slight preference for the OU-HU1 interaction in the high-urea DES, which increases slightly in the 1:1:1 DES, and decreases in intensity in the 1:0.5:0.5 DES. In this low-urea DES, the OU-HU2 interaction becomes noticeably more intense, though the radius of both the OU-HU1 and OU-HU2 interactions remain centred around 2 Å in each case. By contrast to the pure ChCl:urea DES, in which a clear preference for the OU-HU2 interaction was seen by a comparison of coordination numbers, the calculated coordination numbers for the interactions of OU with both HU1 and HU2 are comparable in the ternary DES, although they decrease as the urea content is lowered. Both protons show a stronger association with the NU nitrogen atoms, albeit at greater distances and the increased coordination numbers could be indicative of a degree of clustering between urea molecules. The association between the oxygen and nitrogen atoms (OU-NU) on different urea molecules is also well-defined, with a peak appearing in each DES component ratio at approx. 2.9 Å, indicating hydrogen bonding occurring between the OU and constituents of a second urea molecule.

Coordinations between urea and chloride were examined by considering the interaction of the chloride ions with each constituent of the urea molecule. The closest interaction occurs between the chloride and the HU1/HU2 urea protons, with comparable peak positions and coordination numbers across the ternary DES compositions, though the coordination numbers decrease slightly with decreasing urea content in the DES. A secondary correlation peak for these interactions can also be observed in each case. Whereas there was a strong preference for the HU1 protons indicated in ChCl:urea [75], there was no clear preference indicated in the ternary DES. In the case of ChCl:urea, Hammond and co-workers proposed that the hydrogen bonding between HU1 and Cl1 was preferred due to to the urea adopting an orientation which best allowed the molecule to interact with other components in the system, but it is unlikely that a similar configuration is present within the ternary DES. As compared to the choline-chloride interaction, where only the H4-Cl1 mode showed an intense correlation, strong interactions were also evident between the chloride anion and the NU nitrogen. Cl1-CU and Cl1-OU also appear to be well-defined, although weaker and occurring over greater distances. Unsurprisingly, strong hydrogen bonding interactions were also observed between glycerol and chloride, with an intense peak appearing at an average radius of 1.7 Å at all three DES compositions between the chloride and glycerol hydroxyl protons (HGO), which is at a slightly shorter distance than in pure ChCl:glycerol. The length scale of this interaction is comparable across choline, urea and glycerol, which suggests that chloride ions do not have a significant preference for any one system constituent.

In the case of ChCl:glycerol, a great degree of self-association was apparent between like glycerol molecules at the 1:2 eutectic composition, forming a hydrogen-bonded glycerol network, which underwent a structural transition in the 1:1 composition to accommodate the extra choline ions (discussed above in Section 5.2) [16]. Even at this molar ratio, glycerol clusters formed through strong interactions between glycerol molecules were still present. This is in contrast to systems such as IL/glycerol mixtures [367], where strong interactions between the glycerol and the IL components were preferred compared to self-association. In the ternary DES, where the molar amount of glycerol relative to the moles of ChCl is varied from 0.5 to 1.5, this self-association between glycerol molecules is still evident at each composition. In every case, the coordination number of the interactions between the CG1 carbon and various system constituents increases significantly with increasing glycerol content in the DES. This increase in glycerol content also results in a slight expansion in the molecular-centred RDFs, as well as the CG1-CG2, CG1-OG1 and CG1-HGO correlations, whilst the CG1-OG1 correlation contracts slightly. The high coordination numbers calculated for the interactions between carbon atoms provide further evidence for the strong glycerol-glycerol association. Hydrogen bonds formed between the OG1 oxygen and the hydroxyl hydrogens (HGO) are seen in each case at an average distance of 1.8Å, and these appear to become slightly weaker as the urea content in the DES is increased. By contrast, it was not possible to determine the maximum and minimum radii of the primary correlation peak in the OG1-HG interaction in the case of the 1:1.5:0.5 and 1:1:1 solvents, with a distinct primary correlation peak only becoming apparently in the 1:1.5:0.5 DES.

Finally, in order to determine the effect which the formation of the three component DES has on the structure as compared to the binary ChCl:urea and ChCl:glycerol systems, it is necessary to discuss the interactions between the constituents of choline and urea with glycerol. The partial RDFs between the various atoms of choline and glycerol are overall relatively weak in intensity, with long-range structural correlations seen between the the CG1 glycerol carbon and the choline N1 and C2 atoms, with a preference for the N1-CG1 interaction. The relatively high coordination numbers observed in each case (which increase with the glycerol content in the DES), coupled with the glycerol-glycerol correlations discussed above support the idea of a network of strongly associated glycerol molecules coordinating to the choline component. Interestingly, both the H4-OG1 correlation of the choline hydroxyl proton with the glycerol oxygens and the choline oxygen bonding to the glycerol hydroxyl hydrogen (O1-HGO) have similar intensities across all three component ratios, with the H4-OG1 correlations occurring at slightly greater distances and with slightly higher coordination numbers in each case. It was difficult again to identify the position or nature of the O1-HG correlation, which became less defined in the higher urea DES.

The interaction between urea and glycerol of particular interest in this study, as there is no appropriate literature precedent in the field of DES to which the observations can be compared. The site-site RDFs again appear as a relatively weak set of correlations, but there are a few interesting factors to note. Hydrogen bonding is present between the urea HU1/HU2 protons and the glycerol oxygens (OG1). Initially, the intensities of the first peak maxima suggest that there is a preference for the HU2-NU interaction in the 1:1.5:0.5 DES, but in the 1:0.5:1.5 DES it appears that the HU1-OG1 interaction is slightly more favourable. This could indicate a preferential orientation of the urea molecules with the carbonyl group pointing away from the glycerol molecule at increased glycerol contents in the DES. The length of the CU-CG1 correlation indicates a second shell correlation between urea and glycerol, where the primary associations of urea molecules are with choline and chloride. The NU-CG1 correlation has a bimodal distribution, with peak maxima approximately 1 Å apart in each case. The hydrogen-bonding correlation between NU and HGO appears as a broad peak in each plot at an average distance of 3.5 Å, with an increasing coordination number as the glycerol content in the DES increases. This is not within the radius range where primary shell hydrogen bonding would be expected and is most likely to constitute secondary shell correlations between these molecules.

5.5.4 Hydrogen bonding

It is evident from the discussion of the site-site correlations in the previous section that the three component DES contains several constituents capable of forming hydrogen bonds, and that these interactions regulate the DES structure. In the ChCl:glycerol DES [16] and in pure and aqueous mixtures of glycerol [484, 513], one approach to examining changes to the glycerol hydrogen bonding network has involved an estimation of the total number of hydrogen bonds present within the system at a certain composition. The values needed for this can be determined by integrating the site-site RDFs of hydrogen bonding atom pairs with a primary correlation peak below 2 Å up to a distance of 2.5 Å to find the coordination numbers at this radial distance. By further considering the number of each type of atom within the structure, the total number of hydrogen bonds in the system can be estimated. Table 5.10 shows the coordination numbers calculated for the relevant hydrogen bonding interactions by integrating the RDFs up to 2.5 Å. Note that criteria described above meant that several interactions involving the nitrogen atoms on urea and choline were excluded from the analysis as the primary correlation peak appeared at too great a distance.

Overall, it was estimated that the 1:1.5:0.5 DES contained 6.57 H-bonds, the 1:1:1 DES contained 6.39 H-bonds, and the 1:0.5:1.5 DES contained 6.06 bonds. As predicted, the contributions to the total number of hydrogen bonds arising from interactions between choline and urea decrease with decreasing urea concentration in the DES, whilst those from choline-glycerol correlations increase. However, it is interesting to note that the total number of hydrogen bonds between all relevant species at the specified radius is lowest in the DES with the highest glycerol content. This is the opposite to what might be expected if an extended hydrogen-bonded glycerol network was present in the DES, indeed contradicts the observations of Turner and Holbrey, who calculated a total of 8.14 hydrogen bonds for ChCl:glycerol in a 1:2 ratio, which decreased slightly to 6.974 in the 1:1 solvent [16]. The values determined in this study, even for an equivalent glycerol concentration in the DES suggest that the presence of urea disrupts the ability of glycerol molecules to form these intense short-range correlations with each other.

Table 5.10: Coordination numbers obtained by integrating the relevant site-site RDFs up to a distance of 2.5 Å to describe the hydrogen bonds found in the primary correlation shell at each DES component ratio.

	N_{coord}		
Bond	n_{urea}=1.5	n_{urea}=1	n_{urea}=0.5
Cl1-HGO	0.84	1.48	2.07
Cl1-H4	0.60	0.62	0.61
Cl1-HU1	1.13	0.78	0.38
Cl1-HU2	1.23	0.72	0.40
OG1-HGO	0.12	0.21	0.35
OG1-H4	0.06	0.06	0.05
OG1-HU1	0.27	0.18	0.08
OG1-HU2	0.26	0.19	0.08
O1-HGO	0.08	0.20	0.24
O1-H4	0.02	0.03	0.03
O1-HU1	0.16	0.09	0.06
O1-HU2	0.18	0.18	0.05
OU-HGO	0.19	0.37	0.56

This estimation of the total number of hydrogen bonds at each DES composition is also interesting to discuss with respect to peak in surface tension values in the 1:1:1 solvent mentioned above. The calculated values here would not suggest that the 1:1:1 solvent contains the most hydrogen bonds out of the three component ratios, but there are several correlations within the system which occur at greater length scales and were not accounted for here. Examples include the site-site correlations between the nitrogens on choline/urea (N1/NU) and various protons. It is possible that when the longer-range correlations are taken into account, the greatest number of cohesive interactions may still be present in this DES due to the balance in the behaviour of the constituents at this component ratio.

5.5.4.1 Summary

Now that the key information from the molecular-centred RDFs, the site-site RDFs and the number of hydrogen bonds in the ChCl:urea:glycerol DES has been summarised, it is possible to begin to draw conclusions about the solvent structure.

Chloride anions within the DES coordinate to choline, urea and glycerol, and the primary hydrogen bonding correlation does not vary much in length scale across the DES component ratios. The mean coordination numbers predictably vary as the urea:glycerol ratio changes in the solvent, which suggests a degree of ordering within the structure. In a similar vein, associations are also seen between choline and urea, with a close interaction observed between H4-OU and a second interaction between H4-NU. This latter interaction has calculated coordination numbers commensurate with decreasing urea content in the DES (from n_{urea}=2 in ChCl:urea to n_{urea}=0.5 in the high-glycerol ternary DES, although it occurs at greater distances compared to ChCl:urea. Furthermore, the HU1/HU2 interactions with O1 and N1 appear at longer distances, suggesting secondary correlations between these atom types.

This being said, formation of a complex ion between choline, chloride and urea could still be possible in the presence of the glycerol due to some correlations appearing at similar distances to those observed in ChCl:urea [75]. An inspection of the choline-choline interactions show that the H4-N1 interaction occurs at greater distances than would be expected for strong hydrogen bonds between choline ions, and in each case the radius at which this correlation occurs is at a greater distance than seen in ChCl:urea (approx 1.5-1.8 Å longer), but shorter than in pure ChCl:glycerol, albeit with lower average coordination numbers. Close associations between like urea molecules which are seen in the ChCl:urea DES appear to occur at increased average distances, which are marginally longer in the 1:1:1 DES. In particular, the NU-HU1/HU2 interactions occur at noticeably greater distances as compared to ChCl:urea, but the OU-HU1/HU2 interaction is shorter. The OU-NU interactions between two different urea molecules suggest a degree of urea-urea clustering still occurs within the DES.

There is a good degree of glycerol-glycerol correlation, seen both in the molecular-centred and in the site-site RDFs, but the nature of these correlations is altered as compared to the ChCl:glycerol DES [16]. In the ternary DES, hydrogen bonding associations between the choline hydroxyl hydrogen and the glycerol oxygens (H4-OG1) and the glycerol hydroxyl hydrogens to the choline oxygen (O1-HGO) occur at similar distances within the ternary DES, with no clear preference for one interaction. By contrast, the equivalent O1-HGO in ChCl:glycerol occurs at a greater distance, with the HGO atoms preferentially contributing to the formation of strong glycerol-glycerol hydrogen bonds. In the ternary DES, this glycerol-glycerol self-association is also evidenced by a strong interaction between glycerol oxygens and hydroxyl hydrogens on like molecules (OG1-HGO), however the coordination numbers compared to the ChCl:glycerol DES are much lower than might be otherwise anticipated simply by considering the change in component ratio. The implication of this is that the extended hydrogen-bonded glycerol network is unlikely to persist in the ternary DES.

Other interactions involving glycerol and other DES components can also be briefly summarised. Correlations between the glycerol carbons and hydroxyl proton with chloride occur at shorter distances in the ternary DES than in ChCl:glycerol, but with decreasing coordination numbers of glycerol associated with chloride ions as the glycerol content in the solvent decreases. As discussed already, urea contains many atoms which participate in hydrogen bonding, and already forms primary shell correlations through these with choline and chloride. The correlation between the HU1/HU2 urea protons and OG1 of glycerol also occurs on the expected H-bonding length scale, although there is no preference for either the HU1-OG1 or HU2-OG1 over the other. There is a slight increase in the coordination number of glycerol around urea as the glycerol content in the DES increases, and furthermore long-range urea-glycerol correlations are through consideration of the CU-CG1 and NU-CG1 bonding modes. This participation of the glycerol oxygens in coordinating to urea could be significant enough to cause a disruption to the glycerol hydrogen bonding, which would explain the decreased homo-hydrogen bonding between glycerol molecules.

By consideration of the total number of hydrogen bonds which were present in site-site RDFs below 2.5 Å, it was determined that the fewest hydrogen bonds at this radial distance were in the DES with the highest glycerol content. This was in contrast to the values determined by Turner and Holbrey, which suggested that an increased glycerol content in ChCl:glycerol resulted in an increase in the number of hydrogen bonds due to glycerol self-association [16]. The observations made as part of this work on the ternary DES could therefore further support the theory that urea causes more disruption to the glycerol network than might be expected, even at lower concentrations in the DES. Instead, glycerol-glycerol correlations could instead manifest in the form of clusters and shorter chains. Future work would therefore involve utilising the more advanced analysis routines within the EPSR software to analyse whether either of these are present in the structure.

5.6 Effect of $FeCl_3$ on DES structure

5.6.1 Fits to the data

As discussed previously, $FeCl_3$ was added to the ternary DES with component ratios of 1:1:1 in order to assess the effect on the interactions between various constituents of the system. These data were analysed using EPSR in a similar manner to the data obtained from the experiments on the pure ChCl:urea:glycerol DES discussed in the previous section. $FeCl_3$ was introduced into the model as separate Fe^{3+} and Cl^- ions, and the selection of the relevant Lennard-Jones parameters, simulation box setup and EPSR method are discussed in Section 5.4.5. The neutron diffraction data together with best fits in Q and r space are shown in Figure 5.14. Relevant Lennard-Jones parameters, bond lengths and charges are provided in Appendix B. Overall, a good fit to the data was achieved using the same value of the empirical potential used for the data collected from the pure DES. As before, the main discrepancies between the refined model and the experimental data occur at low values of Q, where the inelastic contributions from protiated DES components are not completely accounted for in the data reduction process, and also where the simultaneous fitting of so many contrasts renders it difficult for the model to find parameters which satisfy every dataset.

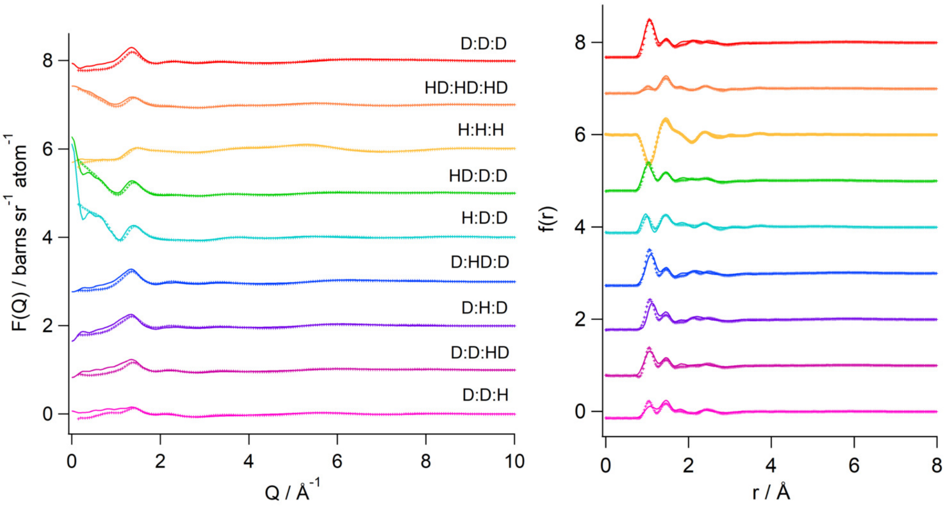

Figure 5.14: Best fits obtained using EPSR (solid lines) to the total neutron scattering profiles (coloured markers) from multiple isotopic contrasts of ChCl:urea:glycerol = 1:1:1 with added $FeCl_3$. The data and fits are plotted as a function of Q (left) and r (right) space.

5.6.2 Molecular centred RDFs

The molecular-centred RDFs for the 1:1:1 component ratio of the ChCl:urea:glycerol DES with added $FeCl_3$ are shown in Figure 5.15. As no significant long-range structural order was observed at radial distances above 16 Å, the data have been truncated accordingly. The positions of the primary correlation peak, $r_{\max}$, and its first minimum in each case, ($r_{\min}$), together with the calculated coordination numbers for each interaction are listed in Table 5.11. For clarity, the same values for the pure 1:1:1 solvent which have been tabulated in previous sections are repeated here to aid the discussion.

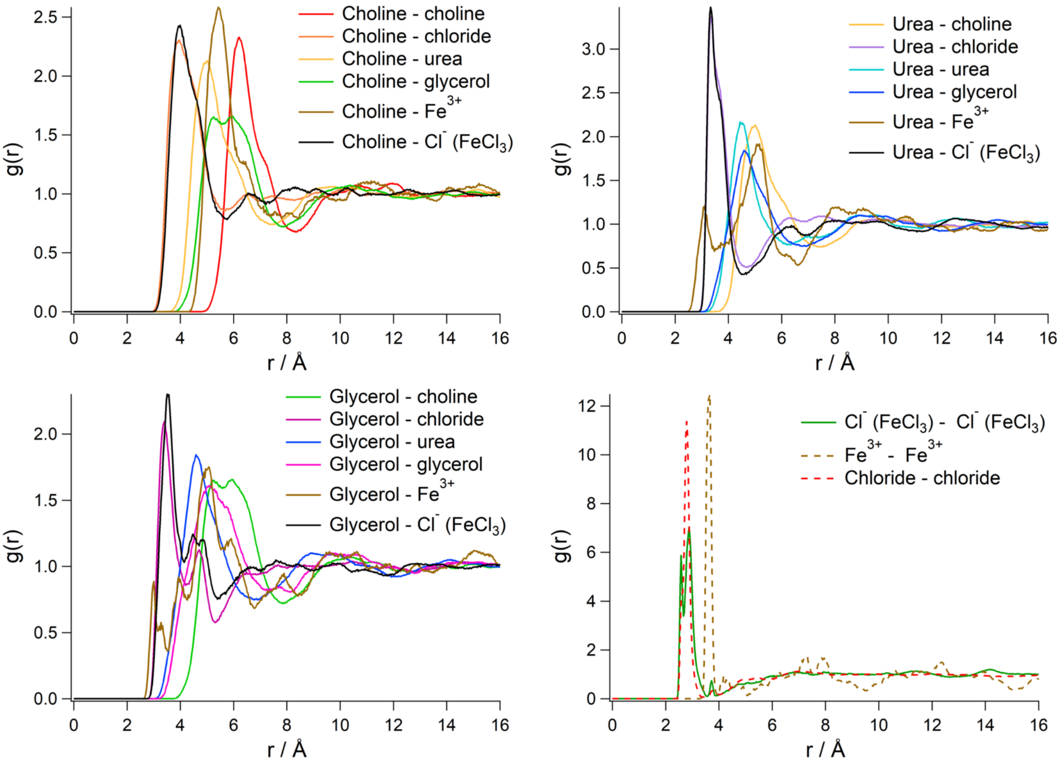

Figure 5.15: Molecular centred radial distribution functions (RDFs) between the various constituents of the DES/$FeCl_3$ with a ChCl:urea:glycerol ratio of 1:1:1. The plots correspond to interactions centred on each of cholinium, urea and glycerol, along with some further interactions between the added Fe^{3+} and chloride species. Molecular centres in this case were approximated as the N1 atom of choline, CU atom of urea and CG1 atom of glycerol.

Table 5.11: Positions of the maxima (r_{max}) and minima (r_{min}) of the primary correlation peaks in the molecular-centred radial distribution functions of the ChCl:urea:glycerol DES with component ratios of 1:1:1, with and without added $FeCl_3$, together with associated calculated coordination numbers (N_{coord}) for each interaction. The atoms N1 (choline), Cl1 (chloride), CU (urea) and CG1 (glycerol) were used as effective molecular centres for these correlations.

	1:1:1 DES		1:1:1 DES + Fe	
p-RDF	$r_{\text{max}}(r_{\text{min}})$	N_{coord}	$r_{\text{max}}(r_{\text{min}})$	N_{coord}
Choline - choline	6.13 (8.19)	5.43	6.24(8.33)	5.34
Choline - chloride	3.93 (5.94)	2.75	3.99(5.36)	1.86
Choline - urea	5.06 (7.03)	3.67	5.02(7.44)	4.23
Choline - glycerol	5.51 (7.78)	4.87	5.56(7.82)	4.81
Choline - Fe^{3+}	-	-	5.43(7.38)	0.60
Choline - Cl^- ($FeCl_3$)	-	-	3.97(5.77)	0.95
Urea - urea	4.38 (5.94)	2.14	4.51(6.37)	2.37
Urea - chloride	3.32 (4.54)	1.12	3.39(4.67)	1.11
Urea - glycerol	4.57 (6.89)	3.34	4.58(6.77)	6.99
Urea - Fe^{3+}	-	-	3.11(3.51)	0.03
Urea - Cl^- ($FeCl_3$)	-	-	3.31(4.58)	0.43
Glycerol - glycerol	5.21 (7.30)	3.82	5.10(7.18)	3.73
Glycerol - chloride	3.40 (4.24)	0.88	3.41(4.21)	0.60
Glycerol - Fe^{3+}	-	-	2.98(3.08)	0.007
Glycerol - Cl^- ($FeCl_3$)	-	-	3.55(4.17)	0.30
Fe^{3+} - Fe^{3+}	-	-	3.66(3.88)	0.15
Chloride - Cl^- ($FeCl_3$)	-	-	2.60(2.65)	0.05
Fe^{3+} - Chloride	-	-	1.70(2.05)	2.60
Fe^{3+} - Cl^- ($FeCl_3$)	-	-	1.70(2.06)	1.17

By examining the RDF plots (Figure 5.15), it is apparent that an intense correlation peak between like Fe^{3+} ions appears in the RDF, however this occurs at increased radial distances and with a low coordination number. Interaction between Fe^{3+} ions within the DES would not be expected due to repulsion between the cations. The interaction between the chloride ions both from ChCl and from $FeCl_3$ with the various DES components appear at the same radial distance, and have comparable intensities. The calculated coordination numbers for the chloride ions from $FeCl_3$ are predictably lower, due to there being fewer of them in the system compared to those from ChCl. Choline-Fe^{3+} correlations are seen at relatively long distances ($r_{\text{max}} = 5.43$ Å), albeit this is still shorter than the choline-choline interactions. Repulsive effects between the positively charged iron and choline ions are likely to result in choline not being present in the primary solvation shell around the Fe^{3+}. The complex, multiple peak structure of the RDFs involving Fe^{3+}, particularly as seen in the urea-Fe^{3+} and glycerol-Fe^{3+} correlations, suggest that there is not one particular preferred configuration of Fe^{3+} around these components in the DES, and instead the ions are dispersed through the structure and interact with these molecules over a range of length scales. It is also possible to consider potential speciation of the Fe^{3+} ions in the DES, particularly with respect to a tendency to form $FeCl_4^-$ ions in the presence of an excess of chloride ions in the DES. In this case, the first coordination shell of Fe would be complete and the complex ion would interact via hydrogen bonds with HBD molecules in the system. The method used to construct the simulation box for EPSR analysis is however not an ideal technique for examining the formation of specific species in this manner, and further experimental or theoretical methods would be required in order to explore this further.

The choline-choline interactions, which are already more distant second shell interactions in the pure DES without added $FeCl_3$, are found at slightly greater distances still in the DES with added $FeCl_3$. A similar observation is also made in the case of the urea-urea interactions, and both instances are likely an effect of increased interactions with added ionic species within the DES. Interestingly, the interactions between like glycerol molecules occur at shorter distances in the DES/Fe^{3+} mixture, but the positions of the primary correlation peaks in the choline-glycerol and urea-glycerol RDFs do not vary by much. The small increase in the choline-urea coordination number in the DES/Fe^{3+} mixture as compared to the pure DES (from 3.67 to 4.23) could arise as a secondary effect from increased choline-chloride correlation, especially if the formation of a complex ion persists in this DES. The calculated coordination number for the urea-glycerol interaction increases markedly from 3.3 Å in the pure DES to approximately 7 Å in the DES/Fe^{3+} mixture. This could suggest that more extensive clustering between urea and glycerol molecules, especially given that the interactions occur at a similar radial distance to those in the pure DES. A brief examination of the relevant site-site correlations (the glycerol OG1 oxygen to the HU1/HU2 protons of urea, and the urea OU oxygen to the HGO glycerol hydroxyl proton), showed little variation from the values determined for the pure 1:1:1 DES, so it is not likely to be caused by a marked increase in close-range hydrogen bond formation.

In a study briefly looking at the effect of adding iron(III) nitrate nonahydrate to the ChCl:urea DES on the solvent structure, the same lengthening of the choline-choline correlation was determined, however most of the effects on component correlations were found to occur in hydrated DES and involved the chloride-water interactions [116]. Whilst there is a suggestion that the increased concentration of ions within the DES can have a cascading effect on some of the interactions between components of the ternary DES in this study, it is not possible to assign an exact cause to this from the data presented in this chapter. The primary motivation behind the addition of $FeCl_3$ to the DES was to attempt to determine why the addition of these species causes a disruption to the structure of C_{16}TAB micelles, as reported in Chapter 4. From the data presented here, it is not yet possible to offer an exact explanation for this. Further investigation would include looking at similar data for the other DES component ratios, and carrying out spatial density analysis to confirm the conformation of components around each other within such a complex system. Additionally, X-ray scattering patterns were not measured as part of this experiment and so were not included in data refinement process, however for systems containing heavier elements such as certain metal ions (as in this case), the inclusion of such a dataset can aid in the data analysis by imposing additional constraints from these on the model.

5.7 Conclusions and future work

In this chapter, total neutron scattering experiments were carried out to analyse a variety of isotopically substituted (H/D) samples of the ChCl:urea:glycerol DES at component ratios of 1:1.5:0.5, 1:1:1 and 1:0.5:1.5. Additionally, data was also collected for samples of the 1:1:1 DES contaning added $FeCl_3$. The datasets were analysed via iterative refinement of a geometric model to the experimental data using EPSR in order to extract information about the key interactions within the system.

An analysis of the molecular-centred RDFs in the pure DES samples showed that the ordering of the interactions remained much the same as the component ratio was varied, although the coordination intensity and number often varied predictably with changing urea:glycerol concentrations within the DES. Interestingly, certain correlations occurred at the greatest or shortest distance in the 1:1:1 DES rather than showing a trend across solvent compositions, and whilst further investigation is required, this could point to a particular balance of interactions within this DES leading to an enhanced solvent cohesion, which explains the observation of an increased surface tension at this composition.

By looking at the partial (site-site) RDFs within the system, it was determined that the complexation between urea, chloride and choline was still probably occurring in the DES. Furthermore, the diminished interactions between the hydrogen-bonding groups in glycerol suggested that the glycerol network might not persist in the ternary DES, even at higher glycerol concentrations and that the presence of urea caused enough disruption to the hydrogen bonding structure to cause this. A summary of the coordination numbers of the various hydrogen bonding interactions within the DES between the relevant atoms showed that the estimated coordination number (and hence number of hydrogen bonds) found up to a radial distance of 2.5 Å appears to decrease with increasing glycerol content in the DES. This was in contrast to previous observations in the literature [16], which found strong glycerol self-association that an increase in the choline concentration within the ChCl:glycerol DES results in a disruption of the hydrogen bond network.

In order to verify these observations, further work would include the use of spatial density function (SDF) analysis on the systems using the EPSR routines, in order to visualise the probable distributions of various DES components around each other. This would involve a calculation of the density distributions of components relative to a central molecule or ion, which could then be plotted as a series of isosurfaces. Although an analysis of the correlation lengths and coordination numbers given in this chapter provides some insight into the preferential associations between system constituents, being able to visualise this via this series of SDF plots would be to great advantage. Further work examining the glycerol network (or lack thereof) within the system would involve an analysis of any clustering or chains of glycerol molecules within the DES to determine the extent to which this disruption occurs, as well as investigating whether the urea molecules also form clusters.

The addition of $FeCl_3$ to an already complex system determined strong anion-cation correlations, with resulting effects on radial distances of interactions between the various DES components. An increased urea-glycerol coordination was observed, but a brief analysis of site-site correlations did not find any noticeable increase in the hydrogen bonding at the relevant radial distances. It is likely that there is an increase in long-range ordering between these DES components. Similar SDF analysis, particularly centred around the urea and glycerol components would also be beneficial in order to determine the composition of the primary and secondary correlation shells. Additionally, the analysis of the DES/$FeCl_3$ mixtures at different component ratios would allow a better comparison of the effect of changing the urea:glycerol ratio in the DES. One final addition to the data analysis would be the inclusion of an X-ray scattering dataset in the co-refinement procedure, as it would further allow constraints to the model to be imposed from the contribution of heavier components (the Fe^{3+} ions).

Chapter 6

Summary and future outlook

DES are alternative solvents with unique structures and qualities which has led to them being widely investigated as replacement solvents in a range of chemical processes. The main aim of this PhD project was to further the understanding of their properties and structure, and to explore the possibilities and limitations of certain applications. This was achieved via three self-contained smaller projects.

In the first section of this project, several experiments were carried out to determine the applicability of a facile solvothermal method for the synthesis of iron oxide nanoparticles in the ChCl:urea DES [11] to the production of alternative transition metal oxides, in particular those relevant to electrocatalysis applications. Primarily, the synthesis of cobalt oxide (Co_3O_4) was explored. It was determined that Co_3O_4 could only be synthesised in hydrated ChCl:urea. Solvothermal reactions carried out in ChCl:urea with varying water contents resulted in the formation of cobalt carbonate, which could be converted to the oxide via a calcination step. Results from XRD and SEM analysis suggested that the particles formed were large aggregates rather than nanoparticles.

The speciation of Co^{2+} ions in the DES was also discussed, together with the formation of stable intermediates at both low and high temperatures which did not react further during heating to form a carbonate or oxide material. Synthesis using nickel-based precursors yielded similar results, whilst a combination of iron(III)-based precursors with various transition metal-based precursors in the reaction mixtures resulted exclusively in formation of iron oxide in each case. Separately, samples of mixed Co-Fe sulfides were synthesised using a PEG200:thiourea DES and a similar solvothermal method. The sulfide products were found to have large particle sizes and high levels of aggregation. The powders were evaluated for their electrocatalytic ability by drop casting of a catalyst ink onto a glassy carbon electrode. Whilst they were found to show some electrocatalytic activity towards the HER, the smallest overpotential calculated was 550 mV, which is still far higher than the most efficient catalysts in literature.

It is clear from these conclusions that far more work is required in order to fully explore the use of DES to form electrocatalyst materials. For example, the reactions for the synthesis of cobalt oxide in hydrated reline should be explored across a range of synthesis conditions to see if the nanostructuring of the products can be improved. The samples should also be evaluated for electrocatalytic activity. An alternative method to explore would be the use of halide-free DES which still contained urea, such as betaine:urea NADES, to determine whether the change in the reaction pathway occurs which facilitates the synthesis of oxide nanoparticles.

One area which remains underinvestigated is the use of electrodeposition techniques for the deposition of oxide, sulfide and even phosphide materials for use in applications such as photo- or electrocatalysis. Electrofinishing applications are discussed in Section 3.3 within Chapter 3. This was briefly investigated towards the end of the project, but results were not sufficient to merit inclusion in the main body of the thesis. Some prelimary results are presented in this section. The synthesis of Co-S deposits was briefly attempted using an electrolyte solution of cobalt(II) chloride (0.1 mol kg^{-1}) and thiourea (0.5 mol kg^{-1}) in ChCl:ethylene glycol. Deposition was carried out onto both a nickel foam and fluorine-doped tin oxide (FTO) coated glass using a three-electrode cell setup (see Appendix). Some evidence of deposition onto both substrates was seen in both cases (Figure 6.1, but this could not be characterised or detected by XRD, SEM or EDX analysis. Electrocatalytic testing of the deposits formed on FTO-coated glass resulted in the material being washed away from the substrate in solution, whereas no apparent electrocatalytic activity could be detected for the deposits on nickel foam.

A more rigorous experimental approach is clearly needed in order to investigate this electrodeposition fully. This would first involve an evaluation of the electrochemical window and stability of the DES in a three-electrode setup containing the substrate of choice as the working electrode, in order to determine the limits within which a sample could be synthesised. A range of deposition conditions and methods (e.g. galvanostatic vs. cyclic voltammetry), using several different DES (ChCl:ethylene glycol, ChCl:glycerol, ChCl:urea) and even DES/water mixtures should be investigated. The precursor concentration should also be varied, and a variety of deposition times, including longer deposition (*ca.* 30 min and above) should be explored to see if enough material can be deposited to allow characterisation.

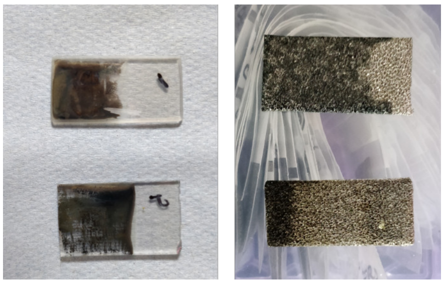

Figure 6.1: Images of deposits obtained from the attempted deposition of Co-S from ChCl:ethylene glycol-based electrolyte onto FTO-coated glass (left) and nickel foam (right). Deposition methods are presented in the Appendix.

During this PhD, electrodeposition using DES-based electrolytes could not be explored further due to equipment failure and restrictions on laboratory access during the COVID-19 pandemic.

The second study introduced a system which contained three components: choline chloride, urea and glycerol. This solvent was originally synthesised with a view to solubilising cationic surfactants, which are often used as soft templates in materials synthesis and are soluble in ChCl:glycerol but not ChCl:urea. As the thermal hydrolysis of urea has been shown to drive solvothermal reactions in DES, the three component system allowed for the dissolution of C_{16}TAB whilst retaining the urea functionality. The DES were prepared in component ratios of 1:1.5:0.5, 1:1:1 and 1.0.5:1.5, and physiochemical properties such as their densities, surface tensions and viscosities were characterised. The CMCs of the surfactant/DES solutions were estimated using fluorescence spectroscopy with pyrene as a fluorescent probe. Small-angle neutron scattering experiments were carried out on 25 mM and 130 mM solutions of C_{16}TAB in the DES. The results from these experiments confirmed that micelles were successfully formed at each DES component ratio, even at low glycerol contents. Guinier analysis and subsequent fitting of the SANS data from 25 mM solutions to an ellipsoidal form factor geometric model showed that the micelle elongation varied greatly between solutions with different DES component ratios, from an estimated elongation of 40.7±6.2 Å in a low-urea solvent to 248±12 Å in a high-urea regime. Data from the 130 mM C_{16}TAB/DES solutions were further fitted using a core-shell ellipsoid model, which confirmed the observations from the dilute system. By a comparison of the SLD values obtained for the micelle shell, it was suggested that the greatest degree of solvent penetration into the headgroup region occurs in the solvent with component ratios of 1:0.5:1.5. The variation in micelle elongation was attributed both to charge-screening effects within the DES, and also the condensation of the surfactant counterion onto the micelle surface due to poor solubility of bromide ions in the DES. Replacing the bromide counterion on $C_{16}TAB$ with a nitrate ion was found to have little effect on micelle morphology. The addition of water (10 mole equivalents) to the $C_{16}TAB$/DES solution (component ratio = 1:1.5:0.5) was found to cause even further elongation than seen in the dry $C_{16}TAB$/DES solutions. This could be due to an increase in free ions in the system facilitated by water addition, but further systematic investigation involving more DES component ratios and varying amounts of water addition would be required to characterise this thoroughly.

The effect of the addition of metal ions (Fe^{3+} and Zn^{2+} was also explored briefly. Fe^{3+} was found to disrupt the micelle structure completely, whilst Zn^{2+} caused a significant morphological change. In the 1:0.5:1.5 DES (low urea), the SANS data could be fitted to a cylinder model with a length of 1549±25 Å. In the case of the solutions in the 1:1.5:0.5 DES (high urea), the presence of multiple morphologies in the DES was proposed both from the SANS data and from phase separation seen within the sample. In order to investigate this further, the apparently larger aggregates within the concentrated surfactant layer should be characterised. Additionally, the concentration of Zn^{2+} could be varied in order to see how the phase separation and micelle morphology is affected. ZnO was synthesised from mixtures of Zn^{2+}/$C_{16}TAB$/DES using a solvothermal reaction followed by a calcination step. This powder was found to be non-porous with a low surface area, so more method development is required to see if this can be improved. Another alternative would be to explore the use of a Zn-based DES analogous to those formed by cerium nitrate and urea as an alternative solvent both for the self-assembly of surfactants, and for the synthesis of porous materials.

In the final project of this PhD, the structure of the three component DES introduced in the previous chapter was investigated using neutron diffraction techniques. Datasets were collected for a series of isotopically substituted samples for the ChCl:urea:glycerol DES in the three component ratios of 1:1.5:0.5, 1:1:1 and 1:0.5:1.5. The data were primarily analysed using Empirical Potential Structure Refinement (EPSR), in which the experimental datasets were iteratively refined to a computational model. By an examination of the molecular-centred and partial (site-site) radial distribution functions it was determined that complexation between the choline, urea and chloride species which was observed in the case of ChCl:urea [75] persisted in the presence of glycerol. Glycerol-glycerol self-association was still apparent within the structure, though to a lesser extent than observed in the case of the ChCl:glycerol DES [16]. The estimated coordination numbers for the interactions were however much lower than would be otherwise anticipated in the the ternary DES as compared to the ChCl:glycerol DES without urea, which suggested that the hydrogen-bonded glycerol network was unlikely to persist within the solvent. This was further corroborated by an estimation of the number of hydrogen bonds at each solvent composition, where the fewest hydrogen bonds at a radial distance of 2.5 Å were found in the DES with the highest glycerol content. It was proposed that the glycerol network in the ChCl:urea:glycerol DES could therefore exist in the form of clustering or short chains of glycerol molecules instead of an extended network. Although an examination of correlations between molecules and individual atom sites can provide a large amount of information about the interactions within the system, further advanced analysis routines are required in order to truly visualise the inferences made from the RDFs. This would include the spherical harmonics (SHARM) routines within the EPSR software used in conjunction with spatial density function (SDF) plots to visualise the average configuration of various DES components around each other. Routines also exist to analyse the nature of both clusters and chains of molecules within the solvent, and ongoing analysis is currently exploring these.

Neutron diffraction data was also collected for mixtures of $FeCl_3$ and the 1:1:1 ChCl:U:Gly DES and analysed using EPSR in the same manner. The parameters extracted from an analysis of the molecular-centred and site-site RDFs were compared to those determined for the pure 1:1:1 DES. This analysis was initially carried out in order to determine why the addition of $FeCl_3$ to solution of C_{16}TAB in ChCl:urea:glycerol resulted in a loss of the micellar structure. Whilst it was determined that some changes to correlation distances and strengths occurred as a result of the increased number of ions in the solution, it was not possible to determine the exact cause of the observations of the C_{16}TAB/DES mixtures. Work is ongoing to characterise the effect of $FeCl_3$ on the other DES compositions. With such a complex system involving numerous components, the same SDF analysis discussed above will be crucial to visualising the ordering of components in the system around each other and determine where the added Fe^{3+} and Cl^- ions lie. Further work would involve including data from X-ray scattering in the EPSR modelling in order to impose further constraints on the model from the contribution of the heavier elements in the system.

References

[1] E. Jónsson, "Ionic liquids as electrolytes for energy storage applications–a modelling perspective," *Energy Storage Materials*, vol. 25, pp. 827–835, 2020.

[2] D. A. Alonso, A. Baeza, R. Chinchilla, G. Guillena, I. M. Pastor, and D. J. Ramón, "Deep eutectic solvents: the organic reaction medium of the century," *European Journal of Organic Chemistry*, vol. 2016, no. 4, pp. 612–632, 2016.

[3] O. S. Hammond and A.-V. Mudring, "Ionic liquids and deep eutectics as a transformative platform for the synthesis of nanomaterials," *Chemical Communications*, vol. 58, no. 24, pp. 3865–3892, 2022.

[4] "Scifinder database." `https://scifinder.cas.org/scifinder/view/scifinder/scifinderExplore.jsf`. Accessed: October 2021.

[5] R. Pynn, "Neutron scattering—a non-destructive microscope for seeing inside matter," in *Neutron applications in earth, energy and environmental sciences*, pp. 15–36, Springer, 2009.

[6] E. Mitchell, P. Kuhn, and E. Garman, "Demystifying the synchrotron trip: a first time user's guide," *Structure*, vol. 7, no. 5, pp. R111–R121, 1999.

[7] M. O. Jones, A. D. Taylor, and S. F. Parker, "Neutron scattering studies of catalyst systems at the ISIS neutron spallation source," *Applied Petrochemical Research*, vol. 2, no. 3, pp. 97–104, 2012.

[8] D. A. Neumann, "Neutron scattering and hydrogenous materials," *Materials Today*, vol. 9, no. 1-2, pp. 34–41, 2006.

[9] C. V. Stan, C. M. Beavers, M. Kunz, and N. Tamura, "X-ray diffraction under extreme conditions at the advanced light source," *Quantum Beam Science*, vol. 2, no. 1, 2018.

[10] S. Sharma, S. Jaiswal, B. Duffy, and A. K. Jaiswal, "Nanostructured materials for food applications: spectroscopy, microscopy and physical properties," *Bioengineering*, vol. 6, no. 1, 2019.

[11] O. S. Hammond, S. Eslava, A. J. Smith, J. Zhang, and K. J. Edler, "Microwave-assisted deep eutectic-solvothermal preparation of iron oxide nanoparticles for photoelectrochemical solar water splitting," *Journal of Materials Chemistry A*, vol. 5, no. 31, pp. 16189–16199, 2017.

[12] M. M. Castellanos, A. McAuley, and J. E. Curtis, "Investigating structure and dynamics of proteins in amorphous phases using neutron scattering," *Computational and Structural Biotechnology Journal*, vol. 15, pp. 117–130, 2017.

[13] R. S. Atri, A. Sanchez-Fernandez, O. S. Hammond, I. Manasi, J. Doutch, J. P. Tellam, and K. J. Edler, "Morphology modulation of ionic surfactant micelles in ternary deep eutectic solvents," *The Journal of Physical Chemistry B*, vol. 124, no. 28, pp. 6004–6014, 2020.

[14] A. Sanchez-Fernandez, T. Arnold, A. J. Jackson, S. L. Fussell, R. K. Heenan, R. A. Campbell, and K. J. Edler, "Micellization of alkyltrimethylammonium bromide surfactants in choline chloride: glycerol deep eutectic solvent," *Physical Chemistry Chemical Physics*, vol. 18, no. 48, pp. 33240–33249, 2016.

[15] C. R. Ashworth, R. P. Matthews, T. Welton, and P. A. Hunt, "Doubly ionic hydrogen bond interactions within the choline chloride–urea deep eutectic solvent," *Physical Chemistry Chemical Physics*, vol. 18, no. 27, pp. 18145–18160, 2016.

[16] A. H. Turner and J. D. Holbrey, "Investigation of glycerol hydrogen-bonding networks in choline chloride/glycerol eutectic-forming liquids using neutron diffraction," *Physical Chemistry Chemical Physics*, vol. 21, no. 39, pp. 21782–21789, 2019.

[17] N. Jakse and A. Pasturel, "Liquid aluminum: Atomic diffusion and viscosity from ab initio molecular dynamics," *Scientific Reports*, vol. 3, no. 1, pp. 1–8, 2013.

[18] B. J. Palmer, "Transverse-current autocorrelation-function calculations of the shear viscosity for molecular liquids," *Physical Review E*, vol. 49, no. 1, pp. 359–366, 1994.

[19] B. Hess, "Determining the shear viscosity of model liquids from molecular dynamics simulations," *The Journal of Chemical Physics*, vol. 116, no. 1, pp. 209–217, 2002.

[20] D. Bowron, A. Soper, K. Jones, S. Ansell, S. Birch, J. Norris, L. Perrott, D. Riedel, N. Rhodes, S. Wakefield, *et al.*, "NIMROD: The Near and InterMediate Range Order Diffractometer of the ISIS second target station," *Review of Scientific Instruments*, vol. 81, no. 3, 2010.

[21] T. Arnold, A. J. Jackson, A. Sanchez-Fernandez, D. Magnone, A. Terry, and K. Edler, "Surfactant behavior of sodium dodecylsulfate in deep eutectic solvent choline chloride/urea," *Langmuir*, vol. 31, no. 47, pp. 12894–12902, 2015.

[22] F. G. Calvo-Flores and C. Mingorance-Sánchez, "Deep eutectic solvents and multicomponent reactions: Two convergent items to green chemistry strategies," *ChemistryOpen*, vol. 10, no. 8, pp. 815–829, 2021.

[23] V. F. Sears, "Neutron scattering lengths and cross sections," *Neutron News*, vol. 3, no. 3, pp. 26–37, 1992.

[24] M. C. Stuart and E. J. Boekema, "Two distinct mechanisms of vesicle-to-micelle and micelle-to-vesicle transition are mediated by the packing parameter of phospholipid–detergent systems," *Biochimica et Biophysica Acta (BBA)-Biomembranes*, vol. 1768, no. 11, pp. 2681–2689, 2007.

[25] C. Tanford, "Micelle shape and size," *The Journal of Physical Chemistry*, vol. 76, no. 21, pp. 3020–3024, 1972.

[26] U. G. Assembly, "Transforming our world: the 2030 agenda for sustainable development, 21 October 2015," tech. rep., A/RES/70/1, 2015.

[27] S. Abou-Shehada, J. H. Clark, G. Paggiola, and J. Sherwood, "Tunable solvents: Shades of Green," *Chemical Engineering and Processing: Process Intensification*, vol. 99, pp. 88–96, 2016.

[28] C. Capello, U. Fischer, and K. Hungerbühler, "What is a green solvent? a comprehensive framework for the environmental assessment of solvents," *Green Chemistry*, vol. 9, no. 9, pp. 927–934, 2007.

[29] L. J. Diorazio, D. R. Hose, and N. K. Adlington, "Toward a more holistic framework for solvent selection," *Organic Process Research & Development*, vol. 20, no. 4, pp. 760–773, 2016.

[30] R. K. Henderson, C. Jiménez-González, D. J. Constable, S. R. Alston, G. G. Inglis, G. Fisher, J. Sherwood, S. P. Binks, and A. D. Curzons, "Expanding GSK's solvent selection guide–embedding sustainability into solvent selection starting at medicinal chemistry," *Green Chemistry*, vol. 13, no. 4, pp. 854–862, 2011.

[31] K. Alfonsi, J. Colberg, P. J. Dunn, T. Fevig, S. Jennings, T. A. Johnson, H. P. Kleine, C. Knight, M. A. Nagy, D. A. Perry, *et al.*, "Green chemistry tools to influence a medicinal chemistry and research chemistry based organisation," *Green Chemistry*, vol. 10, no. 1, pp. 31–36, 2008.

[32] C. J. Clarke, W.-C. Tu, O. Levers, A. Brohl, and J. P. Hallett, "Green and sustainable solvents in chemical processes," *Chemical Reviews*, vol. 118, no. 2, pp. 747–800, 2018.

[33] V. N. Emelyanenko, G. Boeck, S. P. Verevkin, and R. Ludwig, "Volatile times for the very first ionic liquid: understanding the vapor pressures and enthalpies of vaporization of ethylammonium nitrate," *Chemistry–A European Journal*, vol. 20, pp. 11640–11645, 2014.

[34] P. Walden, "Molecular weights and electrical conductivity of several fused salts," *Bulletin de Académie Impériale des Sciences de St. Petersburg*, vol. 1800, 1914.

[35] R. L. Vekariya, "A review of ionic liquids: Applications towards catalytic organic transformations," *Journal of Molecular Liquids*, vol. 227, pp. 44–60, 2017.

[36] J. P. Armstrong, C. Hurst, R. G. Jones, P. Licence, K. R. Lovelock, C. J. Satterley, and I. J. Villar-Garcia, "Vapourisation of ionic liquids," *Physical Chemistry Chemical Physics*, vol. 9, no. 8, pp. 982–990, 2007.

[37] J. N. Canongia Lopes, M. F. Costa Gomes, and A. A. Pádua, "Nonpolar, polar, and associating solutes in ionic liquids," *The Journal of Physical Chemistry B*, vol. 110, no. 34, pp. 16816–16818, 2006.

[38] K. Yavir, Ł. Marcinkowski, R. Marcinkowska, J. Namieśnik, and A. Kloskowski, "Analytical applications and physicochemical properties of ionic liquid-based hybrid materials: A review," *Analytica Chimica Acta*, vol. 1054, pp. 1–16, 2019.

[39] Z. Lei, B. Chen, Y.-M. Koo, and D. R. MacFarlane, "Introduction: ionic liquids," *Chemical Reviews*, vol. 117, no. 10, pp. 6633–6635, 2017.

[40] S. K. Singh and A. W. Savoy, "Ionic liquids synthesis and applications: An overview," *Journal of Molecular Liquids*, vol. 297, 2020.

[41] D. Reinhardt, F. Ilgen, D. Kralisch, B. König, and G. Kreisel, "Evaluating the greenness of alternative reaction media," *Green Chemistry*, vol. 10, no. 11, pp. 1170–1181, 2008.

[42] Y. Zhang, B. R. Bakshi, and E. S. Demessie, "Life cycle assessment of an ionic liquid versus molecular solvents and their applications," *Environmental Science & Technology*, vol. 42, no. 5, pp. 1724–1730, 2008.

[43] J. Hulsbosch, D. E. De Vos, K. Binnemans, and R. Ameloot, "Biobased ionic liquids: solvents for a green processing industry?," *ACS Sustainable Chemistry & Engineering*, vol. 4, no. 6, pp. 2917–2931, 2016.

[44] G. Huet, M. Araya-Farias, R. Alayoubi, S. Laclef, B. Bouvier, I. Gosselin, C. Cézard, R. Roulard, M. Courty, C. Hadad, *et al.*, "New biobased-zwitterionic ionic liquids: efficiency and biocompatibility for the development of sustainable biorefinery processes," *Green Chemistry*, vol. 22, no. 9, pp. 2935–2946, 2020.

[45] M. Messali, "A facile and green microwave-assisted synthesis of new functionalized picolinium-based ionic liquids," *Arabian Journal of Chemistry*, vol. 9, pp. S564–S569, 2016.

[46] A. P. Abbott, G. Capper, D. L. Davies, H. L. Munro, R. K. Rasheed, and V. Tambyrajah, "Preparation of novel, moisture-stable, Lewis-acidic ionic liquids containing quaternary ammonium salts with functional side chains.," *Chemical Communications*, pp. 2010–2011, 2001.

[47] M. M. Buckley and P. Benfield, "Eutectic lidocaine/prilocaine cream," *Drugs*, vol. 46, no. 1, pp. 126–151, 1993.

[48] A. P. Abbott, G. Capper, D. L. Davies, R. K. Rasheed, and V. Tambyrajah, "Novel solvent properties of choline chloride/urea mixtures," *Chemical Communications*, pp. 70–71, 2003.

[49] H. Zhang, Y. Wang, K. Xu, N. Li, Q. Wen, Q. Yang, and Y. Zhou, "Ternary and binary deep eutectic solvents as a novel extraction medium for protein partitioning," *Analytical Methods*, vol. 8, no. 46, pp. 8196–8207, 2016.

[50] F.-Y. Zhong, H.-L. Peng, D.-J. Tao, P.-K. Wu, J.-P. Fan, and K. Huang, "Phenol-based ternary deep eutectic solvents for highly efficient and reversible absorption of NH_3," *ACS Sustainable Chemistry & Engineering*, vol. 7, no. 3, pp. 3258–3266, 2019.

[51] E. L. Smith, A. P. Abbott, and K. S. Ryder, "Deep eutectic solvents (DESs) and their applications," *Chemical Reviews*, vol. 114, pp. 11060–11082, 2014.

[52] Y. H. Choi, J. van Spronsen, Y. Dai, M. Verberne, F. Hollmann, I. W. Arends, G.-J. Witkamp, and R. Verpoorte, "Are natural deep eutectic solvents the missing link in understanding cellular metabolism and physiology?," *Plant Physiology*, vol. 156, no. 4, pp. 1701–1705, 2011.

[53] Y. Liu, J. Garzon, J. B. Friesen, Y. Zhang, J. B. McAlpine, D. C. Lankin, S.-N. Chen, and G. F. Pauli, "Countercurrent assisted quantitative recovery of metabolites from plant-associated natural deep eutectic solvents," *Fitoterapia*, vol. 112, pp. 30–37, 2016.

[54] I. M. Aroso, J. C. Silva, F. Mano, A. S. Ferreira, M. Dionísio, I. Sá-Nogueira, S. Barreiros, R. L. Reis, A. Paiva, and A. R. C. Duarte, "Dissolution enhancement of active pharmaceutical ingredients by therapeutic deep eutectic systems," *European Journal of Pharmaceutics and Biopharmaceutics*, vol. 98, pp. 57–66, 2016.

[55] A. P. Abbott, D. Boothby, G. Capper, D. L. Davies, and R. K. Rasheed, "Deep eutectic solvents formed between choline chloride and carboxylic acids: versatile alternatives to ionic liquids," *Journal of the American Chemical Society*, vol. 126, no. 29, pp. 9142–9147, 2004.

[56] X. Meng, K. Ballerat-Busserolles, P. Husson, and J.-M. Andanson, "Impact of water on the melting temperature of urea+choline chloride deep eutectic solvent," *New Journal of Chemistry*, vol. 40, no. 5, pp. 4492–4499, 2016.

[57] R. K. Ibrahim, M. Hayyan, M. A. Al Saadi, S. Ibrahim, A. Hayyan, and M. A. Hashim, "Physical properties of ethylene glycol-based deep eutectic solvents," *Journal of Molecular Liquids*, vol. 276, pp. 794–800, 2019.

[58] Y. Qiao, H.-L. Cai, X. Yang, Y.-Y. Zang, and Z.-G. Chen, "Effects of natural deep eutectic solvents on lactic acid bacteria viability during cryopreservation," *Applied Microbiology and Biotechnology*, vol. 102, no. 13, pp. 5695–5705, 2018.

[59] M. Francisco, A. van den Bruinhorst, and M. C. Kroon, "Low-transition-temperature mixtures (LTTMs): A new generation of designer solvents," *Angewandte Chemie International Edition*, vol. 52, no. 11, pp. 3074–3085, 2013.

[60] A. P. Abbott, R. C. Harris, K. S. Ryder, C. D'Agostino, L. F. Gladden, and M. D. Mantle, "Glycerol eutectics as sustainable solvent systems," *Green Chemistry*, vol. 13, no. 1, pp. 82–90, 2011.

[61] A. Hayyan, F. S. Mjalli, I. M. AlNashef, T. Al-Wahaibi, Y. M. Al-Wahaibi, and M. A. Hashim, "Fruit sugar-based deep eutectic solvents and their physical properties," *Thermochimica Acta*, vol. 541, pp. 70–75, 2012.

[62] J. A. Coutinho and S. P. Pinho, "Special issue on deep eutectic solvents: a foreword," *Fluid Phase Equilibria*, vol. 448, no. 1, 2017.

[63] M. A. Martins, S. P. Pinho, and J. A. Coutinho, "Insights into the nature of eutectic and deep eutectic mixtures," *Journal of Solution Chemistry*, vol. 48, no. 7, pp. 962–982, 2019.

[64] A. Alhadid, L. Mokrushina, and M. Minceva, "Design of deep eutectic systems: A simple approach for preselecting eutectic mixture constituents," *Molecules*, vol. 25, no. 5, 2020.

[65] H. G. Morrison, C. C. Sun, and S. Neervannan, "Characterization of thermal behavior of deep eutectic solvents and their potential as drug solubilization vehicles," *International Journal of Pharmaceutics*, vol. 378, no. 1-2, pp. 136–139, 2009.

[66] A. P. Abbott, C. D'Agostino, S. J. Davis, L. Gladden, and M. Mantle, "Do group 1 metal salts form deep eutectic solvents?," *Physical Chemistry Chemical Physics*, vol. 18, no. 36, pp. 25528–25537, 2016.

[67] D. J. Van Osch, C. H. Dietz, S. E. Warrag, and M. C. Kroon, “The curious case of hydrophobic deep eutectic solvents: A story on the discovery, design, and applications,” *ACS Sustainable Chemistry & Engineering*, vol. 8, no. 29, pp. 10591–10612, 2020.

[68] C. Florindo, F. S. Oliveira, L. P. N. Rebelo, A. M. Fernandes, and I. M. Marrucho, “Insights into the synthesis and properties of deep eutectic solvents based on cholinium chloride and carboxylic acids,” *ACS Sustainable Chemistry & Engineering*, vol. 2, no. 10, pp. 2416–2425, 2014.

[69] M. C. Gutierrez, M. L. Ferrer, C. R. Mateo, and F. del Monte, “Freeze-drying of aqueous solutions of deep eutectic solvents: a suitable approach to deep eutectic suspensions of self-assembled structures,” *Langmuir*, vol. 25, no. 10, pp. 5509–5515, 2009.

[70] M. C. Gutiérrez, D. Carriazo, A. Tamayo, R. Jiménez, F. Picó, J. M. Rojo, M. L. Ferrer, and F. del Monte, “Deep-eutectic-solvent-assisted synthesis of hierarchical carbon electrodes exhibiting capacitance retention at high current densities,” *Chemistry–A European Journal*, vol. 17, no. 38, pp. 10533–10537, 2011.

[71] L. I. Tome, V. Baiao, W. da Silva, and C. M. Brett, “Deep eutectic solvents for the production and application of new materials,” *Applied Materials Today*, vol. 10, pp. 30–50, 2018.

[72] B. Tang and K. H. Row, “Recent developments in deep eutectic solvents in chemical sciences,” *Monatshefte für Chemie*, vol. 144, no. 10, pp. 1427–1454, 2013.

[73] R. J. Nunes, B. Saramago, and I. M. Marrucho, “Surface tension of dl-menthol: octanoic acid eutectic mixtures,” *Journal of Chemical & Engineering Data*, vol. 64, no. 11, pp. 4915–4923, 2019.

[74] G. Di Carmine, A. P. Abbott, and C. D’Agostino, “Deep eutectic solvents: alternative reaction media for organic oxidation reactions,” *Reaction Chemistry & Engineering*, vol. 6, no. 4, pp. 582–598, 2021.

[75] O. S. Hammond, D. T. Bowron, and K. J. Edler, “Liquid structure of the choline chloride-urea deep eutectic solvent (reline) from neutron diffraction and atomistic modelling,” *Green Chemistry*, vol. 18, no. 9, pp. 2736–2744, 2016.

[76] M. Hayyan, M. A. Hashim, A. Hayyan, M. A. Al-Saadi, I. M. AlNashef, M. E. Mirghani, and O. K. Saheed, “Are deep eutectic solvents benign or toxic?,” *Chemosphere*, vol. 90, no. 7, pp. 2193–2195, 2013.

[77] I. Juneidi, M. Hayyan, and M. A. Hashim, “Evaluation of toxicity and biodegradability for cholinium-based deep eutectic solvents,” *RSC Advances*, vol. 5, no. 102, pp. 83636–83647, 2015.

[78] K. Radošević, M. C. Bubalo, V. G. Srček, D. Grgas, T. L. Dragičević, and I. R. Redovniković, “Evaluation of toxicity and biodegradability of choline chloride based deep eutectic solvents,” *Ecotoxicology and Environmental Safety*, vol. 112, pp. 46–53, 2015.

[79] K. Radošević, I. Čanak, M. Panić, K. Markov, M. C. Bubalo, J. Frece, V. G. Srček, and I. R. Redovniković, “Antimicrobial, cytotoxic and antioxidative evaluation of natural deep eutectic solvents,” *Environmental Science and Pollution Research*, vol. 25, no. 14, pp. 14188–14196, 2018.

[80] A. K. Halder and M. N. D. Cordeiro, “Probing the environmental toxicity of deep eutectic solvents and their components: An *in-silico* modeling approach,” *ACS Sustainable Chemistry & Engineering*, vol. 7, no. 12, pp. 10649–10660, 2019.

[81] M. Bystrzanowska and M. Tobiszewski, “Assessment and design of greener deep eutectic solvents–a multicriteria decision analysis,” *Journal of Molecular Liquids*, vol. 321, 2021.

[82] V. De Santi, F. Cardellini, L. Brinchi, and R. Germani, “Novel Brønsted acidic deep eutectic solvent as reaction media for esterification of carboxylic acid with alcohols,” *Tetrahedron Letters*, vol. 53, no. 38, pp. 5151–5155, 2012.

[83] S. Yasmin, W.-B. Sheng, C.-Y. Peng, A.-u. Rahman, D.-F. Liao, M. I. Choudhary, and W. Wanga, "Highly efficient and green esterification of carboxylic acids in deep eutectic solvents without any other additives," *Synthetic Communications*, vol. 48, no. 1, pp. 68–75, 2018.

[84] Y. Pan, M. A. Alam, Z. Wang, J. Wu, Y. Zhang, and Z. Yuan, "Enhanced esterification of oleic acid and methanol by deep eutectic solvent assisted amberlyst heterogeneous catalyst," *Bioresource Technology*, vol. 220, pp. 543–548, 2016.

[85] S. Khandelwal, Y. K. Tailor, and M. Kumar, "Deep eutectic solvents (DESs) as eco-friendly and sustainable solvent/catalyst systems in organic transformations," *Journal of Molecular Liquids*, vol. 215, pp. 345–386, 2016.

[86] G. Imperato, E. Eibler, J. Niedermaier, and B. König, "Low-melting sugar–urea–salt mixtures as solvents for Diels–Alder reactions," *Chemical Communications*, no. 9, pp. 1170–1172, 2005.

[87] C. M. Le, X. T. Cao, T. T. Tu, W.-K. Lee, and K. T. Lim, "Facile covalent functionalization of carbon nanotubes via diels–alder reaction in deep eutectic solvents," *Applied Surface Science*, vol. 450, pp. 122–129, 2018.

[88] C. Vidal, L. Merz, and J. García-Álvarez, "Deep eutectic solvents: biorenewable reaction media for Au(I)-catalysed cycloisomerisations and one-pot tandem cycloisomerisation/Diels–Alder reactions," *Green Chemistry*, vol. 17, no. 7, pp. 3870–3878, 2015.

[89] S. B. Phadtare and G. S. Shankarling, "Halogenation reactions in biodegradable solvent: Efficient bromination of substituted 1-aminoanthra-9, 10-quinone in deep eutectic solvent (choline chloride: urea)," *Green Chemistry*, vol. 12, no. 3, pp. 458–462, 2010.

[90] N. Azizi and E. Batebi, "Highly efficient deep eutectic solvent catalyzed ring opening of epoxides," *Catalysis Science & Technology*, vol. 2, no. 12, pp. 2445–2448, 2012.

[91] L. Wang, D.-Y. Dai, Q. Chen, and M.-Y. He, "Rapid, sustainable, and gram-scale synthesis of phenols catalyzed by a biodegradable deep eutectic mixture in water," *Asian Journal of Organic Chemistry*, vol. 2, no. 12, pp. 1040–1043, 2013.

[92] C. Vidal, J. García-Álvarez, A. Hernán-Gómez, A. R. Kennedy, and E. Hevia, "Introducing deep eutectic solvents to polar organometallic chemistry: chemoselective addition of organolithium and Grignard reagents to ketones in air," *Angewandte Chemie*, vol. 126, pp. 6079–6083, 2014.

[93] L. Cicco, S. Sblendorio, R. Mansueto, F. M. Perna, A. Salomone, S. Florio, and V. Capriati, "Water opens the door to organolithiums and Grignard reagents: exploring and comparing the reactivity of highly polar organometallic compounds in unconventional reaction media towards the synthesis of tetrahydrofurans," *Chemical Science*, vol. 7, no. 2, pp. 1192–1199, 2016.

[94] X. Marset, A. Khoshnood, L. Sotorríos, E. Gómez-Bengoa, D. A. Alonso, and D. J. Ramón, "Deep eutectic solvent compatible metallic catalysts: Cationic pyridiniophosphine ligands in palladium catalyzed cross-coupling reactions," *ChemCatChem*, vol. 9, no. 7, pp. 1269–1275, 2017.

[95] B. Saavedra, N. González-Gallardo, A. Meli, and D. J. Ramón, "A bipyridine-palladium derivative as general pre-catalyst for cross-coupling reactions in deep eutectic solvents," *Advanced Synthesis & Catalysis*, vol. 361, no. 16, pp. 3868–3879, 2019.

[96] I. Juneidi, M. Hayyan, and M. A. Hashim, "Intensification of biotransformations using deep eutectic solvents: Overview and outlook," *Process Biochemistry*, vol. 66, pp. 33–60, 2018.

[97] V. Gotor-Fernández and C. E. Paul, "Deep eutectic solvents for redox biocatalysis," *Journal of Biotechnology*, vol. 293, pp. 24–35, 2019.

[98] M. Pätzold, A. Weimer, A. Liese, and D. Holtmann, "Optimization of solvent-free enzymatic esterification in eutectic substrate reaction mixture," *Biotechnology Reports*, vol. 22, 2019.

[99] N. Ndizeye, S. Suriyanarayanan, and I. A. Nicholls, "Polymer synthesis in non-ionic deep eutectic solvents," *Polymer Chemistry*, vol. 10, no. 39, pp. 5289–5295, 2019.

[100] G. Colomines, P. Decaen, D. Lourdin, and E. Leroy, "Biofriendly ionic liquids for starch plasticization: a screening approach," *RSC Advances*, vol. 6, no. 93, pp. 90331–90337, 2016.

[101] S. Wang, X. Peng, L. Zhong, S. Jing, X. Cao, F. Lu, and R. Sun, "Choline chloride/urea as an effective plasticizer for production of cellulose films," *Carbohydrate Polymers*, vol. 117, pp. 133–139, 2015.

[102] P. Decaen, A. Rolland-Sabaté, S. Guilois, V. Jury, N. Allanic, G. Colomines, D. Lourdin, and E. Leroy, "Choline chloride vs choline ionic liquids for starch thermoplasticization," *Carbohydrate Polymers*, vol. 177, pp. 424–432, 2017.

[103] W. S. A. Rahma, F. S. Mjalli, T. Al-Wahaibi, and A. A. Al-Hashmi, "Polymeric-based deep eutectic solvents for effective extractive desulfurization of liquid fuel at ambient conditions," *Chemical Engineering Research and Design*, vol. 120, pp. 271–283, 2017.

[104] K. F. Fazende, M. Phachansitthi, J. D. Mota-Morales, and J. A. Pojman, "Frontal polymerization of deep eutectic solvents composed of acrylic and methacrylic acids," *Journal of Polymer Science Part A: Polymer Chemistry*, vol. 55, no. 24, pp. 4046–4050, 2017.

[105] F.-P. Ma, G.-T. Cheng, Z.-G. He, and Z.-H. Zhang, "A new and efficient procedure for friedlaender synthesis of quinolines in low melting tartaric acid-urea mixtures," *Australian Journal of Chemistry*, vol. 65, no. 4, pp. 409–416, 2012.

[106] S. Gore, S. Baskaran, and B. Koenig, "Synthesis of pyrimidopyrimidinediones in a deep eutectic reaction mixture," *Advanced Synthesis & Catalysis*, vol. 354, no. 13, pp. 2368–2372, 2012.

[107] Z. Liang, H. Zheng, and R. Cao, "Importance of electrocatalyst morphology for the oxygen reduction reaction," *ChemElectroChem*, vol. 6, no. 10, pp. 2600–2614, 2019.

[108] E. R. Cooper, C. D. Andrews, P. S. Wheatley, P. B. Webb, P. Wormald, and R. E. Morris, "Ionic liquids and eutectic mixtures as solvent and template in synthesis of zeolite analogues," *Nature*, vol. 430, no. 7003, pp. 1012–1016, 2004.

[109] E. R. Parnham, E. A. Drylie, P. S. Wheatley, A. M. Slawin, and R. E. Morris, "Ionothermal materials synthesis using unstable deep-eutectic solvents as template-delivery agents," *Angewandte Chemie*, vol. 118, no. 30, pp. 5084–5088, 2006.

[110] H. Zhang, Y. Lu, C.-D. Gu, X.-L. Wang, and J.-P. Tu, "Ionothermal synthesis and lithium storage performance of core/shell structured amorphous@crystalline Ni-P nanoparticles," *CrystEngComm*, vol. 14, no. 23, pp. 7942–7950, 2012.

[111] Z. Wu, Y. F. Long, X. Lv, J. Su, and Y. Wen, "Microwave heating synthesis of spindle-like $LiMnPO_4$/c in a deep eutectic solvent," *Ceramics International*, vol. 43, no. 8, pp. 6089–6095, 2017.

[112] J. Jiang, C. Yan, X. Zhao, H. Luo, Z. Xue, and T. Mu, "A PEGylated deep eutectic solvent for controllable solvothermal synthesis of porous $NiCo_2S_4$ for efficient oxygen evolution reaction," *Green Chemistry*, vol. 19, no. 13, pp. 3023–3031, 2017.

[113] J.-Y. Dong, Y.-J. Hsu, D. S.-H. Wong, and S.-Y. Lu, "Growth of ZnO nanostructures with controllable morphology using a facile green antisolvent method," *The Journal of Physical Chemistry C*, vol. 114, no. 19, pp. 8867–8872, 2010.

[114] L. Hu, Z. Yan, J. Zhang, X. Peng, X. Mo, A. Wang, and L. Chen, "Surfactant aggregates within deep eutectic solvent-assisted synthesis of hierarchical ZIF–8 with tunable porosity and enhanced catalytic activity," *Journal of Materials Science*, vol. 54, no. 16, pp. 11009–11023, 2019.

[115] O. S. Hammond, K. J. Edler, D. T. Bowron, and L. Torrente-Murciano, "Deep eutectic-solvothermal synthesis of nanostructured ceria," *Nature Communications*, vol. 8, no. 1, pp. 1–7, 2017.

[116] O. S. Hammond, R. S. Atri, D. T. Bowron, L. De Campo, S. Diaz-Moreno, L. L. Keenan, J. Doutch, S. Eslava, and K. J. Edler, “Structural evolution of iron forming iron oxide in a deep eutectic-solvothermal reaction,” *Nanoscale*, vol. 13, no. 3, pp. 1723–1737, 2021.

[117] K. Radošević, N. Ćurko, V. G. Srček, M. C. Bubalo, M. Tomašević, K. K. Ganić, and I. R. Redovniković, “Natural deep eutectic solvents as beneficial extractants for enhancement of plant extracts bioactivity,” *LWT*, vol. 73, pp. 45–51, 2016.

[118] Z. Wei, X. Qi, T. Li, M. Luo, W. Wang, Y. Zu, and Y. Fu, “Application of natural deep eutectic solvents for extraction and determination of phenolics in Cajanus cajan leaves by ultra performance liquid chromatography,” *Separation and Purification Technology*, vol. 149, pp. 237–244, 2015.

[119] Z.-F. Wei, X.-Q. Wang, X. Peng, W. Wang, C.-J. Zhao, Y.-G. Zu, and Y.-J. Fu, “Fast and green extraction and separation of main bioactive flavonoids from radix scutellariae,” *Industrial Crops and Products*, vol. 63, pp. 175–181, 2015.

[120] L. Duan, L.-L. Dou, L. Guo, P. Li, and E.-H. Liu, “Comprehensive evaluation of deep eutectic solvents in extraction of bioactive natural products,” *ACS Sustainable Chemistry & Engineering*, vol. 4, no. 4, pp. 2405–2411, 2016.

[121] B. Xia, D. Yan, Y. Bai, J. Xie, Y. Cao, D. Liao, and L. Lin, “Determination of phenolic acids in *Prunella vulgaris L.*: a safe and green extraction method using alcohol-based deep eutectic solvents,” *Analytical Methods*, vol. 7, no. 21, pp. 9354–9364, 2015.

[122] Y. Gu, Y. Hou, S. Ren, Y. Sun, and W. Wu, “Hydrophobic functional deep eutectic solvents used for efficient and reversible capture of CO_2,” *ACS Omega*, vol. 5, no. 12, pp. 6809–6816, 2020.

[123] C. Ma, S. Sarmad, J.-P. Mikkola, and X. Ji, “Development of low-cost deep eutectic solvents for CO_2 capture,” *Energy Procedia*, vol. 142, pp. 3320–3325, 2017.

[124] A. Krishnan, K. P. Gopinath, D.-V. N. Vo, R. Malolan, V. M. Nagarajan, and J. Arun, “Ionic liquids, deep eutectic solvents and liquid polymers as green solvents in carbon capture technologies: a review,” *Environmental Chemistry Letters*, pp. 1–24, 2020.

[125] D. Jha, M. B. Haider, R. Kumar, and M. S. Balathanigaimani, “Extractive desulfurization of fuels using diglycol based deep eutectic solvents,” *Journal of Environmental Chemical Engineering*, vol. 8, no. 5, 2020.

[126] M. Rezaee, F. Feyzi, and M. R. Dehghani, “Extractive desulfurization of dibenzothiophene from normal octane using deep eutectic solvents as extracting agent,” *Journal of Molecular Liquids*, vol. 333, 2021.

[127] J. A. Hammons, T. Muselle, J. Ustarroz, M. Tzedaki, M. Raes, A. Hubin, and H. Terryn, “Stability, assembly, and particle/solvent interactions of pd nanoparticles electrodeposited from a deep eutectic solvent,” *The Journal of Physical Chemistry C*, vol. 117, no. 27, pp. 14381–14389, 2013.

[128] Y. Song, J. Tang, J. Hu, H. Yang, W. Gu, Y. Fu, and X. Ji, “Interfacial assistant role of amine additives on zinc electrodeposition from deep eutectic solvents: an in-situ X-ray imaging investigation,” *Electrochimica Acta*, vol. 240, pp. 90–97, 2017.

[129] A. P. Abbott, A. Ballantyne, R. C. Harris, J. A. Juma, and K. S. Ryder, “Bright metal coatings from sustainable electrolytes: the effect of molecular additives on electrodeposition of nickel from a deep eutectic solvent,” *Physical Chemistry Chemical Physics*, vol. 19, no. 4, pp. 3219–3231, 2017.

[130] N. M. Pereira, C. M. Pereira, J. P. Araujo, and A. F. Silva, “Electrodeposition of an ultrathin TiO_2 coating using a deep eutectic solvent based on choline chloride,” *Thin Solid Films*, vol. 645, pp. 391–398, 2018.

[131] S. Fashu, C. Gu, X. Wang, and J. Tu, “Structure, composition and corrosion resistance of Zn-Ni-P alloys electrodeposited from an ionic liquid based on choline chloride,” *Journal of the Electrochemical Society*, vol. 161, no. 7, 2014.

[132] A. M. Sakita, R. Della Noce, C. S. Fugivara, and A. V. Benedetti, "On the cobalt and cobalt oxide electrodeposition from a glyceline deep eutectic solvent," *Physical Chemistry Chemical Physics*, vol. 18, no. 36, pp. 25048–25057, 2016.

[133] A. J. Jackson, "Introduction to the theory of small-angle neutron scattering and neutron reflectometry," tech. rep., NIST Center for Neutron Research, 2008.

[134] L. De Broglie, "Waves and quanta," *Nature*, vol. 112, no. 2815, pp. 540–540, 1923.

[135] L. Feigin, D. I. Svergun, *et al.*, *Structure analysis by small-angle X-ray and neutron scattering*. Springer, 1987.

[136] P. Duke, *Synchrotron radiation: production and properties*, vol. 3. Oxford University Press, 2008.

[137] G. Materlik, T. Rayment, and D. I. Stuart, "Diamond light source: status and perspectives," *Philosophical Transactions of the Royal Society A: Mathematical, Physical and Engineering Sciences*, vol. 373, no. 2036, 2015.

[138] C. J. Carlile, *Reactor Overview*, ch. 5, pp. 621–642. John Wiley & Sons, Ltd, 2011.

[139] G. S. Bauer, "Physics and technology of spallation neutron sources," *Nuclear Instruments and Methods in Physics Research Section A: Accelerators, Spectrometers, Detectors and Associated Equipment*, vol. 463, no. 3, pp. 505–543, 2001.

[140] "ISIS Neutron and Muon Source - Characteristics of a pulsed source." `https://www.isis.stfc.ac.uk/Pages/Characteristics-of-a-pulsed-source.aspx`. Accessed: October 2021.

[141] "NIST Inorganic Crystal Structure Database." `https://icsd.nist.gov/`. Accessed: February 2022.

[142] M. R. Mansor, Z. Mustafa, S. H. S. M. Fadzullah, G. Omar, M. A. Salim, and M. Z. Akop, "Recent advances in polyethylene-based biocomposites," *Natural Fibre Reinforced Vinyl Ester and Vinyl Polymer Composites*, pp. 71–96, 2018.

[143] J. S. Evans and I. R. Evans, "Structure analysis from powder diffraction data: Rietveld refinement in Excel," *Journal of Chemical Education*, vol. 98, no. 2, pp. 495–505, 2020.

[144] K. Akhtar, S. A. Khan, S. B. Khan, and A. M. Asiri, "Scanning electron microscopy: principle and applications in nanomaterials characterization," in *Handbook of Materials Characterization*, pp. 113–145, Springer, 2018.

[145] S. R. Kline, "Reduction and analysis of SANS and USANS data using Igor Pro," *Journal of Applied Crystallography*, vol. 39, no. 6, pp. 895–900, 2006.

[146] J. P. Hallett and T. Welton, "Room-temperature ionic liquids: solvents for synthesis and catalysis," *Chemical Reviews*, vol. 111, no. 5, pp. 3508–3576, 2011.

[147] J. A. Darr, J. Zhang, N. M. Makwana, and X. Weng, "Continuous hydrothermal synthesis of inorganic nanoparticles: applications and future directions," *Chemical Reviews*, vol. 117, no. 17, pp. 11125–11238, 2017.

[148] G. Demazeau, "Solvothermal processes: new trends in materials chemistry," in *Journal of Physics: Conference Series*, vol. 121, IOP Publishing, 2008.

[149] E. A. Drylie, D. S. Wragg, E. R. Parnham, P. S. Wheatley, A. M. Slawin, J. E. Warren, and R. E. Morris, "Ionothermal synthesis of unusual choline-templated cobalt aluminophosphates," *Angewandte Chemie*, vol. 119, no. 41, pp. 7985–7989, 2007.

[150] H. Wen, Y. Zhou, J. Xie, Z. Long, W. Zhang, and J. Wang, "Pure-silica ZSM-22 zeolite rapidly synthesized by novel ionic liquid-directed dry-gel conversion," *RSC Advances*, vol. 4, no. 91, pp. 49647–49654, 2014.

[151] A. Sachse, C. Wuttke, E. Lissner, and M. Oberson de Souza, "Ordered mesoporous ZSM-5 employing an imidazolium-based ionic liquid," *Chemistry–A European Journal*, vol. 20, no. 46, pp. 14996–14999, 2014.

[152] Z. S. Lin and Y. Huang, "Syntheses of high-silica zeolites in urea/choline chloride deep eutectic solvent," *Canadian Journal of Chemistry*, vol. 94, no. 6, pp. 533–540, 2016.

[153] Z. S. Lin and Y. Huang, "Tetraalkylammonium salt/alcohol mixtures as deep eutectic solvents for syntheses of high-silica zeolites," *Microporous and Mesoporous Materials*, vol. 224, pp. 75–83, 2016.

[154] M. C. Gutiérrez, F. Rubio, and F. Del Monte, "Resorcinol-formaldehyde polycondensation in deep eutectic solvents for the preparation of carbons and carbon- carbon nanotube composites," *Chemistry of Materials*, vol. 22, no. 9, pp. 2711–2719, 2010.

[155] D. Carriazo, M. C. Gutierrez, M. L. Ferrer, and F. del Monte, "Resorcinol-based deep eutectic solvents as both carbonaceous precursors and templating agents in the synthesis of hierarchical porous carbon monoliths," *Chemistry of Materials*, vol. 22, no. 22, pp. 6146–6152, 2010.

[156] N. López-Salas, M. C. Gutiérrez, C. O. Ania, M. A. Muñoz-Márquez, M. L. Ferrer, and F. Del Monte, "Nitrogen-doped carbons prepared from eutectic mixtures as metal-free oxygen reduction catalysts," *Journal of Materials Chemistry A*, vol. 4, no. 2, pp. 478–488, 2015.

[157] N. López-Salas, E. O. Jardim, A. Silvestre-Albero, M. C. Gutiérrez, M. L. Ferrer, F. Rodríguez-Reinoso, J. Silvestre-Albero, and F. Del Monte, "Use of eutectic mixtures for preparation of monolithic carbons with CO_2-adsorption and gas-separation capabilities," *Langmuir*, vol. 30, no. 41, pp. 12220–12228, 2014.

[158] Z. Wu, R.-R. Huang, H. Yu, Y.-C. Xie, X.-Y. Lv, J. Su, Y.-F. Long, and Y.-X. Wen, "Deep eutectic solvent synthesis of $LiMnPO_4/C$ nanorods as a cathode material for lithium ion batteries," *Materials*, vol. 10, no. 2, p. 134, 2017.

[159] S. Ravichandran and E. Karthikeyan, "Microwave synthesis-a potential tool for green chemistry," *International Journal of ChemTech Research*, vol. 3, no. 1, pp. 466–70, 2011.

[160] V. Chikan and E. J. McLaurin, "Rapid nanoparticle synthesis by magnetic and microwave heating," *Nanomaterials*, vol. 6, no. 5, 2016.

[161] L. Adhikari, N. E. Larm, N. Bhawawet, and G. A. Baker, "Rapid microwave-assisted synthesis of silver nanoparticles in a halide-free deep eutectic solvent," *ACS Sustainable Chemistry & Engineering*, vol. 6, no. 5, pp. 5725–5731, 2018.

[162] G. M. Thorat, H. S. Jadhav, W.-J. Chung, and J. G. Seo, "Collective use of deep eutectic solvent for one-pot synthesis of ternary Sn/SnO_2@C electrode for supercapacitor," *Journal of Alloys and Compounds*, vol. 732, pp. 694–704, 2018.

[163] O. S. Hammond, D. T. Bowron, and K. J. Edler, "Structure and properties of "Type IV" lanthanide nitrate hydrate: urea deep eutectic solvents," *ACS Sustainable Chemistry & Engineering*, vol. 7, no. 5, pp. 4932–4940, 2019.

[164] H.-G. Liao, Y.-X. Jiang, Z.-Y. Zhou, S.-P. Chen, and S.-G. Sun, "Shape-controlled synthesis of gold nanoparticles in deep eutectic solvents for studies of structure–functionality relationships in electrocatalysis," *Angewandte Chemie International Edition*, vol. 47, no. 47, pp. 9100–9103, 2008.

[165] S. K. Krishnan and Y. Chipatecua Godoy, "Deep eutectic solvent-assisted synthesis of au nanostars supported on graphene oxide as an efficient substrate for SERS-based molecular sensing," *ACS Omega*, vol. 5, no. 3, pp. 1384–1393, 2019.

[166] V. S. Raghuwanshi, M. Ochmann, A. Hoell, F. Polzer, and K. Rademann, "Deep eutectic solvents for the self-assembly of gold nanoparticles: a SAXS, UV–Vis, and TEM investigation," *Langmuir*, vol. 30, no. 21, pp. 6038–6046, 2014.

[167] D. V. Wagle, H. Zhao, and G. A. Baker, "Deep eutectic solvents: sustainable media for nanoscale and functional materials," *Accounts of Chemical Research*, vol. 47, no. 8, pp. 2299–2308, 2014.

[168] J.-Y. Dong, C.-H. Lin, Y.-J. Hsu, S.-Y. Lu, and D. S.-H. Wong, “Single-crystalline mesoporous ZnO nanosheets prepared with a green antisolvent method exhibiting excellent photocatalytic efficiencies,” *CrystEngComm*, vol. 14, no. 14, pp. 4732–4737, 2012.

[169] X. Ge, C. Gu, X. Wang, and J. Tu, “Spinel type CoFe oxide porous nanosheets as magnetic adsorbents with fast removal ability and facile separation,” *Journal of Colloid and Interface Science*, vol. 454, pp. 134–143, 2015.

[170] X. Ge, C. Gu, X. Wang, and J. Tu, “Ionothermal synthesis of cobalt iron layered double hydroxides (LDHs) with expanded interlayer spacing as advanced electrochemical materials,” *Journal of Materials Chemistry A*, vol. 2, no. 40, pp. 17066–17076, 2014.

[171] X. Ge, C. Gu, X. Wang, and J. Tu, “Anomalous self-reduction of layered double hydroxide (LDH): from α-Ni(OH)$_2$ to hexagonal close packing (HCP) Ni/NiO by annealing without a reductant,” *Chemical Communications*, vol. 51, no. 6, pp. 1004–1007, 2015.

[172] Q. Xiong, J. Tu, X. Ge, X. Wang, and C. Gu, “One-step synthesis of hematite nanospindles from choline chloride/urea deep eutectic solvent with highly powerful storage versus lithium,” *Journal of Power Sources*, vol. 274, pp. 1–7, 2015.

[173] F. Chen, S. Xie, J. Zhang, and R. Liu, “Synthesis of spherical Fe_3O_4 magnetic nanoparticles by co-precipitation in choline chloride/urea deep eutectic solvent,” *Materials Letters*, vol. 112, pp. 177–179, 2013.

[174] J. N. Baby, B. Sriram, S.-F. Wang, and M. George, “Effect of various deep eutectic solvents on the sustainable synthesis of mgfe2o4 nanoparticles for simultaneous electrochemical determination of nitrofurantoin and 4-nitrophenol,” *ACS Sustainable Chemistry & Engineering*, vol. 8, no. 3, pp. 1479–1486, 2020.

[175] S. Hong, R. M. Doughty, F. E. Osterloh, and J. V. Zaikina, “Deep eutectic solvent route synthesis of zinc and copper vanadate n-type semiconductors–mapping oxygen vacancies and their effect on photovoltage,” *Journal of Materials Chemistry A*, vol. 7, no. 19, pp. 12303–12316, 2019.

[176] R. Boston, P. Y. Foeller, D. C. Sinclair, and I. M. Reaney, “Synthesis of barium titanate using deep eutectic solvents,” *Inorganic Chemistry*, vol. 56, no. 1, pp. 542–547, 2017.

[177] O. Gómez Rojas and T. Nakayama, “Synthesis and characterisation of metal oxide nanostructures using choline/linear alkyl carboxylate deep eutectic solvents,” *Solids*, vol. 1, no. 1, pp. 31–46, 2020.

[178] O. G. Rojas, T. Nakayama, and S. R. Hall, “Green and cost-effective synthesis of the superconductor BSCCO (Bi-2212), using a natural deep eutectic solvent,” *Ceramics International*, vol. 45, no. 7, pp. 8546–8552, 2019.

[179] H. Zhao, J. Xu, Q. Sheng, J. Zheng, W. Cao, and T. Yue, “$NiCo_2O_4$ nanorods decorated MoS_2 nanosheets synthesized from deep eutectic solvents and their application for electrochemical sensing of glucose in red wine and honey,” *Journal of The Electrochemical Society*, vol. 166, no. 10, p. 404, 2019.

[180] D. P. Jaihindh and Y.-P. Fu, “Facile synthesis of deep eutectic solvent assisted BiOCl/BiVO$_4$@AgNWs plasmonic photocatalysts under visible light enhanced catalytic performance,” *Catalysis Today*, vol. 297, pp. 246–254, 2017.

[181] D. P. Jaihindh, A. Manikandan, Y.-L. Chueh, and Y.-P. Fu, “Deep eutectic solvent-assisted synthesis of ternary heterojunctions for the oxygen evolution reaction and photocatalysis,” *ChemSusChem*, vol. 13, no. 10, pp. 2726–2738, 2020.

[182] K.-Y. Wang, H.-W. Liu, S. Zhang, D. Ding, L. Cheng, and C. Wang, “Selenidostannates and a silver selenidostannate synthesized in deep eutectic solvents: crystal structures and thermochromic study,” *Inorganic Chemistry*, vol. 58, no. 5, pp. 2942–2953, 2019.

[183] T. Cai, J.-N. Zhu, F.-F. Cheng, P. Li, W. Li, M.-Y. Zhao, and W.-W. Xiong, “Growing crystalline selenidostannates in deep eutectic solvent,” *Inorganica Chimica Acta*, vol. 484, pp. 214–218, 2019.

[184] T. Zhang, T. Doert, and M. Ruck, “Synthesis of metal sulfides from a deep eutectic solvent precursor (DESP),” *Zeitschrift für Anorganische und Allgemeine Chemie*, vol. 643, no. 23, pp. 1913–1919, 2017.

[185] J. Jiang, L. Chang, W. Zhao, Q. Tian, and Q. Xu, “An advanced FeCoNi nitro-sulfide hierarchical structure from deep eutectic solvents for enhanced oxygen evolution reaction,” *Chemical Communications*, vol. 55, no. 68, pp. 10174–10177, 2019.

[186] K. Subalakshmi, K. A. Kumar, and J. Senthilselvan, “Effect of PEG as soft template in hydrothermal synthesis of porous TiO_2 nanoparticles for DSSC application,” *Materials Today: Proceedings*, vol. 4, no. 14, pp. 12545–12549, 2017.

[187] X. Zhao, X. Lan, D. Yu, H. Fu, Z. Liu, and T. Mu, “Deep eutectic-solvothermal synthesis of nanostructured Fe_3S_4 for electrochemical N_2 fixation under ambient conditions,” *Chemical Communications*, vol. 54, no. 92, pp. 13010–13013, 2018.

[188] A. J. Exposito, P. J. Barrie, and L. Torrente-Murciano, “Fast synthesis of CeO_2 nanoparticles in a continuous microreactor using deep eutectic reline as solvent,” *ACS Sustainable Chemistry & Engineering*, vol. 8, no. 49, pp. 18297–18302, 2020.

[189] X. Ge, C. Gu, X. Wang, and J. Tu, “Deep eutectic solvents (DESs)-derived advanced functional materials for energy and environmental applications: challenges, opportunities, and future vision,” *Journal of Materials Chemistry A*, vol. 5, no. 18, pp. 8209–8229, 2017.

[190] O. S. Hammond, D. T. Bowron, A. J. Jackson, T. Arnold, A. Sanchez-Fernandez, N. Tsapatsaris, V. Garcia Sakai, and K. J. Edler, “Resilience of malic acid natural deep eutectic solvent nanostructure to solidification and hydration,” *The Journal of Physical Chemistry B*, vol. 121, no. 31, pp. 7473–7483, 2017.

[191] A. Querejeta-Fernández, J. C. Hernández-Garrido, H. Yang, Y. Zhou, A. Varela, M. Parras, J. J. Calvino-Gámez, J. M. González-Calbet, P. F. Green, and N. A. Kotov, “Unknown aspects of self-assembly of PbS microscale superstructures,” *ACS Nano*, vol. 6, no. 5, pp. 3800–3812, 2012.

[192] E. L. Smith, “Deep eutectic solvents (DESs) and the metal finishing industry: where are they now?,” *Transactions of the IMF*, vol. 91, no. 5, pp. 241–248, 2013.

[193] R. Bernasconi, G. Panzeri, A. Accogli, F. Liberale, L. Nobili, and L. Magagnin, “Electrodeposition from deep eutectic solvents,” in *Ionic Liquids* (S. Handy, ed.), ch. 11, Rijeka: IntechOpen, 2017.

[194] F. Nasirpouri, K. Alipour, F. Daneshvar, and M.-R. Sanaeian, “Electrodeposition of anticorrosion nanocoatings,” in *Corrosion Protection at the Nanoscale*, pp. 473–497, Elsevier, 2020.

[195] T. Green, X. Su, and S. Roy, “Pulse plating of copper from deep eutectic solvents,” *ECS Transactions*, vol. 77, no. 11, pp. 1247–1253, 2017.

[196] A. P. Abbott and K. J. McKenzie, “Application of ionic liquids to the electrodeposition of metals,” *Physical Chemistry Chemical Physics*, vol. 8, no. 37, pp. 4265–4279, 2006.

[197] X. Zhao, H. Wang, F. Chen, R. Mao, H. Liu, and J. Qu, “Efficient treatment of an electroplating wastewater containing heavy metal ions, cyanide, and organics by H_2O_2 oxidation followed by the anodic Fenton process,” *Water Science and Technology*, vol. 68, no. 6, pp. 1329–1335, 2013.

[198] M. T. A. Reis and M. R. C. Ismael, “Electroplating wastes,” *Physical Sciences Reviews*, vol. 3, no. 6, 2018.

[199] A. P. Abbott, K. S. Ryder, and U. König, “Electrofinishing of metals using eutectic based ionic liquids,” *Transactions of the IMF*, vol. 86, no. 4, pp. 196–204, 2008.

[200] J. Wang, P. Wang, Q. Wang, H. Mou, B. Cao, D. Yu, D. Wang, S. Zhang, and T. Mu, “Low temperature electrochemical deposition of aluminum in organic bases/thiourea-based deep eutectic solvents,” *ACS Sustainable Chemistry & Engineering*, vol. 6, no. 11, pp. 15480–15486, 2018.

[201] T. Schoetz, O. Leung, C. P. de Leon, C. Zaleski, and I. Efimov, “Aluminium deposition in EMImCl-$AlCl_3$ ionic liquid and ionogel for improved aluminium batteries,” *Journal of The Electrochemical Society*, vol. 167, no. 4, p. 040516, 2020.

[202] A. Bakkar and V. Neubert, “Electrodeposition onto magnesium in air and water stable ionic liquids: from corrosion to successful plating,” *Electrochemistry Communications*, vol. 9, no. 9, pp. 2428–2435, 2007.

[203] Y. D. Gamburg and G. Zangari, “Introduction to electrodeposition: Basic terms and fundamental concepts,” in *Theory and Practice of Metal Electrodeposition*, pp. 1–25, Springer, 2011.

[204] E. S. Ferreira, C. Pereira, and A. Silva, “Electrochemical studies of metallic chromium electrodeposition from a Cr(III) bath,” *Journal of Electroanalytical Chemistry*, vol. 707, pp. 52–58, 2013.

[205] T. Verdonck, P. Verpoort, J. De Strycker, A. De Cleene, D. Banerjee, P. Nockemann, R. Van Deun, and K. Van Hecke, “Chromium (III) in deep eutectic solvents: towards a sustainable chromium (VI)-free steel plating process,” *Green Chemistry*, vol. 21, no. 13, pp. 3637–3650, 2019.

[206] A. P. Abbott, G. Capper, D. L. Davies, R. K. Rasheed, J. Archer, and C. John, “Electrodeposition of chromium black from ionic liquids,” *Transactions of the IMF*, vol. 82, no. 1-2, pp. 14–17, 2004.

[207] A. P. Abbott, J. C. Barron, G. Frisch, S. Gurman, K. S. Ryder, and A. F. Silva, “Double layer effects on metal nucleation in deep eutectic solvents,” *Physical Chemistry Chemical Physics*, vol. 13, no. 21, pp. 10224–10231, 2011.

[208] E. L. Smith, J. C. Barron, A. P. Abbott, and K. S. Ryder, “Time resolved in situ liquid atomic force microscopy and simultaneous acoustic impedance electrochemical quartz crystal microbalance measurements: a study of Zn deposition,” *Analytical Chemistry*, vol. 81, no. 20, pp. 8466–8471, 2009.

[209] A. Abbott, K. El Ttaib, K. S. Ryder, and E. Smith, “Electrodeposition of nickel using eutectic based ionic liquids,” *Transactions of the IMF*, vol. 86, no. 4, pp. 234–240, 2008.

[210] C. Gu and J. Tu, “One-step fabrication of nanostructured Ni film with lotus effect from deep eutectic solvent,” *Langmuir*, vol. 27, no. 16, pp. 10132–10140, 2011.

[211] A. P. Abbott, K. El Ttaib, G. Frisch, K. J. McKenzie, and K. S. Ryder, “Electrodeposition of copper composites from deep eutectic solvents based on choline chloride,” *Physical Chemistry Chemical Physics*, vol. 11, no. 21, pp. 4269–4277, 2009.

[212] P. Sebastián, E. Gómez, V. Climent, and J. M. Feliu, “Copper underpotential deposition at gold surfaces in contact with a deep eutectic solvent: New insights,” *Electrochemistry Communications*, vol. 78, pp. 51–55, 2017.

[213] P. Valverde, T. Green, and S. Roy, “Effect of water on the electrodeposition of copper from a deep eutectic solvent,” *Journal of Applied Electrochemistry*, vol. 50, no. 6, pp. 699–712, 2020.

[214] A. Y. Al-Murshedi, J. M. Hartley, A. P. Abbott, and K. Ryder, “Effect of water on the electrodeposition of copper on nickel in deep eutectic solvents,” *Transactions of the IMF*, vol. 97, no. 6, pp. 321–329, 2019.

[215] R. Bernasconi, M. Zebarjadi, and L. Magagnin, “Copper electrodeposition from a chloride free deep eutectic solvent,” *Journal of Electroanalytical Chemistry*, vol. 758, pp. 163–169, 2015.

[216] M. B. Vukmirovic, R. R. Adzic, and R. Akolkar, “Copper electrodeposition from deep eutectic solvents—voltammetric studies providing insights into the role of substrate: Platinum vs glassy carbon,” *The Journal of Physical Chemistry B*, vol. 124, no. 26, pp. 5465–5475, 2020.

[217] A. P. Abbott, R. C. Harris, Y.-T. Hsieh, K. S. Ryder, and I.-W. Sun, “Aluminium electrodeposition under ambient conditions,” *Physical Chemistry Chemical Physics*, vol. 16, no. 28, pp. 14675–14681, 2014.

[218] V. S. Cvetković, N. M. Vukićević, N. Jovićević, J. S. Stevanović, and J. N. Jovićević, "Aluminium electrodeposition under novel conditions from $AlCl_3$–urea deep eutectic solvent at room temperature," *Transactions of Nonferrous Metals Society of China*, vol. 30, no. 3, pp. 823–834, 2020.

[219] E. Gómez, P. Cojocaru, L. Magagnin, and E. Valles, "Electrodeposition of Co, Sm and SmCo from a deep eutectic solvent," *Journal of Electroanalytical Chemistry*, vol. 658, no. 1-2, pp. 18–24, 2011.

[220] A. P. Abbott, K. El Ttaib, G. Frisch, K. S. Ryder, and D. Weston, "The electrodeposition of silver composites using deep eutectic solvents," *Physical Chemistry Chemical Physics*, vol. 14, no. 7, pp. 2443–2449, 2012.

[221] M. Rahman, R. Bernasconi, and Magagnin, "Electrodeposition of indium from a deep eutectic solvent," *Journal of Optoelectronics and Advanced Materials*, vol. 17, no. 1-2, pp. 122–126, 2015.

[222] H. Wang, Y. Jia, X. Wang, Y. Yao, D. Yue, and Y. Jing, "Electrochemical deposition of magnesium from analogous ionic liquid based on dimethylformamide," *Electrochimica Acta*, vol. 108, pp. 384–389, 2013.

[223] P. Sebastián, E. Vallés, and E. Gómez, "First stages of silver electrodeposition in a deep eutectic solvent. comparative behavior in aqueous medium," *Electrochimica Acta*, vol. 112, pp. 149–158, 2013.

[224] R. Bernasconi, G. Panzeri, G. Firtin, B. Kahyaoglu, L. Nobili, and L. Magagnin, "Electrodeposition of ZnNi alloys from choline chloride/ethylene glycol deep eutectic solvent and pure ethylene glycol for corrosion protection," *The Journal of Physical Chemistry B*, vol. 124, no. 47, pp. 10739–10751, 2020.

[225] S. Fashu, C. Gu, J. Zhang, W. Bai, X. Wang, and J. Tu, "Electrodeposition and characterization of Zn–Sn alloy coatings from a deep eutectic solvent based on choline chloride for corrosion protection," *Surface and Interface Analysis*, vol. 47, no. 3, pp. 403–412, 2015.

[226] H. F. Alesary, H. K. Ismail, N. M. Shiltagh, R. A. Alattar, L. M. Ahmed, M. J. Watkins, and K. S. Ryder, "Effects of additives on the electrodeposition of znsn alloys from choline chloride/ethylene glycol-based deep eutectic solvent," *Journal of Electroanalytical Chemistry*, vol. 874, p. 114517, 2020.

[227] S. Rao, X. Zou, S. Wang, T. Shi, Y. Lu, L. Ji, H.-Y. Hsu, Q. Xu, and X. Lu, "Electrodeposition of porous Sn-Ni-Cu alloy anode for lithium-ion batteries from nickel matte in deep eutectic solvents," *Journal of the Electrochemical Society*, vol. 166, no. 10, 2019.

[228] S. P. Rosoiu, S. Costovici, C. Moise, A. Petica, L. Anicai, T. Visan, and M. Enachescu, "Electrodeposition of ternary Sn-Cu-Ni alloys as lead-free solders using deep eutectic solvents," *Electrochimica Acta*, vol. 398, 2021.

[229] A. Abbott, A. Alhaji, K. Ryder, M. Horne, and T. Rodopoulos, "Electrodeposition of copper–tin alloys using deep eutectic solvents," *Transactions of the IMF*, vol. 94, no. 2, pp. 104–113, 2016.

[230] A. Liu, Z. Shi, and R. G. Reddy, "Mechanism study of Cu–Zn alloys electrodeposition in deep eutectic solvents," *Ionics*, vol. 26, no. 6, pp. 3161–3172, 2020.

[231] M. Steichen, J. Larsen, L. Gütay, S. Siebentritt, and P. Dale, "Preparation of $CuGaSe_2$ absorber layers for thin film solar cells by annealing of efficiently electrodeposited Cu–Ga precursor layers from ionic liquids," *Thin Solid Films*, vol. 519, no. 21, pp. 7254–7258, 2011.

[232] J. Zeng, L. Chen, S. Siwal, and Q. Zhang, "Solvothermal sulfurization in a deep eutectic solvent: a novel route to synthesize Co-doped Ni_3S_2 nanosheets supported on Ni foam as active materials for ultrahigh-performance pseudocapacitors," *Sustainable Energy & Fuels*, vol. 3, no. 8, pp. 1957–1965, 2019.

[233] N. Bai, Q. Li, D. Mao, D. Li, and H. Dong, "One-step electrodeposition of Co/CoP film on Ni foam for efficient hydrogen evolution in alkaline solution," *ACS Applied Materials & Interfaces*, vol. 8, no. 43, pp. 29400–29407, 2016.

[234] J. Andrews and B. Shabani, "Re-envisioning the role of hydrogen in a sustainable energy economy," *International Journal of Hydrogen Energy*, vol. 37, no. 2, pp. 1184–1203, 2012.

[235] S. E. Hosseini and B. Butler, "An overview of development and challenges in hydrogen powered vehicles," *International Journal of Green Energy*, vol. 17, no. 1, pp. 13–37, 2020.

[236] H. M. Mary, "Chapter 23 - hydrogen: An energy carrier," in *Future Energy* (T. M. Letcher, ed.), pp. 495–510, Boston: Elsevier, second edition ed., 2014.

[237] Q. Ma, C. Hu, K. Liu, S.-F. Hung, D. Ou, H. M. Chen, G. Fu, and N. Zheng, "Identifying the electrocatalytic sites of nickel disulfide in alkaline hydrogen evolution reaction," *Nano Energy*, vol. 41, pp. 148–153, 2017.

[238] J. Chen, B. Lim, E. P. Lee, and Y. Xia, "Shape-controlled synthesis of platinum nanocrystals for catalytic and electrocatalytic applications," *Nano Today*, vol. 4, no. 1, pp. 81–95, 2009.

[239] C. Wang, N. M. Markovic, and V. R. Stamenkovic, "Advanced platinum alloy electrocatalysts for the oxygen reduction reaction," *ACS Catalysis*, vol. 2, no. 5, pp. 891–898, 2012.

[240] Z. Wang, X. Ren, Y. Luo, L. Wang, G. Cui, F. Xie, H. Wang, Y. Xie, and X. Sun, "An ultrafine platinum–cobalt alloy decorated cobalt nanowire array with superb activity toward alkaline hydrogen evolution," *Nanoscale*, vol. 10, no. 26, pp. 12302–12307, 2018.

[241] N. Elezović, B. M. Babić, L. Gajić-Krstajić, P. Ercius, V. R. Radmilović, N. Krstajić, and L. M. Vračar, "Pt supported on nano-tungsten carbide as a beneficial catalyst for the oxygen reduction reaction in alkaline solution," *Electrochimica Acta*, vol. 69, pp. 239–246, 2012.

[242] A. Hassan, V. A. Paganin, and E. A. Ticianelli, "Pt modified tungsten carbide as anode electrocatalyst for hydrogen oxidation in proton exchange membrane fuel cell: CO tolerance and stability," *Applied Catalysis B: Environmental*, vol. 165, pp. 611–619, 2015.

[243] R. Subbaraman, D. Tripkovic, D. Strmcnik, K.-C. Chang, M. Uchimura, A. P. Paulikas, V. Stamenkovic, and N. M. Markovic, "Enhancing hydrogen evolution activity in water splitting by tailoring Li^+-$Ni(OH)_2$-Pt interfaces," *Science*, vol. 334, no. 6060, pp. 1256–1260, 2011.

[244] R. Subbaraman, D. Tripkovic, K.-C. Chang, D. Strmcnik, A. P. Paulikas, P. Hirunsit, M. Chan, J. Greeley, V. Stamenkovic, and N. M. Markovic, "Trends in activity for the water electrolyser reactions on 3dM(Ni,Co,Fe,Mn) hydr(oxy)oxide catalysts," *Nature Materials*, vol. 11, no. 6, pp. 550–557, 2012.

[245] S. Cherevko, S. Geiger, O. Kasian, N. Kulyk, J.-P. Grote, A. Savan, B. R. Shrestha, S. Merzlikin, B. Breitbach, A. Ludwig, *et al.*, "Oxygen and hydrogen evolution reactions on Ru, RuO_2, Ir, and IrO_2 thin film electrodes in acidic and alkaline electrolytes: A comparative study on activity and stability," *Catalysis Today*, vol. 262, pp. 170–180, 2016.

[246] I. A. Raj and K. Vasu, "Transition metal-based cathodes for hydrogen evolution in alkaline solution: electrocatalysis on nickel-based ternary electrolytic codeposits," *Journal of Applied Electrochemistry*, vol. 22, no. 5, pp. 471–477, 1992.

[247] J. R. McKone, B. F. Sadtler, C. A. Werlang, N. S. Lewis, and H. B. Gray, "Ni–Mo nanopowders for efficient electrochemical hydrogen evolution," *ACS Catalysis*, vol. 3, no. 2, pp. 166–169, 2013.

[248] Y. Ito, T. Ohto, D. Hojo, M. Wakisaka, Y. Nagata, L. Chen, K. Hu, M. Izumi, J.-i. Fujita, and T. Adschiri, "Cooperation between holey graphene and NiMo alloy for hydrogen evolution in an acidic electrolyte," *ACS Catalysis*, vol. 8, no. 4, pp. 3579–3586, 2018.

[249] Z. Zhuang, S. A. Giles, J. Zheng, G. R. Jenness, S. Caratzoulas, D. G. Vlachos, and Y. Yan, "Nickel supported on nitrogen-doped carbon nanotubes as hydrogen oxidation reaction catalyst in alkaline electrolyte," *Nature Communications*, vol. 7, no. 1, pp. 1–8, 2016.

[250] B. Subramanya, Y. Ullal, S. Shenoy, D. Bhat, and A. Hegde, "Novel Co–Ni–graphene composite electrodes for hydrogen production," *RSC Advances*, vol. 5, no. 59, pp. 47398–47407, 2015.

[251] H. Fei, J. Dong, M. J. Arellano-Jiménez, G. Ye, N. D. Kim, E. L. Samuel, Z. Peng, Z. Zhu, F. Qin, J. Bao, *et al.*, "Atomic cobalt on nitrogen-doped graphene for hydrogen generation," *Nature Communications*, vol. 6, no. 1, pp. 1–8, 2015.

[252] L. Lang, Y. Shi, J. Wang, F.-B. Wang, and X.-H. Xia, "Hollow core–shell structured Ni–Sn@C nanoparticles: a novel electrocatalyst for the hydrogen evolution reaction," *ACS Applied Materials & Interfaces*, vol. 7, no. 17, pp. 9098–9102, 2015.

[253] W. Zhao, X. Lu, M. Selvaraj, W. Wei, Z. Jiang, N. Ullah, J. Liu, and J. Xie, "MXP (M= Co/Ni@ carbon core–shell nanoparticles embedded in 3D cross-linked graphene aerogel derived from seaweed biomass for hydrogen evolution reaction," *Nanoscale*, vol. 10, no. 20, pp. 9698–9706, 2018.

[254] X. Liu, J. Zang, L. Chen, L. Chen, X. Chen, P. Wu, S. Zhou, and Y. Wang, "A microwave-assisted synthesis of CoO@Co core–shell structures coupled with N-doped reduced graphene oxide used as a superior multi-functional electrocatalyst for hydrogen evolution, oxygen reduction and oxygen evolution reactions," *Journal of Materials Chemistry A*, vol. 5, no. 12, pp. 5865–5872, 2017.

[255] L. Yu, H. Zhou, J. Sun, F. Qin, D. Luo, L. Xie, F. Yu, J. Bao, Y. Li, Y. Yu, *et al.*, "Hierarchical Cu@CoFe layered double hydroxide core-shell nanoarchitectures as bifunctional electrocatalysts for efficient overall water splitting," *Nano Energy*, vol. 41, pp. 327–336, 2017.

[256] Y. Zhong, X. Xia, F. Shi, J. Zhan, J. Tu, and H. J. Fan, "Transition metal carbides and nitrides in energy storage and conversion," *Advanced Science*, vol. 3, no. 5, 2016.

[257] H. Vrubel and X. Hu, "Molybdenum boride and carbide catalyze hydrogen evolution in both acidic and basic solutions," *Angewandte Chemie International Edition*, vol. 51, pp. 12703–12706, 2012.

[258] W. Gao, Y. Shi, Y. Zhang, L. Zuo, H. Lu, Y. Huang, W. Fan, and T. Liu, "Molybdenum carbide anchored on graphene nanoribbons as highly efficient all-pH hydrogen evolution reaction electrocatalyst," *ACS Sustainable Chemistry & Engineering*, vol. 4, no. 12, pp. 6313–6321, 2016.

[259] D. Krishnan, K. Raidongia, J. Shao, and J. Huang, "Graphene oxide assisted hydrothermal carbonization of carbon hydrates," *ACS Nano*, vol. 8, no. 1, pp. 449–457, 2014.

[260] W.-F. Chen, C.-H. Wang, K. Sasaki, N. Marinkovic, W. Xu, J. T. Muckerman, Y. Zhu, and R. Adzic, "Highly active and durable nanostructured molybdenum carbide electrocatalysts for hydrogen production," *Energy & Environmental Science*, vol. 6, no. 3, pp. 943–951, 2013.

[261] L. Liao, S. Wang, J. Xiao, X. Bian, Y. Zhang, M. D. Scanlon, X. Hu, Y. Tang, B. Liu, and H. H. Girault, "A nanoporous molybdenum carbide nanowire as an electrocatalyst for hydrogen evolution reaction," *Energy & Environmental Science*, vol. 7, no. 1, pp. 387–392, 2014.

[262] B. Hinnemann, P. G. Moses, J. Bonde, K. P. Jørgensen, J. H. Nielsen, S. Horch, I. Chorkendorff, and J. K. Nørskov, "Biomimetic hydrogen evolution: MoS_2 nanoparticles as catalyst for hydrogen evolution," *Journal of the American Chemical Society*, vol. 127, no. 15, pp. 5308–5309, 2005.

[263] M. Kajbafvala and M. Farbod, "Effective size selection of MoS_2 nanosheets by a novel liquid cascade centrifugation: Influences of the flakes dimensions on electrochemical and photoelectrochemical applications," *Journal of Colloid and Interface Science*, vol. 527, pp. 159–171, 2018.

[264] L. Ye, H. Xu, D. Zhang, and S. Chen, "Synthesis of bilayer MoS_2 nanosheets by a facile hydrothermal method and their methyl orange adsorption capacity," *Materials Research Bulletin*, vol. 55, pp. 221–228, 2014.

[265] Z. Wang and B. Mi, "Environmental applications of 2D molybdenum disulfide (MoS_2) nanosheets," *Environmental Science & Technology*, vol. 51, no. 15, pp. 8229–8244, 2017.

[266] J. Jeon, J. Lee, G. Yoo, J.-H. Park, G. Y. Yeom, Y. H. Jang, and S. Lee, "Size-tunable synthesis of monolayer MoS_2 nanoparticles and their applications in non-volatile memory devices," *Nanoscale*, vol. 8, no. 38, pp. 16995–17003, 2016.

[267] D. Y. Chung, S.-K. Park, Y.-H. Chung, S.-H. Yu, D.-H. Lim, N. Jung, H. C. Ham, H.-Y. Park, Y. Piao, S. J. Yoo, and Y.-E. Sung, "Edge-exposed MoS_2 nano-assembled structures as efficient electrocatalysts for hydrogen evolution reaction," *Nanoscale*, vol. 6, no. 4, pp. 2131–2136, 2014.

[268] J. Xie, H. Zhang, S. Li, R. Wang, X. Sun, M. Zhou, J. Zhou, X. W. Lou, and Y. Xie, "Defect-rich MoS_2 ultrathin nanosheets with additional active edge sites for enhanced electrocatalytic hydrogen evolution," *Advanced Materials*, vol. 25, no. 40, pp. 5807–5813, 2013.

[269] S. Jin, "Are metal chalcogenides, nitrides, and phosphides oxygen evolution catalysts or bifunctional catalysts?," *ACS Energy Letters*, vol. 2, no. 8, pp. 1937–1938, 2017.

[270] J. Jiang, S. Lu, H. Gao, X. Zhang, and H.-Q. Yu, "Ternary $FeNiS_2$ ultrathin nanosheets as an electrocatalyst for both oxygen evolution and reduction reactions," *Nano Energy*, vol. 27, pp. 526–534, 2016.

[271] K. Xiao, L. Zhou, M. Shao, and M. Wei, "Fabrication of $(Ni,Co)_{0.85}Se$ nanosheet arrays derived from layered double hydroxides toward largely enhanced overall water splitting," *Journal of Materials Chemistry A*, vol. 6, no. 17, pp. 7585–7591, 2018.

[272] T. Chen and Y. Tan, "Hierarchical $CoNiSe_2$ nano-architecture as a high-performance electrocatalyst for water splitting," *Nano Research*, vol. 11, no. 3, pp. 1331–1344, 2018.

[273] X. Xu, F. Song, and X. Hu, "A nickel iron diselenide-derived efficient oxygen-evolution catalyst," *Nature Communications*, vol. 7, no. 1, pp. 1–7, 2016.

[274] J. Zhang, Z. Xia, and L. Dai, "Carbon-based electrocatalysts for advanced energy conversion and storage," *Science Advances*, vol. 1, no. 7, 2015.

[275] Y. Zheng, Y. Jiao, L. H. Li, T. Xing, Y. Chen, M. Jaroniec, and S. Z. Qiao, "Toward design of synergistically active carbon-based catalysts for electrocatalytic hydrogen evolution," *ACS Nano*, vol. 8, no. 5, pp. 5290–5296, 2014.

[276] J. Sheng and Y. Li, "Applications of carbon nanotubes in oxygen electrocatalytic reactions," *ACS Applied Materials & Interfaces*, vol. 14, pp. 20455–20462, 2021.

[277] S. A. Ladva, W. Travis, R. Quesada-Cabrera, M. Rosillo-Lopez, A. Afandi, Y. Li, R. B. Jackman, J. C. Bear, I. P. Parkin, C. Blackman, C. G. Salzmann, and R. G. Palgrave, "Nanoscale, conformal films of graphitic carbon nitride deposited at room temperature: a method for construction of heterojunction devices," *Nanoscale*, vol. 9, no. 43, pp. 16586–16590, 2017.

[278] W. Gu, L. Hu, J. Li, and E. Wang, "Hybrid of g-C_3N_4 assisted metal–organic frameworks and their derived high-efficiency oxygen reduction electrocatalyst in the whole pH range," *ACS Applied Materials & Interfaces*, vol. 8, no. 51, pp. 35281–35288, 2016.

[279] D. Xiang, B. Zhang, H. Zhang, and L. Shen, "One-step synthesis of bifunctional nickel phosphide nanowires as electrocatalysts for hydrogen and oxygen evolution reactions," *Frontiers in Chemistry*, vol. 9, 2021.

[280] Y. Wei, C.-H. Shin, G. B. Caleb, E. B. Tetteh, G. Park, and J.-S. Yu, "Positive self-reconstruction in FeNiMo phosphide electrocatalyst for enhanced overall water splitting," *Sustainable Energy & Fuels*, 2021.

[281] S. Xu, H. Zhao, T. Li, J. Liang, S. Lu, G. Chen, S. Gao, A. M. Asiri, Q. Wu, and X. Sun, "Iron-based phosphides as electrocatalysts for the hydrogen evolution reaction: recent advances and future prospects," *Journal of Materials Chemistry A*, vol. 8, no. 38, pp. 19729–19745, 2020.

[282] E. J. Popczun, J. R. McKone, C. G. Read, A. J. Biacchi, A. M. Wiltrout, N. S. Lewis, and R. E. Schaak, "Nanostructured nickel phosphide as an electrocatalyst for the hydrogen evolution reaction," *Journal of the American Chemical Society*, vol. 135, no. 25, pp. 9267–9270, 2013.

[283] B. Kim, T. Kim, K. Lee, and J. Li, "Recent advances in transition metal phosphide electrocatalysts for water splitting under neutral pH conditions," *ChemElectroChem*, vol. 7, no. 17, pp. 3578–3589, 2020.

[284] A. E. Henkes and R. E. Schaak, "Trioctylphosphine: a general phosphorus source for the low-temperature conversion of metals into metal phosphides," *Chemistry of Materials*, vol. 19, no. 17, pp. 4234–4242, 2007.

[285] Q. Guan, W. Li, M. Zhang, and K. Tao, "Alternative synthesis of bulk and supported nickel phosphide from the thermal decomposition of hypophosphites," *Journal of Catalysis*, vol. 263, no. 1, pp. 1–3, 2009.

[286] J. Wang, L. Zhu, G. Dharan, and G. W. Ho, "Electrodeposited cobalt phosphide superstructures for solar-driven thermoelectrocatalytic overall water splitting," *Journal of Materials Chemistry A*, vol. 5, no. 32, pp. 16580–16584, 2017.

[287] L.-A. Stern, L. Feng, F. Song, and X. Hu, "Ni_2P as a janus catalyst for water splitting: the oxygen evolution activity of Ni_2P nanoparticles," *Energy & Environmental Science*, vol. 8, no. 8, pp. 2347–2351, 2015.

[288] Y. Li, Y. Zhao, and Z. Zhang, "A porous graphene/cobalt phosphate composite as an efficient oxygen evolving catalyst," *Electrochemistry Communications*, vol. 48, pp. 35–39, 2014.

[289] H. Kim, J. Park, I. Park, K. Jin, S. E. Jerng, S. H. Kim, K. T. Nam, and K. Kang, "Coordination tuning of cobalt phosphates towards efficient water oxidation catalyst," *Nature Communications*, vol. 6, no. 1, pp. 1–11, 2015.

[290] L. Xie, R. Zhang, L. Cui, D. Liu, S. Hao, Y. Ma, G. Du, A. M. Asiri, and X. Sun, "High-performance electrolytic oxygen evolution in neutral media catalyzed by a cobalt phosphate nanoarray," *Angewandte Chemie International Edition*, vol. 56, no. 4, pp. 1064–1068, 2017.

[291] N.-T. Suen, S.-F. Hung, Q. Quan, N. Zhang, Y.-J. Xu, and H. M. Chen, "Electrocatalysis for the oxygen evolution reaction: recent development and future perspectives," *Chemical Society Reviews*, vol. 46, no. 2, pp. 337–365, 2017.

[292] F. D. Speck, P. G. Santori, F. Jaouen, and S. Cherevko, "Mechanisms of manganese oxide electrocatalysts degradation during oxygen reduction and oxygen evolution reactions," *The Journal of Physical Chemistry C*, vol. 123, no. 41, pp. 25267–25277, 2019.

[293] S. Park, Y. H. Lee, S. Choi, H. Seo, M. Y. Lee, M. Balamurugan, and K. T. Nam, "Manganese oxide-based heterogeneous electrocatalysts for water oxidation," *Energy & Environmental Science*, vol. 13, no. 8, pp. 2310–2340, 2020.

[294] S. Tsunekawa, F. Yamamoto, K.-H. Wang, M. Nagasaka, H. Yuzawa, S. Takakusagi, H. Kondoh, K. Asakura, T. Kawai, and M. Yoshida, "Operando observations of a manganese oxide electrocatalyst for water oxidation using hard/tender/soft X-ray absorption spectroscopy," *The Journal of Physical Chemistry C*, vol. 124, no. 43, pp. 23611–23618, 2020.

[295] J. M. Barforoush, T. E. Seuferling, D. T. Jantz, K. R. Song, and K. C. Leonard, "Insights into the active electrocatalytic areas of layered double hydroxide and amorphous nickel–iron oxide oxygen evolution electrocatalysts," *ACS Applied Energy Materials*, vol. 1, no. 4, pp. 1415–1423, 2018.

[296] K.-L. Ng, K.-Y. Kok, and B.-H. Ong, "Facile synthesis of self-assembled cobalt oxide supported on iron oxide as the novel electrocatalyst for enhanced electrochemical water electrolysis," *ACS Applied Nano Materials*, vol. 1, no. 1, pp. 401–409, 2017.

[297] J. Wang, J. Liu, B. Zhang, H. Wan, Z. Li, X. Ji, K. Xu, C. Chen, D. Zha, L. Miao, *et al.*, "Synergistic effect of two actions sites on cobalt oxides towards electrochemical water-oxidation," *Nano Energy*, vol. 42, pp. 98–105, 2017.

[298] W. Xu, F. Lyu, Y. Bai, A. Gao, J. Feng, Z. Cai, and Y. Yin, "Porous cobalt oxide nanoplates enriched with oxygen vacancies for oxygen evolution reaction," *Nano Energy*, vol. 43, pp. 110–116, 2018.

[299] T. Miura, S. Tsunekawa, S. Onishi, T. Ina, K. Wang, G. Watanabe, C. Hu, H. Kondoh, T. Kawai, and M. Yoshida, "Assessing nickel oxide electrocatalysts incorporating diamines and having improved oxygen evolution activity using operando UV/visible and X-ray absorption spectroscopy," *Physical Chemistry Chemical Physics*, 2021.

[300] Y. Chen, K. Rui, J. Zhu, S. X. Dou, and W. Sun, "Recent progress on nickel-based oxide/(oxy) hydroxide electrocatalysts for the oxygen evolution reaction," *Chemistry–A European Journal*, vol. 25, no. 3, pp. 703–713, 2019.

[301] L. Trotochaud, J. K. Ranney, K. N. Williams, and S. W. Boettcher, "Solution-cast metal oxide thin film electrocatalysts for oxygen evolution," *Journal of the American Chemical Society*, vol. 134, no. 41, pp. 17253–17261, 2012.

[302] Y. Wu, R. Sun, and J. Cen, "Facile synthesis of cobalt oxide as an efficient electrocatalyst for hydrogen evolution reaction," *Frontiers in Chemistry*, vol. 8, 2020.

[303] Y. Zhang, F. Ding, C. Deng, S. Zhen, X. Li, Y. Xue, Y.-M. Yan, and K. Sun, "Crystal plane-dependent electrocatalytic activity of Co_3O_4 toward oxygen evolution reaction," *Catalysis Communications*, vol. 67, pp. 78–82, 2015.

[304] R. Zhang, Y.-C. Zhang, L. Pan, G.-Q. Shen, N. Mahmood, Y.-H. Ma, Y. Shi, W. Jia, L. Wang, X. Zhang, *et al.*, "Engineering cobalt defects in cobalt oxide for highly efficient electrocatalytic oxygen evolution," *ACS Catalysis*, vol. 8, no. 5, pp. 3803–3811, 2018.

[305] C. Xiao, X. Lu, and C. Zhao, "Unusual synergistic effects upon incorporation of Fe and/or Ni into mesoporous Co_3O_4 for enhanced oxygen evolution," *Chemical Communications*, vol. 50, no. 70, pp. 10122–10125, 2014.

[306] M. Tahir, L. Pan, R. Zhang, Y.-C. Wang, G. Shen, I. Aslam, M. Qadeer, N. Mahmood, W. Xu, L. Wang, *et al.*, "High-valence-state NiO/Co_3O_4 nanoparticles on nitrogen-doped carbon for oxygen evolution at low overpotential," *ACS Energy Letters*, vol. 2, no. 9, pp. 2177–2182, 2017.

[307] M. B. Stevens, C. D. Trang, L. J. Enman, J. Deng, and S. W. Boettcher, "Reactive Fe-sites in Ni/Fe(oxy) hydroxide are responsible for exceptional oxygen electrocatalysis activity," *Journal of the American Chemical Society*, vol. 139, no. 33, pp. 11361–11364, 2017.

[308] Q. He, Y. Wan, H. Jiang, Z. Pan, C. Wu, M. Wang, X. Wu, B. Ye, P. M. Ajayan, and L. Song, "Nickel vacancies boost reconstruction in nickel hydroxide electrocatalyst," *ACS Energy Letters*, vol. 3, no. 6, pp. 1373–1380, 2018.

[309] B. Dong, M. Li, S. Chen, D. Ding, W. Wei, G. Gao, and S. Ding, "Formation of g-C_3N_4@$Ni(OH)_2$ honeycomb nanostructure and asymmetric supercapacitor with high energy and power density," *ACS Applied Materials & Interfaces*, vol. 9, no. 21, pp. 17890–17896, 2017.

[310] X. Li, X. Hao, A. Abudula, and G. Guan, "Nanostructured catalysts for electrochemical water splitting: current state and prospects," *Journal of Materials Chemistry A*, vol. 4, no. 31, pp. 11973–12000, 2016.

[311] F. Song, L. Bai, A. Moysiadou, S. Lee, C. Hu, L. Liardet, and X. Hu, "Transition metal oxides as electrocatalysts for the oxygen evolution reaction in alkaline solutions: an application-inspired renaissance," *Journal of the American Chemical Society*, vol. 140, no. 25, pp. 7748–7759, 2018.

[312] J. S. Sagu, D. Mehta, and K. U. Wijayantha, "Electrocatalytic activity of $CoFe_2O_4$ thin films prepared by AACVD towards the oxygen evolution reaction in alkaline media," *Electrochemistry Communications*, vol. 87, pp. 1–4, 2018.

[313] H.-Y. Wang, S.-F. Hung, H.-Y. Chen, T.-S. Chan, H. M. Chen, and B. Liu, "In operando identification of geometrical-site-dependent water oxidation activity of spinel Co_3O_4," *Journal of the American Chemical Society*, vol. 138, no. 1, pp. 36–39, 2016.

[314] W. Zhang, L. Cui, and J. Liu, "Recent advances in cobalt-based electrocatalysts for hydrogen and oxygen evolution reactions," *Journal of Alloys and Compounds*, vol. 821, 2020.

[315] X. Peng, X. Jin, B. Gao, Z. Liu, and P. K. Chu, "Strategies to improve cobalt-based electrocatalysts for electrochemical water splitting," *Journal of Catalysis*, vol. 398, pp. 54–66, 2021.

[316] O. S. Hammond, D. T. Bowron, and K. J. Edler, "The effect of water upon deep eutectic solvent nanostructure: An unusual transition from ionic mixture to aqueous solution," *Angewandte Chemie International Edition*, vol. 56, no. 33, pp. 9782–9785, 2017.

[317] J. Ren, T. Lin, L. W. Sprague, I. Peng, and L.-Q. Wang, "Exploring chemical equilibrium for alcohol-based cobalt complexation through visualization of color change and UV–vis spectroscopy," *Journal of Chemical Education*, vol. 97, no. 2, pp. 509–516, 2019.

[318] N. M. Dang, W.-W. Zhao, S.-i. Yusa, H. Noguchi, and K. Nakashima, "Cobalt oxide hollow nanoparticles as synthesized by templating a tri-block copolymer micelle with a core–shell–corona structure: a promising anode material for lithium ion batteries," *New Journal of Chemistry*, vol. 39, no. 6, pp. 4726–4730, 2015.

[319] A. El Bachiri, L. Soussi, O. Karzazi, A. Louardi, A. Rmili, H. Erguig, and B. El Idrissi, "Electrochromic and photoluminescence properties of cobalt oxide thin films prepared by spray pyrolysis," *Spectroscopy Letters*, vol. 52, no. 1, pp. 66–73, 2019.

[320] G. B. Kauffman, "Early experimental studies of cobalt-ammines," *Isis*, vol. 68, no. 3, pp. 392–403, 1977.

[321] R. Bala, R. P. Sharma, U. Sharma, A. D. Burrows, and K. Cassar, "Hexaamminecobalt(III) complexes as multiple hydrogen bond donors: Synthesis, characterization and X-ray structural study of mixed anion complexes $[Co(NH_3)_6]Br_2(BF_4)$ and $[Co(NH_3)_6]C_{l2}(HC_2O_4)\cdot H_2O$," *Journal of Molecular Structure*, vol. 832, no. 1-3, pp. 156–163, 2007.

[322] G. B. Kauffman, N. Sugisaka, K. Emerson, L. A. Bares, and C. C. Houk, "Hexaamminecobalt (II) chloride," *Inorganic Syntheses*, vol. 9, pp. 157–160, 1967.

[323] J. Hilbert, C. Näther, and W. Bensch, "Applying Ni(II) amine complexes and sodium thiostannate as educts for the generation of thiostannates at room temperature," *Crystal Growth & Design*, vol. 17, no. 9, pp. 4766–4775, 2017.

[324] X. Ge, C. Gu, Y. Lu, X. Wang, and J. Tu, "A versatile protocol for the ionothermal synthesis of nanostructured nickel compounds as energy storage materials from a choline chloride-based ionic liquid," *Journal of Materials Chemistry A*, vol. 1, no. 43, pp. 13454–13461, 2013.

[325] H. S. Devi and T. D. Singh, "Synthesis of Mn_2O_3 nanoparticles using choline chloride-ethylene glycol deep eutectic solvent: A green solvent," *Integrated Ferroelectrics*, vol. 185, no. 1, pp. 82–89, 2017.

[326] J. N. Baby, B. Sriram, S.-F. Wang, M. George, M. Govindasamy, and X. B. Joseph, "Deep eutectic solvent-based manganese molybdate nanosheets for sensitive and simultaneous detection of human lethal compounds: comparing the electrochemical performances of M-molybdate (M= Mg, Fe, and Mn) electrocatalysts," *Nanoscale*, vol. 12, no. 38, pp. 19719–19731, 2020.

[327] C. Zhang, B. Xin, T. Chen, H. Ying, Z. Li, and J. Hao, "Deep eutectic solvent strategy enables an octahedral Ni-Co precursor for creating high-performance $NiCo_2O_4$ catalyst toward oxygen evolution reaction," *Green Energy & Environment*, 2021.

[328] C. Mukesh, D. Mondal, M. Sharma, and K. Prasad, "Choline chloride–thiourea, a deep eutectic solvent for the production of chitin nanofibers," *Carbohydrate Polymers*, vol. 103, pp. 466–471, 2014.

[329] W. Chen, X. Bai, Z. Xue, H. Mou, J. Chen, Z. Liu, and T. Mu, "The formation and physicochemical properties of PEGylated deep eutectic solvents," *New Journal of Chemistry*, vol. 43, no. 22, pp. 8804–8810, 2019.

[330] S.-Y. Huang, D. Sodano, T. Leonard, S. Luiso, and P. S. Fedkiw, "Cobalt-doped iron sulfide as an electrocatalyst for hydrogen evolution," *Journal of The Electrochemical Society*, vol. 164, no. 4, p. F276, 2017.

[331] F. Yang, L. Xin, A. Uzunoglu, Y. Qiu, L. Stanciu, J. Ilavsky, W. Li, and J. Xie, "Investigation of the interaction between Nafion ionomer and surface functionalized carbon black using both ultrasmall angle X-ray scattering and cryo-TEM," *ACS Applied Materials & Interfaces*, vol. 9, no. 7, pp. 6530–6538, 2017.

[332] A. J. Bard and L. R. Faulkner, *Electrochemical Methods: Fundamentals and Applications.* New York: Wiley New York, second ed., 2001.

[333] M. Regue, S. Sibby, I. Y. Ahmet, D. Friedrich, F. F. Abdi, A. L. Johnson, and S. Eslava, "TiO_2 photoanodes with exposed {010} facets grown by aerosol-assisted chemical vapor deposition of a titanium oxo/alkoxy cluster," *Journal of Materials Chemistry A*, vol. 7, no. 32, pp. 19161–19172, 2019.

[334] K. Wang, W. Guo, S. Yan, H. Song, and Y. Shi, "Hierarchical Co–FeS_2/CoS_2 heterostructures as a superior bifunctional electrocatalyst," *RSC Advances*, vol. 8, no. 50, pp. 28684–28691, 2018.

[335] Y. Gao, K. Wang, H. Song, H. Wu, S. Yan, X. Xu, and Y. Shi, "Fabrication of C/Co-FeS_2/CoS_2 with highly efficient hydrogen evolution reaction," *Catalysts*, vol. 9, no. 6, 2019.

[336] I. Manasi, M. R. Andalibi, R. Castaing, L. Torrente-Murciano, and K. J. Edler, "Surfactant effects on the synthesis of porous cerium oxide from a type IV deep eutectic solvent," *Journal of Materials Chemistry A*, vol. 35, pp. 18422–18430, 2022.

[337] M. Wang, L. Zhang, Y. He, and H. Zhu, "Recent advances in transition-metal-sulfide-based bifunctional electrocatalysts for overall water splitting," *Journal of Materials Chemistry A*, vol. 9, no. 9, pp. 5320–5363, 2021.

[338] A. Sanchez-Fernandez, O. Hammond, K. Edler, T. Arnold, J. Doutch, R. Dalgliesh, P. Li, K. Ma, and A. Jackson, "Counterion binding alters surfactant self-assembly in deep eutectic solvents," *Physical Chemistry Chemical Physics*, vol. 20, no. 20, pp. 13952–13961, 2018.

[339] M. Corrin and W. D. Harkins, "The effect of salts on the critical concentration for the formation of micelles in colloidal electrolytes," *Journal of the American Chemical Society*, vol. 69, no. 3, pp. 683–688, 1947.

[340] A. Al-Sabagh, N. Nasser, M. Migahed, and N. Kandil, "Effect of chemical structure on the cloud point of some new non-ionic surfactants based on bisphenol in relation to their surface active properties," *Egyptian Journal of Petroleum*, vol. 20, no. 2, pp. 59–66, 2011.

[341] "Chapter 26 - polymer–surfactant interactions," in *Cosmetic Science and Technology* (K. Sakamoto, R. Y. Lochhead, H. I. Maibach, and Y. Yamashita, eds.), pp. 449–469, Amsterdam: Elsevier, 2017.

[342] N. Anton, P. Pierrat, L. Lebeau, T. F. Vandamme, and P. Bouriat, "A study of insoluble monolayers by deposition at a bubble interface," *Soft Matter*, vol. 9, no. 42, pp. 10081–10091, 2013.

[343] J. N. Israelachvili, D. J. Mitchell, and B. W. Ninham, "Theory of self-assembly of hydrocarbon amphiphiles into micelles and bilayers," *Journal of the Chemical Society, Faraday Transactions 2: Molecular and Chemical Physics*, vol. 72, pp. 1525–1568, 1976.

[344] R. Nagarajan, "Molecular packing parameter and surfactant self-assembly: the neglected role of the surfactant tail," *Langmuir*, vol. 18, no. 1, pp. 31–38, 2002.

[345] L. Matthews, Ż. Przybyłowicz, S. E. Rogers, P. Bartlett, A. J. Johnson, R. Sochon, and W. H. Briscoe, "The curious case of sds self-assembly in glycerol: Formation of a lamellar gel," *Journal of Colloid and Interface Science*, vol. 572, pp. 384–395, 2020.

[346] R. Nagarajan and C.-C. Wang, "Theory of surfactant aggregation in water/ethylene glycol mixed solvents," *Langmuir*, vol. 16, no. 12, pp. 5242–5251, 2000.

[347] T. Tan, Z. Shen, Y. Wang, Z. Guo, J. Hu, and Y. Zhang, "Self-assembly of pentapeptides in ethanol to develop organogels," *Soft Matter*, vol. 16, no. 46, pp. 10567–10573, 2020.

[348] J. Zhang, L. Peng, and B. Han, "Amphiphile self-assemblies in supercritical CO_2 and ionic liquids," *Soft Matter*, vol. 10, no. 32, pp. 5861–5868, 2014.

[349] T. L. Greaves and C. J. Drummond, "Solvent nanostructure, the solvophobic effect and amphiphile self-assembly in ionic liquids," *Chemical Society Reviews*, vol. 42, no. 3, pp. 1096–1120, 2013.

[350] T. L. Greaves, A. Weerawardena, and C. J. Drummond, "Nanostructure and amphiphile self-assembly in polar molecular solvents: amides and the "solvophobic effect"," *Physical Chemistry Chemical Physics*, vol. 13, no. 20, pp. 9180–9186, 2011.

[351] D. F. Evans, A. Yamauchi, R. Roman, and E. Z. Casassa, "Micelle formation in ethylammonium nitrate, a low-melting fused salt," *Journal of Colloid and Interface Science*, vol. 88, no. 1, pp. 89–96, 1982.

[352] J. L. Anderson, V. Pino, E. C. Hagberg, V. V. Sheares, and D. W. Armstrong, "Surfactant solvation effects and micelle formation in ionic liquids," *Chemical Communications*, no. 19, pp. 2444–2445, 2003.

[353] C. R. López-Barrón and N. J. Wagner, "Structural transitions of CTAB micelles in a protic ionic liquid," *Langmuir*, vol. 28, no. 35, pp. 12722–12730, 2012.

[354] Z. Chen, T. L. Greaves, C. Fong, R. A. Caruso, and C. J. Drummond, "Lyotropic liquid crystalline phase behaviour in amphiphile–protic ionic liquid systems," *Physical Chemistry Chemical Physics*, vol. 14, no. 11, pp. 3825–3836, 2012.

[355] D. Yalcin, C. J. Drummond, and T. L. Greaves, "Lyotropic liquid crystal phase behavior of a cationic amphiphile in aqueous and non-stoichiometric protic ionic liquid mixtures," *Soft Matter*, vol. 16, no. 41, pp. 9456–9470, 2020.

[356] A. Dolan, R. Atkin, and G. G. Warr, "The origin of surfactant amphiphilicity and self-assembly in protic ionic liquids," *Chemical Science*, vol. 6, no. 11, pp. 6189–6198, 2015.

[357] T. L. Greaves, S. T. Mudie, and C. J. Drummond, "Effect of protic ionic liquids (PILs) on the formation of non-ionic dodecyl poly(ethylene oxide) surfactant self-assembly structures and the effect of these surfactants on the nanostructure of PILs," *Physical Chemistry Chemical Physics*, vol. 13, no. 45, pp. 20441–20452, 2011.

[358] T. Misono, H. Sakai, K. Sakai, M. Abe, and T. Inoue, "Surface adsorption and aggregate formation of nonionic surfactants in a room temperature ionic liquid, 1-butyl-3-methylimidazolium hexafluorophosphate ($bmimPF_6$)," *Journal of Colloid and Interface Science*, vol. 358, no. 2, pp. 527–533, 2011.

[359] T. Inoue, K. Kawashima, and Y. Miyagawa, "Aggregation behavior of nonionic surfactants in ionic liquid mixtures," *Journal of colloid and interface science*, vol. 363, no. 1, pp. 295–300, 2011.

[360] D. W. Bruce, C. P. Cabry, J. N. Canongia Lopes, M. L. Costen, L. D'Andrea, I. Grillo, B. C. Marshall, K. G. McKendrick, T. K. Minton, S. M. Purcell, *et al.*, "Nanosegregation and structuring in the bulk and at the surface of ionic-liquid mixtures," *The Journal of Physical Chemistry B*, vol. 121, no. 24, pp. 6002–6020, 2017.

[361] X. Tan, J. Zhang, T. Luo, X. Sang, C. Liu, B. Zhang, L. Peng, W. Li, and B. Han, "Micellization of long-chain ionic liquids in deep eutectic solvents," *Soft Matter*, vol. 12, no. 24, pp. 5297–5303, 2016.

[362] M. K. Banjare, K. Behera, M. L. Satnami, S. Pandey, and K. K. Ghosh, "Self-assembly of a short-chain ionic liquid within deep eutectic solvents," *RSC advances*, vol. 8, no. 15, pp. 7969–7979, 2018.

[363] S. McDonald, T. Murphy, S. Imberti, G. G. Warr, and R. Atkin, "Amphiphilically nanostructured deep eutectic solvents," *The Journal of Physical Chemistry Letters*, vol. 9, no. 14, pp. 3922–3927, 2018.

[364] J. J. Buzolic, H. Li, Z. M. Aman, G. G. Warr, and R. Atkin, "Self-assembled nanostructure induced in deep eutectic solvents via an amphiphilic hydrogen bond donor," *Journal of Colloid and Interface Science*, vol. 616, pp. 121–128, 2022.

[365] S. N. Butler and F. Müller-Plathe, "Nanostructures of ionic liquids do not break up under shear: A molecular dynamics study," *Journal of Molecular Liquids*, vol. 192, pp. 114–117, 2014.

[366] K. Tomita, M. Mizukami, S. Nakano, N. Ohta, N. Yagi, and K. Kurihara, "X-ray diffraction and resonance shear measurement of nano-confined ionic liquids," *Physical Chemistry Chemical Physics*, vol. 20, no. 20, pp. 13714–13721, 2018.

[367] T. Murphy, R. Hayes, S. Imberti, G. G. Warr, and R. Atkin, "Nanostructure of an ionic liquid–glycerol mixture," *Physical Chemistry Chemical Physics*, vol. 16, no. 26, pp. 13182–13190, 2014.

[368] T. Murphy, R. Hayes, S. Imberti, G. G. Warr, and R. Atkin, "Ionic liquid nanostructure enables alcohol self assembly," *Physical Chemistry Chemical Physics*, vol. 18, no. 18, pp. 12797–12809, 2016.

[369] T. Burankova, J. F. M. Cardozo, D. Rauber, A. Wildes, and J. P. Embs, "Linking structure to dynamics in protic ionic liquids: A neutron scattering study of correlated and single-particle motions," *Scientific Reports*, vol. 8, no. 1, pp. 1–10, 2018.

[370] S. J. Bryant, K. Wood, R. Atkin, and G. G. Warr, "Effect of protic ionic liquid nanostructure on phospholipid vesicle formation," *Soft Matter*, vol. 13, no. 7, pp. 1364–1370, 2017.

[371] D. Constatinescu, C. Herrmann, and H. Weingärtner, "Patterns of protein unfolding and protein aggregation in ionic liquids," *Physical Chemistry Chemical Physics*, vol. 12, no. 8, pp. 1756–1763, 2010.

[372] K. D. Weaver, R. M. Vrikkis, M. P. Van Vorst, J. Trullinger, R. Vijayaraghavan, D. M. Foureau, I. H. McKillop, D. R. MacFarlane, J. K. Krueger, and G. D. Elliott, "Structure and function of proteins in hydrated choline dihydrogen phosphate ionic liquid," *Physical Chemistry Chemical Physics*, vol. 14, no. 2, pp. 790–801, 2012.

[373] Q. Han, S. J. Brown, C. J. Drummond, and T. L. Greaves, "Protein aggregation and crystallization with ionic liquids: Insights into the influence of solvent properties," *Journal of Colloid and Interface Science*, vol. 608, pp. 1173–1190, 2022.

[374] T. B. Dinis, F. Sousa, and M. G. Freire, "Insights on the DNA stability in aqueous solutions of ionic liquids," *Frontiers in Bioengineering and Biotechnology*, vol. 8, p. 1207, 2020.

[375] S. K. Soni, S. Sarkar, N. Mirzadeh, P. Selvakannan, and S. K. Bhargava, "Self-assembled functional nanostructure of plasmid DNA with ionic liquid [Bmim][PF_6]: Enhanced efficiency in bacterial gene transformation," *Langmuir*, vol. 31, no. 16, pp. 4722–4732, 2015.

[376] A. Dolan, D. A. Sherman, R. Atkin, and G. G. Warr, "Kamlet–Taft solvation parameters of solvate ionic liquids," *ChemPhysChem*, vol. 17, no. 19, pp. 3096–3101, 2016.

[377] A. Pandey, R. Rai, M. Pal, and S. Pandey, "How polar are choline chloride-based deep eutectic solvents?," *Physical Chemistry Chemical Physics*, vol. 16, no. 4, pp. 1559–1568, 2014.

[378] A. Pandey and S. Pandey, "Solvatochromic probe behavior within choline chloride-based deep eutectic solvents: effect of temperature and water," *The Journal of Physical Chemistry B*, vol. 118, no. 50, pp. 14652–14661, 2014.

[379] D. Rengstl, V. Fischer, and W. Kunz, "Low-melting mixtures based on choline ionic liquids," *Physical Chemistry Chemical Physics*, vol. 16, no. 41, pp. 22815–22822, 2014.

[380] M. Pal, R. Rai, A. Yadav, R. Khanna, G. A. Baker, and S. Pandey, "Self-aggregation of sodium dodecyl sulfate within (choline chloride + urea) deep eutectic solvent," *Langmuir*, vol. 30, no. 44, pp. 13191–13198, 2014.

[381] M. Pal, R. K. Singh, and S. Pandey, "Evidence of self-aggregation of cationic surfactants in a choline chloride + glycerol deep eutectic solvent," *ChemPhysChem*, vol. 16, no. 12, pp. 2538–2542, 2015.

[382] A. Sanchez-Fernandez, K. J. Edler, T. Arnold, R. K. Heenan, L. Porcar, N. J. Terrill, A. Terry, and A. J. Jackson, "Micelle structure in a deep eutectic solvent: a small-angle scattering study," *Physical Chemistry Chemical Physics*, vol. 18, no. 20, pp. 14063–14073, 2016.

[383] M. Bergström and J. S. Pedersen, "Structure of pure SDS and DTAB micelles in brine determined by small-angle neutron scattering (SANS)," *Physical Chemistry Chemical Physics*, vol. 1, no. 18, pp. 4437–4446, 1999.

[384] C. A. Dreiss, "Wormlike micelles: where do we stand? recent developments, linear rheology and scattering techniques," *Soft Matter*, vol. 3, no. 8, pp. 956–970, 2007.

[385] A. Sanchez-Fernandez, O. S. Hammond, A. J. Jackson, T. Arnold, J. Doutch, and K. J. Edler, "Surfactant–solvent interaction effects on the micellization of cationic surfactants in a carboxylic acid-based deep eutectic solvent," *Langmuir*, vol. 33, no. 50, pp. 14304–14314, 2017.

[386] Q. Li, J. Wang, N. Lei, M. Yan, X. Chen, and X. Yue, "Phase behaviours of a cationic surfactant in deep eutectic solvents: from micelles to lyotropic liquid crystals," *Physical Chemistry Chemical Physics*, vol. 20, no. 17, pp. 12175–12181, 2018.

[387] S. S. Berr, M. J. Coleman, R. R. M. Jones, and J. S. Johnson Jr, "Small-angle neutron scattering study of the structural effects of substitution of tetramethylammonium for sodium as the counterion in dodecyl sulfate micelles," *The Journal of Physical Chemistry*, vol. 90, no. 24, pp. 6492–6499, 1986.

[388] Z. Chen, S. McDonald, P. FitzGerald, G. G. Warr, and R. Atkin, "Small angle neutron scattering study of the conformation of poly(ethylene oxide) dissolved in deep eutectic solvents," *Journal of Colloid and Interface Science*, vol. 506, pp. 486–492, 2017.

[389] R. Stefanovic, G. B. Webber, and A. J. Page, "Polymer solvation in choline chloride deep eutectic solvents modulated by the hydrogen bond donor," *Journal of Molecular Liquids*, vol. 279, pp. 584–593, 2019.

[390] I. Manasi, M. R. Andalibi, R. S. Atri, J. Hooton, S. M. King, and K. J. Edler, "Self-assembly of ionic and non-ionic surfactants in type IV cerium nitrate and urea based deep eutectic solvent," *The Journal of Chemical Physics*, vol. 155, no. 8, p. 084902, 2021.

[391] A. Sanchez-Fernandez, K. Edler, T. Arnold, D. A. Venero, and A. Jackson, "Protein conformation in pure and hydrated deep eutectic solvents," *Physical Chemistry Chemical Physics*, vol. 19, no. 13, pp. 8667–8670, 2017.

[392] M. Pal, A. Yadav, and S. Pandey, "Aggregation of carbocyanine dyes in choline chloride-based deep eutectic solvents in the presence of an aqueous base," *Langmuir*, vol. 33, no. 38, pp. 9781–9792, 2017.

[393] K. Xu, P. Xu, and Y. Wang, "Aqueous biphasic systems formed by hydrophilic and hydrophobic deep eutectic solvents for the partitioning of dyes," *Talanta*, vol. 213, p. 120839, 2020.

[394] M. C. Gutiérrez, M. L. Ferrer, L. Yuste, F. Rojo, and F. del Monte, "Bacteria incorporation in deep-eutectic solvents through freeze-drying," *Angewandte Chemie*, vol. 122, no. 12, pp. 2204–2208, 2010.

[395] S. J. Bryant, R. Atkin, and G. G. Warr, "Spontaneous vesicle formation in a deep eutectic solvent," *Soft Matter*, vol. 12, no. 6, pp. 1645–1648, 2016.

[396] S. J. Bryant, R. Atkin, and G. G. Warr, "Effect of deep eutectic solvent nanostructure on phospholipid bilayer phases," *Langmuir*, vol. 33, no. 27, pp. 6878–6884, 2017.

[397] A. Sanchez-Fernandez, G. L. Moody, L. C. Murfin, T. Arnold, A. J. Jackson, S. M. King, S. E. Lewis, and K. J. Edler, "Self-assembly and surface behaviour of pure and mixed zwitterionic amphiphiles in a deep eutectic solvent," *Soft Matter*, vol. 14, no. 26, pp. 5525–5536, 2018.

[398] J. A. Hammons, F. Zhang, and J. Ilavsky, "Extended hierarchical solvent perturbations from curved surfaces of mesoporous silica particles in a deep eutectic solvent," *Journal of Colloid and Interface Science*, vol. 520, pp. 81–90, 2018.

[399] J. S. Beck, J. C. Vartuli, W. J. Roth, M. E. Leonowicz, C. Kresge, K. Schmitt, C. Chu, D. H. Olson, E. Sheppard, S. McCullen, J. Higgins, and J. Scklenker, "A new family of mesoporous molecular sieves prepared with liquid crystal templates," *Journal of the American Chemical Society*, vol. 114, no. 27, pp. 10834–10843, 1992.

[400] J. Sarkar, V. T. John, J. He, C. Brooks, D. Gandhi, A. Nunes, G. Ramanath, and A. Bose, "Surfactant-templated synthesis and catalytic properties of patterned nanoporous titania supports loaded with platinum nanoparticles," *Chemistry of Materials*, vol. 20, no. 16, pp. 5301–5306, 2008.

[401] M. Shibayama, "Small-angle neutron scattering on polymer gels: phase behavior, inhomogeneities and deformation mechanisms," *Polymer Journal*, vol. 43, no. 1, pp. 18–34, 2011.

[402] S. S. Begum, V. K. Aswal, and R. P. Ramasamy, "Small-angle neutron scattering and spectroscopic investigations of Ag fractal formation in chitosan–Ag nanocomposite facilitated by hydrazine hydrate," *The Journal of Physical Chemistry C*, vol. 120, no. 4, pp. 2400–2410, 2016.

[403] J. M. McMullan and N. J. Wagner, "Directed self-assembly of colloidal crystals by dielectrophoretic ordering observed with small angle neutron scattering (SANS)," *Soft Matter*, vol. 6, no. 21, pp. 5443–5450, 2010.

[404] E. Mahieu and F. Gabel, "Biological small-angle neutron scattering: recent results and development," *Acta Crystallographica Section D: Structural Biology*, vol. 74, no. 8, pp. 715–726, 2018.

[405] F. G. Brunetti, R. Kumar, and F. Wudl, "Organic electronics from perylene to organic photovoltaics: painting a brief history with a broad brush," *Journal of Materials Chemistry*, vol. 20, no. 15, pp. 2934–2948, 2010.

[406] L. Herbst, H. Hoffmann, J. Kalus, K. Reizlein, U. Schmelzer, and K. Ibel, "Small angle neutron scattering on nematic lyotropic liquid crystals," *Berichte der Bunsengesellschaft für Physikalische Chemie*, vol. 89, no. 10, pp. 1050–1064, 1985.

[407] V. Degiorgio, G. Banfi, G. Righini, and A. Rennie, "Small-angle neutron scattering study of semiconductor microcrystallites in optical glasses," *Applied Physics Letters*, vol. 57, no. 27, pp. 2879–2881, 1990.

[408] "SasView for small angle scattering analysis.." `http://sasview.org`. Retrieved: October 2021.

[409] A. Isihara, "Determination of molecular shape by osmotic measurement," *The Journal of Chemical Physics*, vol. 18, no. 11, pp. 1446–1449, 1950.

[410] A. Guinier and G. Fournet, *Small-angle scattering of X-rays.* John Wiley and Sons, Inc., 1955.

[411] G. Fournet, "Influence of the size and shape of particles on the interpretation of the x-ray diffuse diagrams," *Discussions of the Faraday Society*, vol. 11, pp. 121–125, 1951.

[412] J. S. Pedersen, "Analysis of small-angle scattering data from colloids and polymer solutions: modeling and least-squares fitting," *Advances in Colloid and Interface Science*, vol. 70, pp. 171–210, 1997.

[413] H. Zuidema and G. Waters, "Ring method for the determination of interfacial tension," *Industrial & Engineering Chemistry Analytical Edition*, vol. 13, no. 5, pp. 312–313, 1941.

[414] M. A. Kadhom, G. H. Abdullah, and N. Al-Bayati, "Studying two series of ternary deep eutectic solvents (choline chloride–urea–glycerol) and (choline chloride–malic acid–glycerol), synthesis and characterizations," *Arabian Journal for Science and Engineering*, vol. 42, no. 4, pp. 1579–1589, 2017.

[415] H. Li, D. Hu, F. Liang, X. Huang, and Q. Zhu, "Influence factors on the critical micelle concentration determination using pyrene as a probe and a simple method of preparing samples," *Royal Society Open Science*, vol. 7, no. 3, 2020.

[416] N. Kundu, D. Banik, A. Roy, J. Kuchlyan, and N. Sarkar, "Modulation of the aggregation properties of sodium deoxycholate in presence of hydrophilic imidazolium based ionic liquid: water dynamics study to probe the structural alteration of the aggregates," *Physical Chemistry Chemical Physics*, vol. 17, no. 38, pp. 25216–25227, 2015.

[417] M. Pisárčik, F. Devínsky, and M. Pupák, "Determination of micelle aggregation numbers of alkyltrimethylammonium bromide and sodium dodecyl sulfate surfactants using time-resolved fluorescence quenching," *Open Chemistry*, vol. 13, no. 1, 2015.

[418] L. Piñeiro, M. Novo, and W. Al-Soufi, "Fluorescence emission of pyrene in surfactant solutions," *Advances in Colloid and Interface Science*, vol. 215, pp. 1–12, 2015.

[419] S. Simeonov and C. A. Afonso, "Basicity and stability of urea deep eutectic mixtures," *RSC Advances*, vol. 6, no. 7, pp. 5485–5490, 2016.

[420] O. Arnold, J.-C. Bilheux, J. Borreguero, A. Buts, S. I. Campbell, L. Chapon, M. Doucet, N. Draper, R. F. Leal, M. Gigg, *et al.*, "Mantid—data analysis and visualization package for neutron scattering and μSR experiments," *Nuclear Instruments and Methods in Physics Research Section A: Accelerators, Spectrometers, Detectors and Associated Equipment*, vol. 764, pp. 156–166, 2014.

[421] R. B. Leron, D. S. H. Wong, and M.-H. Li, "Densities of a deep eutectic solvent based on choline chloride and glycerol and its aqueous mixtures at elevated pressures," *Fluid Phase Equilibria*, vol. 335, pp. 32–38, 2012.

[422] A. Yadav, S. Trivedi, R. Rai, and S. Pandey, "Densities and dynamic viscosities of (choline chloride + glycerol) deep eutectic solvent and its aqueous mixtures in the temperature range (283.15–363.15) k," *Fluid Phase Equilibria*, vol. 367, pp. 135–142, 2014.

[423] I. Adamenko, L. Bulavin, V. Ilyin, S. Zelinsky, and K. Moroz, "Anomalous behavior of glycerol–water solutions," *Journal of Molecular Liquids*, vol. 127, no. 1-3, pp. 90–92, 2006.

[424] D. F. Evans, "Self-organization of amphiphiles," *Langmuir*, vol. 4, no. 1, pp. 3–12, 1988.

[425] K. A. Silverstein, A. Haymet, and K. A. Dill, "A simple model of water and the hydrophobic effect," *Journal of the American Chemical Society*, vol. 120, no. 13, pp. 3166–3175, 1998.

[426] G. G. Warr and R. Atkin, "Solvophobicity and amphiphilic self-assembly in neoteric and nanostructured solvents," *Current Opinion in Colloid & Interface Science*, vol. 45, pp. 83–96, 2020.

[427] N. Vargaftik, B. Volkov, and L. Voljak, "International tables of the surface tension of water," *Journal of Physical and Chemical Reference Data*, vol. 12, no. 3, pp. 817–820, 1983.

[428] T. L. Greaves and C. J. Drummond, "Ionic liquids as amphiphile self-assembly media," *Chemical Society Reviews*, vol. 37, no. 8, pp. 1709–1726, 2008.

[429] Y. Xie, H. Dong, S. Zhang, X. Lu, and X. Ji, "Effect of water on the density, viscosity, and CO_2 solubility in choline chloride/urea," *Journal of Chemical & Engineering Data*, vol. 59, no. 11, pp. 3344–3352, 2014.

[430] M. Jablonsky, A. Skulcova, A. Haz, J. Sima, and V. Majová, "Long-term isothermal stability of deep eutectic solvents," *BioResources*, vol. 13, no. 4, pp. 7545–7559, 2018.

[431] M. J. Iqbal, M. A. Rauf, and N. Ijaz, "Surface tension measurements of glycerol with organic cosolvents," *Journal of Chemical and Engineering Data*, vol. 37, no. 1, pp. 45–47, 1992.

[432] M. L. Kijevčanin, E. M. Živković, B. D. Djordjević, I. R. Radović, J. Jovanović, and S. P. Šerbanović, "Experimental determination and modeling of excess molar volumes, viscosities and refractive indices of the binary systems (pyridine+1-propanol, +1,2-propanediol, +1,3-propanediol, and +glycerol). new UNIFAC-VISCO parameters determination," *The Journal of Chemical Thermodynamics*, vol. 56, pp. 49–56, 2013.

[433] O. S. Hammond, "Plant metabolites as green solvents," Master's thesis, University of Bath, United Kingdom, 2015.

[434] N. Scholz, T. Behnke, and U. Resch-Genger, "Determination of the critical micelle concentration of neutral and ionic surfactants with fluorometry, conductometry, and surface tension—a method comparison," *Journal of Fluorescence*, vol. 28, no. 1, pp. 465–476, 2018.

[435] "NCNR SANS and USANS data reduction and analysis.." `https://ncnr.nist.gov/programs/sans/data/red_anal.html`. Retrieved: October 2021.

[436] "Igor Pro 6.3 by Wavemetrics.." `https://www.wavemetrics.com/order/order_igordownloads6.htm`. Retrieved: October 2021.

[437] J. B. Hayter and J. Penfold, "An analytic structure factor for macroion solutions," *Molecular Physics*, vol. 42, no. 1, pp. 109–118, 1981.

[438] J. K. Percus and G. J. Yevick, "Analysis of classical statistical mechanics by means of collective coordinates," *Physical Review*, vol. 110, no. 1, p. 1, 1958.

[439] G. D'Errico, O. Ortona, L. Paduano, and V. Vitagliano, "Transport properties of aqueous solutions of alkyltrimethylammonium bromide surfactants at 25C," *Journal of Colloid and Interface Science*, vol. 239, no. 1, pp. 264–271, 2001.

[440] F. Palazzesi, M. Calvaresi, and F. Zerbetto, "A molecular dynamics investigation of structure and dynamics of SDS and SDBS micelles," *Soft Matter*, vol. 7, no. 19, pp. 9148–9156, 2011.

[441] S. Berr, "Solvent isotope effects on alkytrimethylammonium bromide micelles as a function of alkyl chain length," *Journal of Physical Chemistry*, vol. 91, no. 18, pp. 4760–4765, 1987.

[442] J. B. Hayter and J. Penfold, "Determination of micelle structure and charge by neutron small-angle scattering," *Colloid and Polymer Science*, vol. 261, no. 12, pp. 1022–1030, 1983.

[443] S. A. Buckingham, C. J. Garvey, and G. G. Warr, "Effect of head-group size on micellization and phase behavior in quaternary ammonium surfactant systems," *The Journal of Physical Chemistry*, vol. 97, no. 39, pp. 10236–10244, 1993.

[444] Y. Lin, X. Han, J. Huang, H. Fu, and C. Yu, "A facile route to design ph-responsive viscoelastic wormlike micelles: smart use of hydrotropes," *Journal of colloid and interface science*, vol. 330, no. 2, pp. 449–455, 2009.

[445] A. Soper and K. Edler, "Coarse-grained empirical potential structure refinement: Application to a reverse aqueous micelle," *Biochimica et Biophysica Acta (BBA)-General Subjects*, vol. 1861, no. 6, pp. 1652–1660, 2017.

[446] R. Nagarajan and E. Ruckenstein, "Theory of surfactant self-assembly: a predictive molecular thermodynamic approach," *Langmuir*, vol. 7, no. 12, pp. 2934–2969, 1991.

[447] S. Pandey, R. P. Bagwe, and D. O. Shah, "Effect of counterions on surface and foaming properties of dodecyl sulfate," *Journal of Colloid and Interface Science*, vol. 267, no. 1, pp. 160–166, 2003.

[448] L. Horváth, B. Mihaljević, V. Tomašić, D. Risović, and N. Filipović-Vinceković, "Counterion binding to ionic micelles: Effects of counterion specificity," *Journal of Dispersion Science and Technology*, vol. 22, no. 2-3, pp. 221–229, 2001.

[449] V. A. Rabinovich and Z. I. Khavin, *Kratkii Khimicheskii Spravochnik (Concise Handbook of Chemistry).* Leningrad: Khimiia, 1978.

[450] S. P. Pinho and E. A. Macedo, "Solubility of NaCl, NaBr, and KCl in water, methanol, ethanol, and their mixed solvents," *Journal of Chemical & Engineering Data*, vol. 50, no. 1, pp. 29–32, 2005.

[451] B. Kang, H. Tang, Z. Zhao, and S. Song, "Hofmeister series: Insights of ion specificity from amphiphilic assembly and interface property," *ACS Omega*, vol. 5, no. 12, pp. 6229–6239, 2020.

[452] W. Kunz, "Specific ion effects in colloidal and biological systems," *Current Opinion in Colloid & Interface Science*, vol. 15, no. 1-2, pp. 34–39, 2010.

[453] "Materials Safety Database Sheet for hexadecyltrimethylammonium bromide (C_{16}TAB)." `https://www.sigmaaldrich.com/GB/en/sds/aldrich/855820`. Accessed: December 2021.

[454] T. Imae, R. Kamiya, and S. Ikeda, "Formation of spherical and rod-like micelles of cetyltrimethylammonium bromide in aqueous NaBr solutions," *Journal of Colloid and Interface Science*, vol. 108, no. 1, pp. 215–225, 1985.

[455] A. Sanchez-Fernandez, A. J. Jackson, S. F. Prévost, J. J. Doutch, and K. J. Edler, "Long-range electrostatic colloidal interactions and specific ion effects in deep eutectic solvents," *Journal of the American Chemical Society*, vol. 143, no. 35, pp. 14158–14168, 2021.

[456] M. A. Gebbie, A. M. Smith, H. A. Dobbs, G. G. Warr, X. Banquy, M. Valtiner, M. W. Rutland, J. N. Israelachvili, S. Perkin, and R. Atkin, "Long range electrostatic forces in ionic liquids," *Chemical Communications*, vol. 53, no. 7, pp. 1214–1224, 2017.

[457] C. Ma, A. Laaksonen, C. Liu, X. Lu, and X. Ji, "The peculiar effect of water on ionic liquids and deep eutectic solvents," *Chemical Society Reviews*, vol. 47, no. 23, pp. 8685–8720, 2018.

[458] J. Yao, W. Tjandra, Y. Z. Chen, K. C. Tam, J. Ma, and B. Soh, "Hydroxyapatite nanostructure material derived using cationic surfactant as a template," *Journal of Materials Chemistry*, vol. 13, no. 12, pp. 3053–3057, 2003.

[459] B. Purnawira, H. Purwaningsih, Y. Ervianto, V. Pratiwi, D. Susanti, R. Rochiem, and A. Purniawan, "Synthesis and characterization of mesoporous silica nanoparticles (MSNp) MCM-41 from natural waste rice husk," in *IOP Conference Series: Materials Science and Engineering*, vol. 541, IOP Publishing, 2019.

[460] F. Xu, P. Zhang, A. Navrotsky, Z.-Y. Yuan, T.-Z. Ren, M. Halasa, and B.-L. Su, "Hierarchically assembled porous ZnO nanoparticles: synthesis, surface energy, and photocatalytic activity," *Chemistry of Materials*, vol. 19, no. 23, pp. 5680–5686, 2007.

[461] M. L. Kahn, M. Monge, V. Collière, F. Senocq, A. Maisonnat, and B. Chaudret, "Size- and shape-control of crystalline zinc oxide nanoparticles: a new organometallic synthetic method," *Advanced Functional Materials*, vol. 15, no. 3, pp. 458–468, 2005.

[462] R.-q. Chen, C.-w. Zou, X.-d. Yan, and G. Wei, "Zinc oxide nanostructures and porous films produced by oxidation of zinc precursors in wet-oxygen atmosphere," *Progress in Natural Science: Materials International*, vol. 21, no. 2, pp. 81–96, 2011.

[463] X. Han, J. Harris, and L. Šiller, "Synthesis of porous zinc-based/zinc oxide composites via sol–gel and ambient pressure drying routes," *Journal of Materials Science*, vol. 53, no. 11, pp. 8170–8179, 2018.

[464] "SasView user documentation." `https://www.sasview.org/docs/user/models/cylinder.html`. Accessed: October 2021.

[465] A. E. Ünlü, A. Arıkaya, and S. Takaç, "Use of deep eutectic solvents as catalyst: A mini-review," *Green Processing and Synthesis*, vol. 8, no. 1, pp. 355–372, 2019.

[466] W. Muhammad, N. Ullah, M. Haroon, and B. H. Abbasi, "Optical, morphological and biological analysis of zinc oxide nanoparticles (ZnO NPs) using Papaver somniferum L.," *RSC Advances*, vol. 9, no. 51, pp. 29541–29548, 2019.

[467] R. Stefanovic, M. Ludwig, G. B. Webber, R. Atkin, and A. J. Page, "Nanostructure, hydrogen bonding and rheology in choline chloride deep eutectic solvents as a function of the hydrogen bond donor," *Physical Chemistry Chemical Physics*, vol. 19, no. 4, pp. 3297–3306, 2017.

[468] S. Kaur, S. Sharma, and H. K. Kashyap, "Bulk and interfacial structures of reline deep eutectic solvent: A molecular dynamics study," *The Journal of Chemical Physics*, vol. 147, no. 19, p. 194507, 2017.

[469] J. Płotka-Wasylka, M. De la Guardia, V. Andruch, and M. Vilková, "Deep eutectic solvents vs ionic liquids: Similarities and differences," *Microchemical Journal*, 2020.

[470] O. S. Hammond and K. J. Edler, *Structure and Implications*, ch. 2, pp. 25–42. John Wiley & Sons, Ltd, 2019.

[471] S. Kaur, M. Kumari, and H. K. Kashyap, "Microstructure of deep eutectic solvents: Current understanding and challenges," *The Journal of Physical Chemistry B*, vol. 124, no. 47, pp. 10601–10616, 2020.

[472] S. J. Bryant, A. J. Christofferson, T. L. Greaves, C. F. McConville, G. Bryant, and A. Elbourne, "Bulk and interfacial nanostructure and properties in deep eutectic solvents: Current perspectives and future directions," *Journal of Colloid and Interface Science*, vol. 608, pp. 2430–2454, 2022.

[473] C. D'Agostino, R. C. Harris, A. P. Abbott, L. F. Gladden, and M. D. Mantle, "Molecular motion and ion diffusion in choline chloride based deep eutectic solvents studied by ^{1}H pulsed field gradient NMR spectroscopy," *Physical Chemistry Chemical Physics*, vol. 13, no. 48, pp. 21383–21391, 2011.

[474] J. M. Rimsza and L. R. Corrales, "Adsorption complexes of copper and copper oxide in the deep eutectic solvent 2:1 urea–choline chloride," *Computational and Theoretical Chemistry*, vol. 987, pp. 57–61, 2012.

[475] H. Sun, Y. Li, X. Wu, and G. Li, "Theoretical study on the structures and properties of mixtures of urea and choline chloride," *Journal of Molecular Modeling*, vol. 19, no. 6, pp. 2433–2441, 2013.

[476] S. L. Perkins, P. Painter, and C. M. Colina, "Molecular dynamic simulations and vibrational analysis of an ionic liquid analogue," *The Journal of Physical Chemistry B*, vol. 117, no. 35, pp. 10250–10260, 2013.

[477] S. L. Perkins, P. Painter, and C. M. Colina, "Experimental and computational studies of choline chloride-based deep eutectic solvents," *Journal of Chemical & Engineering Data*, vol. 59, no. 11, pp. 3652–3662, 2014.

[478] G. Garcia, M. Atilhan, and S. Aparicio, "An approach for the rationalization of melting temperature for deep eutectic solvents from DFT," *Chemical Physics Letters*, vol. 634, pp. 151–155, 2015.

[479] E. S. Ferreira, I. V. Voroshylova, C. M. Pereira, and M. N. DS Cordeiro, "Improved force field model for the deep eutectic solvent ethaline: Reliable physicochemical properties," *The Journal of Physical Chemistry B*, vol. 120, no. 38, pp. 10124–10137, 2016.

[480] T. Zhekenov, N. Toksanbayev, Z. Kazakbayeva, D. Shah, and F. S. Mjalli, "Formation of type III deep eutectic solvents and effect of water on their intermolecular interactions," *Fluid Phase Equilibria*, vol. 441, pp. 43–48, 2017.

[481] D. V. Wagle, G. A. Baker, and E. Mamontov, "Differential microscopic mobility of components within a deep eutectic solvent," *The journal of Physical Chemistry Letters*, vol. 6, no. 15, pp. 2924–2928, 2015.

[482] E. O. Fetisov, D. B. Harwood, I.-F. W. Kuo, S. E. Warrag, M. C. Kroon, C. J. Peters, and J. I. Siepmann, "First-principles molecular dynamics study of a deep eutectic solvent: Choline chloride/urea and its mixture with water," *The Journal of Physical Chemistry B*, vol. 122, no. 3, pp. 1245–1254, 2018.

[483] L. Gontrani, M. Bonomo, N. V. Plechkova, D. Dini, and R. Caminiti, "X-ray structure and ionic conductivity studies of anhydrous and hydrated choline chloride and oxalic acid deep eutectic solvents," *Physical Chemistry Chemical Physics*, vol. 20, no. 48, pp. 30120–30124, 2018.

[484] J. Towey, A. Soper, and L. Dougan, "The structure of glycerol in the liquid state: a neutron diffraction study," *Physical Chemistry Chemical Physics*, vol. 13, no. 20, pp. 9397–9406, 2011.

[485] A. P. Abbott, R. C. Harris, and K. S. Ryder, "Application of hole theory to define ionic liquids by their transport properties," *The Journal of Physical Chemistry B*, vol. 111, no. 18, pp. 4910–4913, 2007.

[486] A. Faraone, D. V. Wagle, G. A. Baker, E. Novak, M. Ohl, D. Reuter, P. Lunkenheimer, A. Loidl, and E. Mamontov, "Glycerol hydrogen-bonding network dominates structure and collective dynamics in a deep eutectic solvent," *The Journal of Physical Chemistry B*, vol. 122, no. 3, pp. 1261–1267, 2018.

[487] S. Kaur, A. Gupta, and H. K. Kashyap, "Nanoscale spatial heterogeneity in deep eutectic solvents," *The Journal of Physical Chemistry B*, vol. 120, no. 27, pp. 6712–6720, 2016.

[488] B. Guchhait, S. Das, S. Daschakraborty, and R. Biswas, "Interaction and dynamics of (alkylamide+ electrolyte) deep eutectics: Dependence on alkyl chain-length, temperature, and anion identity," *The Journal of Chemical Physics*, vol. 140, no. 10, p. 104514, 2014.

[489] M. A. R. Martins, E. A. Crespo, P. V. A. Pontes, L. P. Silva, M. Bl̈ow, G. J. Maximo, E. A. Batista, C. Held, S. P. Pinho, and J. A. P. Coutinho, "Tunable hydrophobic eutectic solvents based on terpenes and monocarboxylic acids," *ACS Sustainable Chemistry & Engineering*, vol. 6, no. 7, pp. 8836–8846, 2018.

[490] A. Malik and H. K. Kashyap, "Heterogeneity in hydrophobic deep eutectic solvents: SAXS prepeak and local environments," *Physical Chemistry Chemical Physics*, vol. 23, no. 6, pp. 3915–3924, 2021.

[491] Y. Dai, G.-J. Witkamp, R. Verpoorte, and Y. H. Choi, "Tailoring properties of natural deep eutectic solvents with water to facilitate their applications," *Food Chemistry*, vol. 187, pp. 14–19, 2015.

[492] E. Posada, N. López-Salas, R. J. Riobóo, M. L. Ferrer, M. C. Gutiérrez, and F. Del Monte, "Reline aqueous solutions behaving as liquid mixtures of H-bonded co-solvents: microphase segregation and formation of co-continuous structures as indicated by Brillouin and ^{1}H NMR spectroscopies," *Physical Chemistry Chemical Physics*, vol. 19, no. 26, pp. 17103–17110, 2017.

[493] A. Yadav and S. Pandey, "Densities and viscosities of (choline chloride+urea) deep eutectic solvent and its aqueous mixtures in the temperature range 293.15 K to 363.15 K," *Journal of Chemical & Engineering Data*, vol. 59, no. 7, pp. 2221–2229, 2014.

[494] D. Shah and F. S. Mjalli, "Effect of water on the thermo-physical properties of reline: An experimental and molecular simulation based approach," *Physical Chemistry Chemical Physics*, vol. 16, no. 43, pp. 23900–23907, 2014.

[495] P. Kumari, S. Shobhna, S. Kaur, and H. K. Kashyap, "Influence of hydration on the structure of reline deep eutectic solvent: A molecular dynamics study," *ACS Omega*, vol. 3, no. 11, pp. 15246–15255, 2018.

[496] L. Sapir and D. Harries, "Restructuring a deep eutectic solvent by water: The nanostructure of hydrated choline chloride/urea," *Journal of Chemical Theory and Computation*, vol. 16, no. 5, pp. 3335–3342, 2020.

[497] L. Weng and M. Toner, "Janus-faced role of water in defining nanostructure of choline chloride/glycerol deep eutectic solvent," *Physical Chemistry Chemical Physics*, vol. 20, no. 35, pp. 22455–22462, 2018.

[498] A. K. Soper, "GudrunN and GudrunX. programs for correcting raw neutron and x-ray total scattering data to differential cross section," tech. rep., Rutherford Appleton Laboratory, 2011.

[499] A. Yadav, J. R. Kar, M. Verma, S. Naqvi, and S. Pandey, "Densities of aqueous mixtures of (choline chloride+ethylene glycol) and (choline chloride+malonic acid) deep eutectic solvents in temperature range 283.15–363.15 K," *Thermochimica Acta*, vol. 600, pp. 95–101, 2015.

[500] N. Metropolis, A. W. Rosenbluth, M. N. Rosenbluth, A. H. Teller, and E. Teller, "Equation of state calculations by fast computing machines," *The Journal of Chemical Physics*, vol. 21, no. 6, pp. 1087–1092, 1953.

[501] S. A. Hollingsworth and R. O. Dror, "Molecular dynamics simulation for all," *Neuron*, vol. 99, no. 6, pp. 1129–1143, 2018.

[502] H. S. Salehi, H. M. Polat, F. de Meyer, C. Houriez, C. Coquelet, T. J. H. Vlugt, and O. A. Moultos, "Vapor pressures and vapor phase compositions of choline chloride urea and choline chloride ethylene glycol deep eutectic solvents from molecular simulation," *The Journal of Chemical Physics*, vol. 155, no. 11, 2021.

[503] B. Guillot, "A reappraisal of what we have learnt during three decades of computer simulations on water," *Journal of Molecular Liquids*, vol. 101, no. 1-3, pp. 219–260, 2002.

[504] K. J. Edler and D. T. Bowron, "Combining wide-angle and small-angle scattering to study colloids and self-assembly," *Current Opinion in Colloid & Interface Science*, vol. 20, no. 4, pp. 227–234, 2015.

[505] T. Yamaguchi, K. Yoshida, T. Yamaguchi, Y. Kameda, K. Ikeda, and T. Otomo, "Analysis of prepeak structure of concentrated organic lithium electrolyte by means of neutron diffraction with isotopic substitution and molecular dynamics simulation," *The Journal of Physical Chemistry B*, vol. 121, no. 21, pp. 5355–5362, 2017.

[506] A. K. Soper, "Empirical potential Monte Carlo simulation of fluid structure," *Chemical Physics*, vol. 202, no. 2-3, pp. 295–306, 1996.

[507] A. K. Soper, "Computer simulation as a tool for the interpretation of total scattering data from glasses and liquids," *Molecular Simulation*, vol. 38, no. 14-15, pp. 1171–1185, 2012.

[508] A. K. Soper, "Tests of the empirical potential structure refinement method and a new method of application to neutron diffraction data on water," *Molecular Physics*, vol. 99, no. 17, pp. 1503–1516, 2001.

[509] A. K. Soper, "Partial structure factors from disordered materials diffraction data: An approach using empirical potential structure refinement," *Physical Review B*, vol. 72, no. 10, p. 104204, 2005.

[510] B. Rousseau, C. Van Alsenoy, R. Keuleers, and H. Desseyn, "Solids modelled by ab-initio crystal field methods. study of the structure and vibrational spectrum of urea in the gas phase and in its P421m crystal phase," *The Journal of Physical Chemistry A*, vol. 102, no. 32, pp. 6540–6548, 1998.

[511] A. K. Soper, "Inelasticity corrections for time-of-flight and fixed wavelength neutron diffraction experiments," *Molecular Physics*, vol. 107, no. 16, pp. 1667–1684, 2009.

[512] A. K. Soper, E. W. Castner Jr, and A. Luzar, "Impact of urea on water structure: a clue to its properties as a denaturant?," *Biophysical Chemistry*, vol. 105, no. 2-3, pp. 649–666, 2003.

[513] J. J. Towey, A. K. Soper, and L. Dougan, "Molecular insight into the hydrogen bonding and micro-segregation of a cryoprotectant molecule," *The Journal of Physical Chemistry B*, vol. 116, no. 47, pp. 13898–13904, 2012.

[514] J. R. Lu, M. Hromadova, E. A. Simister, R. K. Thomas, and J. Penfold, "Neutron reflection from hexadecyltrimethylammonium bromide adsorbed at the air/liquid interface: The variation of the hydrocarbon chain distribution with surface concentration," *The Journal of Physical Chemistry*, vol. 98, no. 44, pp. 11519–11526, 1994.

[515] Z. Lu, Z. Chang, W. Zhu, and X. Sun, "Beta-phased Ni$(OH)_2$ nanowall film with reversible capacitance higher than theoretical Faradic capacitance," *Chemical Communications*, vol. 47, no. 34, pp. 9651–9653, 2011.

Appendix A

Supplementary data from Chapter 4

A.1 Differential scanning calorimetry results

DSC measurements were carried out according to the method described in Chapter 4, Section 4.5.4.3. The samples were first equilibrated at 50 °C and held for 1 min, cooled to -75 °C at a ramp rate of 10 °C min^{-1} and held for 10 min, before heating to 30 °C at a ramp rate of 5 °C min^{-1}. The results from those measurements are presented here for the ChCl:U:Gly DES in urea:glycerol ratios of 1.5:0.5 (Figure A.1), 1:1 (Figure A.2), and 0.5:1.5 (Figure A.3).

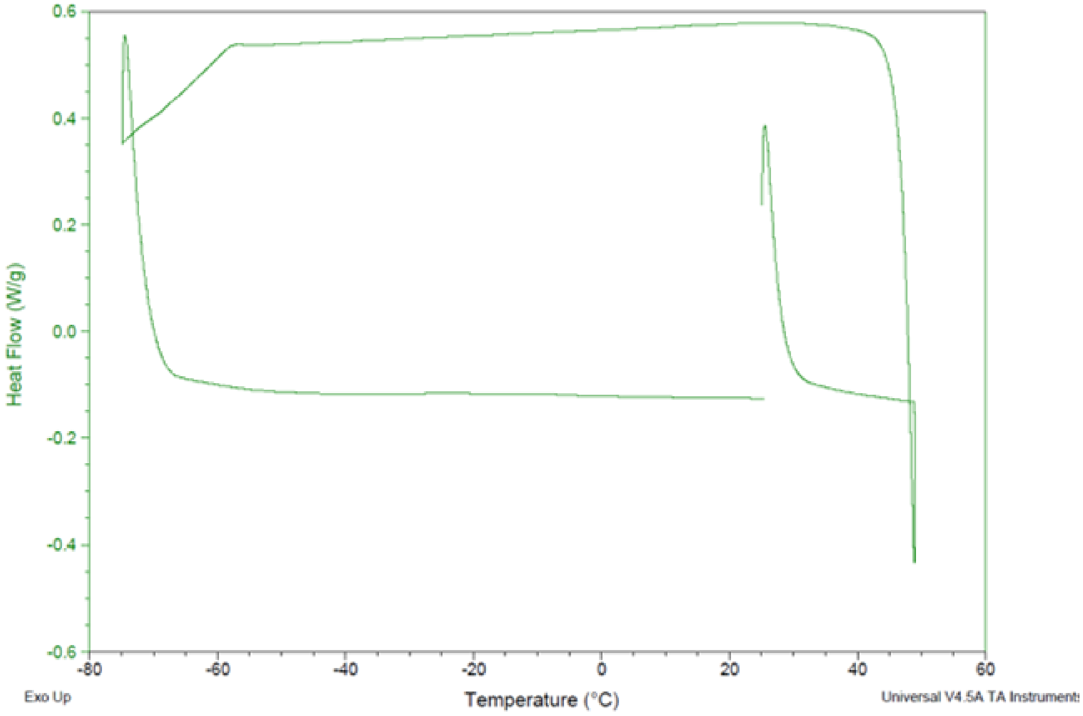

Figure A.1: DSC measurements for ChCl:U:Gly DES with a urea:glycerol ratio of 1.5:0.5. Reprinted with permission from Reference [13]. Copyright 2020, American Chemical Society.

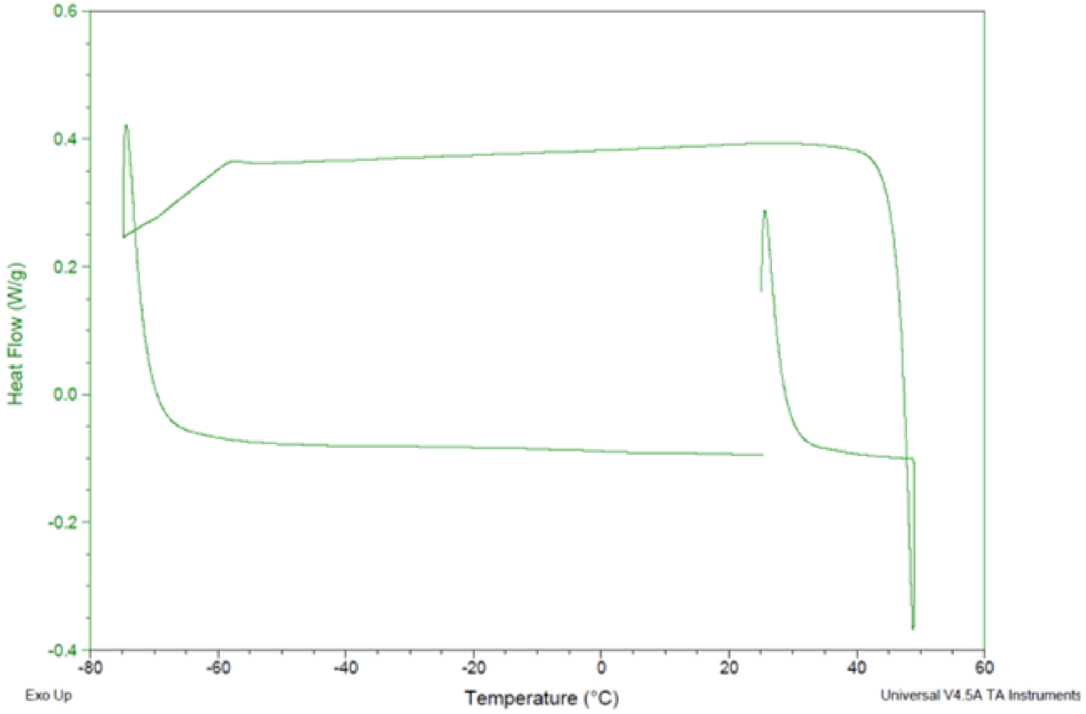

Figure A.2: DSC measurements for ChCl:U:Gly DES with a urea:glycerol ratio of 1.5:0.5. Reprinted with permission from Reference [13]. Copyright 2020, American Chemical Society.

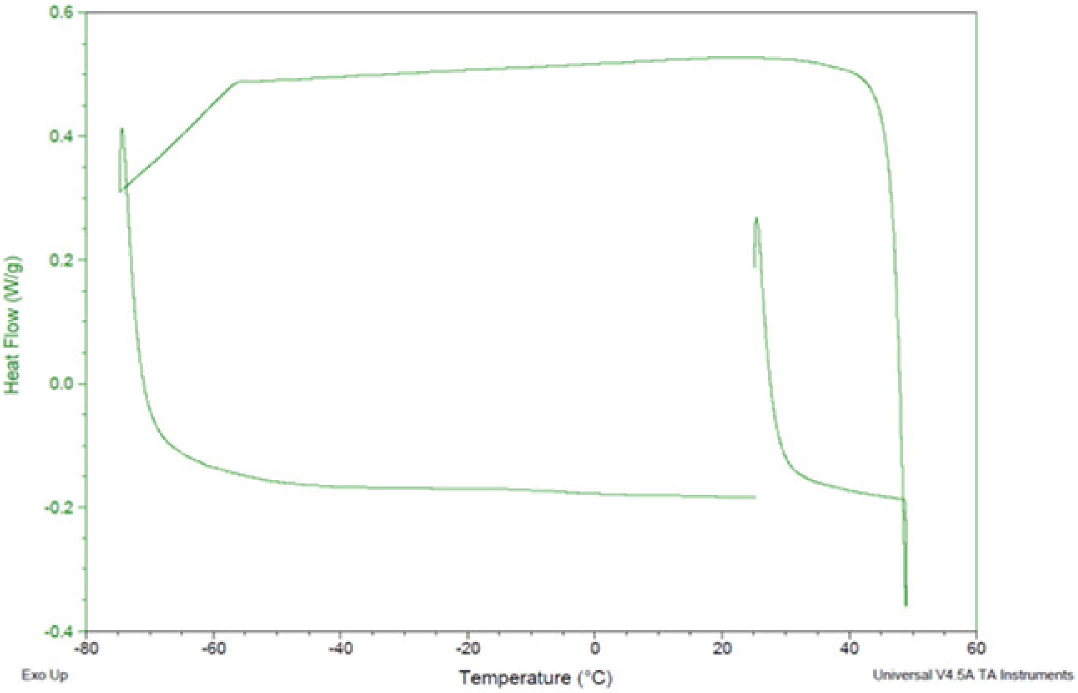

Figure A.3: DSC measurements for ChCl:U:Gly DES with a urea:glycerol ratio of 1.5:0.5. Reprinted with permission from Reference [13]. Copyright 2020, American Chemical Society.

A.2 Data plots from fluorescence spectroscopy results

Fluorescence spectroscopy using pyrene as a probe molecule was used to estimate the CMCs of SDS, C_{12}TAB in ChCl:urea:glycerol (urea:glycerol = 1.5:0.5), and for C_{16}TAB in ChCl:urea:glycerol (urea:glycerol = 1.5:0.5, 1:1, 0.5:1.5). Graphs showing the data plotted as concentration vs. the I_1/I_3 ratio are given in Figures A.4 and A.5.

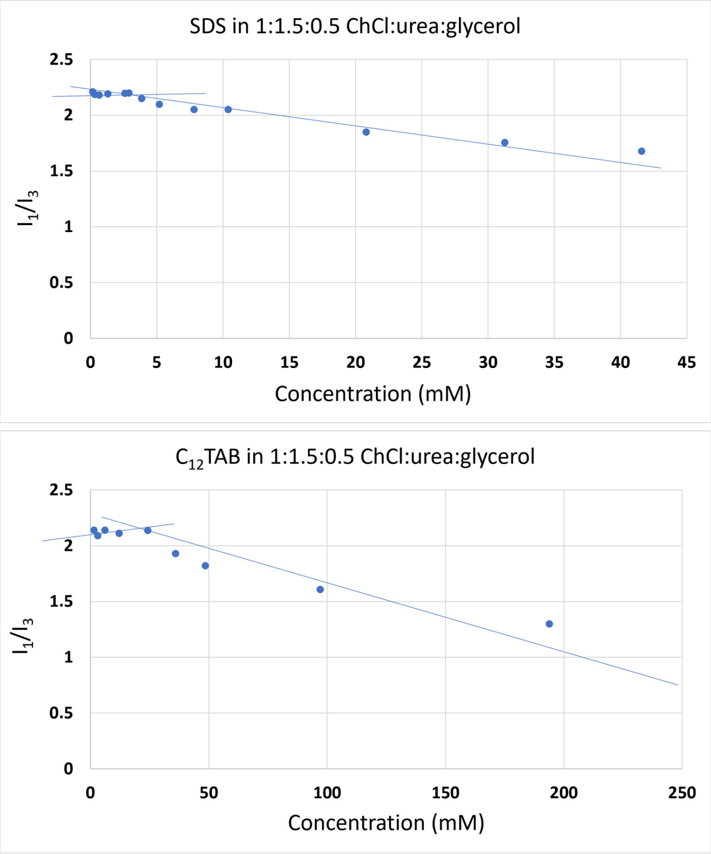

Figure A.4: Plots of concentration (mM) vs. I_1/I_3 derived from pyrene fluorescence spectroscopy measurements of solutions of SDS (top) and C_{12}TAB (bottom) in ChCl:urea:glycerol with urea:glycerol ratio of 1.5:0.5.

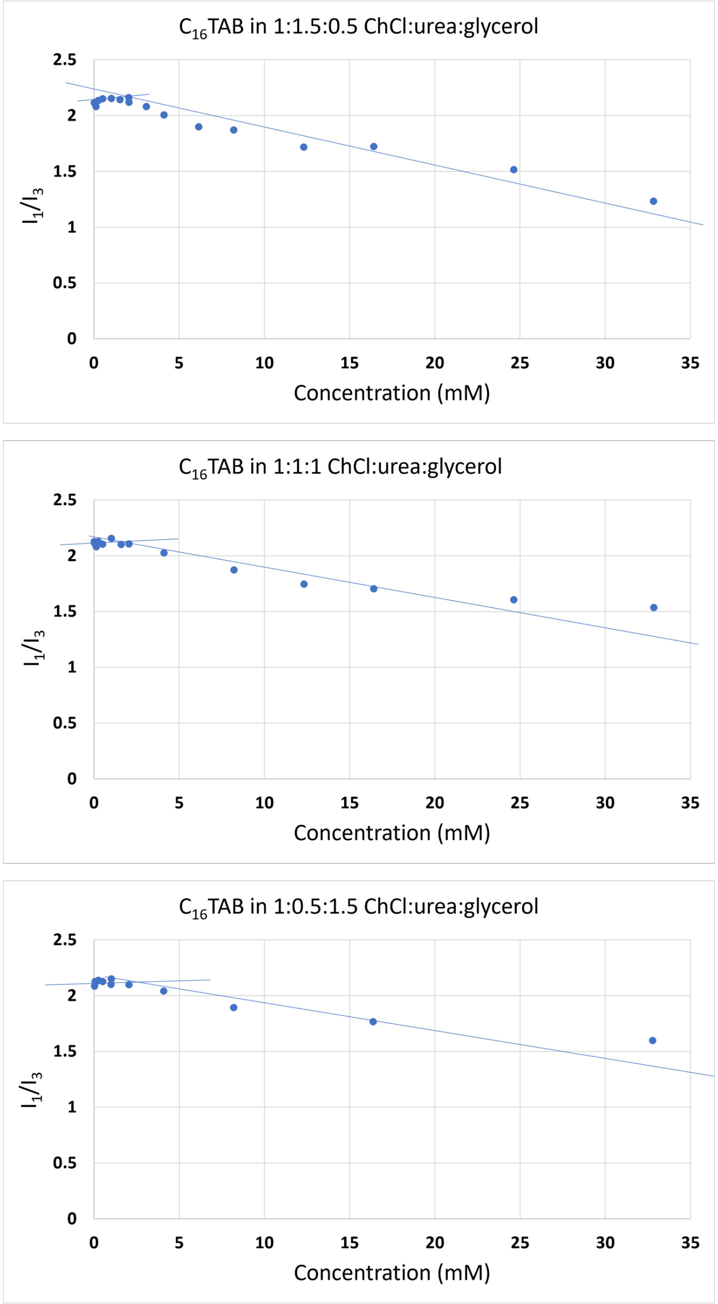

Figure A.5: Plots of concentration (mM) vs. I_1/I_3 derived from pyrene fluorescence spectroscopy measurements of solutions of C_{16}TAB in ChCl:urea:glycerol with urea:glycerol ratios of 1.5:0.5 (top), 1:1 (middle) and 0.5:1.5 (bottom).

A.3 SLD values of system constituents

Table A.1: Extended lengths (where relevant), volumes, neutron scattering lengths (b_{coh}), and scattering length density values of the various constituents of the ternary DES system and surfactant molecules used in this study. The neutron scattering length of each component was calculated as the sum of the individual scattering lengths of the atoms within each unit. Extended lengths for surfactants were taken from a previous publication (Ref [14]), and were originally calculated by the authors from Tanford equations [25].

Unit	Length (Å)	Volume (Å^3)	b_{coh} (fm)	SLD (x10^{-6}Å^{-2})
$C_5H_{14}NOCl$	-	198	5.6	0.28
$C_5H_5D_9NOCl$	-	198	99.3	4.91
CH_4N_2O	-	76	16.2	2.15
CD_4N_2O	-	76	57.9	7.66
$C_3H_8O_3$	-	126	7.4	0.612
$C_3D_8O_3$	-	126	90.7	7.48
H_2O	-	30	-1.68	-0.56
D_2O	-	30	19.14	6.4
C_3H_9NBr	-	135 [514]	2.41	0.18
C_3D_9NBr	-	135 [514]	96.1	7.12
$C_{16}H_{33}$	21.74 [14]	458 [14]	-17.2	0.37
$C_{16}D_{33}$	21.74 [14]	458 [14]	326	7.12

Table A.2: Calculated SLDs for the ternary DES investigated in this study. SLDs were obtained by considering the neutron scattering lengths of the individual components together with their mole fractions in each DES. Component ratios are reported as the ratio of ChCl:urea:glycerol. Where water has been added to the DES, the amount added was 10 molar equivalents relative to the molar amount of ChCl in the DES.

DES ratio	Isotopic mixture	SLD ($\times 10^{-6}$ Å^{-2})
1:1.5:0.5	H:H:H	0.92
1:1.5:0.5	D:D:D	6.32
1:1.5:0.5 + 10 mol. equiv. H_2O	H:H:H:H	0.251
1:1.5:0.5 + 10 mol. equiv. D_2O	D:D:D:D	6.26
1:1:1	H:H:H	0.74
1:1:1	D:D:D	6.37
1:0.5:1.5	H:H:H	0.60
1:0.5:1.5	D:D:D	6.41

Appendix B

Supplementary data from Chapter 5

B.1 Lennard-Jones parameters and intramolecular bond lengths

Table B.1 gives the Lennard-Jones (ϵ and σ) and charge (q) parameters initially assigned to the various constituents of ChCl:urea:glycerol DES (with/without $FeCl_3$) when defining the reference potential in the Empirical Potential Structure Refinement (EPSR) model. As discussed in the main text, parameters used for choline chloride were derived from previous work on the choline chloride:urea DES [75], parameters for urea were derived from those presented by Rousseau et al. for urea in its crystal phase [510], whilst parameters for glycerol were derived from those previously assigned by Towey et al. in their analysis of the liquid structure of glycerol [484].

Table B.1: Lennard-Jones (ϵ and σ) and charge (q) parameters initially assigned to the various constituents of the system for the reference potential component of the Empirical Potential Structure Refinement (EPSR) model.

Atom type	ϵ (kJ mol^{-1})	σ (Å)	q (e)
Choline chloride			
Cl1	0.80	3.2	-1.000
C1	0.80	3.7	-0.180
H1	0.20	0.258	0.060
H2	0.20	0.258	0.060
H3	0.20	0.258	0.060
N1	0.70	3.2	1.000
C2	0.80	3.7	-0.120
C3	0.80	3.7	0.145
O1	0.65	3.1	-0.683
H4	0.00	0.00	0.418
Urea			
CU	0.439	3.75	0.142
OU	0.878	2.96	-0.390
NU	0.711	3.20	-0.542
HU1	0.00	0.00	0.333
HU2	0.00	0.00	0.333
Glycerol			
CG1	0.80	3.70	0.170
OG1	0.65	3.10	-0.625
CG2	0.80	3.70	0.107
HG	0.00	0.00	0.063
HGO	0.00	0.00	0.392
FeCl$_3$			
Fe1	0.105	1.90	3.000
ClF	0.80	3.20	-1.000

Table B.2: Assigned interatomic bond lengths between pairs of atoms in the model. Atom labels are taken from those presented in Figure 5.6.

Atom 1	Atom 2	Bond length (Å)
Choline chloride		
C1	H1	1.12
C1	N1	1.49
N1	C2	1.51
C2	H2	1.13
C2	C3	1.53
C3	H3	1.12
C3	O1	1.41
O1	H4	0.97
Urea		
CU	OU	1.26
CU	NU	1.33
NU	HU1	0.99
NU	HU2	0.99
Glycerol		
CG1	OG1	1.42
CG1	CG2	1.53
OG1	HG	1.13
OG1	HGO	0.97
OG1	CG2	1.41
CG2	HG	1.12

B.2 Partial radial distribution functions for ChCl:U:Gly = 1:1.5:0.5

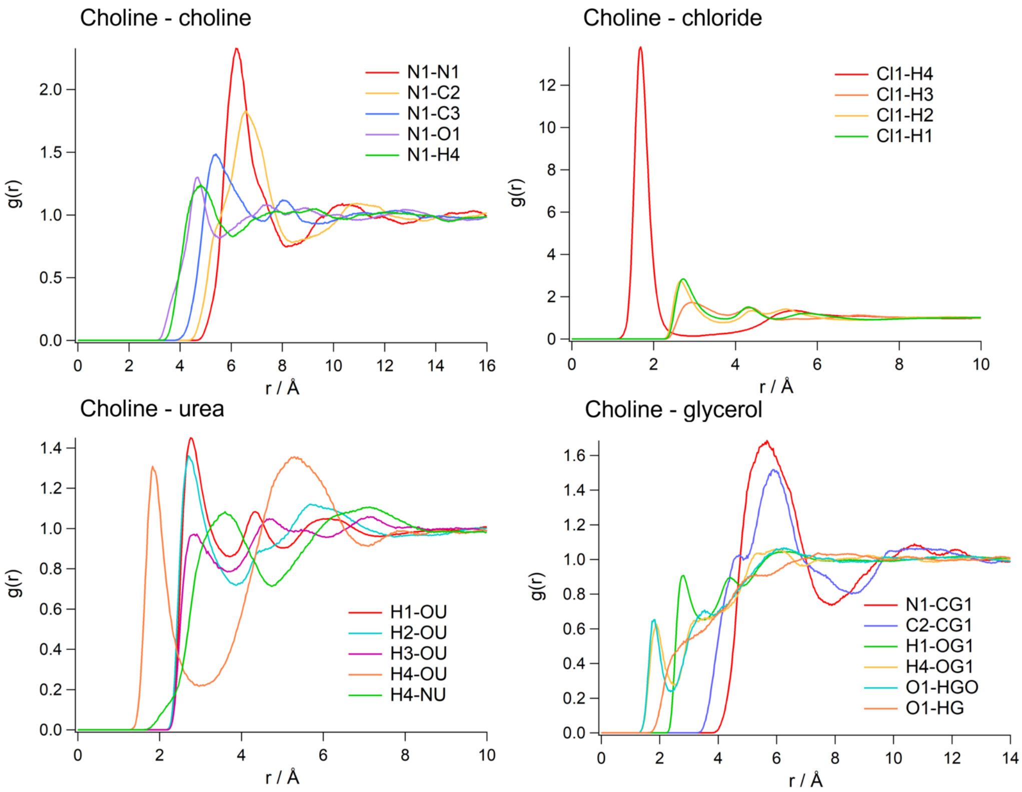

Figure B.1: Partial (site-site) radial distribution functions for various species included in the EPSR refinement of diffraction data from the 1:1.5:0.5 ChCl:U:Gly DES, centred on choline. For clarity, the p-RDFs presented in this figure are those centred on the interactions which provide the most structural information about the systems.

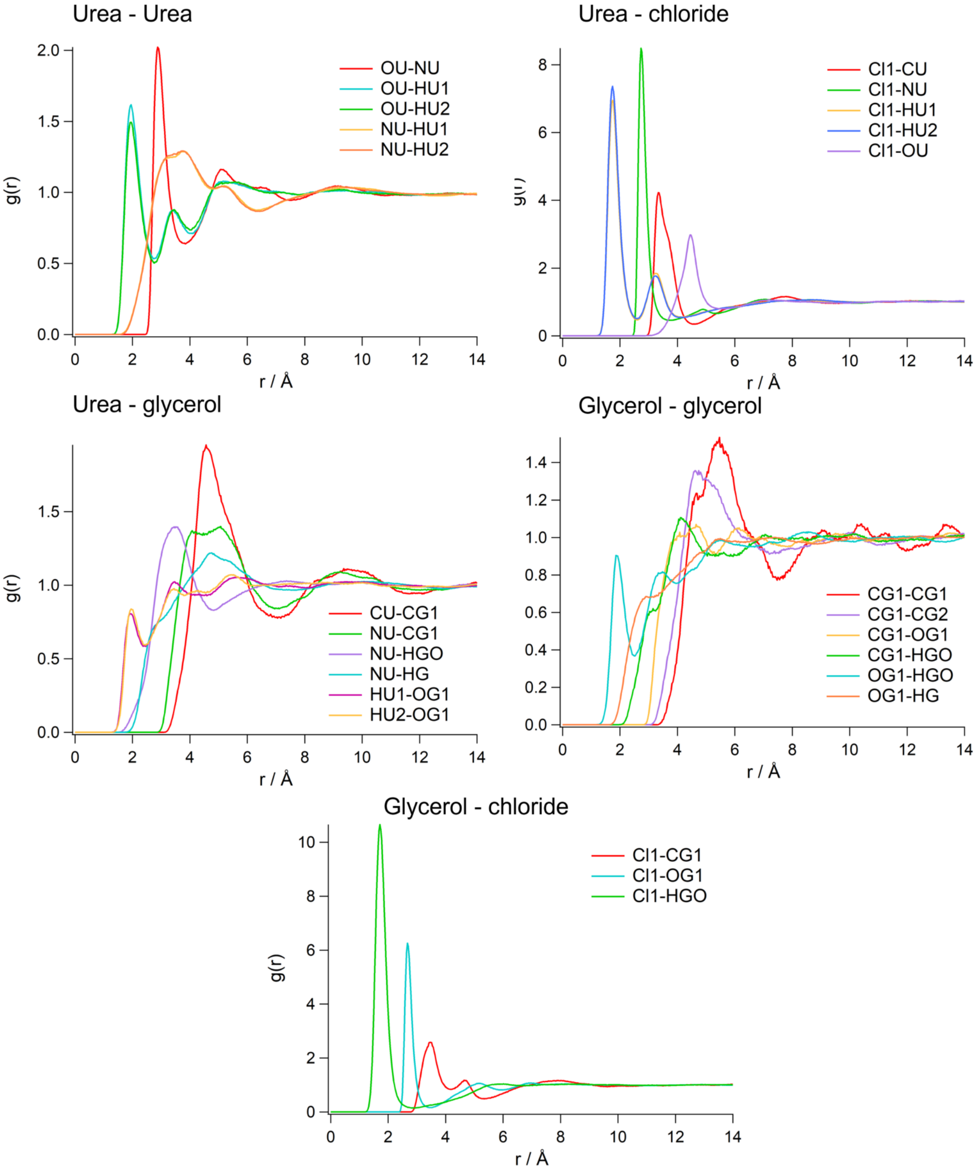

Figure B.2: Partial (site-site) radial distribution functions for various species included in the EPSR refinement of diffraction data from the 1:1.5:0.5 ChCl:U:Gly DES, centred on urea and glycerol. For clarity, the p-RDFs presented in this figure are those centred on the interactions which provide the most structural information about the systems.

B.3 Partial radial distribution functions for ChCl:U:Gly = 1:0.5:1.5

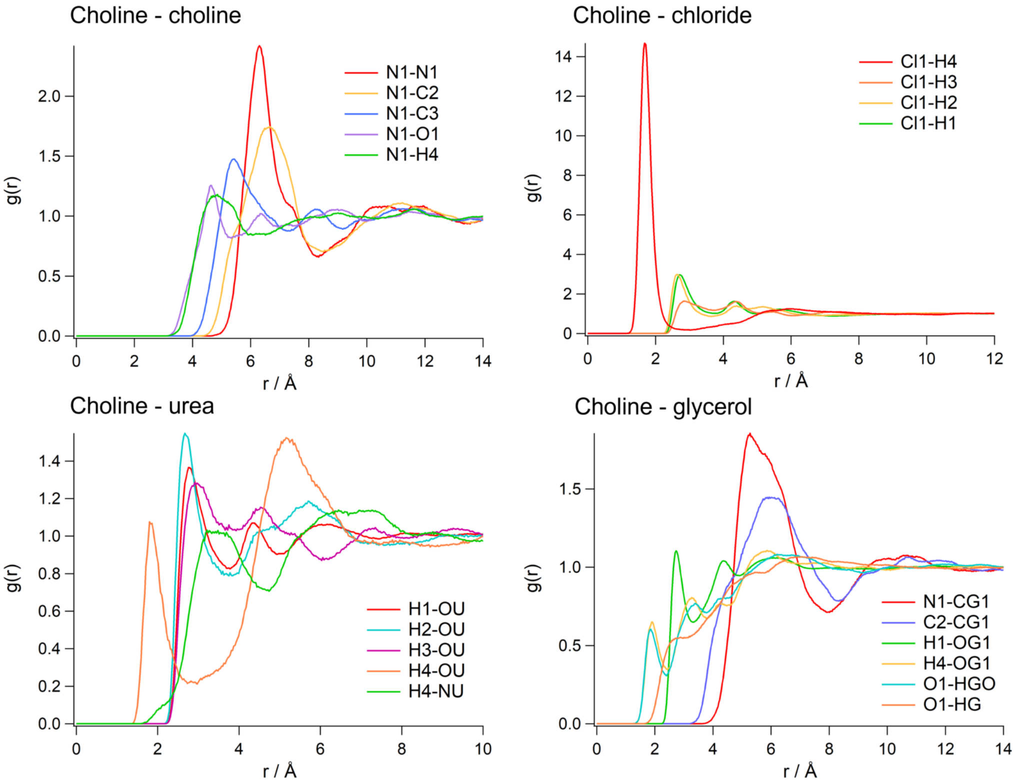

Figure B.3: Partial (site-site) radial distribution functions for various species included in the EPSR refinement of diffraction data from the 1:0.5:1.5 ChCl:U:Gly DES, centred on choline. For clarity, the p-RDFs presented in this figure are those centred on the interactions which provide the most structural information about the systems.

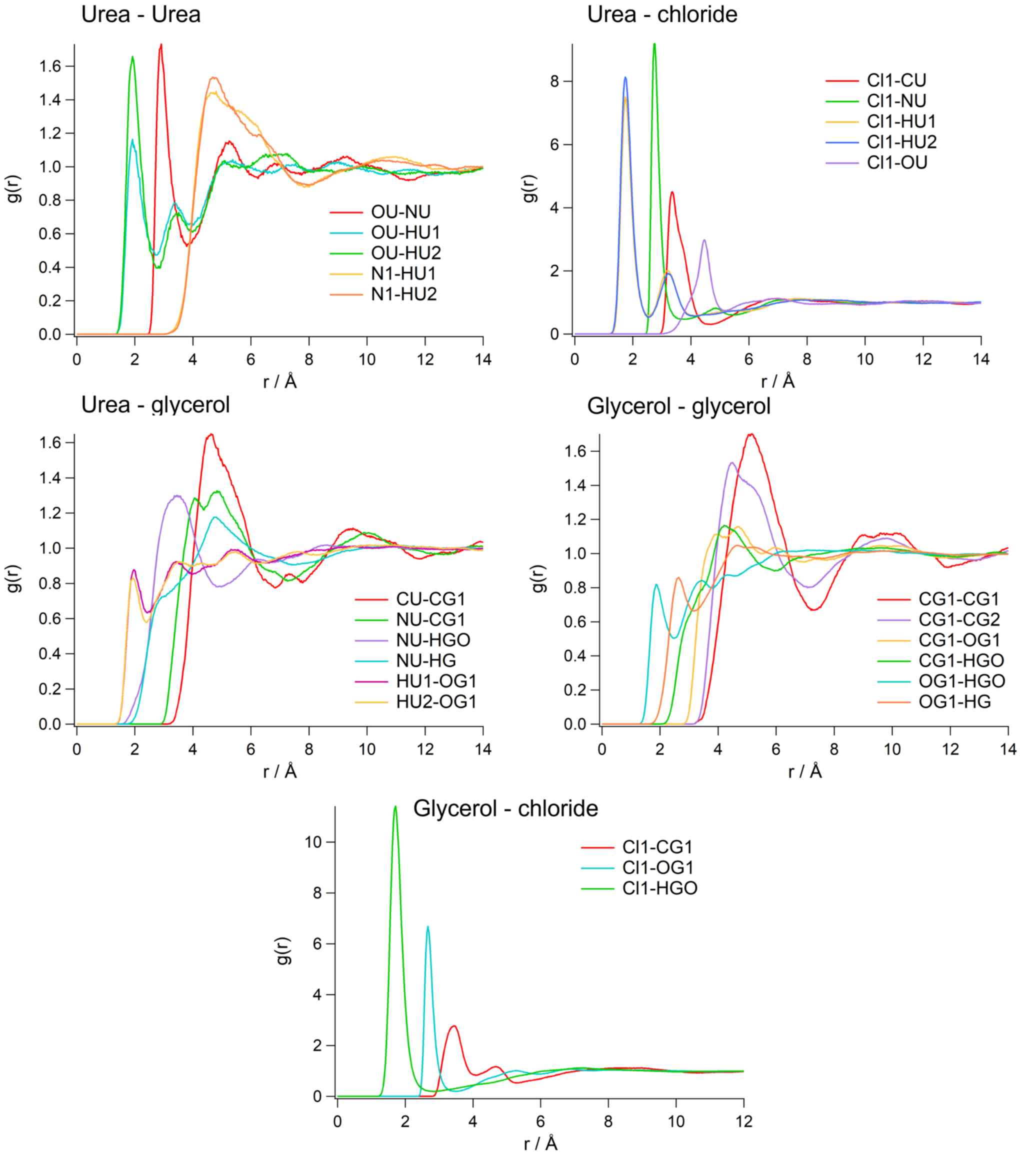

Figure B.4: Partial (site-site) radial distribution functions for various species included in the EPSR refinement of diffraction data from the 1:0.5:1.5 ChCl:U:Gly DES, centred on urea and glycerol. For clarity, the p-RDFs presented in this figure are those centred on the interactions which provide the most structural information about the systems.

Appendix C

Method for electrodeposition of Co-S from DES-based electrolyte

C.1 Preparation of substrates and electrolyte

Fluorine-doped tin oxide (FTO) coated alumininoborosilicate glass substrates of size 10 mm x 30 mm were first cleaned by sonication in each of a 2 % solution of Hellmanex (III) soap, deionised water, acetone and isopropyl alcohol. The substrates were then washed with deionised water and dried using a gentle stream of nitrogen gas.

Nickel foam substrates were cut to a size of 10 mm x 30 mm and cleaned by first by sonication for 10 min in concentrated hydrochloric acid (37 wt.%) to remove the any surface oxidation, followed by sonicating for 5 min in each of deionised water and ethanol to remove any residual acid and other debris, before drying under a gentle stream of nitrogen [515].

ChCl:ethylene glycol (molar ratio 1:2) was prepared according to the methods described in Chapter 2. Co(II) chloride, $CoCl_2$, and thiourea were added to the DES in concentrations of 0.1 mol kg^{-1} and 0.5 mol kg^{-1}, respectively and mixed, with stirring at 50 °C until a homogeneous solution was formed.

C.2 Electrodeposition method

Electrodeposition was carried out using a three-electrode cell setup comprising the substrate (FTO-coated glass or nickel foam) as the working electrode, a Pt wire as the counter electrode and an Ag/AgCl reference electrode. The samples shown in the images in Chapter 6 were synthesised by applying a potential of -1.2 V relative to the Ag/AgCl counterelectrode for 10 min. After the deposition process was complete, the substrates were gently washed with deionised water and ethanol and dried under a gentle stream of nitrogen gas.